Quantitative X-ray Microanalysis of Heterogeneous Materials using Electron Microscopy

Yu Yuan

Department of Mining and Materials Engineering

McGill University, Montreal

November 2020

A thesis submitted to McGill University in partial fulfillment of the requirements of the degree of Doctor of Philosophy

Abstract

Accurate and efficient methods have been developed for the quantitative electron-induced X-ray microanalysis of homogeneous materials in order to calculate the chemical composition from the characteristic X-ray intensities measured using energy-dispersive spectrometry (EDS) or wavelength-dispersive spectrometry (WDS). However, for heterogeneous materials, quantitative X-ray microanalysis still faces some difficulties. For example, the accuracy of forward modeling, i.e., to predict X-ray emission with prior knowledge of the specimen and experimental setup, is influenced by the secondary fluorescence effect. Also, the complex structures of heterogeneous materials make it difficult to develop a universal inverse modeling algorithm to extract the compositional and structural information simultaneously from a series of X-ray measurements. The objective of this work is to improve the accuracy and universality of quantitative X-ray microanalysis applied to heterogeneous materials.

In this work, a secondary fluorescence correction program was first developed for bulk and multilayer materials and then extended to apply to three-dimensional (3D) heterogeneous materials. The program calculates both the characteristic and bremsstrahlung fluorescence using a hybrid model that combines Monte Carlo simulations and an analytical model. For a wide range of sample structures, including bulk, multilayers, material couples, and spherical inclusions embedded inside the matrix, simulation results of the program were compared with both the experimental data from the literature and simulation data from other Monte Carlo software. The accuracy and practicality of the program were evaluated. The program provides a fast and accurate calculation of secondary fluorescence, which significantly improves the accuracy of forward modeling.

Moreover, an inverse modeling algorithm was proposed for determining both the composition and structure of two-dimensional (2D) heterogeneous materials simultaneously from a series of X-ray measurements under different beam energies and beam positions. The effects of the input parameters, including beam energies, beam positions, and voxel size, were discussed. Several examples of applications were presented for different types of phantom samples with one-dimensional (1D) and 2D structures, and the sources of errors were analyzed. As a proof-of-

concept work, the feasibility of the inverse modeling algorithm was confirmed. This algorithm, in principle, can be extended to be applied to arbitrary 3D heterogeneous materials.

Also, the 3D quantitative X-ray microanalysis at the nanoscale was studied by combining the quantification approach with electron tomographic reconstruction. A quantification approach was introduced for quantifying the reconstructed 3D elemental distribution map obtained from EDS-STEM tomography and HAADF-EDS bimodal tomography (HEBT). The reconstructed image qualities both before and after the quantification were compared for EDS-STEM tomography and HEBT. The two reconstruction techniques and the corresponding quantification processes were successfully applied to an experimental dataset. HEBT showed advantages in image contrast and noise reduction in comparison to EDS-STEM tomography. The HEBT technique will play an essential role in the characterization of beam-sensitive samples for which the EDS maps are quite noisy and in reducing experimental acquisition time.

Résumé

Des méthodes ont été développées pour la microanalyse quantitative des rayons X induite par les électrons de matériaux homogènes afin de calculer la composition chimique à partir des intensités de rayons X caractéristiques mesurées à l'aide du spectromètre à dispersion d'énergie des rayons X (EDS) ou du spectromètre à dispersion de longueur d'onde (WDS). Ces méthodes sont très précises et efficaces. Cependant, pour les matériaux hétérogènes, la microanalyse quantitative aux rayons X a des difficultés. Par exemple, la précision de la modélisation directe, c'est-à-dire pour prédire l'émission de rayons X avec une connaissance préalable de l'échantillon et de la configuration expérimentale, est influencée par l'effet de la fluorescence secondaire. En outre, les structures complexes de matériaux hétérogènes rendent difficile le développement d'un algorithme de modélisation inverse universel pour extraire simultanément les informations de composition et de géométrie. L'objectif de ce travail est d'améliorer la précision et l'universalité de la microanalyse quantitative aux rayons X appliquée à des matériaux hétérogènes.

Dans ce travail, un programme pour la correction de fluorescence secondaire est d'abord développé pour les matériaux homogènes et multicouches, puis étendu pour les matériaux hétérogènes tridimensionnels (3D). Le programme calcule à la fois la fluorescence caractéristique et bremsstrahlung en utilisant un modèle hybride qui combine les simulations de Monte Carlo et un modèle analytique. Les résultats de simulation du programme sont comparés à la fois aux données expérimentales de la littérature et aux données de simulation d'autres logiciels de Monte Carlo pour un large éventail de géométries d'échantillons comme: les échantillons homogènes, les multicouches, les couples de diffusion et les inclusions sphériques dans une matrice. La fonctionnalité du programme est évaluée et comparée à d'autres logiciels. Le programme fournit un calcul rapide et précis de la fluorescence secondaire, ce qui améliore considérablement la précision de la modélisation directe.

De plus, un algorithme de modélisation inverse est proposé pour déterminer à la fois la composition et la structure de matériaux hétérogènes bidimensionnels (2D) simultanément à partir d'une série de mesures aux rayons X sous différentes énergies et positions du faisceau. Les effets des paramètres d'entrée comme: les énergies du faisceau, les positions du faisceau et la taille des

voxels sont discutées. Plusieurs exemples d'applications sont présentés pour différents types d'échantillons fantômes avec des structures unidimensionnelles (1D) et 2D, et les sources d'erreurs sont analysées. Comme preuve de concept, la faisabilité de cet algorithme de modélisation inverse est confirmée. Cet algorithme, en principe, peut être étendu à des matériaux hétérogènes 3D arbitraires.

De plus, la microanalyse quantitative des rayons X à l'échelle nanométrique est étudiée en combinant l'approche de quantification avec la reconstruction tomographique électronique. Une approche de quantification est introduite pour quantifier la distribution spatiale élémentaire en 3D obtenue à partir de la tomographie EDS-STEM et de la tomographie bimodale HAADF-EDS (HEBT). Les qualités d'image reconstruites avant et après la quantification sont comparées pour la tomographie EDS-STEM et HEBT. Les techniques de reconstruction et les processus de quantification correspondants sont appliqués avec succès à un ensemble de données expérimentales. HEBT donne des images avec un meilleur contraste et de réduction du bruit par rapport à la tomographie EDS-STEM. La technique HEBT jouera un rôle important dans la caractérisation des échantillons sensibles au faisceau pour lesquels les cartes EDS sont assez bruyantes et dans la réduction du temps d'acquisition expérimental.

Acknowledgements

First, I would like to express my sincerest gratitude to my supervisor, Prof. Raynald Gauvin, for his support, guidance, and encouragement throughout my PhD project. I have learnt a lot from him not only on how to be a good microscopy scientist, but also on how to be a better person.

I would like to thank Dr. Hendrix Demers, a former post-doctor in our group, for his patient and valuable guidance at the beginning of my PhD study and for sharing his profound knowledge with me even when he is away from McGill. I am very grateful for his prospective advice. My appreciation also goes to Mr. Nicolas Brodusch, for helping me in experiment design and operation.

I would like to acknowledge all my colleagues in McGill Electron Microscopy Research Group: Dr. Samantha Rudinsky, Dr. Chaoyi Teng, Mr. Frédéric Voisard, Dr. Maryam Golozar, Ms. Stéphanie Bessette, Mr. Seyedmahmoud Bayazid, Mr. Nicolas Dumaresq, Mr. Ali Jaberi, for their helps. I would like to extend my thanks to all the professors, staffs, and students in the Department of Mining and Materials Engineering. I also appreciate all my friends in Montreal for bringing so much happiness to my life.

I would like to offer my sincere gratitude to Dr. Katherine Macarthur and Prof. Rafal E. Dunin-Borkowski from Ernst Ruska-Centre for Microscopy and Spectroscopy with Electrons Physics of Nanoscale Systems and Dr. Sean M. Collins from School of Chemical and Process Engineering in University of Leeds. Thanks for their help in STEM experiments and very fruitful discussion.

I acknowledge the financial support from McGill Engineering Doctoral Award (MEDA).

I would like to take this opportunity to acknowledge my parents, Mrs. Xuezhen Guo and Mr. Haijun Yuan and my family for their support and love.

I would like to express my special gratitude to my boyfriend and future husband, Dr. Xianglong Wang for his love and accompany during the whole journey.

Contribution of authors

This thesis was prepared using a manuscript-based format according to the guidelines published by the Graduate and Postdoctoral Studies office of McGill University (http://www.mcgill.ca/gps/thesis/guidelines). The following four manuscripts are included in the present thesis:

1. Y. Yuan, H. Demers, S. Rudinsky, R. Gauvin, Secondary Fluorescence Correction for Characteristic and Bremsstrahlung X-Rays Using Monte Carlo X-ray Depth Distributions Applied to Bulk and Multilayer Materials, Microscopy and Microanalysis, 25 (2019) 92-104 (Chapter 3).
2. Y. Yuan, H. Demers, X. Wang, R. Gauvin, Secondary Fluorescence of 3D Heterogeneous Materials Using a Hybrid Model, Microscopy and Microanalysis, 26 (2020) 484-496 (Chapter 4).
3. Y. Yuan, H. Demers, N. Brodusch, X. Wang, R. Gauvin, Inverse Modeling for Quantitative X-ray Microanalysis Applied to 2D Heterogeneous Materials, Ultramicroscopy, 219 (2020) 113117. (Chapter 5).
4. Y. Yuan, K. E. MacArthur, S. M. Collins, N. Brodusch, F. Voisard, R. E. Dunin-Borkowski, R. Gauvin, Extraction of 3D Quantitative Maps using EDS-STEM Tomography and HAADF-EDS Bimodal Tomography, Ultramicroscopy, 220 (2021) 113166. (Chapter 6).

Ms. Yu Yuan developed all the programs, conducted all the simulations, analyzed the results, and wrote the manuscripts. All the manuscripts were supervised by Prof. Raynald Gauvin, who provided guidance and supplied scientific advice throughout the whole project. Dr. Hendrix Demers provided technical expertise and assisted in code development for Chapters 3 and 4. He was also involved in the discussion of the results and the manuscript revision for Chapters 3, 4 and 5. Dr. Samantha Rudinsky helped in the revision of the manuscript for Chapter 3. Dr. Xianglong Wang provided some advice for the revision of the manuscript of Chapter 4 and produced the figure for the voxel-based sample structure in Chapter 5. Mr. Nicolas Brodusch contributed to the discussion of the results in Chapter 5 and helped in the experiment design for Chapter 6. The work in Chapter 6 was conducted with collaborations with Dr. Katherine E. MacArthur and Prof. Rafal

E. Dunin-Borkowski from Ernst Ruska-Centre for Microscopy and Spectroscopy with Electrons Physics of Nanoscale Systems and Dr. Sean M. Collins from School of Chemical and Process Engineering in University of Leeds. They provided the specimen, a particle of the flux melted metal-organic framework glass, conducted the STEM experiments, and assisted in the post-processing of the STEM dataset in Chapter 6. They were also actively involved in the discussion of all the results and the revision of the manuscript in Chapter 6. Mr. Frédéric Voisard helped in the development of the project in Chapter 6.

Table of Contents

Abbreviations

ADF	annular dark-field
ART	algebraic reconstruction technique
BF	bright-field
CTEM	conventional transmission electron microscopy
DF	dark-field
EDS	energy-dispersive spectrometry
EPMA	electron probe microanalysis
ESF	edge spread function
FIB	focused ion beam
HAADF	high-angle annular dark-field
HEBT	HAADF-EDS bimodal tomography/tomographic
MSE	mean squared error
NL	layer number
NW	number of energy windows
PIXE	proton induced X-ray emission spectroscopy
SDD	silicon drift detectors
SEM	scanning electron microscopy
SF	secondary fluorescence
SIRT	simultaneous iterative reconstruction technique
SNR	signal-to-noise ratio
SSIM	structural similarity index
STEM	scanning transmission electron microscopy
TEM	transmission electron microscopy
TVM	total variation minimization
WDS	wavelength-dispersive spectrometry

XRFA	X-ray fluorescence analysis
1D	one-dimensional
2D	two-dimensional
3D	three-dimensional

Lists of tables

Lists of figures

Chapter 1. Introduction

Quantitative X-ray microanalysis can be performed using different incident beams: the electron beam (electron microscopy), X-ray beam [X-ray fluorescence analysis (XRFA)] [1], and proton beam [proton induced X-ray emission spectroscopy (PIXE)] [2], among which the electron beam provides the finest spatial resolution [3].

Conventional quantitative X-ray microanalysis in electron microscopy calculates the chemical composition of an unknown specimen using the characteristic X-ray intensities, which are measured by wavelength-dispersive spectrometry (WDS) or energy-dispersive spectrometry (EDS). For homogeneous specimens, accurate and efficient quantitative analyses can be implemented using the k-ratio method, which has been widely applied in the field of materials science and geology science [4]. However, there are still some difficulties in the quantitative X-ray microanalysis of heterogeneous materials, and those difficulties will be discussed in the following paragraphs.

The quantitative X-ray microanalysis of heterogeneous materials, also termed X-ray microanalysis inverse modeling, requires the extraction of both the compositional and structural information of an unknown specimen [5]. This includes, for example, the thickness and composition determination of a thin film in a multilayer sample [6], and the estimation of the size and composition of a particle embedded in a matrix [7]. For those heterogeneous materials, the traditional quantitative methods are not available due to the complex relationship between the X-ray emission and the composition and structure of the specimen. Instead, the Monte Carlo method is used.

The Monte Carlo method is typically used to perform the forward modeling of the X-ray microanalysis, i.e., to predict the emitted X-ray intensity with prior knowledge of the composition and structure of the specimen [8]. It utilizes random numbers and physical models to simulate the incident electron trajectory inside the specimen step by step. The X-ray emission (for both characteristic and bremsstrahlung X-rays) for each electron trajectory segment is then calculated to obtain the full X-ray spectrum. Since the electron is tracked step by step as it travels through

the specimen, the chemical composition of the specimen can be different from one place to another, which means that this method can be applied to arbitrary heterogeneous materials. However, in real applications, the lack of secondary fluorescence limits its accuracy, especially for materials with complex structures [9, 10]. Secondary fluorescence X-rays are generated through the interaction of the primary X-rays (electron-induced) with the specimen. Since X-rays can travel longer distances than electrons, secondary fluorescence may occur in the places away from the primary interaction volume, thus increasing the measured X-ray intensity. In this work, secondary fluorescence correction was first studied to improve the accuracy of forward modeling.

With an accurate forward modeling approach, we can next focus on the inverse modeling of the X-ray microanalysis. Previous research has been conducted for the inverse modeling of specimens with one-dimensional (1D) or two-dimensional (2D) structures. Those inverse modeling methods typically require prior knowledge about the specimen and are only available for a specific sample structure. For example, Campos et al. [11] calculated the thickness of thin films deposited on silicon (Si) substrates by least-squares fitting of the simulated k-ratios, obtained using the Monte Carlo method, as a function of the film thickness; Gauvin et al. [7] computed the calibration curves using the Monte Carlo method to determine the size and depth of spherical manganese sulfide (MnS) inclusions embedded in an iron (Fe) matrix. Great progress was made by Wagner et al. [5], who developed a more general inverse modeling algorithm that is applicable to arbitrary 2D and 1D structures. The algorithm used the simulated annealing method to extract the structural information from a series of X-ray measurements under different beam energies and beam positions. It, however, requires prior knowledge of the possible compositions of the specimen. The three-dimensional (3D) inverse modeling is currently implemented through a combination of the focused ion beam (FIB) and scanning electron microscopy (SEM)-EDS [12]. However, this technique is destructive. Therefore, it is necessary to develop a general non-destructive inverse modeling algorithm to extract the compositional and structural information simultaneously for an arbitrary heterogeneous material.

The development of scanning transmission electron microscopy (STEM) brings new opportunities to 3D quantitative X-ray microanalysis at the nanoscale [13]. The spatial resolution for STEM is much improved in comparison to conventional SEM because the increase in beam energy reduces the beam broadening in thin specimens. High-angle annular dark-field (HAADF)

STEM tomography and EDS-STEM tomography have been widely applied to 3D morphology characterization and chemical analysis by acquiring a tilt series of 2D projections and reconstructing the 3D structure [14]. Traditional EDS-STEM tomography can be used to extract element-specific information and perform quantitative analysis. However, it is with low signal-to-noise ratio (SNR) due to low count rates arising from limited detector solid angles for X-ray detection [15]. Zhong et al. [14] proposed a HAADF-EDS bimodal tomographic (HEBT) reconstruction technique, which significantly improves the SNR of the reconstructed element maps, making use of high-resolution information from the HAADF signal. The reconstructed element maps, however, cannot be directly converted to quantitative compositional information. Therefore, we proposed a quantification approach to calculate 3D elemental weight fraction maps from the HEBT reconstruction. This approach was applied to both the simulated and experimental datasets.

This thesis consists of seven chapters. Chapter 1 introduces the background and objectives of this work. An extensive literature review is presented in Chapter 2. Chapter 3 presents the developed secondary fluorescence correction program using a hybrid model that combines the Monte Carlo simulation with analytical modeling applied to bulk or multilayer specimens. A similar strategy is used in Chapter 4 to extend the secondary fluorescence program to apply to arbitrary 3D heterogeneous samples. A novel inverse modeling algorithm is proposed in Chapter 5 to extract the compositional and structural information simultaneously from a series of X-ray intensity measurements under different beam positions and beam energies. Chapter 6 describes the quantification approaches for both EDS-STEM tomography and HEBT to obtain high-resolution 3D element maps at the nanoscale. Chapter 7 presents the major conclusions, contributions to original knowledge, and future work.

References

1. Bertin, E.P., *Principles and practice of X-ray spectrometric analysis*. 2012: Springer Science & Business Media.
2. Govil, I., *Proton Induced X-ray Emission–A tool for non-destructive trace element analysis.* Current Science, 2001: p. 1542-1549.
3. Demers, H., *Two facets of the x-ray microanalysis at low voltage: the secondary fluorescence x-rays emission and the microcalorimeter energy-dispersive spectrometer*. 2008: McGill University.

4. Castaing, R., *Application of electron probes to local chemical and crystallographic analysis.* Ph. D. Thesis (University of Paris), 1951.
5. Wagner, H.W., et al., *Electron probe microanalysis inverse modeling.* Nuclear Instruments and Methods in Physics Research Section B: Beam Interactions with Materials and Atoms, 2001. **184**(3): p. 450-457.
6. Waldo, R., *An iteration procedure to calculate film compositions and thicknesses in electron-probe microanalysis.* Microbeam Analysis, 1988: p. 310-314.
7. Gauvin, R., G. L'Espérance, and S. St-Laurent, *Quantitative x-ray microanalysis of spherical inclusions embedded in a matrix using a SEM and Monte Carlo simulations.* Scanning, 1992. **14**(1): p. 37-48.
8. Joy, D.C., *Monte Carlo modeling for electron microscopy and microanalysis*. 1995: Oxford University Press.
9. Pfeiffer, A., C. Schiebl, and J. Wernisch, *Continuous fluorescence correction in electron probe microanalysis applying an electron scattering model.* X-Ray Spectrometry, 1996. **25**(3): p. 131-137.
10. Borisova, A.Y., et al., *Secondary fluorescence effects in microbeam analysis and their impacts on geospeedometry and geothermometry.* Chemical Geology, 2018. **490**: p. 22-29.
11. Campos, C.S., et al., *Thickness determination of ultra-thin films on Si substrates by EPMA.* Microchimica Acta, 2004. **145**(1-4): p. 13-17.
12. Burdet, P., S.A. Croxall, and P.A. Midgley, *Enhanced quantification for 3D SEM–EDS: using the full set of available X-ray lines.* Ultramicroscopy, 2015. **148**: p. 158-167.
13. Pennycook, S.J. and P.D. Nellist, *Scanning transmission electron microscopy: imaging and analysis*. 2011: Springer Science & Business Media.
14. Zhong, Z., et al., *A bimodal tomographic reconstruction technique combining EDS-STEM and HAADF-STEM.* Ultramicroscopy, 2017. **174**: p. 35-45.
15. Slater, T.J., et al., *STEM-EDX tomography of bimetallic nanoparticles: A methodological investigation.* Ultramicroscopy, 2016. **162**: p. 61-73.

Chapter 2. Literature review

Electron microscopy is an important technique for the observation and characterization of various materials on a micrometer to nanometer scale [1]. Using different types of equipment including SEM, transmission electron microscope (TEM), and STEM and a variety of detectors, many characteristics of the specimen can be examined such as chemical composition, surface topography, and crystallography. This work focuses on the extraction of chemical composition and structure information through quantitative microanalysis of the electron-induced X-ray signals captured using a WDS or EDS.

In this chapter, the interaction of electrons with the specimen and the process of X-ray emission are first introduced (section 2.1). The detection of X-ray signals and several traditional methods for quantitative X-ray microanalysis of homogeneous materials are then presented (section 2.2). The Monte Carlo method is introduced, followed by a brief review of current Monte Carlo software programs, which provides an accurate simulation of X-ray emission from heterogeneous materials with the correction of secondary fluorescence effect (section 2.3 and 2.4). The inverse modeling methods for different kinds of heterogeneous materials are reviewed (section 2.5). Finally, the STEM tomography for 3D morphology characterization and chemical analysis at the nanoscale is introduced (section 2.6).

2.1 Electron-induced X-ray emission

In this section, the physical process of X-ray generation through the interaction of an electron beam with a solid is introduced (section 2.1.1 and 2.1.2), and the interaction of X-rays with the solid is described (section 2.1.3 and 2.1.4).

2.1.1 Electron-matter interaction

The incident electrons interact with the solid atoms through a variety of physical processes, which can be broadly classified into elastic and inelastic scattering [1].

Elastic scattering occurs when the incident electron is deflected by the electrical field of an atom, causing the incident electron to change its direction. There is no energy interchange between the incident electron and the atom [2]. Although the electron scattering angle is typically a few degrees, deviations ranging from 0° to 180° are possible. One or multiple elastic scattering events may result in an electron being backscattered.

Inelastic scattering happens when the incident electron interacts with the orbital electrons of the atom. It causes the progressive energy loss of the incident electron until, eventually, its energy is too low to travel farther, and the specimen absorbs it. There are a variety of energy loss processes: ejection of outer-shell atomic electrons with high potential energy to produce secondary electrons; ejection of inner-shell atomic electrons, which may result in the generation of characteristic X-rays, Auger electrons, or Coster-Kronig transitions; deceleration of the incident electrons in the vicinity of the nuclear field with production of bremsstrahlung X-rays; generation of plasmons, oscillations of the free electron gas density; and heating of the specimen [3-5]. Although the energy loss is a discontinuous process, one can treat it as a continuous process as long as the energy loss at each scattering event is small compared with the electron energy. One of the most commonly used models of energy loss is the continuous slowing down approximation [6], which will be introduced in detail in section 2.3.1.

2.1.2 X-ray generation

Two types of X-rays are generated through the interaction of an electron beam with a specimen: characteristic X-rays and bremsstrahlung X-rays.

Characteristic X-rays

A characteristic X-ray is generated when a vacancy formed by inner-shell ionization is filled by an atomic electron from the outer shell, and the energy of the characteristic X-ray equals the difference between the energies of the initial and final states. Since the energy states of an element are sharply defined, the energy of the characteristic X-ray line from a certain element and a certain transition is characteristic, which can be used to identify the elements present in an unknown specimen. Two processes of the characteristic X-ray generation will be discussed successively: inner-shell ionization and atom relaxation [4].

An atom can be ionized with the ejection of an inner-shell electron through the inelastic scattering with an incident electron. The energy of the incident electron must be greater than (or at least equal to) the ionization energy to ionize the atom, which is the minimum energy needed to move an atomic electron out of its orbital beyond the effective influence of the nuclear charge. The ionization energies for the K-, L_3-, M_5-subshells relative to the atomic number are presented in Figure 2.1. For the same element, the ionization energy of different subshells follows: $E_K > E_{L3} > E_{M5}$. Moreover, for the same subshell, the ionization energy increases as the atomic number increases. The probability of ionization is expressed using the ionization cross-section σ. The model of calculating the ionization cross-section has been studied by many researchers [7-17]. Bote et al. [17] proposed an analytical formula, which yields relative differences within about 1% between the calculated cross-sections and those in the numerical database. Figure 2.2 shows the excellent agreement of the ionization cross-sections of gold (Au) between data from the numerical database [16] and from the analytical formula of Bote et al. [17] for a wide range of accelerating voltages. As shown in Figure 2.2 b), the relative differences for all shells are within 1%.

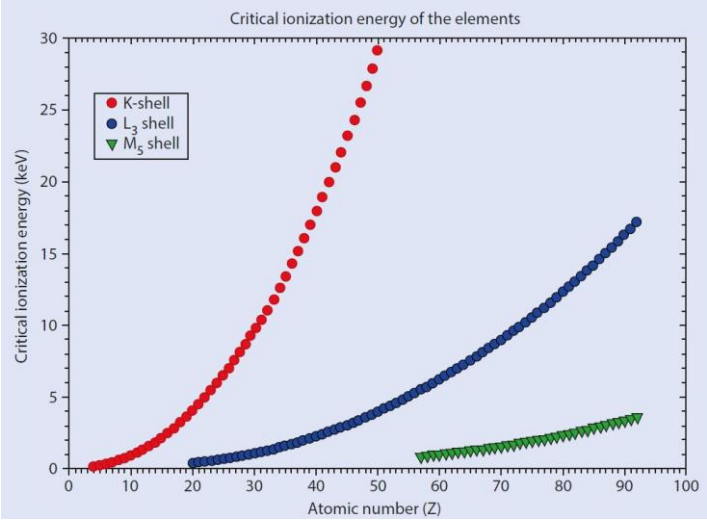

Figure 2.1 Ionization energy for the K-, L_3-, and M_5-subshells from Ref. [1]

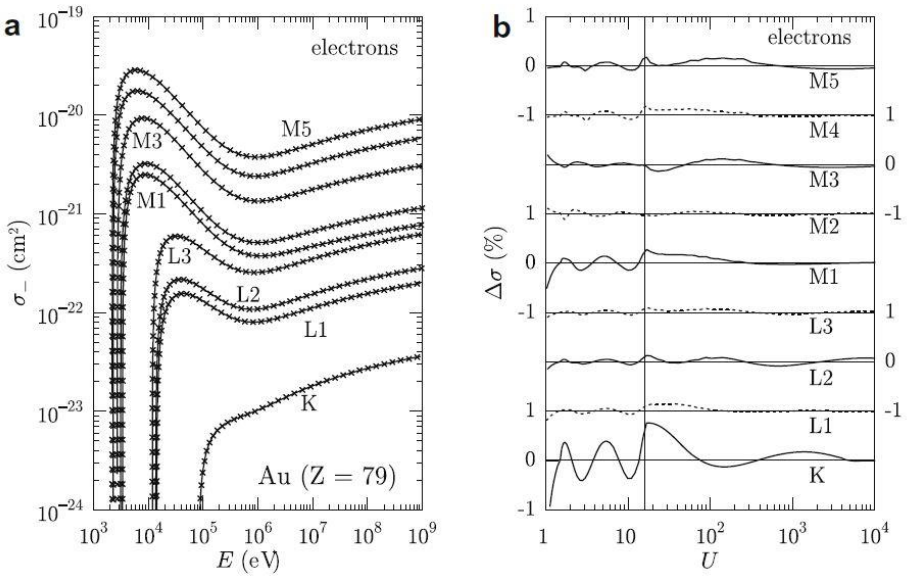

Figure 2.2 a) Comparison of the ionization cross-section of subshells of Au from the numerical database (crosses) [16] and the analytical formulas (solid line) described by Bote et al. [17]. b) Relative differences between the cross-sections from the numerical database and analytical formulas described by Bote et al. relative to the overvoltage (the ratio of the accelerating voltage to the ionization energy). For all subshells presented, the vertical axis ranges from -1% to 1%. The figures are from Ref. [17].

Three atom relaxation processes are possible after the inner-shell ionization: X-ray emission, Auger electron emission, and Coster-Kronig transition (as shown in Figure 2.3). When an outer-shell atomic electron fills the inner-shell vacancy, the energy can be released in the form of X-ray emission (Figure 2.3 a). Alternatively, possibly, the energy can be transferred into another atomic electron, resulting in the ejection of that electron, which is called an Auger electron (Figure 2.3 b). This process becomes a Coster-Kronig transition if the ejected electron and the outer-shell electron that fills the vacancy are at the same shell (Figure 2.3 c).

The fluorescence yield ω is the probability of X-ray emission as a de-excitation process when a vacancy in a certain subshell is created [18]. Several databases are available for the values of fluorescence yield [19-22]. The fluorescence yields of K-shell, L_3-shell, and M_5-shell are presented in Figure 2.4 [20]. It is observed that the fluorescence yields depend strongly on the atomic number, and, for a certain element, $\omega_K > \omega_{L_3} > \omega_{M_5}$.

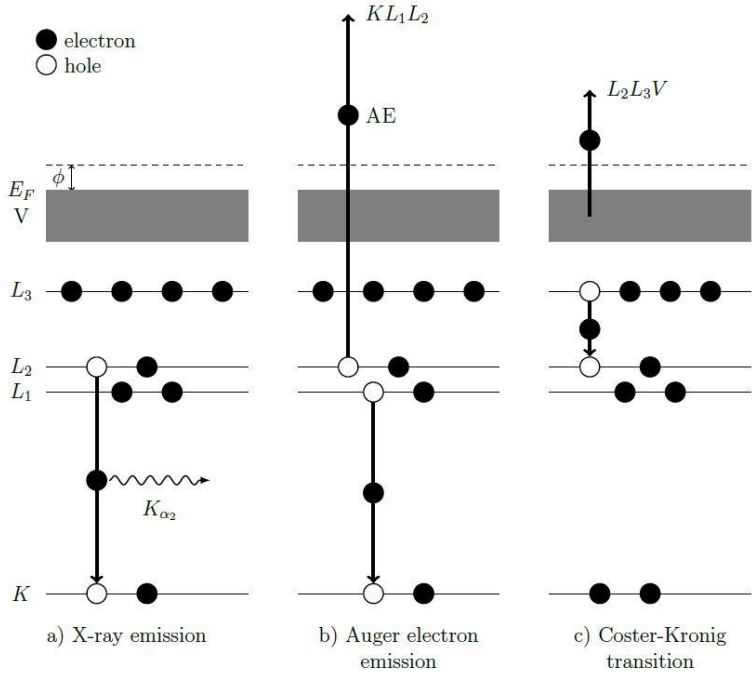

Figure 2.3 a) X-ray emission, b) Auger electron emission, c) Coster-Kronig transition as possible de-excitation processes after the K- or L-shell ionization from Ref. [5].

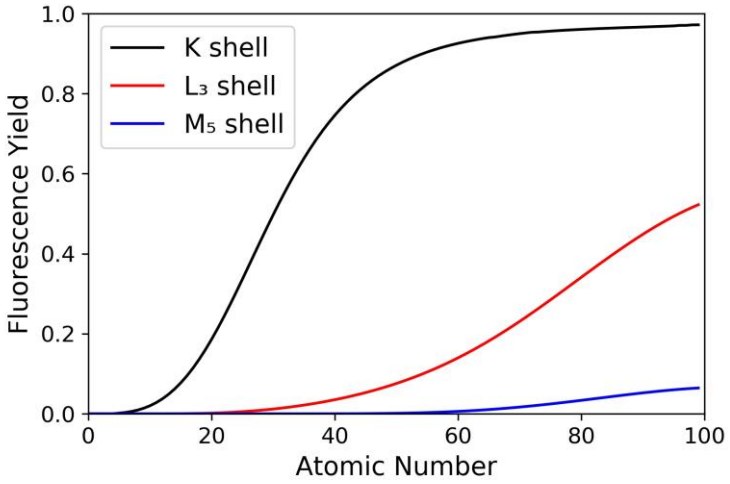

Figure 2.4 Fluorescence yield of K-shell, L_3-shell, and M_5-shell. Data from Ref. [20].

For a certain vacancy, different types of characteristic X-rays may be generated depending on which subshell the filling electron is from. For example, for copper (Cu), a K-shell vacancy can be filled by an electron from L_3-shell, which produces a Cu $K\alpha_1$ X-ray, or from L_2-shell, which produces a Cu $K\alpha_2$ X-ray. The possible shell transitions for the vacancies of K-shell, L-shell, and M-shell are shown in Figure 2.5. X-ray transition energies for different atomic numbers are

available from Ref. [19, 23-27]. The relative transition probability p is the weight of a single characteristic X-ray line of a series and can be found from Ref. [20, 28, 29].

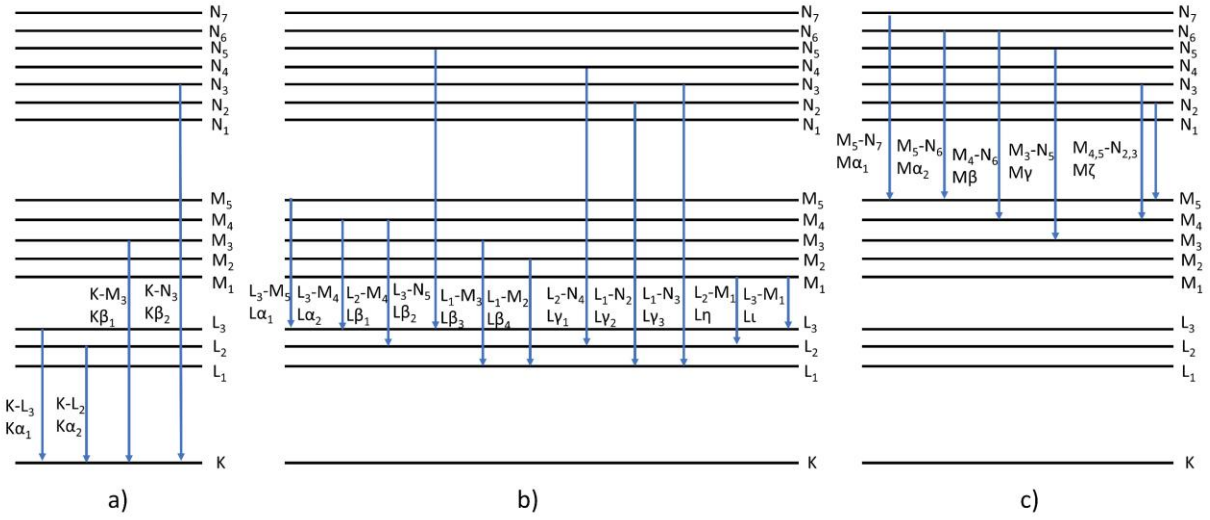

Figure 2.5 Atomic shell energy level diagrams for possible a) K-shell vacancy-filling transitions, b) L-shell vacancy-filling transitions, c) M-shell vacancy-filling transitions from Ref. [3].

Bremsstrahlung X-rays

Bremsstrahlung X-rays are generated when the incident electron undergoes deceleration because of the negative charge cloud of the atomic electrons and loses kinetic energy [3]. The lost kinetic energy can be any value ranging from 0 to the total incident electron energy E_0. The generated X-ray intensity decreases as the X-ray photon energy increases. The cut-off energy where the X-ray intensity turns to 0 is also called the Duane-Hunt limit, which is often used to monitor the incident beam energy during the experiment since the generated X-ray energy cannot be greater than the incident electron energy [30, 31]. Kramers [32] describes the variation of the bremsstrahlung X-ray intensity relative to the X-ray energy expressed as follows:

$$I(E) = kZ\frac{E_0 - E}{E} \tag{2.1}$$

where $I(E)$ is the intensity of the bremsstrahlung X-rays with energy E, k is a constant, Z is the atomic number, and E_0 is the incident beam energy. This equation is adapted to the cases when the absorption from the specimen or the X-ray detector is not strong. The bremsstrahlung cross-section

models are available in Ref. [33, 34]. Bremsstrahlung X-rays are not generated isotropically concerning the angular distribution. They tend to be enhanced in the direction along which the incident electron travels [35-37].

2.1.3 X-ray absorption

X-ray absorption

When traveling in the matter, the generated X-rays may be absorbed through three mechanisms: Compton scattering, Rayleigh scattering, and photoelectric effect [2]. Compton scattering is an inelastic scattering between an X-ray and an atom, resulting in the reduction of X-ray energy. It is negligible within the typical energy range of electron-induced X-ray microanalysis: 1–30 keV [4]. Rayleigh scattering is the interaction of the X-ray photon with the whole atom, resulting in the deflection of the X-ray with no change in energy. Rayleigh scattering is important only for the absorption of collimated beams. The photoelectric effect is the most important absorption mechanism, in which the X-ray photon is completely absorbed with the ejection of an atomic electron.

The photoelectric effect happens only when the energy of the X-ray is greater than or equal to the binding energy of the atomic electron. The Beer-Lambert law describes the absorption of X-rays in a bulk sample, expressed as follows [4]:

$$I = I_0 \exp[-(\frac{\mu}{\rho})\rho x] \tag{2.2}$$

where I is the X-ray intensity after absorption, I_0 is the incident X-ray intensity, ρx refers to the mass thickness of the specimen, which is the product of the density and thickness, μ/ρ is the mass absorption coefficient. Mass absorption coefficients of X-rays with different energies in different elements have been tabulated in units of cm^2/g [38, 39]. Figure 2.6 presents the variation of the mass absorption coefficient as a function of the X-ray photon energy in a Cu specimen. The mass absorption coefficient typically decreases as the X-ray photon energy increases. However, when the X-ray photon energy is just slightly higher than the excitation energy of a certain shell, the mass absorption coefficient increases abruptly, and this abrupt increase is called an absorption edge [2]. The absorption edges for K- and L-shells of Cu are marked in Figure 2.6 [40].

The mass absorption coefficient of a compound is calculated by summing up the weighted contributions of all the constituent elements according to their weight fractions, expressed as follows [3]:

$$(\mu/\rho)^i_{comp} = \sum_j (\mu/\rho)^i_j c_j \tag{2.3}$$

where $(\mu/\rho)^i_{comp}$ is the mass absorption coefficient of X-ray *i* in a compound, $(\mu/\rho)^i_j$ is the mass absorption coefficient of X-ray *i* in pure element *j*, and c_j is the weight fraction of element *j* in the compound.

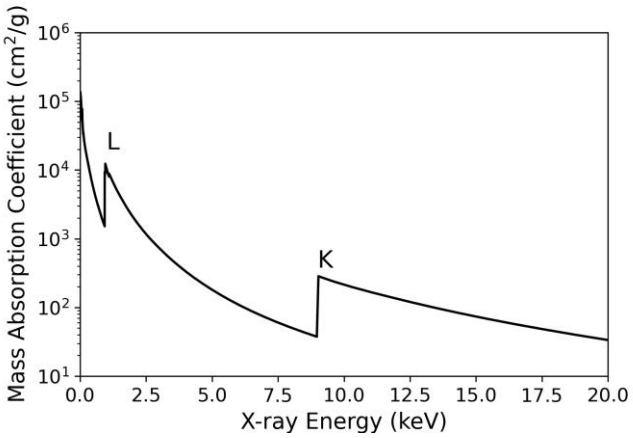

Figure 2.6 Mass absorption coefficient as a function of the X-ray photon energy for a Cu specimen from Ref. [40]

ϕ(ρz) curve

ϕ(ρz) curve describes the distribution of characteristic X-ray production as a function of depth, defined as the ratio of X-ray intensity from a thin layer of a bulk specimen with a mass thickness of $\Delta(\rho z)$ located at the mass depth (ρz), $I(\rho z)$ to that from a thin, unsupported film with the same thickness $I(\Delta\rho z)$. Thus, the total X-ray intensity for a thick sample I_{sam} is given by,

$$I_{sam} = I(\Delta\rho z)\int_0^\infty \phi(\rho z)d(\rho z) \tag{2.4}$$

Figure 2.7 presents the generated (without absorption) and emitted (with absorption) *ϕ(ρz)* curves for the aluminium (Al) Kα line in a bulk Al sample at 15 keV. It is observed that the X-ray production in the first layer of the sample is greater than that in the thin unsupported film, i.e., $\phi(0) > 1$. This is because some backscattered electrons travel back through the first layer to

escape the sample, which produces more X-rays. As the increase of the depth, the curves first rise due to the increase of elastic scattering, which increases the travel lengths of the electrons in each thin layer. X-ray production starts to decrease with further increase in depth because of the decrease in the electron number and reduced energies of the electrons as a result of energy loss. Then the X-ray production continuously decreases to zero [3].

$\phi(\rho z)$ curves can be obtained experimentally using the tracer method by Casting and Descamps [41] or the wedge technique by Schmitz [42]. Also, a lot of analytical models have been proposed to calculate $\phi(\rho z)$ curves, including thin film model (1966) [43], square model (1974) [44], the quadrilateral model (1984) [45], Gaussian model [46-48], parabolic (PAP) model [49, 50], and exponential (XPP) model [51, 52]. Furthermore, one can also use the Monte Carlo method (section 2.3.1).

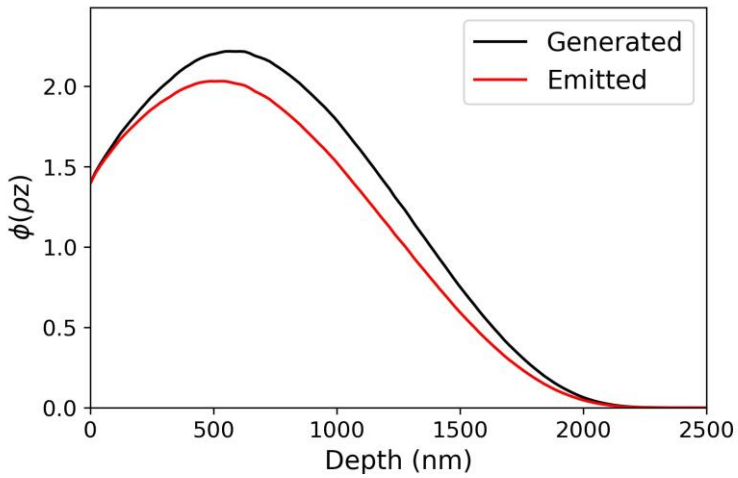

Figure 2.7 Generated and emitted $\phi(\rho z)$ curves for the Al Kα line in pure Al at 15 keV, simulated using MC X-ray [53]

2.1.4 X-ray fluorescence

As a result of photoelectric absorption, the atom will undergo a de-excitation process, as mentioned in section 2.1.2. If the energy of the electron-induced X-ray is greater than the excitation energy of a certain shell of the targeted atom, a secondary X-ray might be produced, which is termed X-ray fluorescence. More details of X-ray fluorescence are presented in section 2.4.

2.2 Quantitative X-ray microanalysis

Following the basic principles of electron-induced X-ray emission, two questions are answered in this section: how X-rays are detected and how to calculate the composition of an unknown specimen with the detected spectrum.

2.2.1 X-ray detection

Once the generated X-rays get out of the sample, some of them are detected by the X-ray detector, through which their energies or wavelengths and counts are measured. Two systems are available for such analysis: WDS and EDS.

WDS selects the X-rays to be counted according to their wavelengths using Bragg diffraction [54]. Bragg's law gives the n order reflection condition of an incident X-ray with a wavelength λ_X to be reflected by an analyzing crystal with lattice-plane spacing d at a certain glancing angle θ, expressed as follows:

$$n\lambda_X = 2d \sin\theta \tag{2.5}$$

The first order reflection (n = 1) is the most intense reflection and normally used in wavelength dispersive analysis. A crystal spectrometer can only detect X-rays of a certain wavelength at a time. A range of wavelengths can be achieved by rotating the crystal and detector at the same time, but the range is still limited by the range of rotating angle (θ typically ranges from 15º to 70º) [5]. To measure the full X-ray range, different crystals are needed. Normally, two or more WDS are equipped to cover the full X-ray range at a time. X-rays are detected with a gas-filled proportional counter through which the mean amplitude of the output pulse is proportional to the energy of the X-ray photon. For commercial EDS systems, the energy resolution of a WDS is about 10 eV [4]; however, some WDS analyzers can produce an energy resolution below 1 eV [55].

EDS, on the contrary, detects X-rays with different energies simultaneously using a semiconductor (normally Si). X-rays are first absorbed in the semiconductor through the photoelectric effect, which results in the generation of several electron-hole pairs with a mean energy $\epsilon_{e\text{-}h}$ (3.8 eV for Si). The number of electron-hole pairs $N_{e\text{-}h}$ is proportional to the X-ray photon energy, E_X:

$$N_{e-h} = \frac{E_X}{\epsilon_{e-h}} \tag{2.6}$$

The free electrons and positively charged holes then move to two sides of the crystal as a result of a strong electric field. The current is measured by a preamplifier to determine the energy of the X-ray photon [4]. Two kinds of EDS detectors are widely used: the lithium-drifted silicon (Si(Li)) detector [56] and silicon drift detector (SDD) [57, 58]. The latter detector is more advanced and has a higher count rate than the former. The energy resolution of an EDS is mainly limited by the noise amplitude of the preamplifier and the peak broadening because the number of generated electron-hole pairs yields a statistical fluctuation.

Since EDS can detect X-rays with varying energies simultaneously, it takes less time for EDS to measure the full X-ray spectrum than WDS. People, therefore, prefer to use EDS for qualitative analysis. On the other hand, the energy resolution of WDS is around ten times better than EDS. WDS also shows advantages in count rate and peak to background ratio. Thus, WDS is more likely to be used for trace elements quantitative analysis. However, the difference between EDS and WDS is becoming smaller. Recently, research has been conducted to show that EDS measurement can get similar precision and accuracy as WDS for the analyses of major and minor elements [59, 60].

2.2.2 Traditional quantification approaches

Quantitative X-ray microanalysis calculates the composition of an unknown sample using the measured characteristic X-ray intensities. Two quantification methods are widely applied to bulk materials: the k-ratio method and the f-ratio method.

k-ratio method

The k-ratio method was first proposed by Castaing [61] and improved by many scientists [3, 4]. The k-ratio (k) is the ratio of the measured characteristic X-ray intensity of the target element in an unknown specimen (I_{unk}) to that in a standard (I_{std}) [2],

$$k = \frac{I_{unk}}{I_{std}} \tag{2.7}$$

And the concentration of the target element in the unknown specimen c_{unk} is calculated using the following equation:

$$c_{unk} = c_{std} \cdot k \cdot \text{ZAF} \tag{2.8}$$

where c_{std} is the concentration of the target element in the standard, and ZAF is the matrix correction factor to correct for the differences between the unknown specimen and the standard in the electron interaction, which includes the atomic number factor (Z), X-ray absorption factor (A), and X-ray fluorescence factor (F).

There are two approaches to calculating the matrix correction factor (ZAF) [3]. One approach calculates the three factors (Z, A, and F) directly using fundamental equations that describe the physical processes [62-66]. The *ϕ(ρz)* technique uses the *ϕ(ρz)* curve to calculate Z and A and an analytical equation to calculate characteristic fluorescence (F). Bastin and Heijligers performed 1113 analyses of samples with known compositions to compare the accuracy of the two approaches [67]. They calculated the ratio of the calculated k-ratio to the measure k-ratio and plotted the error histogram of the number of analyses versus the ratio for the two approaches (as presented in Figure 2.8 [3]). The *ϕ(ρz)* technique (Figure 2.8 b) shows better performance than the ZAF approach (Figure 2.8 a).

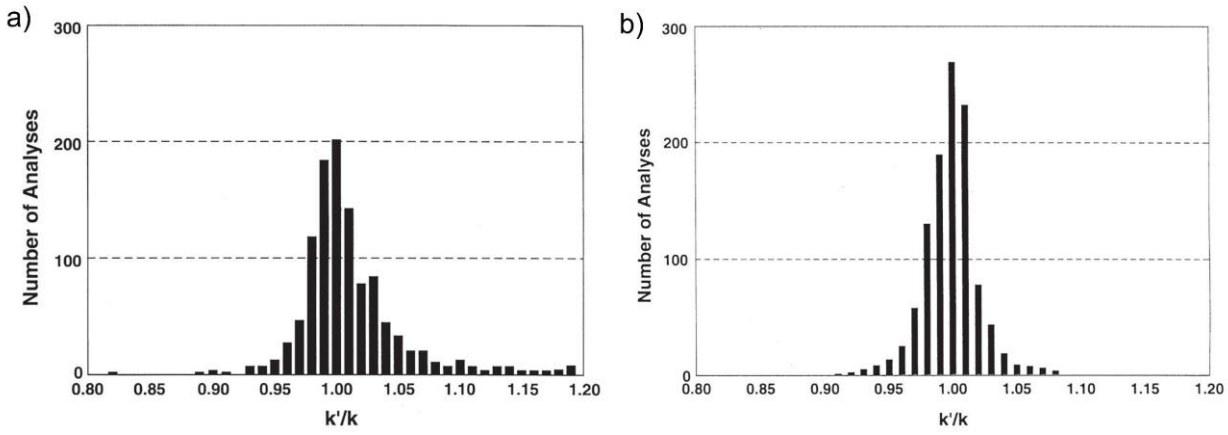

Figure 2.8 Error histogram of a) the ZAF approach and b) the *ϕ(ρz)* technique relative to the ratio of the calculated k-ratio to the measured k-ratio (figure from Ref. [3] and data originally from Ref. [67]). The data contained 1113 analyses.

In real applications, since the value of the ZAF factor depends strongly on the composition of the sample, which is unknown until the ZAF factor is obtained, an iteration process is typically performed [54].

One disadvantage of the k-ratio method is that the measurements for the unknown specimen and standard must be carried out under identical analysis conditions, which is not always achievable.

f-ratio method

Another emerging quantification approach is the f-ratio method [68-70]. This method is similar to the Cliff and Lorimer ratio method [71], which connects the ratio of the characteristic X-ray intensities of two constitute elements *A* and *B* of the specimen to the ratio of their element concentrations as follows:

$$\frac{c_A}{c_B} = K_{AB}\frac{I_A}{I_B} \tag{2.9}$$

where K_{AB} is the Cliff and Lorimer K factor, which can be calculated experimentally using a standard. Since the characteristic X-ray intensities are obtained from the same spectrum, the identical analysis condition that is required for the k-ratio method is not necessary. The Cliff and Lorimer method is typically applied to thin films, while the f-ratio method can be applied to bulk specimens.

In a binary system with element *A* and *B*, the f-ratio is defined as [72]:

$$f_A = \frac{I_A}{I_A + I_B} \tag{2.10}$$

where I_A and I_B are characteristic X-ray intensities of elements *A* and *B*, respectively. The benefit of the f-ratio method is that even when the concentration of element *B* is low and I_B is close to 0, the f-ratio is still relatively stable [73]. Normally, a calibration curve of the f-ratio versus the element concentration is first computed using either Monte Carlo simulation or analytical models, and the measured f-ratio is used to determine the concentration in the unknown sample through interpolation. The f-ratio method has been successfully applied to binary [68, 70] and multi-element systems [74].

For the mentioned quantification methods and other methods that are currently available, one identical restriction is that they can only deal with homogeneous samples or samples that are homogeneous within the interaction volume.

2.3 Monte Carlo simulation

For materials with complex geometries like multilayer materials and particles inside matrices, the traditional quantitative X-ray microanalysis methods that have been mentioned in section 2.2.2 are not applicable. The Monte Carlo method is a useful tool to simulate electron-solid interaction and estimate X-ray emissions and is available for materials with arbitrary geometries [2].

2.3.1 Monte Carlo method

The Monte Carlo method uses random numbers to predict the result of an event [75]. In electron-induced X-ray microanalysis, it is used to compute the travel direction and travel distance after each elastic collision of the incident electron with the solid to simulate the whole electron trajectory. Then, the X-ray emission in each electron trajectory segment is calculated to obtain the full X-ray spectrum. In this section, we briefly introduce one of the most popular models of simulating electron-solid interaction using the Monte Carlo method, the single scattering model. A more detailed description of the Monte Carlo method and other models can be found in Ref. [75-78].

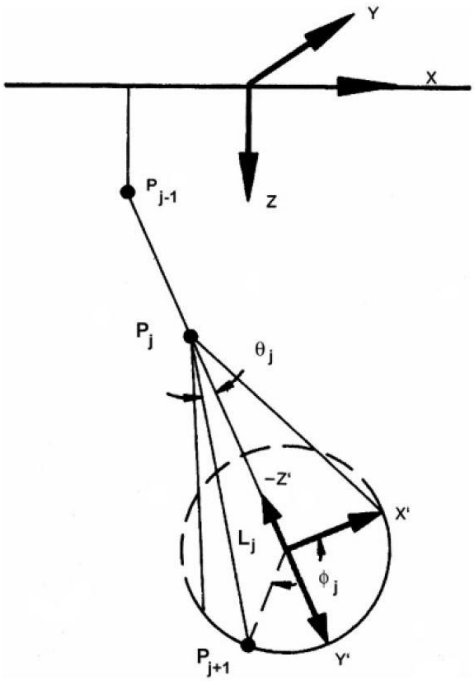

Figure 2.9 Geometry used to simulate the trajectory of an electron using the single scattering model from Ref. [79].

The single scattering model assumes that only elastic scattering events determine the trajectory of a given electron, and the process of how an electron loses its energy is continuous [75]. Figure 2.9 presents the geometry used to simulate the electron trajectory using the single scattering model [79]. An electron travels to point P_j after undergoing an elastic scattering at point P_{j-1}. To determine the position of the next scattering point P_{j+1}, the travel distance L_j and travel direction are required. Since it is assumed that only elastic scattering events are considered to determine the electron trajectory, the distance is related to the elastic mean free path, defined as follows:

$$\lambda = \frac{A}{N_0 \rho \sigma_E} \tag{2.11}$$

where A is the atomic weight of the target, N_0 is Avogadro's number, ρ is the density of the target, and σ_E is the elastic cross-section. The travel distance L_j is given by,

$$L_j = -\lambda \cdot ln(RND) \tag{2.12}$$

where RND is a random number that is uniformly distributed between 0 and 1. The travel direction depends on the polar angle θ and azimuthal angle ϕ. When using the partial Rutherford cross-section, they are expressed as [79]:

$$\cos(\theta) = 1 - \frac{2\alpha RND}{1 + \alpha - RND} \tag{2.13}$$

$$\phi = 2\pi \cdot RND \tag{2.14}$$

where α is the screening parameter. With both the travel distance and direction known, the coordinates of point P_{j+1} can be calculated. Notice that RND in equation (2.12) to (2.14) are different and generated randomly each time before being used. The energy loss during the travel from P_j to P_{j+1} is determined by the continuous slowing down approximation using the following equation:

$$E_{j+1} = E_j + \frac{dE}{dS} L_j \tag{2.15}$$

where dE/dS is the stopping power, which is typically calculated using Bethe's model [6] or its modification [80]. Please refer to Ref. [75] for a detailed explanation. The electron trajectory is simulated step by step until the electron energy is small enough or the electron escapes out of the specimen. Although the same equations are used for all the electrons, the trajectories of the electrons vary because of the use of random numbers in each step. Therefore, with a great number

of simulated electrons, the Monte Carlo method can simulate the actual electron-solid interaction in experiments. Figure 2.10 shows the electron trajectories of 200 electrons in carbon (C) at 10 keV using a Monte Carlo software program CASINO2 [81]. Red curves represent the trajectories of backscattered electrons.

The X-ray production (both characteristic and bremsstrahlung) is calculated for each segment of the electron trajectories and summed up to obtain the total X-ray intensity. The characteristic X-ray intensity in a certain segment *j* is calculated using the following equation [75]:

$$I_{cha,j} = \sigma N_A \rho \omega \cdot L_j / A \tag{2.16}$$

where σ is the ionization cross-section for the emission of characteristic X-rays, ω is the fluorescence yield, and L_j is the segment length. The bremsstrahlung X-ray intensity is calculated as follows:

$$I_{brem,j} = Q N_A \rho \cdot L_j / A \tag{2.17}$$

where Q is the ionization cross-section for the emission of bremsstrahlung X-rays. An X-ray spectrum of a Si substrate with a 200 nm chromium (Cr) coating simulated using MC X-ray [53] at 15 keV is presented in Figure 2.11 a).

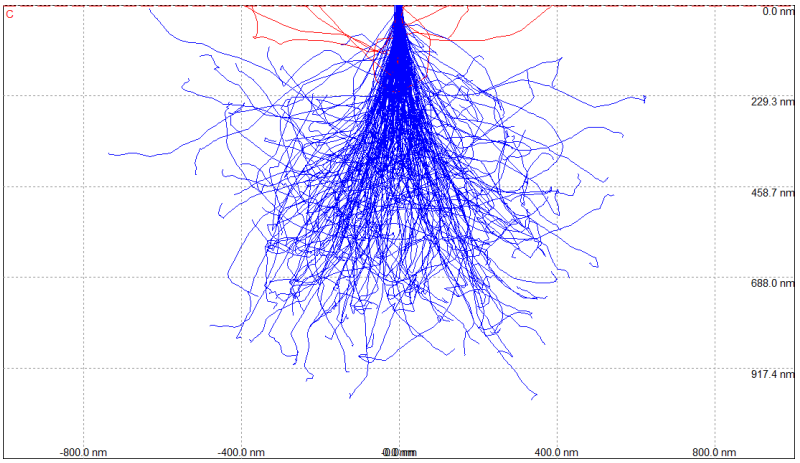

Figure 2.10 Electron trajectories of 200 electrons at 10 keV in carbon using CASINO2 [81]

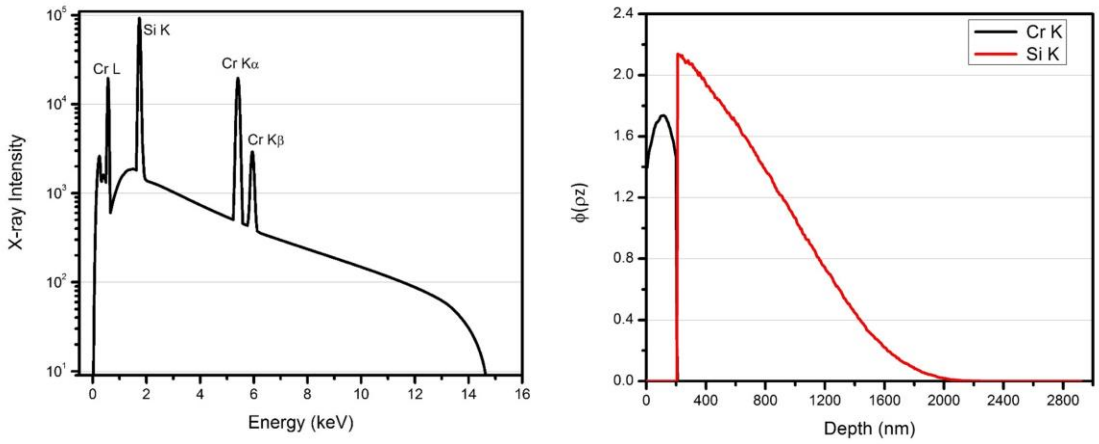

Figure 2.11 a) Simulated X-ray spectrum and b) $\phi(\rho z)$ curves for a Si substrate with a 200 nm Cr coating at 15 keV using MC X-ray [53]

Monte Carlo simulation has also been widely used in studying the spatial distribution of electrons and X-rays in bulk samples [82-85]. Good agreements in $\phi(\rho z)$ curves between the Monte Carlo simulation and experiments were found [85]. Figure 2.11 b) presents the generated depth distribution curves for both the Si K line and Cr K line for a Si substrate with a 200 nm Cr coating, in which the boundary at a depth of 200 nm is clearly shown.

Monte Carlo simulations are also applicable to heterogeneous materials, for example, multilayer materials [86, 87], particles [88], and grain boundaries [89].

2.3.2 Monte Carlo program

In this section, three commonly used Monte Carlo programs for X-ray microanalysis are briefly introduced: MC X-ray [53], DTSA-II [90], and PENEPMA [91].

Gauvin's group developed MC X-ray [53] as an extension of CASINO [81, 92] and Win X-ray [79]. It computes the full X-ray spectrum for materials with various types of structures, which can be a combination or subtraction of several basic structures: box, sphere, and cylinder. It uses the single scattering model and continuous slowing down model and allows users to choose different physical models. The graphical user interface (GUI) of MC X-ray makes it easy to use. Furthermore, MC X-ray can also output the spatial distribution of the emitted X-rays. Recently, it has been integrated into Dragonfly, a software platform for image analysis, to provide more flexibility in simulated specimens and improve simulation efficiency [93].

DTSA-II [90] is an important tool to visualize, compare, manipulate, and quantify the measured spectra, and also provides a fast simulation of X-ray spectrum for arbitrary complex samples. Similar to MC X-ray, it uses the continuous slowing down approximation for calculating X-ray emission. One advantage of DTSA-II is that it includes the calculation of secondary fluorescence, which improves the accuracy of the simulated X-ray spectrum [35].

PENEPMA, on the contrary, uses a different approach to simulating the electron-solid interaction based on a general-purpose MC package, PENELOPE, which simulates the coupled transport of electrons and photons [91]. It tracks not only the primary electrons but also all secondary (or even higher order) electrons and photons generated during the interaction. This generality provides a more sophisticated simulation; however, it also requires much more simulation time.

2.4 Secondary fluorescence effect

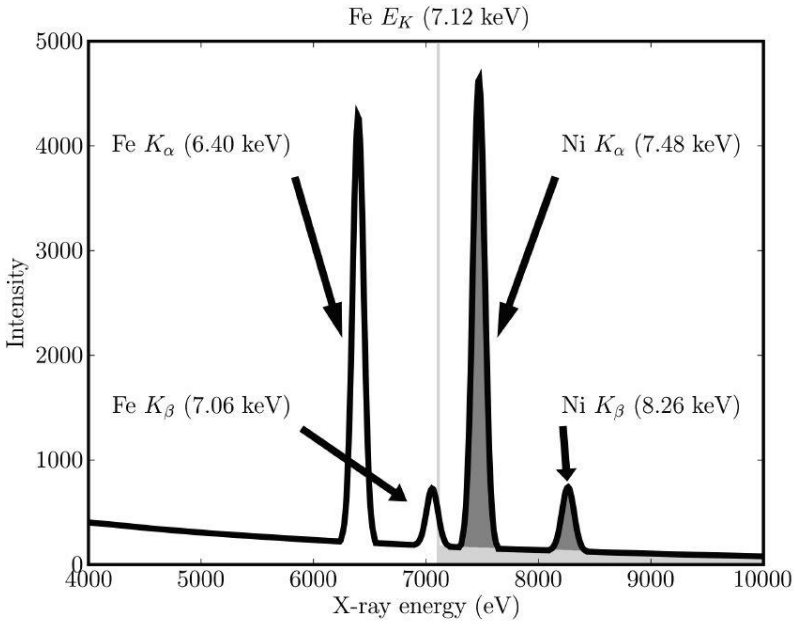

Figure 2.12 Secondary fluorescence of the Fe Kα line in an Fe-Ni alloy from the characteristic X-rays (dark gray) and bremsstrahlung X-rays (light gray) from Ref. [4]. The spectrum is obtained from Win X-ray with a beam energy of 15 keV and a take-off angle of 40º.

Secondary fluorescence is generated due to the photoelectric absorption of the primary X-rays by the solid atom, which produces an inner-shell vacancy and further emits a secondary X-ray when an outer-shell electron fills the vacancy. To produce a secondary fluorescence X-ray, the

energy of the primary X-ray has to be greater than the excitation energy of the target X-ray line. Two types of secondary fluorescence may occur depending on the type of primary X-rays: characteristic fluorescence and bremsstrahlung fluorescence. As shown in Figure 2.12, to emit Fe Kα X-rays through secondary fluorescence, the energy of the primary X-rays must be greater than the excitation energy 7.12 keV. For characteristic X-rays, both Ni Kα and Ni Kβ X-rays contribute to the emission of the Fe Kα line, termed characteristic fluorescence. The bremsstrahlung X-rays shown in the light area can cause the fluorescence of the Fe Kα line, which is called bremsstrahlung fluorescence.

2.4.1 The importance of secondary fluorescence

The magnitude of secondary fluorescence is typically small for homogeneous materials [1]; however, it can be large in some cases when two elements with close atomic numbers are present, which may result in strong characteristic fluorescence for the element with a lower atomic number. Furthermore, since X-rays can travel a greater distance than electrons, the interaction volume of secondary fluorescence is much larger than the primary interaction volume [2]. As a result, secondary fluorescence may occur in a region that is far from the primary interaction volume. This brings difficulties in quantitative analysis of heterogeneous materials or even qualitative analysis in some cases. Several examples are presented in the following paragraph.

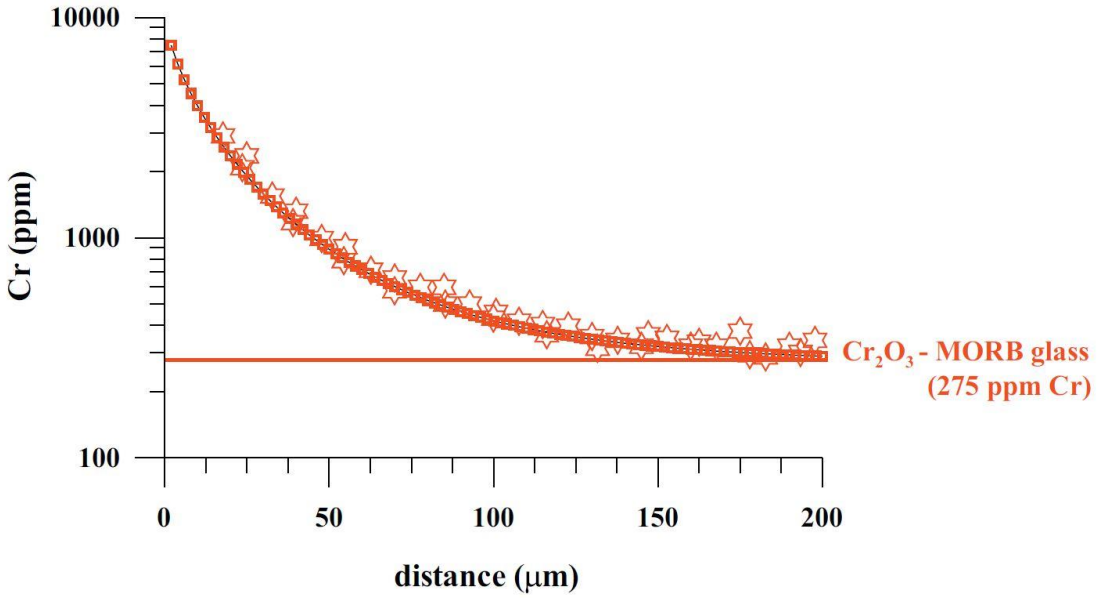

Figure 2.13 Variation of measured (stars) and calculated (squares) Cr concentration (in ppm) for a coupled mid-ocean ridge basalt (MORB) glass and Cr_2O_3 at 15 keV from Ref. [94]. The solid straight line represents the referenced concentration of Cr in the MORB glass: 275 ppm.

Borisova et al. [94] showed that a second phase could affect the quantitative analysis of a minor element through secondary fluorescence even when the distance between the boundary and beam position is 100 μm or larger. They performed quantitative analyses using both experimental and simulated data to obtain the Cr concentration in a mid-ocean ridge basalt (MORB) glass, which is coupled with a Cr_2O_3 as the change of the distance between the beam position and the crystal-glass interface. As presented in Figure 2.13, the estimated Cr concentration decreases as the distance increases and gets close to the reference value (275 ppm) only when the distance is greater than 125 μm. Cox et al. [95] mentioned that for a thin film coated on a substrate, the contribution of the secondary fluorescence could amount to 20% when the element in the thin film is fluoresced by the primary X-rays generated in the substrate. Pfeiffer et al. [96] computed the k-ratios of the molybdenum (Mo) Kα line with and without bremsstrahlung fluorescence for a Mo thin film coated on a Si substrate with various film thicknesses at 25 keV and 35 keV, as shown in Figure 2.14. The difference resulting from the fluorescence correction can rise to 22%.

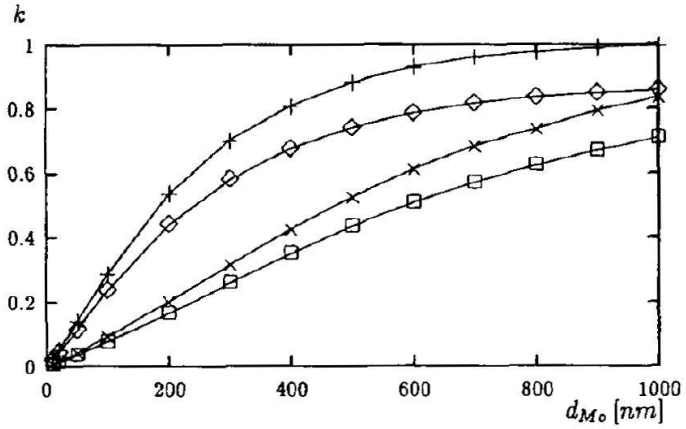

Figure 2.14 k-ratios for the Mo Kα line of Mo films with various thicknesses deposited on a Si substrate with and without bremsstrahlung florescence correction at beam energies of 25 keV (with ◊ and without +) and 35 keV (with □ and without ×) [96].

2.4.2 Fluorescence correction approaches

Currently, there are three available approaches to the secondary fluorescence correction: the Monte Carlo method, analytical modeling, and hybrid modeling that combines the former two.

Monte Carlo method

The Monte Carlo method has been introduced in section 2.3. It uses random numbers and physical models to simulate the result of an event. To compute the secondary fluorescence, the primary X-ray is propagated into a random direction for a random distance determined by the mean free path of photoelectric absorption, calculated by [35],

$$\lambda = \frac{1}{(\mu/\rho)_M \rho_M} \tag{2.18}$$

where $(\mu/\rho)_M$ is the mass absorption coefficient in the sample and ρ_M is the density of the sample. If the X-ray trajectory terminates within the sample, a secondary fluorescence event may occur at the position where the trajectory ends. The advantage of the Monte Carlo method is that it can be applied to materials with arbitrary geometries. However, this method requires a long computation time. Both DTSA-II and PENEPMA use the Monte Carlo method to compute secondary fluorescence [35]. With the help of variance reduction techniques, DTSA-II is orders of magnitude more efficient in computation than PENEPMA when similar accuracies are obtained [35].

Analytical modeling

The second approach is the analytical modeling. It computes the probability of secondary fluorescence considering the physical process consisting of three steps: the primary X-ray travels through the sample, a target element absorbs the primary X-ray, and the secondary X-ray is emitted. The analytical modeling takes much less time than the Monte Carlo method; however, it is limited in the specimen geometry and mostly based on some simplifications or approximations.

a) Bulk samples

Castaing [61] first proposed a formula for characteristic fluorescence correction of bulk homogeneous samples, and the formula was improved by Reed [66, 97] using the primary intensity formula given by Green and Cosslett [98]. The improved formula calculates the characteristic fluorescence ratio, the ratio of the fluorescence intensity of element *A* emitted by the primary X-rays of the element *B* to the primary intensity of element *A*, and is expressed as follows [66]:

$$\frac{I_{f,A}}{I_{p,A}} = 0.5 C_B \frac{\mu_B^A}{\mu_B} \frac{r_A - 1}{r_A} \omega_B \frac{A_A}{A_B} \cdot \left(\frac{U_B - 1}{U_A - 1}\right)^{1.67} \cdot \left(\frac{\ln(1+x)}{x} + \frac{\ln(1+y)}{y}\right) \tag{2.19}$$

where C_B is the weight fraction of element B, μ_B^A and μ_B are the mass absorption coefficient of pure A and the specimen respectively for the primary X-rays of element B, r_A is the jump ratio of element A, ω_B is the fluorescence yield of element B, A_A and A_B are the atomic weight of element A and B, U_A and U_B are the overvoltage for element A and B, x and y are absorption parameters calculated by,

$$x = \left(\frac{\mu_A}{\mu_B}\right) cosec(\theta) \tag{2.20}$$

$$y = \sigma/\mu_B \tag{2.21}$$

where μ_A is the mass absorption coefficient of the specimen for the X-ray of element A, θ is the take-off angle, and σ is the electron mass absorption coefficient (Lenard coefficient) representing the depth distribution of the primary X-rays. The factor $\left(\frac{U_B-1}{U_A-1}\right)^{1.67}$ represents the dependent of the primary X-ray intensity ratio of B to A on the incident beam energy. The main assumptions made

to apply equation (2.19) are that all primary X-rays are generated from the same point located on the surface of the specimen, and the X-ray depth distribution follows a simple exponential form.

Springer [99] proposed a bremsstrahlung fluorescence model for homogeneous bulk materials, expressed as follows:

$$\frac{I_{f,A}}{I_{p,A}} = 4.34 \times 10^{-6} \frac{r_A - 1}{r_A} A_A \bar{Z} E_k \frac{\mu_K^A}{\mu_K} f_{abs} \tag{2.22}$$

where $\bar{Z}$ is the mean atomic number of the specimen, which is calculated by $\bar{Z} = \sum C_i Z_i$, E_k is the excitation energy of X-ray radiation of element A, μ_K^A and μ_K are the mass absorption coefficients of pure A and the specimen on the high side of the absorption edge, and f_{abs} is the absorption factor [97, 100]. This equation has been modified or simplified by several researchers [101-103]. In general, the correction is mostly smaller than 1% and no larger than 5% [100, 104].

b) Thin films and multilayer samples

In terms of thin films and multilayer samples, Cox et al. [95] developed an analytical model to calculate the secondary X-rays generated in a coating caused by the characteristic X-rays of the substrate with the thin film assumption, i.e., the mean mass depth of X-ray production is much greater than the mass thickness of the film. Youhua et al. [105] extended Cox's model and made it available for both thin films and multilayers with multicomponent. Benhayoune [106] computed both the characteristic and bremsstrahlung fluorescence of thin coating with an oblique surface based on the formula from Cox et al. All these models ignore the depth distribution of the primary X-ray production and assume that the characteristic X-rays are generated from the mid-point of a certain layer.

Waldo [107] derived an equation for multilayer samples and incorporated $\phi(\rho z)$ analytical models into the fluorescence correction to take the depth distribution of the primary X-ray production into account. The final solution was obtained analytically, which makes it applicable to all multilayer samples but extremely complicated because of multiple integrals and the complex expression of $\phi(\rho z)$ models. Waldo also evaluated the performance of multiple $\phi(\rho z)$ models, including the PAP model from Pouchou and Pichoir [52], linear-exponential models, and Gaussian model from Packwood and Brown [46].

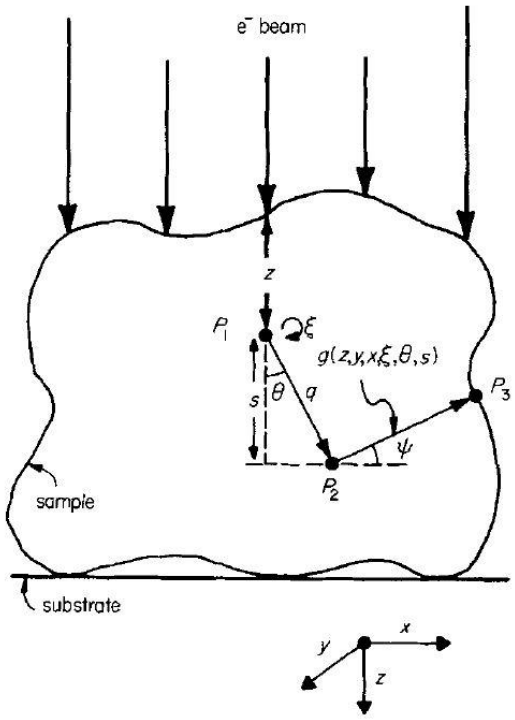

Figure 2.15 Schematic for the characteristic fluorescence in an irregular sample from Ref. [108].

Armstrong and Buseck [108] developed a general formula that applies to bulks, thin films, and single particles, and the solution of the formula can be obtained using numerical integration. For an irregular specimen, 3D X-ray distribution [$\phi\ (x, y, z)$] must be known in advance instead of the depth distribution. The schematic for the characteristic fluorescence is presented in Figure 2.15. The total characteristic fluorescence intensity of the *k* line of element *A*, I_{f,A_k} is expressed as [108],

$$I_{f,A_k} = C_A \frac{r_A - 1}{r_A} \omega_{A_k} p_k \frac{\Delta\Omega}{(4\pi)^2} \sum_B \sum_j I''_{B,j} \mu^j_{B,A} \times \int_{z=0}^{T} \frac{1}{a_0} \int_{y=\alpha_1(z)}^{\alpha_2(z)} \int_{x=\beta_1(y,z)}^{\beta_2(y,z)} \int_{\xi=0}^{2\pi} \int_{\theta=0}^{\pi} \int_{s=\gamma_1(z,y,x,\xi,\theta)}^{\gamma_2(z,y,x,\xi,\theta)} \times \left[\phi_{B,j}(x, y, z) \tan\theta\, e^{-\mu^j_B \sec\theta s} e^{-\mu^k_A g(z,y,x,\xi,\theta,s)}\right] \times ds\, d\theta\, d\xi\, dx\, dy\, dz \tag{2.23}$$

where C_A is the weight fraction of element *A* at P2, r_A is the absorption jump ratio, ω_{A_k} is the fluorescence yield of the *k* line of element *A*, p_k is the relative intensity, $\Delta\Omega$ is the solid angle, *B* and *j* represent the X-ray line *j* of element *B* that can fluoresce the *k* line of element *A*, $I''_{B,j}$ is the

generated X-ray intensity of the *j* line of element *B*, $\mu_{B,A}^{j}$ is the mass absorption coefficient of pure A for the primary X-ray of the *j* line of element *B*, *x*, *y*, and *z* represent the coordinates of P_1, where the primary X-rays are generated, a_0 is the projected area of the top surface of the specimen, ξ, θ, and s determine the position of P_2, where the secondary X-rays are generated (as shown in Figure 2.15), $\phi_{B,j}(x, y, z)$ is the spatial distribution of the primary X-rays of the *j* line of element *B*, μ_B^j and μ_A^k are the mass absorption coefficients of the specimen for the *j* line of element *B* and the *k* line of element *A*, respectively, $e^{-\mu_B^j \sec\theta s}$ represents the absorption factor of the primary X-rays during the path from P_1 to P_2, and $e^{-\mu_A^k g(z,y,x,\xi,\theta,s)}$ represents the absorption factor of the secondary fluorescence X-rays during the path from P_2 to P_3. Please refer to Ref. [108] for more details about the derivation.

As for bremsstrahlung florescence, only Pfeiffer et al. [96] developed a model for film-substrate samples using a depth distribution function for the bremsstrahlung X-rays to calculate their contributions to secondary fluorescence.

c) Non-diffusion couples

The secondary fluorescence of non-diffusion couples is also an important topic. A non-diffusion couple is formed when two different materials are separated by a sharp boundary and no diffusion is allowed between the two materials. Henoc et al. [109] and Escuder et al. [110] developed the equations of both characteristic and bremsstrahlung fluorescence for non-diffusion couples that are separated by vertical boundaries. The derivation was based on the assumption that all primary X-rays are generated from a point source that locates at the surface of the sample (see Figure 2.16 for the schematic). Bastin et al. [111] extended the model for characteristic fluorescence to be applied to more cases of two homogeneous alloys separated by both straight and curved boundaries, as shown in Figure 2.17.

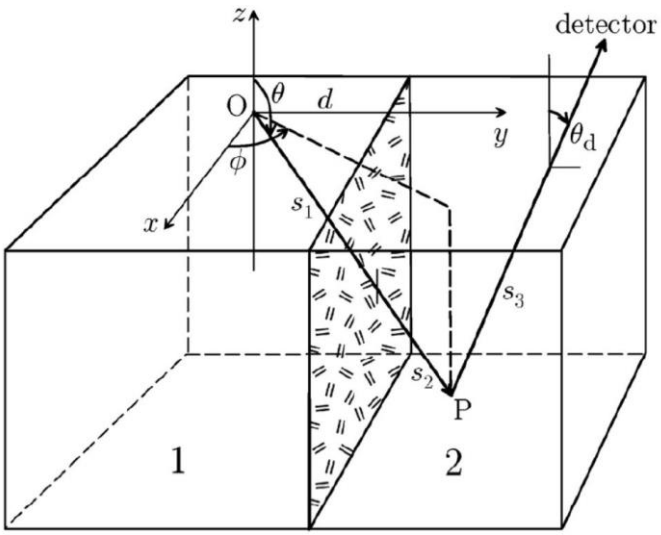

Figure 2.16 Schematic of fluorescence correction for non-diffusion couples separated by a vertical boundary from Ref. [112]. O is the beam position at which the primary X-rays are generated, and P is the position where secondary X-rays are emitted. 1 and 2 represent two different materials. *d* is the distance between the beam position and the vertical boundary.

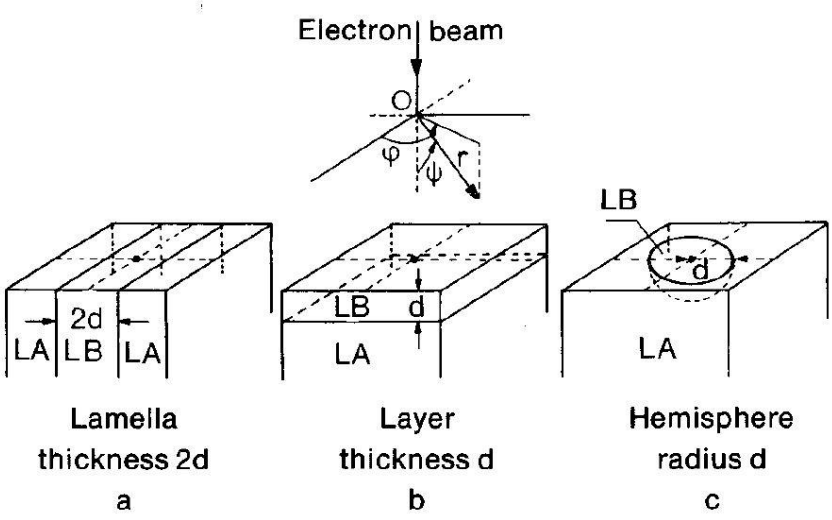

Figure 2.17 Sample geometries of a) a lamella embedded in a matrix, b) a thin layer on the top of a substrate, c) a hemisphere embedded in a matrix. The figure is from Ref. [111]. LA and LB represent two different materials.

Hybrid modeling

The third approach is the hybrid modeling, which combines the Monte Carlo method and analytical modeling. Specifically, Monte Carlo simulations are used to obtain some required physical parameters to be used in the analytical modeling for the fluorescence calculation.

Armigliato et al. [113] performed the characteristic fluorescence calculation for elements from thin films fluoresced by the primary X-rays generated from substrates using $\phi(\rho z)$ curves obtained from Monte Carlo simulations and an analytical model that incorporates $\phi(\rho z)$ data numerically. Myklebust and Newbury [114] used Monte Carlo simulations to calculate the discrete distribution of primary X-ray generation and an analytical expression to calculate characteristic fluorescence intensity for a non-diffusion couple. Llovet et al. [115] extracted the required physical interaction parameters from the Monte Carlo program PENEPMA and used them in an analytical model for both characteristic and bremsstrahlung fluorescence of bulks and non-diffusion couples. The numerical results from the hybrid model were compared with both experimental data and simulation data from PENEPMA, in which close agreements were found [115]. The hybrid modeling is more efficient than the Monte Carlo method and more accurate than the analytical modeling.

2.5 Inverse modeling of heterogeneous materials

X-ray microanalysis forward modeling is used to predict the intensity of X-ray emission with prior knowledge of the specimen and experimental setup. Inverse modeling, on the contrary, extracts the structure and composition information of an unknown specimen from a series of X-ray intensity measurements [116]. The inverse modeling of 1D, 2D, and 3D materials will be introduced in the following sections.

2.5.1 1D samples

1D samples are heterogeneous along the depth direction (the direction that is perpendicular to the specimen surface) and homogeneous on the plane that is parallel to the specimen surface. 1D samples include thin films on substrates and multilayer samples. The inverse modeling of 1D samples typically aims to determine the thickness or composition of a thin layer from the measured k-ratios.

Methods have been developed to determine the thickness of a thin film when the composition of each layer of the specimen is known [86, 117-119]. For example, Armigliato et al. [86] constructed a calibration curve of the k-ratio versus the film thickness using a Monte Carlo code and fit the measured k-ratio to determine the film thickness. Similarly, the calibration curve can be computed using analytical models [120]. Youhua [118] developed an iteration method to

calculate the mass thickness of each layer in a multilayer specimen by fitting the predicted k-ratios from a simplified Monte Carlo simulation to the measured experimental k-ratios. The calculated thicknesses agree well with the measured data.

A similar method as Youhua's method [118] was used by Hu and Pan [121] to calculate the chemical composition of a thin film deposited on a substrate with knowledge of the film thickness and the composition of the substrate. Good agreements were found with the referenced compositions, even for a film with a thickness of the order of 0.01 μm.

Waldo [122] developed an iteration procedure to calculate both the composition and thickness of materials with two thin films and a substrate simultaneously using the experimental k-ratios of each element in each layer. The sample geometry is shown in Figure 2.18. Figure 2.19 presents a flowchart of the iteration procedure. With knowledge of the experimental k-ratios, the procedure starts with the initialization of the film thickness and composition. Then, the analytical $\phi(\rho z)$ model is used to calculate the initial theoretical k-ratios $k_{i,1}$. The new concentrations and film thickness, for the first iteration, are then computed by comparing the experimental and theoretical k-ratios $k_{i,exp}$ and $k_{i,1}$. This process is repeated until the experimental and theoretical k-ratios are close enough. The method to calculate the new compositions and thicknesses for the m^{th} iteration is given by the following equations.

For the surface layer,

$$c_{i,m+1} = c_{i,m}\frac{k_{i,exp}}{k_{i,m}} \tag{2.24}$$

$$\delta_{m+1}^{f1} = \delta_m^{f1}\frac{\sum_i k_{i,exp}}{\sum_i k_{i,m}} \tag{2.25}$$

For the subsurface layer,

$$c_{i,m+1} = c_{i,m}\frac{k_{i,exp}}{k_{i,m}}\frac{\exp\left[-\delta_m^{f1}(\chi' - \chi)\right]}{\exp\left[-\delta_{m+1}^{f1}(\chi' - \chi)\right]} \tag{2.26}$$

$$(\delta_{m+1}^{f2} - \delta_{m+1}^{f1}) = (\delta_m^{f2} - \delta_m^{f1})\frac{\sum_i k_{i,exp}}{\sum_i k_{i,m}} \tag{2.27}$$

For the substrate,

$$c_{i,m+1} = c_{i,m}\frac{k_{i,exp}}{k_{i,m}}\frac{\exp\left[-\delta_m^{f1}(\chi'-\chi)\right]}{\exp\left[-\delta_{m+1}^{f1}(\chi'-\chi)\right]}\frac{\exp\left[-(\delta_m^{f2}-\delta_m^{f1})(\chi''-\chi)\right]}{\exp\left[-(\delta_{m+1}^{f2}-\delta_{m+1}^{f1})(\chi''-\chi)\right]} \quad (2.28)$$

where i represents an element in the target layer, χ, χ' and χ'' are the absorption term in the subsurface layer, surface layer, and substrate, respectively (see details in Ref. [122]). The accuracy of this method greatly depends on the accuracy of the $\phi(\rho z)$ model. Examples show that good convergence can be obtained within ten iterations. However, this method requires that no common element is present in different layers, or the k-ratios of the common element from different layers are measured separately.

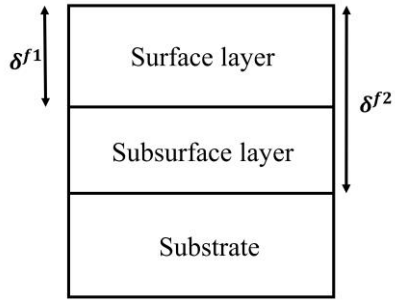

Figure 2.18 Sample geometry for Waldo's model [122]

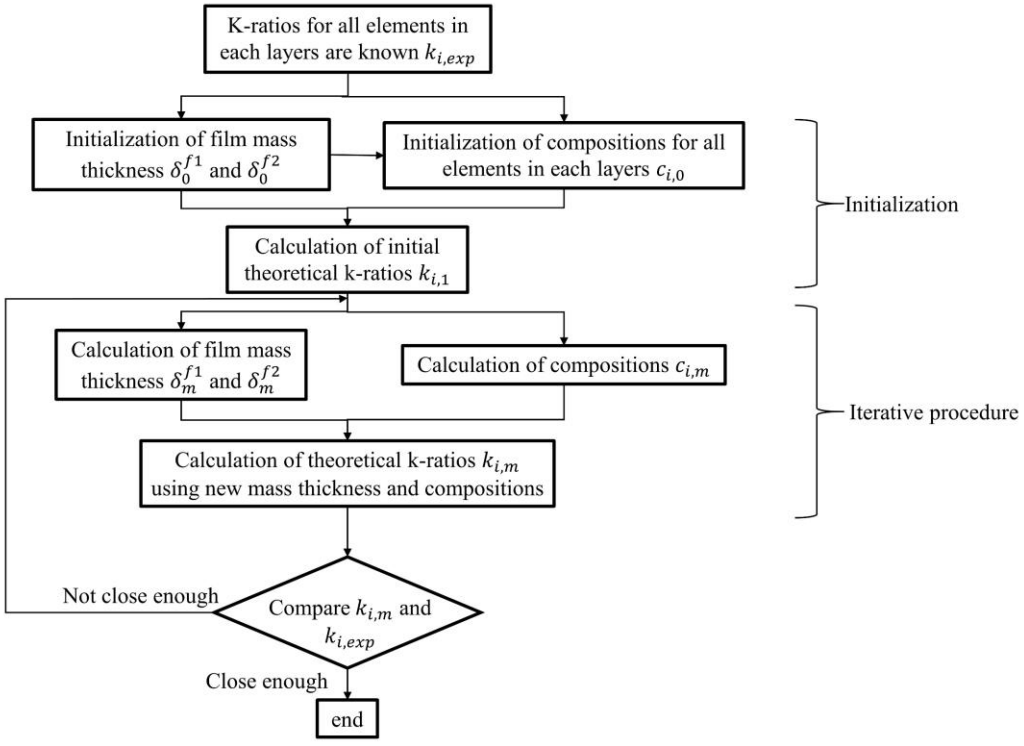

Figure 2.19 Flowchart of the iteration procedure in Waldo's model [122]

A software program, GMRFILM [123], was developed based on Waldo's model [122]. There are other software programs available to determine the composition and film thickness simultaneously, including XFILM [124], Strata [120], and Multifilm [120].

2.5.2 2D samples

The structures of 2D samples are more complex than those described above, and as a result, the analytical $\phi(\rho z)$ models are not applicable to the computation of the X-ray emission. Only the Monte Carlo method can be used for the forward modeling of 2D samples.

With prior knowledge about the structure or compositions of a specimen, a specific problem about the specimen may be solved. For example, Ro et al. [125] estimated the chemical composition of a single homogeneous particle that lies on a flat surface with known composition using an iteration procedure. In each iteration, the simulated characteristic X-ray intensities are calculated using a Monte Carlo simulation, and a new concentration is generated by successive approximation,

$$C_i^{(k+1)} = \frac{C_i^{(k)} I_{i,exp}}{I_{i,sim}^{(k)} \sum_{j=1}^{n} \left(\frac{C_j^{(k)} I_{j,exp}}{I_{j,sim}^{(k)}} \right)} \tag{2.29}$$

where $C_i^{(k+1)}$ is the *(k+1)th* approximation for the concentration of the *i*th element, $I_{i,exp}$ and $I_{i,sim}^{(k)}$ are the experimental and the *k*th simulated X-ray intensity for the *i*th element. They also estimated the C layer thickness coated on a glass particle with known composition using the simulated calibration curves of the C/O intensity ratio versus the C layer thickness at various accelerating voltages [125].

Gauvin et al. [126] constructed a calibration curve using Monte Carlo simulations to determine the depth and size of a spherical MnS inclusion embedded in an iron matrix.

Wagner [116] developed a procedure using the simulated annealing method to extract the structural information of arbitrary 2D structures from a set of X-ray intensity measurements at different beam energies and beam positions. The procedure is based on $\chi 2$ minimization between the experimental and theoretical X-ray intensities, and the theoretical X-ray intensities are computed using the Monte Carlo method. Figure 2.20 presents a flowchart of Wagner's method.

The simulated annealing is an optimization algorithm similar to the physical process of annealing of solids [127]. Slow cooling of a liquid enables the freezing and crystallization of a material into a state of minimum energy. The objective function to be minimized is the analog of the energy of the state of the crystal, and the control parameter is the analog of the temperature. In each iteration, a random modification of the state is generated, and the modification is either accepted or rejected depending on the change in the objective function and the control parameter. If the state is improved like the decrease of energy, it is always accepted. If the energy is increased, this modification is accepted with a probability $p = exp\ (-\Delta E/T)$, where ΔE is the change of energy and T is the control parameter. The control parameter T is slowly decreased to make the resulting state close to the global optimum. The objective function here refers to the $\chi 2$ deviation between the experimental and theoretical X-ray intensities. Figure 2.20 also presents the variation of the cost function and simulated sample structure relative to the control parameter for three Al_2Cu precipitates of varying sizes and depths embedded in a matrix of Al with 2 wt% Cu on a Si substrate. As the control parameter slowly decreases, the simulated structure converges to the real structure. However, the method is based on the assumption that the possible compositions of the specimen are known in advance.

Current 2D inverse modeling methods are available only with prior knowledge of the specimen (either the composition or structure).

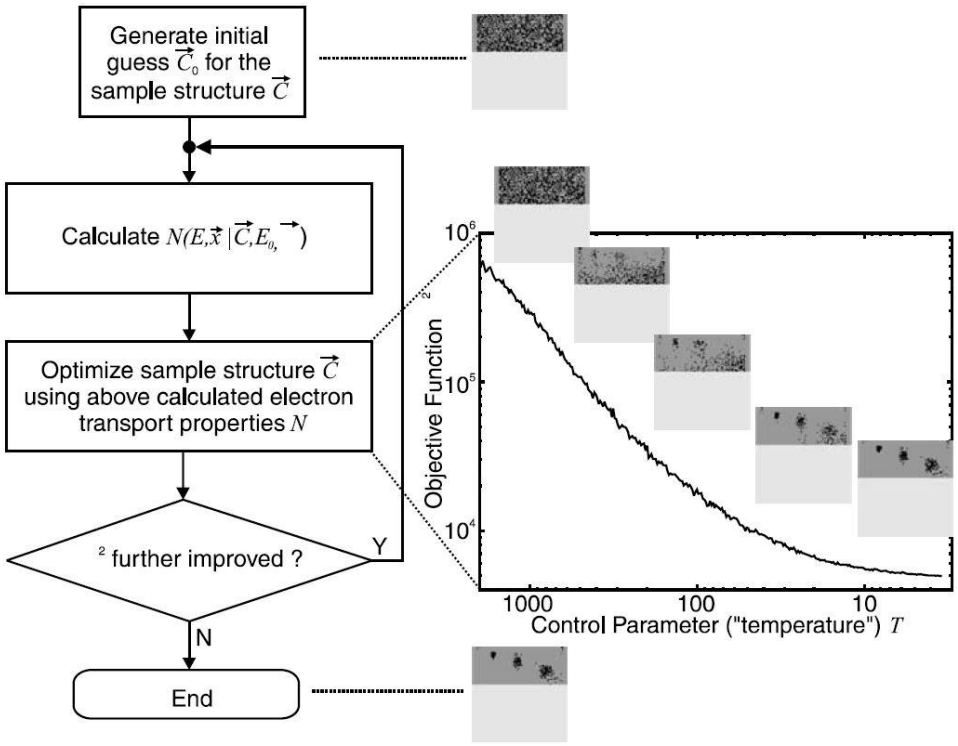

Figure 2.20 Flowchart of the inverse modeling using the simulated annealing algorithm [116]

2.5.3 3D samples

The inverse modeling of 3D samples is normally implemented using a dual-beam microscope formed by an SEM equipped with a FIB by sequentially sectioning a specimen and performing the EDS mapping for each slice [128]. Figure 2.21 shows the 3D elemental distribution of a ceramic sample of (Ca)MgTiOx reconstructed from a series of EDS mapping.

Burdet et al. [129] proposed an enhanced quantification method of 3D EDS microanalysis to correct EDS data for the effects of the large volume of X-ray emissions. The benefit of this method is that for a tiny detail that is smaller than the X-ray emission volume, the X-ray emitted from the deeper features is corrected during the milling so that an improved quantification is obtained. However, this method is not perfect. By using FIB, the samples are destructed, which means the measurement could only be performed once no matter how the result is.

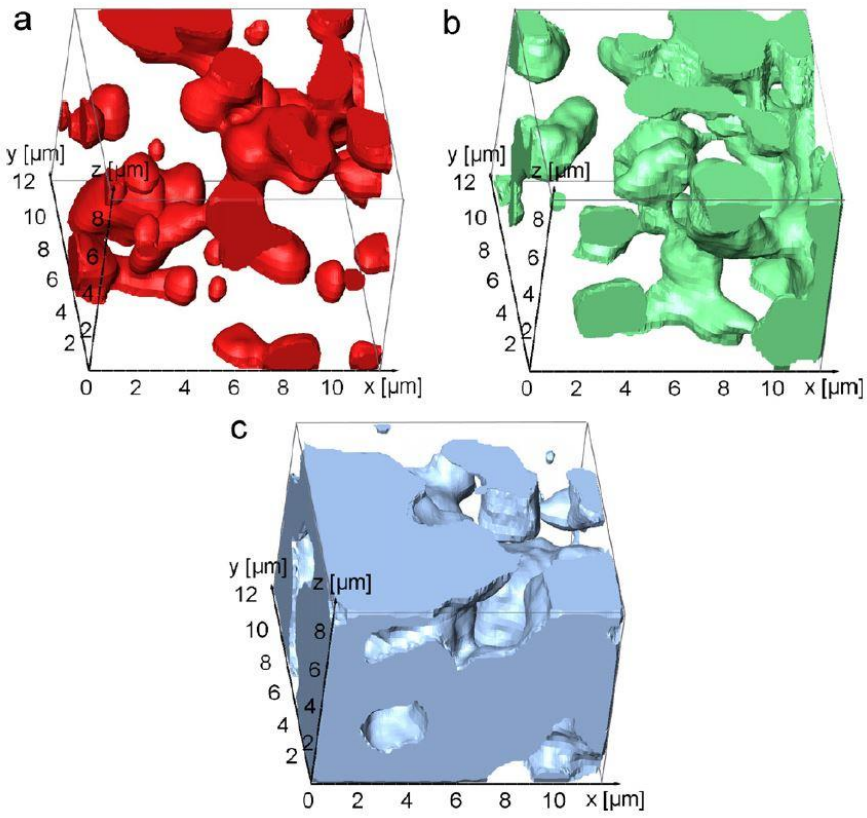

Figure 2.21 3D elemental distribution of the a) calcium (Ca), b) magnesium (Mg), and c) titanium (Ti) reconstructed from EDS data [128]

2.6 STEM tomography

STEM is a technique used to characterize a wide range of materials in nanoscale or atomic scale by scanning the specimen with a fine-focused electron beam in a raster pattern and detecting the transmitted electrons [130]. Compared to conventional transmission electron microscopy (CTEM), in which electrons that emerge from an area of the specimen are projected onto a screen [131], STEM shows advantages in image resolution and lacking interference artifacts due to incoherent imaging [132]. It is also able to detect different kinds of signals simultaneously using a lower total current, which is beneficial for beam sensitive samples [130, 133].

2.6.1 Imaging modes in STEM

Different imaging modes are available in STEM: bright-field (BF), dark-field (DF), and annular dark-field (ADF). BF imaging collects the direct-beam electrons that are not scattered

when traveling through the specimen. DF imaging, on the contrary, selects the scattered electrons and shows complementary images to BF images. It can be done using the BF detector by simply shifting the stationary diffraction pattern. Alternatively, we can use an annular detector in which DF imaging is termed ADF imaging. When the collection angle of the annular detector is relatively high, typically larger than 80 mrad [130], the high-angle (HA) ADF images are formed [131]. Since low-angle scattering is mainly dominated by diffraction effects [134], BF images show diffraction contrast information, while ADF and HAADF images predominately present Z-contrast.

Combing with EDS, STEM can be applied to chemical composition analysis. The EDS signals provide element-specific information but have much worse SNR compared with ADF or HAADF signals [130]. Recently, by incorporating multiple SDDs, the new generation EDS system has the advantage of increased solid angle, which provides an improvement in count rate. The acquisition of high-resolution (atomic resolution) EDS maps is, therefore, possible [135].

2.6.2 Quantitative EDS analysis using STEM

There are two traditional approaches to EDS quantification of thin specimens: the Cliff-Lorimer (k-ratio) method and the ζ-factor method. The Cliff-Lorimer method [71] has been introduced in section 2.2.2 [equation (2.9)]. The Cliff-Lorimer factor (k-ratio), K_{AB} can be estimated using theoretical calculations or experiments [136]. The theoretical calculation is easy to implement but with relatively low accuracy, while experimental determination is with little error but complicated to perform. The experimental determination requires multi-elements thin film standards, which may not always be available. Another limitation emerges from X-ray absorption correction, since prior knowledge of the specimen (mass thickness and composition) is required to apply the absorption correction, whose measurements in turn may bring some errors [136].

Those two limitations are overcome by the ζ-factor method, which assumes that the X-ray intensity of element A is proportional to its weight fraction C_A and the mass-thickness of the specimen ρt, written as follows [136]:

$$\rho t = \zeta_A \frac{I_A}{C_A D_e} \tag{2.30}$$

where ζ_A is the ζ-factor and D_e is the total electron dose. Since the ζ-factor is only related to one constitute element, the pure standard can be used instead of a multi-element standard. Moreover,

with known mass-thickness, the X-ray absorption correction is much easier than the Cliff-Lorimer factor method.

2.6.3 3D STEM tomography

Electron tomography is a technique used to retrieve 3D structural or morphological information in nanoscale from a tilt series of 2D projection images [137]. The input data for tomography reconstruction needs to satisfy the projection requirement, that the intensity of the signal is a monotonic function of the reconstructed quantity [133, 138]. HAADF-STEM images are thus the most suitable due to its Z-contrast and high resolution.

The basic principle of electron tomography is demonstrated in Figure 2.22 [139], that the projection image $\boldsymbol{b}$ can be calculated as a matrix multiplication of the projection matrix $\boldsymbol{A}$ and the object $\boldsymbol{x}$,

$$\boldsymbol{b} = \boldsymbol{A}\boldsymbol{x} \tag{2.31}$$

where an element $a_{i,j}$ in the matrix **A** represents the contribution of the pixel x_i to the projection ray b_j. The purpose of tomographic reconstruction is to determine the object $\boldsymbol{x}$ to minimize the difference between $\boldsymbol{b}$ and $\boldsymbol{Ax}$.

Tomographic reconstruction algorithms include direct back-projection [140], weighted back-projection [141], algebraic reconstruction technique (ART) [142], simultaneous iterative reconstruction technique (SIRT) [143], and total variation minimization (TVM) reconstruction algorithm [144]. Only SIRT is briefly introduced in this section. SIRT starts from a reconstructed object obtained using the back-projection algorithm and updates the object in each iteration by comparing the re-projections of the object simultaneously with the experimental projections. In each iteration, the updated object is expressed as follows [145]:

$$x^{k+1} = x^k + CA^T R(b - Ax^k) \tag{2.32}$$

where C and R are the diagonal matrices of the inverse column and row sums of matrix $\boldsymbol{A}$, respectively. The process is repeated until convergence, which typically takes 20 to 30 iterations. SIRT is tolerant of noise of the measured data and has been widely applied to tomography reconstruction [146].

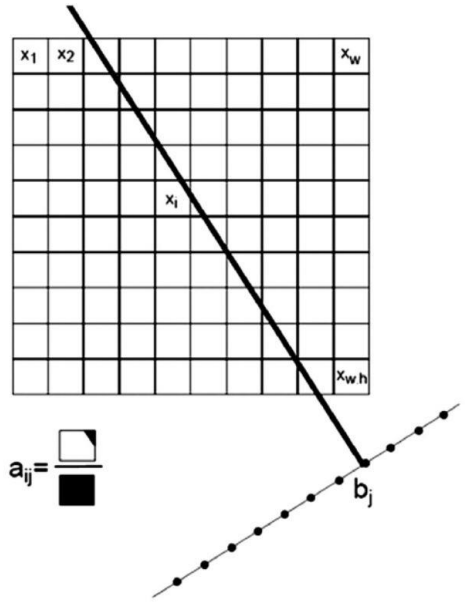

Figure 2.22 Schematic for projection in a tomographic experiment from Ref. [139]. X represents the object to be projected with size $w \times h$. a_{ij} is an element in the projection matrix.

In summary, the interaction of electrons with the specimen and the process of X-ray emission have been explicitly introduced. Several traditional quantitative X-ray microanalysis methods of homogeneous materials have been presented. The Monte Carlo method has been presented. Brief reviews on secondary fluorescence correction, inverse modeling of heterogeneous materials, and STEM tomography have also been presented. In the following chapters, the results of this work will be shown.

2.7 References

1. Goldstein, J.I., et al., *Scanning electron microscopy and X-ray microanalysis*. 2017: Springer.
2. Scott, V.D., G. Love, and S.J.B. Reed, *Quantitative electron-probe microanalysis*. 1995.
3. Goldstein, J.I., et al., *Scanning electron microscopy and X-ray microanalysis*. 2003: Springer.
4. Demers, H., *Two facets of the x-ray microanalysis at low voltage: the secondary fluorescence x-rays emission and the microcalorimeter energy-dispersive spectrometer*. 2008: McGill University.
5. Reimer, L., *Scanning electron microscopy: physics of image formation and microanalysis*. Vol. 45. 2013: Springer.
6. Bethe, H., *Zur theorie des durchgangs schneller korpuskularstrahlen durch materie.* Annalen der Physik, 1930. **397**(3): p. 325-400.
7. Gryzinski, M., *Two-Particle Collisions, n. Coulomb Collisions in the Laboratory System of Coordinates. Rept. No.* PAN-447/XVII17 Inst. Nuclear Res., Polish Acad. Sci.(Warsaw), 1963.
8. Gryziński, M., *Classical theory of atomic collisions. I. Theory of inelastic collisions.* Physical Review, 1965. **138**(2A): p. A336.
9. Bethe, H., *Theory of the passage of fast corpuscular rays through matter*, in *Selected Works Of Hans A Bethe: (With Commentary)*. 1997, World Scientific. p. 77-154.
10. Inokuti, M., *Inelastic collisions of fast charged particles with atoms and molecules—the Bethe theory revisited.* Reviews of modern physics, 1971. **43**(3): p. 297.
11. Casnati, E., A. Tartari, and C. Baraldi, *An empirical approach to K-shell ionisation cross section by electrons.* Journal of Physics B: Atomic and Molecular Physics, 1982. **15**(1): p. 155.
12. Powell, C., *Evaluation of formulas for inner-shell ionization cross sections.* NBS Special Publication, 1976. **460**: p. 97.
13. Powell, C.J., *Cross sections for ionization of inner-shell electrons by electrons.* Reviews of modern Physics, 1976. **48**(1): p. 33.
14. Powell, C.J., *Cross sections for ionization of inner-shell electrons by electron impact*. 1976, American Vacuum Society.
15. Segui, S., M. Dingfelder, and F. Salvat, *Distorted-wave calculation of cross sections for inner-shell ionization by electron and positron impact.* Physical Review A, 2003. **67**(6): p. 062710.
16. Bote, D. and F. Salvat, *Calculations of inner-shell ionization by electron impact with the distorted-wave and plane-wave Born approximations.* Physical Review A, 2008. **77**(4): p. 042701.
17. Bote, D., et al., *Cross sections for ionization of K, L and M shells of atoms by impact of electrons and positrons with energies up to 1 GeV: Analytical formulas.* Atomic Data and Nuclear Data Tables, 2009. **95**(6): p. 871-909.
18. Fink, R., et al., *Atomic fluorescence yields.* Reviews of Modern Physics, 1966. **38**(3): p. 513.
19. Crawford, J., et al., *Calculated K, L, and M shell X-ray line intensities for light ion impact on selected targets from Z= 6 to 100*. 2011: Australian Nuclear Science and Technology Organisation.

20. Perkins, S., et al., *Tables and graphs of atomic subshell and relaxation data derived from the LLNL Evaluated Atomic Data Library (EADL), Z= 1--100*. 1991, Lawrence Livermore National Lab., CA (United States).
21. Krause, M.O., *Atomic radiative and radiationless yields for K and L shells.* Journal of physical and chemical reference data, 1979. **8**(2): p. 307-327.
22. Bambynek, W., et al., *X-ray fluorescence yields, Auger, and Coster-Kronig transition probabilities.* Reviews of modern physics, 1972. **44**(4): p. 716.
23. Bearden, J.A., *X-ray wavelengths.* Reviews of Modern Physics, 1967. **39**(1): p. 78.
24. Bearden, J.A. and A. Burr, *Reevaluation of X-ray atomic energy levels.* Reviews of Modern Physics, 1967. **39**(1): p. 125.
25. Deslattes, R., et al., *X-ray Transition Energies (version 1.0)*. 2003.
26. Deslattes, R.D., et al., *X-ray transition energies: new approach to a comprehensive evaluation.* Reviews of Modern Physics, 2003. **75**(1): p. 35.
27. Jonnard, P. and C. Bonnelle, *Cauchois and Sénémaud Tables of wavelengths of X-ray emission lines and absorption edges.* X-Ray Spectrometry, 2011. **40**(1): p. 12-16.
28. Heinrich, K.F., C. Fiori, and R. Myklebust, *Relative transition probabilities for the x-ray lines from the K level.* Journal of Applied Physics, 1979. **50**(9): p. 5589-5591.
29. Williams, J.H., *Relative intensities and transition probabilities of the K-series lines of the elements 24 to 52 by the ionization chamber method.* Physical Review, 1933. **44**(3): p. 146.
30. Duane, W. and F.L. Hunt, *On X-ray wave-lengths.* Physical Review, 1915. **6**(2): p. 166-172.
31. Solosky, L. and D. Beaman, *A simple method for determining the acceleration potential in electron probes and scanning electron microscopes.* Review of Scientific Instruments, 1972. **43**(8): p. 1100-1102.
32. Kramers, H.A., *XCIII. On the theory of X-ray absorption and of the continuous X-ray spectrum.* The London, Edinburgh, and Dublin Philosophical Magazine and Journal of Science, 1923. **46**(275): p. 836-871.
33. Kirkpatrick, P. and L. Wiedmann, *Theoretical continuous X-ray energy and polarization.* Physical Review, 1945. **67**(11-12): p. 321.
34. Seltzer, S.M. and M.J. Berger, *Bremsstrahlung spectra from electron interactions with screened atomic nuclei and orbital electrons.* Nuclear Instruments and Methods in Physics Research Section B: Beam Interactions with Materials and Atoms, 1985. **12**(1): p. 95-134.
35. Ritchie, N.W., *Efficient Simulation of Secondary Fluorescence Via NIST DTSA-II Monte Carlo.* Microscopy and Microanalysis, 2017. **23**(3): p. 618-633.
36. Acosta, E., et al., *Monte Carlo simulation of x-ray emission by kilovolt electron bombardment.* Journal of applied physics, 1998. **83**(11): p. 6038-6049.
37. Kissel, L., C. Quarles, and R. Pratt, *Shape functions for atomic-field bremsstrahlung from electrons of kinetic energy 1–500 keV on selected neutral atoms $1 \leqslant Z \leqslant 92$.* Atomic data and nuclear data tables, 1983. **28**(3): p. 381-460.
38. Heinrich, K., *Mass absorption coefficients for electron probe microanalysis.* Proc. 11th Int. Congr. on X-Ray Optics and Microanalysis, 1986: p. 67-119.
39. Henke, B.L., E.M. Gullikson, and J.C. Davis, *X-ray interactions: photoabsorption, scattering, transmission and reflection E= 50-30,000 eV, Z= 1-92.* Atomic data and nuclear data tables, 1993. **54**(2).

40. Chantler, C.T., et al., *X-ray form factor, attenuation, and scattering tables.* http://physics.nist. gov/FFast, 2003. **52**.
41. Castaing, R. and J. Descamps, *Sur les bases physiques de l'analyse ponctuelle par spectrographie X*. Journal de physique et le Radium, 1955. **16**(4): p. 304-317.
42. Schmitz, U., P. Ryder, and W. Pitsch. *An experimental method for determining the depth distribution of characteristic X-rays in electron microprobe specimens*. in *Vth International Congress on X-Ray Optics and Microanalysis/V. Internationaler Kongreß für Röntgenoptik und Mikroanalyse/Ve Congrès International sur l'Optique des Rayons X et la Microanalyse*. 1969. Springer.
43. Duncumb, P. and D. Melford, *X-ray Optics and Microanalysis, eds.* R. Castaing, P. Deschamps and J. Philibert (Paris: Hermann) p, 1966. **240**.
44. Bishop, H., *The prospects for an improved absorption correction in electron probe microanalysis.* Journal of Physics D: Applied Physics, 1974. **7**(14): p. 2009.
45. Love, G., D. Sewell, and V. Scott, *An improved absorption correction for quantitative analysis.* Le Journal de Physique Colloques, 1984. **45**(C2): p. C2-21-C2-24.
46. Packwood, R. and J. Brown, *A Gaussian expression to describe ϕ (ρz) curves for quantitative electron probe microanalysis.* X-Ray Spectrometry, 1981. **10**(3): p. 138-146.
47. Brown, J. and R. Packwood, *Quantitative electron probe microanalysis using Gaussian ϕ (ρz) curves.* X-Ray Spectrometry, 1982. **11**(4): p. 187-193.
48. Bastin, G., F. Van Loo, and H. Heijligers, *Evaluation of the use of Gaussian ϕ (ρz) curves in quantitative electron probe microanalysis: a new optimization.* X-Ray Spectrometry, 1984. **13**(2): p. 91-97.
49. Pouchou, J. and F. Pichoir, *Quantitative microanalytic possibilities using a new formulation of matrix effects.* Journal de Physique, 1984. **45**(NC-2): p. 17-20.
50. Pouchou, J. and F. Pichoir, *Un nouveau modèle de calcul pour la microanalyse quantitative par spectrométrie de rayons X*. La recherche aérospatiale, 1984. **3**(167): p. 92.
51. Pouchou, J. and F. Pichoir, *A simplified version of the PAP model for matrix corrections in EPMA.* Microbeam analysis, 1988: p. 315-318.
52. Pouchou, J.-L. and F. Pichoir, *Quantitative analysis of homogeneous or stratified microvolumes applying the model "PAP"*, in *Electron probe quantitation*. 1991, Springer. p. 31-75.
53. Gauvin, R. and P. Michaud, *MC X-Ray, a new Monte Carlo program for quantitative X-ray microanalysis of real materials.* Microscopy and Microanalysis, 2009. **15**(S2): p. 488-489.
54. Reed, S.J.B., *Electron microprobe analysis and scanning electron microscopy in geology*. 2005: Cambridge university press.
55. Terauchi, M., et al., *A new WDS spectrometer for valence electron spectroscopy based on electron microscopy.* JEOL News, 2012. **47**(1): p. 23-28.
56. Fitzgerald, R., K. Keil, and K.F. Heinrich, *Solid-state energy-dispersion spectrometer for electron-microprobe X-ray analysis.* Science, 1968. **159**(3814): p. 528-530.
57. Gatti, E. and P. Rehak, *Semiconductor Drift Chamber: an application of a novel charge transport scheme*. 1983, Brookhaven National Lab.
58. Strüder, L., et al., *High-resolution high-count-rate X-ray spectroscopy with state-of-the-art silicon detectors.* Journal of synchrotron radiation, 1998. **5**(3): p. 268-274.

59. Çubukçu, H.E., et al., *WDS versus silicon drift detector EDS: A case report for the comparison of quantitative chemical analyses of natural silicate minerals.* Micron, 2008. **39**(2): p. 88-94.
60. Ritchie, N.W., D.E. Newbury, and J.M. Davis, *EDS measurements of X-ray intensity at WDS precision and accuracy using a silicon drift detector.* Microscopy and Microanalysis, 2012. **18**(4): p. 892-904.
61. Castaing, R., *Application of electron probes to local chemical and crystallographic analysis.* Ph. D. Thesis (University of Paris), 1951.
62. Duncumb, P. and S. Reed, *The calculation of stopping power and backscattering effects in electron microprobe analysis.* Quantitative Electron Microprobe Analysis, National Bureau of Standards Special Publication, 1968. **298**: p. 133-154.
63. Philibert, J., *A method for calculating the absorption correction in electron probe microanalysis.* X-ray Optics and X-ray Microanalysis, 1963: p. 379-392.
64. Duncumb, P. and P. Shields, *Effect of critical excitation potential on the absorption correction.* The electron microprobe, 1966: p. 284-295.
65. Heinrich, K.F., *Present state of the classical theory of quantitative electron probe microanalysis*. Vol. 521. 1970: US National Bureau of Standards.
66. Reed, S., *Characteristic fluorescence corrections in electron-probe microanalysis.* British Journal of Applied Physics, 1965. **16**(7): p. 913.
67. Bastin, G. and H. Heijligers, *Quantitative electron probe microanalysis of boron in binary borides.* 1986.
68. Horny, P., *Development of a quantification method for X-ray microanalysis with an electron microscope*. 2006: McGill University Libraries.
69. Teng, C., H. Demers, and R. Gauvin, *The standard-based f-ratio quantitative x-ray microanalysis method for a field emission SEM.* Microscopy and Microanalysis, 2018. **24**(S1): p. 732-733.
70. Horny, P., et al., *Development of a new quantitative X-ray microanalysis method for electron microscopy.* Microscopy and Microanalysis, 2010. **16**(6): p. 821-830.
71. Cliff, G. and G.W. Lorimer, *The quantitative analysis of thin specimens.* Journal of Microscopy, 1975. **103**(2): p. 203-207.
72. Brodusch, N., H. Demers, and R. Gauvin, *Field emission scanning electron microscopy: New perspectives for materials characterization*. 2017: Springer.
73. Gauvin, R., N. Brodusch, and P. Michaud. *Determination of Diffusion Coefficients with Quantitative X-Ray Microanalysis at High-Spatial Resolution*. in *Defect and Diffusion Forum*. 2012. Trans Tech Publ.
74. Teng, C., Y. Yuan, and R. Gauvin, *The f-ratio quantification method applied to standard minerals with a cold field emission SEM/EDS.* Talanta, 2019.
75. Joy, D.C., *Monte Carlo modeling for electron microscopy and microanalysis*. 1995: Oxford University Press.
76. Heinrich, K.F., D.E. Newbury, and H. Yakowitz, *Use of Monte Carlo calculations in electron probe microanalysis and scanning electron microscopy: proceedings of a workshop held at the National Bureau of Standards, Gaithersburg, Maryland, October 1-3, 1975*. Vol. 460. 1976: US Department of Commerce, National Bureau of Standards.
77. Kyser, D., et al., *Electron Beam Interactions with Solids for Microscopy, Microanalysis and Microlithography.* Monterey, 1982: p. 1984.

78. Shimizu, R. and D. Ze-Jun, *Monte Carlo modelling of electron-solid interactions.* Reports on Progress in Physics, 1992. **55**(4): p. 487.
79. Gauvin, R., et al., *Win X-ray: a new Monte Carlo program that computes X-ray spectra obtained with a scanning electron microscope.* Microsc Microanal, 2006. **12**(1): p. 49-64.
80. Joy, D. and S. Luo, *An empirical stopping power relationship for low-energy electrons.* Scanning, 1989. **11**(4): p. 176-180.
81. Drouin, D., et al., *CASINO V2. 42—a fast and easy-to-use modeling tool for scanning electron microscopy and microanalysis users.* Scanning: The Journal of Scanning Microscopies, 2007. **29**(3): p. 92-101.
82. Curgenven, L. and P. Duncumb, *Simulation of electron trajectories in a solid target by a simple Monte Carlo technique*. 1971: TI Research Laboratories.
83. Love, G., M. Cox, and V. Scott, *A simple Monte Carlo method for simulating electron-solid interactions and its application to electron probe microanalysis.* Journal of Physics D: Applied Physics, 1977. **10**(1): p. 7.
84. Joy, D.C., *An introduction to Monte Carlo simulations.* Scanning microscopy, 1991. **5**(2): p. 329-337.
85. Karduck, P. and W. Rehbach, *The Use of Tracer Experiments and Monte Carlo Calculations in the φ (ρz) Determination for Electron Probe Microanalysis*, in *Electron Probe Quantitation*. 1991, Springer. p. 191-217.
86. Armigliato, A., et al., *THICKNESS DETERMINATION OF Al FILMS ON Si BY A MONTE CARLO CODE INCLUDING A SECONDARY FLUORESCENCE CORRECTION.* Le Journal de Physique Colloques, 1984. **45**(C2): p. C2-29-C2-32.
87. Fitzgerald, A., A. Gillies, and H. Watton, *A comparison of the composition of thin films on substrates determined by EDX and surface analysis.* Surface and Interface Analysis, 1990. **16**(1-12): p. 163-167.
88. Newbury, D.E., et al., *Monte Carlo electron trajectory simulation, an aid for particle analysis.* Characterization of Particles, 1980. **460**: p. 39-62.
89. Llovet, X., E. Valovirta, and E. Heikinheimo, *Monte Carlo simulation of secondary fluorescence in small particles and at phase boundaries.* Microchimica Acta, 2000. **132**(2): p. 205-212.
90. Ritchie, N.W., *Spectrum simulation in DTSA-II.* Microscopy and Microanalysis, 2009. **15**(5): p. 454-468.
91. Llovet, X. and F. Salvat, *PENEPMA: a Monte Carlo program for the simulation of X-ray emission in electron probe microanalysis.* Microscopy and Microanalysis, 2017. **23**(3): p. 634-646.
92. Hovington, P., D. Drouin, and R. Gauvin, *CASINO: A new Monte Carlo code in C language for electron beam interaction—Part I: Description of the program.* Scanning, 1997. **19**(1): p. 1-14.
93. Rudinsky, S., et al., *Extending Monte Carlo Simulations of Electron Microscopy Images and Hyperspectral Images in a User-Friendly Framework.* Microscopy and Microanalysis, 2019. **25**(S2): p. 222-223.
94. Borisova, A.Y., et al., *Secondary fluorescence effects in microbeam analysis and their impacts on geospeedometry and geothermometry.* Chemical Geology, 2018. **490**: p. 22-29.

95. Cox, M., G. Love, and V. Scott, *A characteristic fluorescence correction for electron-probe microanalysis of thin coatings.* Journal of Physics D: Applied Physics, 1979. **12**(9): p. 1441.
96. Pfeiffer, A., C. Schiebl, and J. Wernisch, *Continuous fluorescence correction in electron probe microanalysis applying an electron scattering model.* X-Ray Spectrometry, 1996. **25**(3): p. 131-137.
97. Reed, S., *The present state of quantitative electron probe microanalysis.* Review of Physics in Technology, 1971. **2**(2): p. 92-115.
98. Green, M. and V. Cosslett, *The efficiency of production of characteristic X-radiation in thick targets of a pure element.* Proceedings of the Physical Society, 1961. **78**(6): p. 1206.
99. Springer, G. and A. Neues Jahrbuch für Mineralogie, *The correction for "continuous fluorescence" in electronprobe microanalysis.* Neues Jahrbuch für Mineralogie, Abhandlungen, 1967. **106**: p. 241-256.
100. Springer, G. and B. Rosner. *The Magnitude of the "Continuous" Fluorescence Correction in Electronprobe Analysis*. in *Vth International Congress on X-Ray Optics and Microanalysis/V. Internationaler Kongreß für Röntgenoptik und Mikroanalyse/Ve Congrès International sur l'Optique des Rayons X et la Microanalyse*. 1969. Springer.
101. Henoc, J., *Quantitative electron probe microanalysis.* NBS Special Publication, 1968. **298**.
102. Merlet, C., *An accurate computer correction program for quantitative electron probe microanalysis.* Microchimica Acta, 1994. **114**(1): p. 363-376.
103. Reed, S., et al., *Fluorescence effects in quantitative microprobe analysis.* Microbeam analysis, 1990: p. 109-114.
104. Duncumb, P., P. Shields-Mason, and C. Da Casa. *Accuracy of atomic number and absorption corrections in electron probe microanalysis*. in *Vth International Congress on X-Ray Optics and Microanalysis/V. Internationaler Kongreß für Röntgenoptik und Mikroanalyse/Ve Congrès International sur l'Optique des Rayons X et la Microanalyse*. 1969. Springer.
105. Youhua, H., H. Yuencai, and C. Jiaguang, *The calculation equations of characteristic fluorescence for multi-layer films.* Journal of Physics D: Applied Physics, 1988. **21**(7): p. 1221.
106. Benhayoune, H., *Characteristic and continuous fluorescence correction for electron probe microanalysis of thin coatings at oblique incidence.* Journal of Analytical Atomic Spectrometry, 1996. **11**(11): p. 1113-1117.
107. Waldo, R., *A characteristic x-ray fluorescence correction for thin-film analysis by electron microprobe.* Microbeam Analysis, 1991: p. 45.
108. Armstrong, J.T. and P.R. Buseck, *A general characteristic fluorescence correction for the quantitative electron microbeam analysis of thick specimens, thin films and particles.* X-Ray Spectrometry, 1985. **14**(4): p. 172-182.
109. Henoc, M., M.F. Maurice, and M.A. Zemskoff. *Phenomenes de fluorescence aux limites de phases*. in *Vth International Congress on X-Ray Optics and Microanalysis/V. Internationaler Kongreß für Röntgenoptik und Mikroanalyse/Ve Congrès International sur l'Optique des Rayons X et la Microanalyse*. 1969. Springer.
110. Escuder, J., et al. *Numerical correction for secondary fluorescence across phase boundaries in EPMA.* in *IOP Conference Series: Materials Science and Engineering*. 2010. IOP Publishing.

111. Bastln, G., et al., *A correction procedure for characteristic fluorescence encountered in microprobe analysis near phase boundaries.* Scanning, 1983. **5**(4): p. 172-183.
112. Escuder, J.A., et al., *Numerical correction for secondary fluorescence across phase boundaries in EPMA.* IOP Conference Series: Materials Science and Engineering, 2010. **7**: p. 012008.
113. Armigliato, A., A. Desalvo, and R. Rosa, *A Monte Carlo code including an X-ray characteristic fluorescence correction for electron probe microanalysis of a thin film on a substrate.* Journal of Physics D: Applied Physics, 1982. **15**(10): p. L121.
114. Myklebust, R.L. and D.E. Newbury, *Monte Carlo modeling of secondary x-ray fluorescence across phase boundaries in electron probe microanalysis.* Scanning, 1995. **17**(4): p. 235-242.
115. Llovet, X., et al., *Secondary fluorescence in electron probe microanalysis of material couples.* Journal of Physics D: Applied Physics, 2012. **45**(22): p. 225301.
116. Wagner, H.W., et al., *Electron probe microanalysis inverse modeling.* Nuclear Instruments and Methods in Physics Research Section B: Beam Interactions with Materials and Atoms, 2001. **184**(3): p. 450-457.
117. Campos, C.S., et al., *Thickness determination of ultra-thin films on Si substrates by EPMA.* Microchimica Acta, 2004. **145**(1-4): p. 13-17.
118. Youhua, H., *The calculation method of mass thickness of multi-layer films by Monte Carlo simulation and iteration.* Journal of Physics D: Applied Physics, 1990. **23**(11): p. 1420.
119. Ng, F., et al., *Metallic thin film depth measurements by X-ray microanalysis.* Applied surface science, 2006. **252**(11): p. 3972-3976.
120. Pouchou, J. and F. Pichoir, *Electron probe X-ray microanalysis applied to thin surface films and stratified specimens.* Scanning Microscopy International(USA), 1992: p. 167-190.
121. Hu, Y. and Y. Pan, *Method for the calculation of the chemical composition of a thin film by Monte Carlo simulation and electron probe microanalysis.* X-Ray Spectrometry: An International Journal, 2001. **30**(2): p. 110-115.
122. Waldo, R., *An iteration procedure to calculate film compositions and thicknesses in electron-probe microanalysis.* Microbeam Analysis, 1988: p. 310-314.
123. Waldo, R.A., M.C. Militello, and S.W. Gaarenstroom, *Quantitative thin-film analysis with an energy-dispersive x-ray detector.* Surface and interface analysis, 1993. **20**(2): p. 111-114.
124. Llovet, X. and C. Merlet, *Electron probe microanalysis of thin films and multilayers using the computer program XFILM.* Microscopy and Microanalysis, 2010. **16**(1): p. 21-32.
125. Ro, C.-U., et al., *A Monte Carlo program for quantitative electron-induced X-ray analysis of individual particles.* Analytical Chemistry, 2003. **75**(4): p. 851-859.
126. Gauvin, R., G. L'Espérance, and S. St-Laurent, *Quantitative x-ray microanalysis of spherical inclusions embedded in a matrix using a SEM and Monte Carlo simulations.* Scanning, 1992. **14**(1): p. 37-48.
127. Aarts, E. and J. Korst, *Simulated annealing and Boltzmann machines*. 1998, John Wiley & Sons Essex, UK.
128. Schaffer, M., et al., *Automated three-dimensional X-ray analysis using a dual-beam FIB.* Ultramicroscopy, 2007. **107**(8): p. 587-597.

129. Burdet, P., C. Hébert, and M. Cantoni, *Enhanced quantification for 3D energy dispersive spectrometry: Going beyond the limitation of large volume of X-ray emission.* Microscopy and Microanalysis, 2014. **20**(5): p. 1544-1555.
130. MacArthur, K.E., *The use of annular dark-field scanning transmission electron microscopy for quantitative characterisation.* Johnson Matthey Technol. Rev, 2016. **60**(2): p. 117-131.
131. David, B.W. and C. C Barry, *Transmission electron microscopy*. 2009: Springer Science+ Business Media, LLC.
132. Pennycook, S.J., B. Rafferty, and P.D. Nellist, *Z-contrast Imaging in an Aberration-corrected Scanning Transmission Electron Microscope.* Microscopy and Microanalysis, 2002. **6**(4): p. 343-352.
133. Weyland, M., *Electron Tomography of Catalysts.* Topics in Catalysis, 2002. **21**(4): p. 175-183.
134. Pennycook, S., *Z-contrast STEM for materials science.* Ultramicroscopy, 1989. **30**(1-2): p. 58-69.
135. MacArthur, K.E., et al., *Quantitative energy-dispersive X-ray analysis of catalyst nanoparticles using a partial cross section approach.* Microscopy and Microanalysis, 2016. **22**(1): p. 71-81.
136. Watanabe, M. and D. Williams, *The quantitative analysis of thin specimens: a review of progress from the Cliff-Lorimer to the new ζ-factor methods.* Journal of microscopy, 2006. **221**(2): p. 89-109.
137. Slater, T., et al. *Understanding the limitations of the Super-X energy dispersive X-ray spectrometer as a function of specimen tilt angle for tomographic data acquisition in the S/TEM*. in *Journal of Physics: Conference Series*. 2014. IOP Publishing.
138. Hawkes, P., *Electron Tomography: 3D imaging in the TEM*. 1992, New York: Plenum.
139. Goris, B., et al., *Advanced reconstruction algorithms for electron tomography: from comparison to combination.* Ultramicroscopy, 2013. **127**: p. 40-47.
140. Herman, G.T., *Image reconstruction from projections.* The fundamental of computerized tomography, 1980: p. 260-276.
141. Gilbert, P., *The reconstruction of three-dimensional structure from projections and its application to electron microscopy II. Direct methods.* Proceedings of the Royal Society of London. Series B. Biological Sciences, 1972. **182**(1066): p. 89-102.
142. Gordon, R., R. Bender, and G.T. Herman, *Algebraic reconstruction techniques (ART) for three-dimensional electron microscopy and X-ray photography.* Journal of theoretical Biology, 1970. **29**(3): p. 471-481.
143. Gilbert, P., *Iterative methods for the three-dimensional reconstruction of an object from projections.* Journal of theoretical biology, 1972. **36**(1): p. 105-117.
144. Goris, B., et al., *Electron tomography based on a total variation minimization reconstruction technique.* Ultramicroscopy, 2012. **113**: p. 120-130.
145. Gregor, J. and T. Benson, *Computational analysis and improvement of SIRT.* IEEE transactions on medical imaging, 2008. **27**(7): p. 918-924.
146. Bangliang, S., et al., *The use of simultaneous iterative reconstruction technique for electrical capacitance tomography.* Chemical Engineering Journal, 2000. **77**(1-2): p. 37-41.

Chapter 3. Secondary fluorescence correction for characteristic and bremsstrahlung X-rays using Monte Carlo X-ray depth distributions applied to bulk and multilayer materials

In electron microscopy, the accuracy of the prediction of X-ray emission for heterogeneous materials is limited by the lack of secondary fluorescence correction. This chapter introduces a secondary fluorescence correction program for both characteristic and bremsstrahlung fluorescence of bulk and multilayer materials using a hybrid model. The hybrid model that combines the Monte Carlo method and analytical modeling has shown great accuracy and efficiency. Through the addition of the correction program, the accuracy of X-ray intensity predictions of MC X-ray is significantly improved.

- This chapter has been published as: Y. Yuan*, H. Demers, S. Rudinsky, R. Gauvin, Secondary Fluorescence Correction for Characteristic and Bremsstrahlung X-Rays Using Monte Carlo X-ray Depth Distributions Applied to Bulk and Multilayer Materials, Microscopy and Microanalysis, 25 (2019) 92-104.

3.1 Abstract

Secondary fluorescence effects are important sources of characteristic X-ray emissions, especially for materials with complicated geometries. Currently, three approaches are used to calculate fluorescence X-ray intensities. One is using Monte Carlo simulations, which are accurate but have drawbacks such as long computation time. The second one is to use analytical models, which are computational efficient but limited to specific geometries. The last approach is a hybrid model, which combines Monte Carlo simulations and analytical calculations. In this article, a program is developed by combining Monte Carlo simulations for X-ray depth distributions and an analytical model to calculate the secondary fluorescence. The X-ray depth distribution curves of both the characteristic and bremsstrahlung X-rays obtained from Monte Carlo program MC X-ray allow us to quickly calculate the total fluorescence X-ray intensities. The fluorescence correction program can be applied to both bulk and multilayer materials. Examples for both cases are shown. Simulated results of our program are compared with both experimental data from the literature and simulation data from PENEPMA and DTSA-II. The practical application of the hybrid model is presented by comparing with the complete Monte Carlo program.

3.2 Introduction

MC X-ray [1, 2], an extension of CASINO [3] and Win X-ray [4], is one of the most well-known Monte Carlo programs for quantitative X-ray microanalysis. It can predict full X-ray spectra obtained from energy dispersive spectroscopy (EDS) by simulating electron trajectories and calculating X-ray intensities. It also allows different kinds of sample geometries such as spheres, cylinders, and boxes. Furthermore, MC X-ray provides full X-ray depth distributions [$\phi(\rho z)$] for both characteristic and bremsstrahlung X-rays. With a user-friendly graphical user interface, simulations can be performed easily and rapidly. However, as a compromise to ensure a fast computation, the secondary fluorescence X-rays are not simulated, which limits its accuracy.

Secondary fluorescence X-rays are emitted by primary X-rays instead of electrons, and their intensities are normally in small magnitudes for bulk materials [5]. But for materials with complex geometries, like multilayer materials, couples, and particles, the contribution of secondary fluorescence can be significant [6, 7]. This is because the range of X-ray-emitted secondary fluorescence far exceeds the primary X-ray range as X-rays have a larger mean free path than electrons. Thus, materials far away from the primary interaction volume can contribute to the X-ray emission. Cox et al. [8] mentioned that the difference in total intensity resulting from the fluorescence effect can reach 15%. It is therefore necessary to make corrections for fluorescence effects during quantitative X-ray microanalysis.

The intention of this paper is to improve the accuracy of MC X-ray in the case of complex geometries by calculating secondary fluorescence effect for bulk and multilayer materials.

As noted, there are three approaches to secondary fluorescence correction: Monte Carlo simulations, analytical models, and hybrid models. The Monte Carlo method uses random numbers and physical models to determine whether secondary fluorescence happens and where secondary X-rays are emitted. This method can be applied to any geometry. However, it requires long computation time. Only two widely used Monte Carlo programs include secondary fluorescence, PENEPMA [9], which is based on PENELOPE [10], and DTSA-II [11]. PENELOPE simulates the coupled transport of electrons and photons using a combination of numerical and analytical differential cross-sections. This means that not only the primary X-rays, but also the secondary X-rays (and higher order fluorescence) are simulated [9]. Unsurprisingly, this generality with

minimal approximations results in long computation time. DTSA-II uses a simpler continuous slowing down model for electron transport, after which the ionization of the primary X-ray is modeled in each electron trajectory segment [12]. Then the secondary fluorescence is simulated by propagating the primary X-rays isotropically. DTSA-II is much faster than PENEPMA but still not as efficient as analytical models [12].

Analytical modeling calculates the probability of secondary fluorescence X-rays being emitted by primary X-rays. It considers the physical process which dictates how the primary X-ray travels through the sample, the primary X-ray is absorbed by a target element, and a secondary X-ray is emitted. It is much faster than the Monte Carlo method but also has some limitations. In the early days, fluorescence correction analytical methods, mostly characteristic fluorescence corrections, were either based on some simplification or limited in application. For example, Cox et al. [8] developed an equation for X-ray fluorescence produced in a coating by characteristic X-rays generated in the substrate material with the assumption that the mass thickness of the coating is much less than the mass depth of X-ray production in the target, i.e., thin coating. Benhayoune [13] calculated the characteristic and bremsstrahlung fluorescence at oblique incidence based on Cox et al.'s equation. Later, Youhua et al. [14] derived an equation, which allows the computation for both thin and thick films. However, they assumed characteristic X-rays in certain films were emitted from the mid-point of the films. This assumption is overly simplistic because the emitted X-ray intensity arises from different depths and varies a lot within a thick film. As the X-ray depth distribution [$\phi(\rho z)$] models improved, people started to apply $\phi(\rho z)$ models to the fluorescence equation derivations. Waldo [15] developed an equation which could be applied to multilayer samples. He evaluated the performance of different $\phi(\rho z)$ models including the Pouchou and Pichoir (PAP) model [16], linear-exponential model, and Gaussian model from Packwood & Brown [17]. The final solution became extremely complicated because of complex $\phi(\rho z)$ expressions and multiple integrals. Other attempts have been made to compute the $\phi(\rho z)$ model numerically. However, the methods are not readily used by readers as they require multiple steps including determining the $\phi(\rho z)$ expression, computing the $\phi(\rho z)$, and then calculating the multiple integral in the fluorescence correction equation numerically [18, 19]. As for the bremsstrahlung fluorescence correction, only a few papers have discussed the method [6, 20, 21], in which the correction for film-substrate samples was only mentioned once [6]. In general, analytical models

are fast to compute, but the accuracy of the method cannot be guaranteed due to all the simplifications and approximations and the limitations of applicability of $\phi(\rho z)$ models.

Some have tried to combine the Monte Carlo method and analytical models together. Llovet et al. [22] developed a hybrid model applied to material couples by obtaining some physical parameters and the primary intensity from Monte Carlo simulations. However, the calculation of the secondary fluorescence is only for bulk material and material couples. Armigliato et al. [23] performed the characteristic fluorescence corrections for a thin film on a substrate using Monte Carlo simulations for the computation of the X-ray $\phi(\rho z)$ curves and analytical models for the calculation of the secondary fluorescence. Monte Carlo simulations provide accurate numerical predictions of X-ray $\phi(\rho z)$ curves [4]. On the other hand, analytical models can be used to develop a fluorescence correction equation from one thin layer to another. The known X-ray depth distribution permits a rigorous computation of the fluorescence excitation by integrating over thin layers numerically. This method provides an accurate and fast secondary fluorescence correction model. In this paper, the X-ray $\phi(\rho z)$ curves are obtained directly from MC X-ray. The physical processes which cause characteristic and bremsstrahlung fluorescence are the same. They differ only by the energy of the exciting X-rays. A consistent equation for the bremsstrahlung and characteristic fluorescence correction is developed. This method is applied to bulk and multilayer materials as a start and will be extended to arbitrary materials in the future.

In the present study, a fluorescence correction program, which is available for bulk and multilayer materials, is constructed. The effects of two simulation parameters on the calculation of the fluorescence correction are discussed. By comparing calculated results with experimental data and simulated data from PENEPMA [9] and DTSA-II [11], the reliability and efficiency of the program are assessed. Through the addition of our correction program, the accuracy of X-ray intensity predictions of MC X-ray is improved.

3.3 Method

A derivation of the secondary fluorescence correction from both characteristic and bremsstrahlung X-rays is carried out for a multilayer sample. The electron-induced primary X-ray, X_b, can be either a characteristic or bremsstrahlung X-ray. Using MC X-ray, its mass depth distribution intensity [$I(\rho z)$] was obtained and used as input for the fluorescence correction

program. And then, the fluorescence intensity of element E_a's X-ray line X_a, $I_{X_a,chaf}$ and $I_{X_a,bremf}$ are computed, where $I_{X_a,chaf}$ and $I_{X_a,bremf}$ represent the characteristic fluorescence intensity and bremsstrahlung fluorescence intensity, respectively. Figure 3.1 shows the geometry used for the equation derivation.

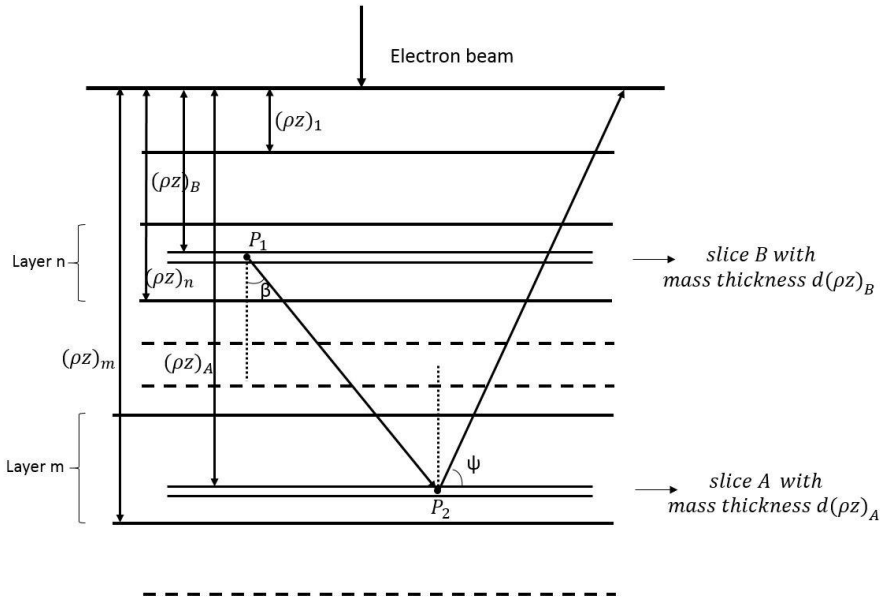

Figure 3.1 Schematic representation of the derivation of the secondary fluorescence correction for slice A, emitted by X-ray X_b, the electron-induced primary X-ray which are generated at P_1.

In Figure 3.1, $d(\rho z)_B$ and $d(\rho z)_A$ are the slice mass thicknesses in layer n (where X-ray X_b is generated) and layer m (where X-ray X_a is excited by X-ray X_b), respectively, which are determined by the layer number (NL) in MC X-ray. The NL is the number of thin differential slices within the primary X-ray range of the sample and it determines the step size of the depth distribution curve calculation.

In reality, the emission of the bremsstrahlung X-rays is not isotropic. However, considering the extremely high computational expense required to compute anisotropic emissions, the following calculation assumes that the emission of the bremsstrahlung X-rays is isotropic. For bulk materials, the difference between the correct angular distribution and isotropic production is not significant [11]. In the case of a thin film where the approximation is not valid [12], the effect of the approximation on the bremsstrahlung fluorescence correction can be ignored as the

bremsstrahlung intensity generated from the thin film is relatively small. The energy of the bremsstrahlung X-rays involved in the computation is determined by the number of energy windows (NW) in MC X-ray. The energy of the bremsstrahlung X-rays for the i^{th} energy window is $(i-1/2)E_0/NW$, where E_0 is the beam energy [4]. The depth distribution curve for each energy window is computed by MC X-ray [4]. The effects of the NL and NW on the accuracy of secondary fluorescence emissions are discussed in the next section.

Let us consider the secondary fluorescence emission of slice *A* (in layer *m*), whose mass depth ranges from $(\rho z)_A$ to $(\rho z)_A + d(\rho z)_A$, as an example. Here P_2 represents the emission position, and it must be noted that the excitations from the primary X-rays of all slices in the sample need to be taken into account. Slice *B*, whose mass depth ranges from $(\rho z)_B$ to $(\rho z)_B + d(\rho z)_B$, is where the primary X-ray X_b is generated. X_b can be either a characteristic or bremsstrahlung X-ray, whose energy is greater than the ionization energy of X-ray X_a. The generated primary X-ray intensity of X_b in slice *B* is known as $I_{X_b,p}((\rho z)_B)$. Thus, the fluorescence X-ray intensity of X_a, which is generated in slice *A* and excited by X-ray X_b in slice *B*, $I_{X_a,f}((\rho z)_A, (\rho z)_B)$, is expressed as follows [6, 8, 14, 15, 18, 23]:

$$I_{X_a,f}((\rho z)_A, (\rho z)_B) = \frac{1}{2}\, c_{E_a} d(\rho z)_A \left(\frac{\mu}{\rho}\right)_{E_a} \frac{r_{X_a}-1}{r_{X_a}} \omega_{X_a} p_{X_a} \left(E_1\left[\sum_{i=n}^{m} (\rho s)_i \left(\frac{\mu}{\rho}\right)_i\right]\right) \cdot I_{X_b,p}((\rho z)_B), \tag{3.1}$$

where c_{E_a} is the weight fraction of element E_a in layer *m*, $d(\rho z)_A$ is the mass thickness of slice *A*, r_{X_a} is the jump ratio of X-ray line X_a, ω_{X_a} is the fluorescence yield of X-ray line X_a, p_{X_a} is the relative intensity, $(\rho s)_i$ is the mass distance during which X-ray X_b travels in layer *i*, $(\mu/\rho)_{E_a}$ and $(\mu/\rho)_i$ are the mass absorption coefficient of X-ray X_b absorbed by pure E_a and layer *i*, respectively, and $E_1(t)$ is the exponential integral [24] whose value can be directly obtained through the C++ library boost [25].

The details of the equation derivation are given in Appendix A.

Equation (3.1) is valid if slice *B* does not overlap with slice *A*. However, when they are the same slice (or at the same mass depth), the above equation is not available, and the fluorescence intensity is calculated using numerical integration, which is described in Appendix B in detail.

In equation (3.1), some factors depend on the mass depth, while some are either constant or composition related. Those factors are divided into two parts, factor F_c (for constants and composition-related factors) and factor F_d (for mass depth dependent factors):

$$F_c = \frac{1}{2}\, c_{E_a} d(\rho z)_A \left(\frac{\mu}{\rho}\right)_{E_a} \frac{r_{X_a} - 1}{r_{X_a}} \omega_{X_a} p_{X_a}, \tag{3.2}$$

$$F_d = E_1 \left[\sum_{i=n}^{m} (\rho s)_i \left(\frac{\mu}{\rho}\right)_i\right]. \tag{3.3}$$

So,

$$I_{X_a,f}((\rho z)_A, (\rho z)_B) = F_c \cdot F_d \cdot I_{X_b,p}((\rho z)_B). \tag{3.4}$$

The fluorescence intensity of X_a generated in the entire layer m emitted by X-ray X_b generated in the entire layer n is then obtained by integrating over $(\rho z)_B$ and $(\rho z)_A$,

$$I_{X_a,f}(m,n) = F_c \int_{(\rho z)_{m-1}}^{(\rho z)_m} \int_{(\rho z)_{n-1}}^{(\rho z)_n} F_d I_{X_b,p}((\rho z)_B)\; d(\rho z)_B d(\rho z)_A. \tag{3.5}$$

For the characteristic fluorescence, a summation over all lines with energy greater than the ionization energy of X-ray X_a is needed:

$$I_{X_a,cf}(m,n) = \sum_{all\ sublines\ of\ X_b} \Big(I_{X_a,f}(m,n)\Big). \tag{3.6}$$

As for the bremsstrahlung fluorescence, an integral over E_{Brem}, which is the energy of the bremsstrahlung X-ray, from the ionization energy of X-ray line X_a, E_{x,X_a}, to the beam energy E_0 is applied. So,

$$I_{X_a,bf}(m,n) = \int_{E_{x,X_a}}^{E_0} I_{X_a,f}(m,n) dE_{Brem}. \tag{3.7}$$

The total fluorescence intensity in the whole sample is calculated by summing up intensities from layer 1 to layer N, where N represents the NL in the whole sample:

$$I_{X_a,f} = \sum_{m=1}^{N} \sum_{n=1}^{N} I_{X_a,(cf/bf)}(m,n). \tag{3.8}$$

In the program, the calculation for $I_{X_a,(cf/bf)}(m,n)$ is performed only when two criteria are met: element E_a exists in layer m and X-ray X_b is generated in layer n. Those integrals and summations are numerically calculated in the program through iterations. Notice that the above-mentioned X-ray intensities are all generated intensities and the absorption needs to be considered to calculate the emitted intensities (see Appendix A for more details).

3.4 Results and discussion

3.4.1 The effect of parameters – the Layer Numbers and the Number of Energy Windows

Two parameters in MC X-ray determine the step size of the numerical integral. One is the Layer Number in z (NL), and another one is the Number of Energy Windows (NW) (which only matters for the bremsstrahlung fluorescence correction). In this part, their effects on the accuracy of the fluorescence correction are discussed. An Al thin film on the top of a Si substrate is taken as an example.

NL, the number of slices in the entire sample, determines the mass thickness of a differential slice, $d(\rho z)$. When a larger NL is used, the slices get thinner, which results in a smoother depth distribution curve; however, the computations for both MC X-ray and the fluorescence correction program become more time-consuming because the number of calculations increases with an increasing number of slices. One should notice that the number of electrons should also be increased when increasing the NL, otherwise the noise of the curve will increase. This is because fewer electrons are distributed in each layer so that the appropriate distribution cannot be obtained.

Figure 3.2 shows the variation of the fluorescence ratio $I_{E_a,f}/I_{E_a,p}$ of the Al Kα line versus the NL at 30 keV for a 10nm Al film on a Si substrate. $I_{E_a,f}$ and $I_{E_a,p}$ are the secondary fluorescence intensity and primary intensity, respectively. It is observed that as the NL increases, the simulated fluorescence ratio decreases dramatically for low NLs and then reaches a plateau. The blue labels show corresponding slice thicknesses for different NLs. When the NL is smaller than 1000, the slice thickness is larger than the Al film thickness (10 nm). In this case, the depth distribution curve expected for the Al film has only one data point, and the slice represented by this data point is partly (or even mostly) composed of the Si substrate. Thus, the factor $d(\rho z)_A$ is overestimated, which makes the fluorescence ratio deviate tremendously. On the other hand, a large NL implies

a longer simulation time. The time taken for the Monte Carlo simulations was 3 minutes for a NL of 1024 and 20 minutes for a NL of 6,000 when 10,000 electrons were simulated. All the simulation results in this paper were obtained using a computer with Windows® 7, an Intel® Core ™ i7-970 processor and 16 GB RAM. As for the fluorescence correction, the computation time was <1 s and around 2 s when the NLs were 1,024 and 6,000, respectively. The NL needs to be properly chosen. It should neither be too small to accurately describe the fluorescence effect, nor too large so that the simulation is slowed down with little improvement in accuracy. Figure 3.2 shows that the fluorescence ratio stabilizes when the NL is larger than 4,000, where the differential slice thickness is around 1/5 of the thin film thickness. This can be taken as a reference for choosing the NL in other cases.

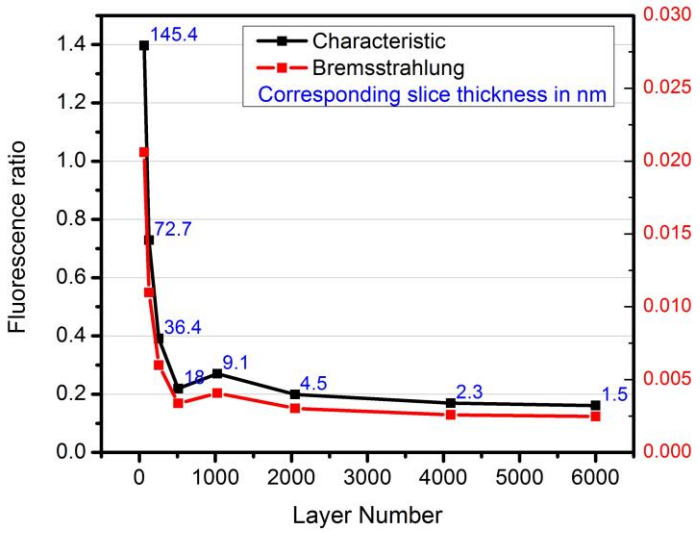

Figure 3.2 Variation of the fluorescence ratio as a function of the NL at 30 keV for the Al Kα line of a 10 nm Al film on a Si substrate. Blue labels are the slice thicknesses in nm. The take-off angle is 40°.

NW is the number of energy windows of the bremsstrahlung X-rays included in the calculation of the X-ray intensity depth distribution (equally distributed between 0 and the beam energy). It is only considered in the bremsstrahlung fluorescence correction. When the bremsstrahlung X-ray energy varies near the absorption edge of element E_a, the mass absorption coefficient changes greatly, which affects the fluorescence correction significantly.

Figure 3.3 shows the case of a 138nm Al film on a Si substrate. The variation of the bremsstrahlung fluorescence ratio versus the NW for Al Kα and Si Kα at different beam energies (as shown in Figure 3.3 a) exhibit the same trend as that for NL: the value varies dramatically at the beginning and then converges toward a stable value. However, the deviation induced by the change of the NW for the Si Kα line is much smaller than that for the Al Kα line. In addition, for the Al Kα line, with the increase of the beam energy (from 10 keV to 30 keV), the fluorescence ratio plateaued after a larger NW. This phenomenon is better demonstrated in Figure 3.3 b), in which the difference between values with different NW was calculated by $\left|R_{NW,E_0} - R_{1024,E_0}\right| / R_{1024,E_0}$, where R_{NW,E_0} represents the fluorescence ratio when the beam energy is E_0 for certain NW. To obtain a fluorescence ratio with a difference smaller than 5% (the blue line) for the Al Kα line, the smallest NW for 10, 20, and 30 keV is around 100, 256 and 490, respectively. For the Si Kα line, however, the difference is always smaller than 5%. This is affected by the relationship between the excitation energy of the secondary emitted photons and the bremsstrahlung X-ray energies. Take a beam energy of 20 keV as an example. For the Al Kα line, the excitation energy is 1.56 keV. The bremsstrahlung energy window just above the absorption edge of the Al Kα line corresponds to an energy of 1.88 and 1.58 keV, when the NWs are 64 and 1,024, respectively. The corresponding mass absorption coefficients are 2,713.91 and 3,981.01 cm^2/g. Given that the latter is 50% larger than the former, it is to be expected that the difference in the bremsstrahlung ratios for the two cases is 28%. The effect tends to be more serious as the beam energy increases due to the increase of the energy interval of energy windows. However, for the Si Kα line whose excitation energy is 1.84 keV, the bremsstrahlung energy window just above its absorption edge corresponds to 1.88 and 1.86 keV when the NWs are 64 and 1,024, respectively. The difference of the corresponding mass absorption coefficient is 2% only. Thus, the fluorescence ratio does not vary a lot. Consequently, the variation of the fluorescence ratio with respect to the NW depends on both the elements and the beam energy.

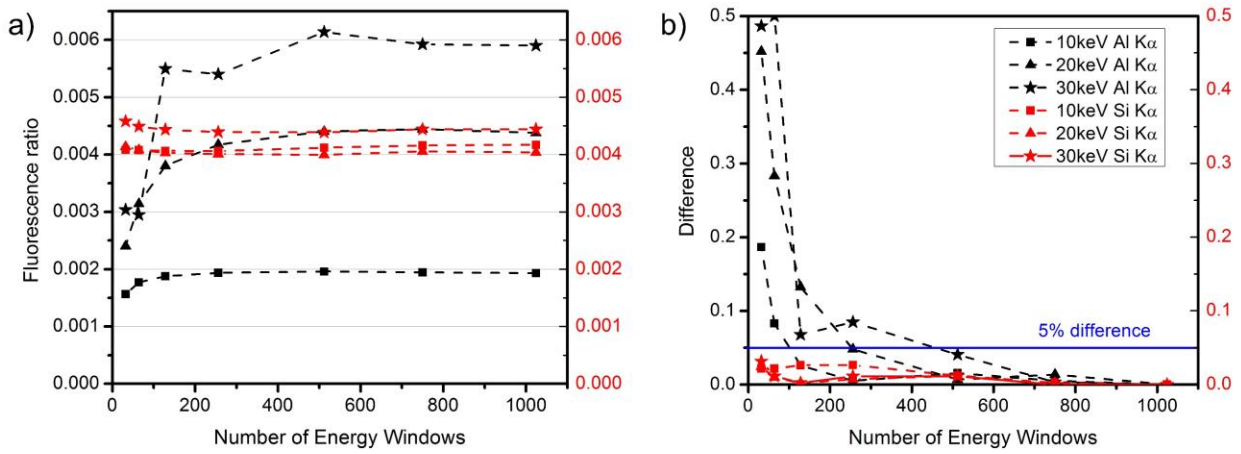

Figure 3.3 a) Variation of the bremsstrahlung fluorescence ratio with the NW at 10 keV (squares), 20 keV (triangles), and 30 keV (stars) for a 138 nm-thick Al film on a Si substrate. b) The difference with the corresponding value when the NW is 1,024 with respect to the NW. Black points represent data for the Al Kα line and red points represent data for the Si Kα line. The take-off angle is 40°.

Still, in general, a larger NW can result in more accurate results. However, increased simulation time is required to compute the bremsstrahlung X-ray intensity depth distribution in MC X-ray for a larger NW. One possible solution is to use an interpolation scheme so that the NW used in the fluorescence calculation can be increased without increasing it in the Monte Carlo simulations [4]. This method has not been implemented yet. For now, to choose the NW, the excitation energy of emitted photons and the bremsstrahlung X-ray energies should be compared.

3.4.2 Bulk example: Fe-Ni system

The fluorescence correction of a bulk material was performed using the Fe-Ni system. In Fe-Ni alloys, the X-ray energy of the Ni Kα line is 7.48 keV, which is greater than the ionization energy of the Fe Kα line, 7.11 keV. Consequently, both the characteristic fluorescence and bremsstrahlung fluorescence need to be corrected. Figure 3.4 a) shows the depth distribution curve of the Fe Kα line for a material of 40% Fe and 60% Ni (in weight fractions) at 30 keV. The black curve shows the depth distribution curve [$\phi(\rho z)$] for the primary characteristic X-ray, which was directly obtained from MC X-ray. And the blue and red curves are the $\phi(\rho z)$ curves with bremsstrahlung fluorescence and with characteristic fluorescence, respectively, which were computed through the correction program. The top-right figure magnifies the portion of the $\phi(\rho z)$ curve, which approaches 0 in log-log scale. It is shown that the interaction volume of secondary fluorescence X-rays is much larger than that of primary X-rays.

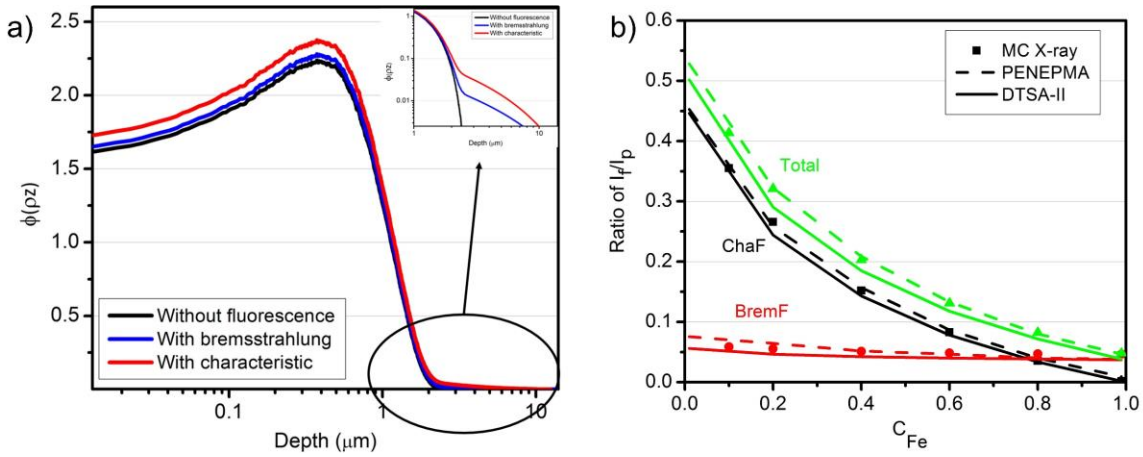

Figure 3.4 a) Depth distribution curve of the Fe Kα line for an Fe concentration of 40% in a bulk Fe-Ni alloy at 30 keV obtained from MC X-ray. b) The fluorescence ratio I_f/I_p with respect to the Fe concentration at 30 keV for the Fe Kα line for the three software [MC X-ray (points), DTSA-II (solid lines), and PENEPMA (dashed lines)]. Black (ChaF) represents results for characteristic fluorescence only, red (BremF) represents results for bremsstrahlung fluorescence only. and green (Total) represents results for both characteristic and bremsstrahlung fluorescence. The take-off angle is 40°.

Figure 3.4 b) shows the variation of the fluorescence ratio of the Fe Kα line with respect to the Fe concentration at 30 keV. The fluorescence ratio, I_f/I_p, is the ratio between the fluorescence intensity and the primary intensity. The bremsstrahlung fluorescence ratio (red point) changes by a minimal amount with respect to the concentration of Fe because the bremsstrahlung intensity is proportional to the mean atomic number of the material and Fe and Ni have close atomic numbers. On the other hand, the characteristic fluorescence ratio (black points) decreases drastically when the Fe concentration increases. This is due to the fact that the intensities of the Ni K lines (including $K\alpha_1$, $K\alpha_2$, and $K\beta_1$), as the source of the characteristic fluorescence, decrease significantly when the Ni concentration decreases. When comparing the simulation results from DTSA-II and PENEPMA, it is shown that the simulation results from PENEPMA are slightly larger than those from MC X-ray, while the results from DTSA-II are slightly lower. It should be noted that in the following text, "MC X-ray" denotes the results computed through our fluorescence correction program, where the $\phi(\rho z)$ curves are obtained by MC X-ray. The characteristic fluorescence ratios obtained from the three pieces of software are similar. The average difference between the characteristic fluorescence ratios computed by MC X-ray and DTSA-II is around 6.5%, while the difference between MC X-ray and PENEPMA is around 6.2%. For the bremsstrahlung ratio, the

results from PENEPMA yield a better match with MC X-ray showing an average difference of 11%. The value from DTSA-II compared with MC X-ray has an average difference of 23%. The difference in bremsstrahlung fluorescence ratio is partly explained by the use of a variety of models to compute the bremsstrahlung X-ray intensities, which will be discussed later.

3.4.3 Bulk example: Alloy steel, Ag-Cr, and Bi-Cr

In this section, the simulated fluorescence intensity (both characteristic and bremsstrahlung) of the Cr Kα line from our program is compared with the calculated data from Llovet et al. [22] for different bulk samples. Llovet et al. calculated the characteristic and bremsstrahlung fluorescence data using a hybrid model by performing Monte Carlo simulations using PENEPMA to get physical interaction parameters and the primary intensities and calculating the fluorescence intensity using an analytical model. Figure 3.5 shows the results from three specimens, an alloy steel (composition Si 0.26 wt%, Cr 1.16 wt%, Mn 0.47 wt%, Fe 96.44 wt%, Ni 0.10 wt%, Cu 0.06 wt% and Mo 1.42 wt%), a Ag-Cr system (Ag 99 wt% and Cr 1 wt%), and a Bi-Cr system (Bi 99 wt% and Cr 1 wt%). For each specimen, the variation of the simulated fluorescence intensity and the primary intensity with respect to the beam energy is displayed.

It is observed that the X-ray intensities (both the primary intensities and the fluorescence intensities) increase as the beam energy increases. Strong agreements between the results from MC X-ray and Llovet et al. are shown in all three cases. The average differences for the primary intensities, the characteristic fluorescence and the bremsstrahlung fluorescence intensities are 6.4, 12.2, and 9.7%, respectively.

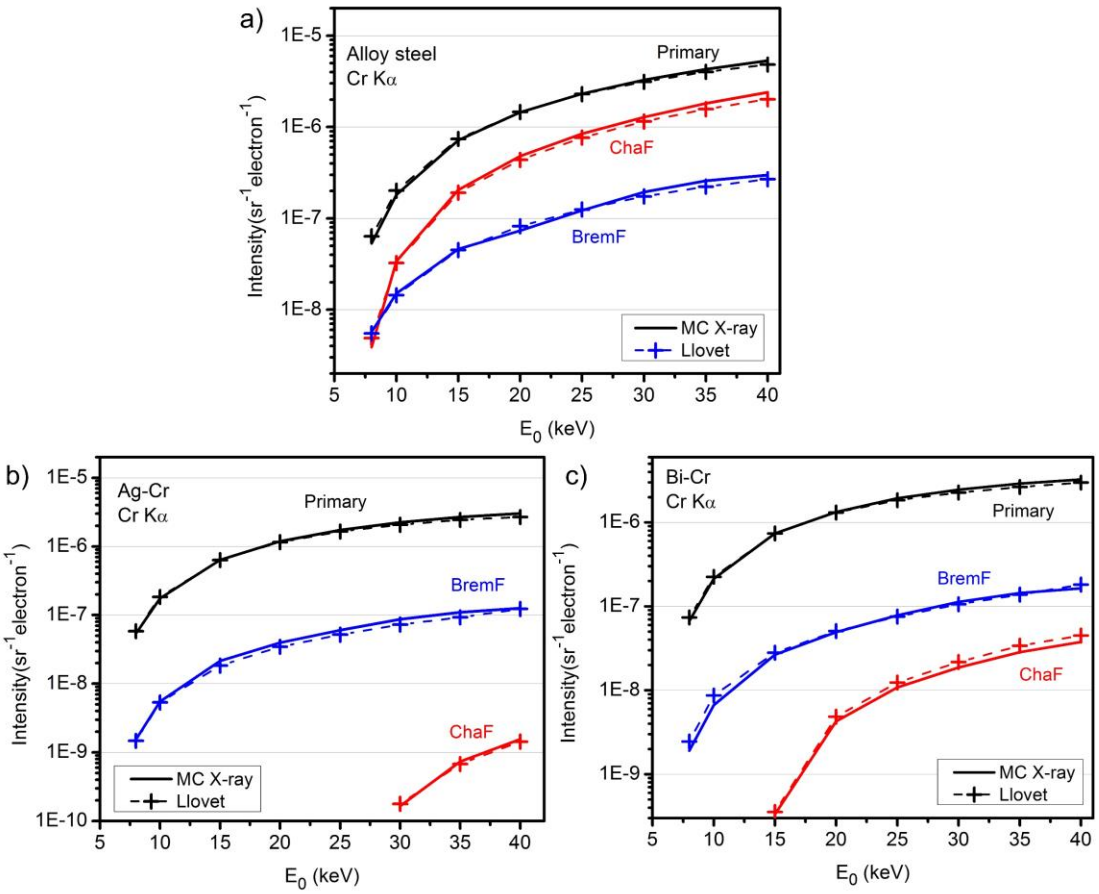

Figure 3.5 Primary, characteristic fluorescence (ChaF) and bremsstrahlung fluorescence (BremF) intensities for the Cr Kα line emitted from three homogeneous specimens a) an alloy steel, b) Ag-Cr, and c) Bi-Cr with respect to the beam energy. Solid lines are results from MC X-ray and crosses connected with dash lines are results from Llovet et al. [22].

3.4.4 Thin film on a substrate

Pd coating on a Ti substrate

To further test the bremsstrahlung fluorescence model, a 400 μg/cm^2 Pd coating on a Ti substrate was investigated. This is a case where a thick heavy element coating is put on a light element substrate and the primary intensity of the substrate can be 0 at low beam energies. Under these circumstances, all emitted X-rays from the substrate element are due to the fluorescence effect. By comparing with experimental data, the accuracy of the fluorescence correction program can be determined. The experimental data was obtained from Bastin & Heijligers [26]. The X-ray energy of the Pd Lα line is smaller than the ionization energy of the Ti K shell. Thus, for the Ti Kα line, only the bremsstrahlung fluorescence effect is possible.

Figure 3.6 shows the variation of the k-ratio for the Ti Kα line as a function of the beam energy. The solid lines represent the k-ratio, which is the ratio of the X-ray intensity from the specimen (with fluorescence) and that from the standard (with fluorescence). The standard is pure Ti in this case. The dashed lines represent the contribution from the primary intensity, which is the ratio of the primary X-ray intensity from the specimen (without fluorescence) and the total intensity from the standard (with fluorescence). Thus, the difference between the solid line and dashed line is the contribution of the fluorescence effect. Black, red, and green lines represent results from our program (with the primary intensity obtained from MC X-ray), DTSA-II, and PENEPMA, respectively.

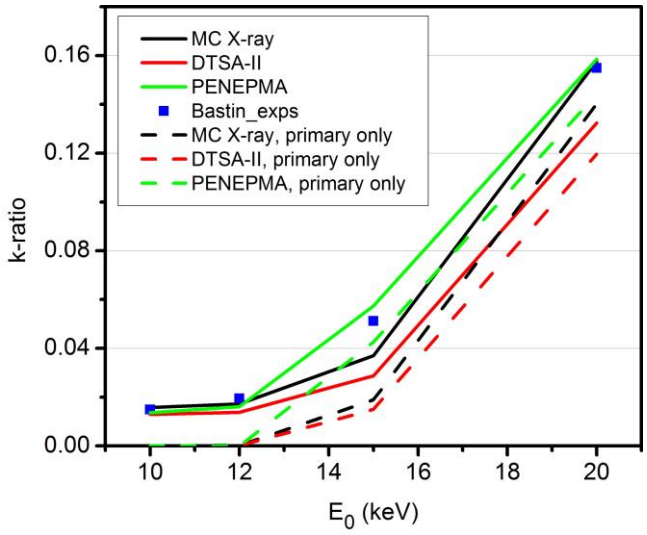

Figure 3.6 Variation of the k-ratio of the Ti Kα line with the beam energy for a 400 μg/cm^2 Pd coating on a Ti substrate. Black lines are the results from MC X-ray, red lines are the results from DTSA-II, and blue points are the experimental data from Bastin & Heijligers [26]. Solid lines represent the k-ratios and dashed lines represent the contribution from the primary X-rays. The take-off angle is 40°.

When the beam energy is smaller than 12 keV, the contribution from the primary X-ray intensity is 0 (as shown by the dashed line). The fluorescence effect contributes entirely to the emitted X-rays. It is observed that the k-ratio from MC X-ray approaches experimental results, which demonstrates the accurate correction of our program. As the beam energy increases, PENEPMA shows higher k-ratios than MC X-ray while DTSA-II produces the lowest values. The best matches with experiments are obtained from PENEPMA. Since the difference between the

solid line and dashed line remains constant for the three software, the difference in k-ratios mainly comes from the discrepancy in the primary intensities.

Ni coating on an Fe substrate

Characteristic fluorescence has a significant effect when two elements have close atomic numbers. For example, in the case of a 1.17 μm Ni coating on an Fe substrate, the Fe Kα line can be strongly excited by the Ni K line. The sources of Fe Kα X-rays include the primary electron-induced X-rays, characteristic fluorescence X-rays, and bremsstrahlung fluorescence X-rays.

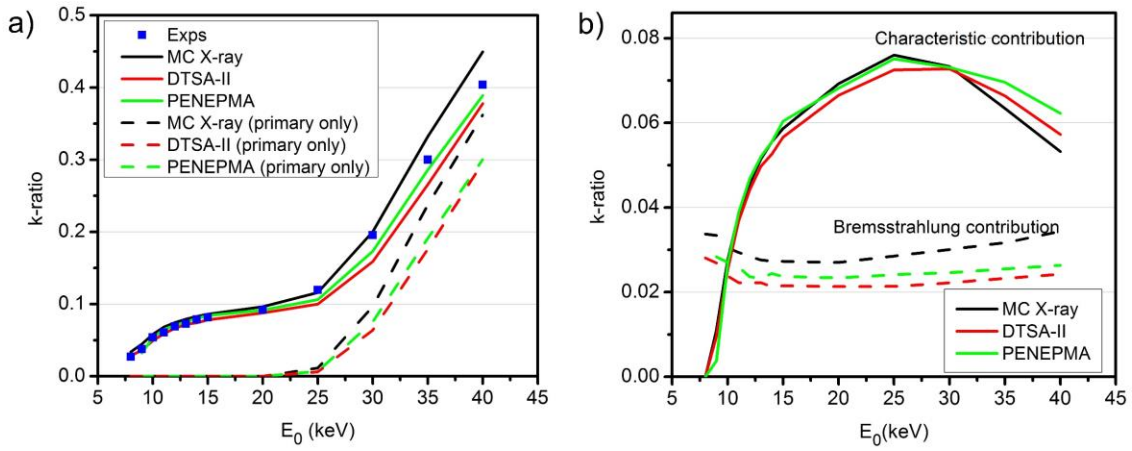

Figure 3.7 a) k-ratio of Fe Kα line for 1.17 μm Ni coating on an Fe substrate, solid lines represent k-ratios, and dashed lines represent relative intensities resulting from the primary X-ray intensity only. b) Relative intensities of the characteristic fluorescence contribution (solid line) and of the bremsstrahlung fluorescence contribution (dash line). The take-off angle is 40°.

Figure 3.7 a) shows the k-ratio of the Fe Kα line obtained from different software. The results from DTSA-II and PENEPMA were compared with our calculations. Blue points represent the experimental data from Pouchou & Pichoir [27]. Solid lines represent the k-ratios with fluorescence correction, and the dashed lines represent the contributions from primary intensities only, which are calculated by the ratio of primary intensities in the specimen and the total X-ray intensities in the standard. At low beam energies (lower than 25 keV), the three software all show very similar results with the experimental data. The primary intensity is 0 and the contribution from the fluorescence effect reaches up to 10% at 20 keV, which again demonstrates the necessity for the fluorescence correction. At high beam energies (higher than 25 keV), the three curves diverge and the result from MC X-ray are larger than the experimental data, while DTSA-II and

PENEPMA are a bit lower. Correspondingly, the primary X-ray contribution also shows the same trend, that the data from MC X-ray is larger than the other two, which explains the difference observed.

To better investigate the fluorescence intensity itself, the k-ratios containing contributions from the characteristic fluorescence (solid line) and bremsstrahlung fluorescence (dashed line) are shown in Figure 3.7 b). They are the ratio between the fluorescence intensity (characteristic and bremsstrahlung, respectively) in the specimen and the total intensity of the standard. The characteristic fluorescence data from the three software is, overall, consistent even though there are small deviations at high beam energies. As for the bremsstrahlung fluorescence contribution, although they all show the same trend, the values from MC X-ray are higher than the other two. This is due to the difference in the bremsstrahlung X-ray intensities resulting from the difference in bremsstrahlung generation cross-section models [4, 28-30]. DTSA-II and PENEPMA use the Seltzer and Berger model [29], while MC X-ray uses the Kirkpatrick and Wiedmann model [28]. As shown in Figure 3.8, the generated bremsstrahlung X-ray intensities for different X-ray energies at different beam energies are different for MC X-ray (solid line) and PENEPMA (dashed line). The bremsstrahlung emission from MC X-ray is consistently larger than that from PENEPMA, which results in larger bremsstrahlung fluorescence intensities in MC X-ray. It is hard to say which cross-section model is more accurate until further investigation is made.

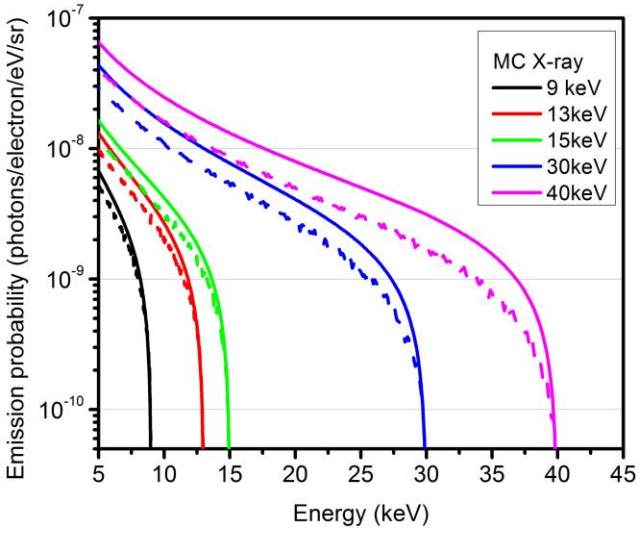

Figure 3.8 Bremsstrahlung X-ray generated intensities for different X-ray energies comparing MC X-ray and PENEPMA. Solid lines are results from MC X-ray, and dashed lines are results from PENEPMA.

3.4.5 Practicality of different models

Besides accuracy, another important feature of the secondary fluorescence correction model is the ability to compute the correction in a few minutes. Three models were compared using a Ni coating on an Fe substrate sample at different beam energies. The simulations were repeated 10 times to evaluate the uncertainty of the model. Table 3.1 shows the time per simulation (seconds), and the average and standard deviation of the total intensity (including the primary, characteristic fluorescence, and bremsstrahlung fluorescence intensity). To facilitate the comparison of the three models, an efficiency-like value was computed for a quantity Q, using a equation defined by Llovet & Salvat [30],

$$\epsilon_Q = (\frac{\bar{Q}}{\sigma_Q})^2 \frac{1}{T} \tag{3.9}$$

where $\bar{Q}$ is the average value of Q after N simulations, σ_Q is the standard deviation of Q, and T is the average simulation time for a single simulation with units of second. The simulated electron number for all the simulations was 1,000. Table 3.2 shows the parameters used in MC X-ray. A PENEPMA input file (take 10 keV as an example) is shown in Appendix C. The same electron number and take-off angle are used in DTSA-II. Figure 3.9 compares the average X-ray intensities (primary, characteristic fluorescence, bremsstrahlung fluorescence, and total) obtained from the three pieces of software at different beam energies. It is shown that in all three cases, similar results are obtained. Figure 3.10 compares the simulation efficiencies of the total X-ray intensity computed from each piece of software. It is observed that the efficiencies of MC X-ray at low beam energies (smaller than 15 keV) are larger than DTSA-II. When the beam energy is greater than 15 keV, DTSA-II has a better efficiency than MC X-ray. The efficiencies of PENEPMA are much lower than the other two software. Table 3.1 shows that PENEPMA is faster to simulate 1,000 electrons for all energies; however, the uncertainties for the total intensity are between 22 and 138%. In contrast, uncertainties for DTSA-II are below 5% (except for 8 and 9 keV) and uncertainties are below 2.5% at all energies for MC X-ray with a simulation time of $<$90 s. It is concluded that MC X-ray together with our program provides a practical fluorescence correction method.

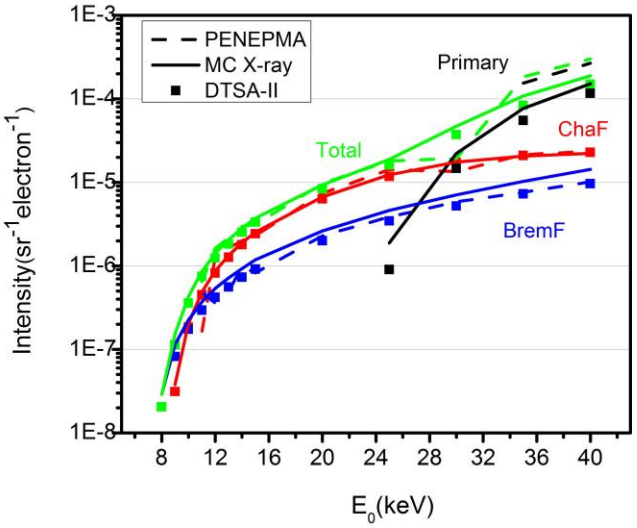

Figure 3.9 The variation of X-ray intensities (primary, characteristic fluorescence, bremsstrahlung fluorescence, and total) as a function of the beam energy for a Ni coating on an Fe substrate. Solid lines represent data from MC X-ray, points represent data from DTSA-II, and dash lines represent data from PENEPMA.

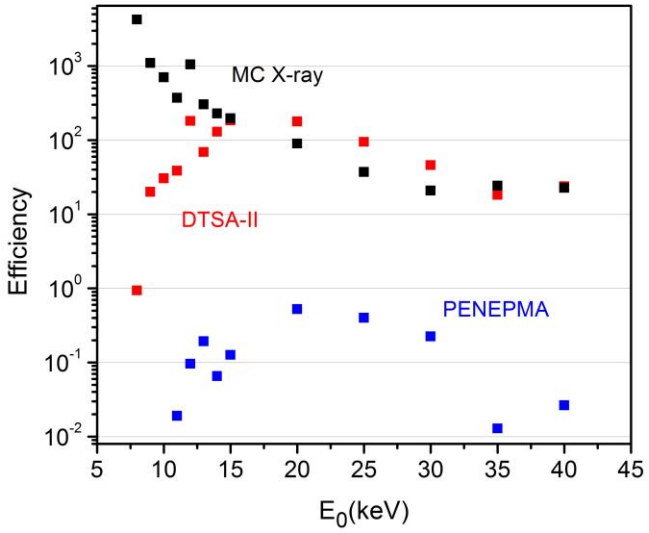

Figure 3.10 The variation of the efficiencies of the total X-ray intensity as a function of the beam energy for a Ni coating on an Fe substrate. Black represents results from MC X-ray, red represents results from DTSA-II, and blue represents results from PENEPMA.

Table 3.1 Comparison of three software

	MC X-ray					DTSA-II			
E_0(kev)	Time per simulation (s)	Intensity($sr^{-1}electron^{-1}$)	Uncertainty ($sr^{-1}electron^{-1}$)	Uncertainty (%)	Efficiency	Time per simulation (s)	Intensity($sr^{-1}electron^{-1}$)	Uncertainty ($sr^{-1}electron^{-1}$)	Uncertainty (%)
8	16	2.90e-8	1.12e-10	0.38	4220	15	2.05e-8	5.48e-9	26.70
9	28	1.53e-7	8.72e-10	0.57	1097	18	1.13e-7	5.97e-9	5.27
10	34	4.30e-7	2.79e-9	0.65	701.5	21	3.57e-7	1.41e-8	3.96
11	45	8.58e-7	6.63e-9	0.77	371.5	24	7.45e-7	2.45e-8	3.29
12	53	1.41e-6	6.00e-9	0.42	1045	25	1.24e-6	1.84e-8	1.49
13	58	2.06e-6	1.55e-8	0.75	302.7	28	1.82e-6	4.15e-8	2.28
14	65	2.82e-6	2.32e-8	0.82	228.6	31	2.52e-6	3.98e-8	1.58
15	69	3.73e-6	3.20e-8	0.86	196.5	34	3.33e-6	4.22e-8	1.27
20	83	9.33e-6	1.08e-7	1.16	89.85	36	8.32e-6	1.04e-7	1.25
25	82	1.88e-5	3.41e-7	1.81	37.19	48	1.61e-5	2.39e-7	1.49
30	80	4.69e-5	1.15e-6	2.45	20.82	61	3.72e-5	7.03e-7	1.89
35	77	1.08e-4	2.51e-6	2.32	24.13	73	8.33e-5	2.29e-6	2.74
40	76	1.88e-4	4.54e-6	2.41	22.63	89	1.49e-4	3.24e-6	2.18

	PENEPMA				
Efficiency	Time per simulation (s)	Intensity(sr^{-1}electron^{-1})	Uncertainty (sr^{-1}electron^{-1})	Uncertainty (%)	Efficiency
0.935	18				
20.0	31				
30.4	31				
38.5	31	6.51e-7	8.48e-7	130.26	0.0190
181	32	1.63e-6	9.30e-7	57.06	0.0960
68.8	32	2.15e-6	8.66e-7	40.28	0.193
129	33	2.98e-6	2.03e-6	68.12	0.0653
184	32	3.14e-6	1.56e-6	49.68	0.127
178	39	9.70e-6	2.15e-6	22.16	0.522
94.3	40	1.81e-5	4.52e-6	24.97	0.401
45.8	41	1.93e-5	6.36e-6	32.95	0.225
18.2	41	1.83e-4	2.52e-4	137.75	0.0129
23.7	40	3.01e-4	2.93e-4	97.35	0.0264

Table 3.2 Simulation parameters used in MC X-ray

Electron number	1000
Number of energy windows (NW)	256
Number of layer in z (NL)	256
Take off angle	40

3.5 Conclusion

An equation for secondary fluorescence correction for both characteristic and bremsstrahlung X-rays was derived. The numerical calculations of multiple integrals using the $\phi(\rho z)$ curves obtained from MC X-ray not only simplify the equation derivation but also improve the reliability. The equation is applicable to homogeneous bulk materials and multilayer materials.

The depth distribution intensity is obtained from MC X-ray, in which two parameters strongly affect the accuracy of the fluorescence correction: the NL (Layer Number in z) and NW (Number of Energy Windows). Their effects on the fluorescence ratio were discussed, and results showed that the NL should be chosen to have five differential slices in the thin film. As for the NW, an interpolation scheme will help increase the accuracy of the bremsstrahlung fluorescence correction without increasing the NW in MC X-ray.

Cases for both bulk and thin films on a substrate were presented and simulation results were compared with both experimental data from references and simulation data from other software (DTSA-II and PENEPMA). The characteristic fluorescence correction showed a good match with other software, while the bremsstrahlung fluorescence gave larger values in an Fe substrate with a Ni coating. The differences in bremsstrahlung fluorescence were explained by the differences in the bremsstrahlung X-ray intensities, which is due to different cross-section models used for bremsstrahlung X-ray emission.

The three software were compared when 1,000 electrons were simulated. PENEPMA took shorter time to run but had high uncertainties. The uncertainties for DTSA-II and MC X-ray were much lower, although MC X-ray performed better. The uncertainties for MC X-ray were below 2.5% at all energies for a simulation time less than 90 s. MC X-ray together with our fluorescence correction model provides a practical quantitative correction for X-ray microanalysis.

3.6 Acknowledgments

Yu Yuan acknowledges the financial support from McGill Engineering Doctoral Awards (MEDA).

3.7 References

1. Gauvin, R. and P. Michaud, *MC X-Ray, a new Monte Carlo program for quantitative X-ray microanalysis of real materials.* Microscopy and Microanalysis, 2009. **15**(S2): p. 488-489.
2. Michaud, P., et al., *Simulated X-ray spectra and X-ray maps: evaluation of models used in MC X-ray Monte Carlo simulation program and comparison with experimental data.* Microscopy and Microanalysis, 2012. **18**(S2): p. 1022.
3. Hovington, P., D. Drouin, and R. Gauvin, *CASINO: A new Monte Carlo code in C language for electron beam interaction—Part I: Description of the program.* Scanning, 1997. **19**(1): p. 1-14.

4. Gauvin, R., et al., *Win X-ray: A new Monte Carlo program that computes X-ray spectra obtained with a scanning electron microscope.* Microscopy and Microanalysis, 2006. **12**(1): p. 49-64.
5. Goldstein, J., et al., *Scanning electron microscopy and X-ray microanalysis: a text for biologists, materials scientists, and geologists*. 2012: Springer Science & Business Media.
6. Pfeiffer, A., C. Schiebl, and J. Wernisch, *Continuous fluorescence correction in electron probe microanalysis applying an electron scattering model.* X-Ray Spectrometry, 1996. **25**(3): p. 131-137.
7. Yuan, Y., et al., *X-ray Emission From Thin Films on a Substrate-Experiments and Simulation.* Microscopy and Microanalysis, 2016. **22**(S3): p. 400-401.
8. Cox, M., G. Love, and V. Scott, *A characteristic fluorescence correction for electron-probe microanalysis of thin coatings.* Journal of Physics D: Applied Physics, 1979. **12**(9): p. 1441.
9. Llovet, X. and F. Salvat. *PENEPMA: a Monte Carlo programme for the simulation of X-ray emission in EPMA*. in *IOP Conference Series: Materials Science and Engineering*. 2016. IOP Publishing.
10. Salvat, F., J.M. Fernández-Varea, and J. Sempau. *PENELOPE-2008: A code system for Monte Carlo simulation of electron and photon transport*. in *the Workshop Proceedings, June*. 2009.
11. Ritchie, N.W., *Spectrum simulation in DTSA-II.* Microscopy and Microanalysis, 2009. **15**(5): p. 454-468.
12. Ritchie, N.W., *Efficient Simulation of Secondary Fluorescence Via NIST DTSA-II Monte Carlo.* Microscopy and Microanalysis, 2017. **23**(3): p. 618-633.
13. Benhayoune, H., *Characteristic and continuous fluorescence correction for electron probe microanalysis of thin coatings at oblique incidence.* Journal of Analytical Atomic Spectrometry, 1996. **11**(11): p. 1113-1117.
14. Youhua, H., H. Yuencai, and C. Jiaguang, *The calculation equations of characteristic fluorescence for multi-layer films.* Journal of Physics D: Applied Physics, 1988. **21**(7): p. 1221.
15. Waldo, R., *A characteristic x-ray fluorescence correction for thin-film analysis by electron microprobe.* Microbeam Analysis, 1991: p. 45.
16. Pouchou, J.-L. and F. Pichoir, *Quantitative analysis of homogeneous or stratified microvolumes applying the model "PAP"*, in *Electron probe quantitation*. 1991, Springer. p. 31-75.
17. Packwood, R. and J. Brown, *A Gaussian expression to describe $\phi(\rho z)$ curves for quantitative electron probe microanalysis.* X-Ray Spectrometry, 1981. **10**(3): p. 138-146.
18. Armstrong, J.T. and P.R. Buseck, *A general characteristic fluorescence correction for the quantitative electron microbeam analysis of thick specimens, thin films and particles.* X-Ray Spectrometry, 1985. **14**(4): p. 172-182.
19. Demers, H., *Two facets of the x-ray microanalysis at low voltage: the secondary fluorescence x-rays emission and the microcalorimeter energy-dispersive spectrometer*. 2008: McGill University.
20. Henoc, J., *Quantitative electron probe microanalysis.* NBS Special Publication, 1968. **298**.

21. Springer, G. and B. Rosner. *The Magnitude of the "Continuous" Fluorescence Correction in Electronprobe Analysis*. in *Vth International Congress on X-Ray Optics and Microanalysis/V. Internationaler Kongreß für Röntgenoptik und Mikroanalyse/Ve Congrès International sur l'Optique des Rayons X et la Microanalyse*. 1969. Springer.
22. Llovet, X., et al., *Secondary fluorescence in electron probe microanalysis of material couples.* Journal of Physics D: Applied Physics, 2012. **45**(22): p. 225301.
23. Armigliato, A., A. Desalvo, and R. Rosa, *A Monte Carlo code including an X-ray characteristic fluorescence correction for electron probe microanalysis of a thin film on a substrate.* Journal of Physics D: Applied Physics, 1982. **15**(10): p. L121.
24. Geller, M. and E.W. Ng, *A table of integrals of the exponential integral.* Journal of Research of the National Bureau of Standards, 1969. **71**: p. 120.
25. John Maddock, S.C., *C++ Type Traits.* Dr. Dobb's Hournal, 2000. **25**(1).
26. Bastin, G. and H. Heijligers, *A systematic database of thin-film measurements by EPMA Part II—Palladium films.* X-Ray Spectrometry, 2000. **29**(5): p. 373-397.
27. Pouchou, J. and F. Pichoir, *Surface film X-ray microanalysis.* Scanning, 1990. **12**(4): p. 212-224.
28. Kirkpatrick, P. and L. Wiedmann, *Theoretical continuous X-ray energy and polarization.* Physical Review, 1945. **67**(11-12): p. 321.
29. Seltzer, S.M. and M.J. Berger, *Bremsstrahlung spectra from electron interactions with screened atomic nuclei and orbital electrons.* Nuclear Instruments and Methods in Physics Research Section B: Beam Interactions with Materials and Atoms, 1985. **12**(1): p. 95-134.
30. Llovet, X. and F. Salvat. *PENEPMA, A Monte Carlo code for the simulation of X-ray emission spectra using PENELOPE*. in *Workshop Manual, Madison, Wisconsin*. 2006.
31. Chantler, C.T., *Theoretical form factor, attenuation, and scattering tabulation for Z= 1–92 from E= 1–10 eV to E= 0.4–1.0 MeV.* Journal of Physical and Chemical Reference Data, 1995. **24**(1): p. 71-643.
32. Chantler, C.T., *Detailed tabulation of atomic form factors, photoelectric absorption and scattering cross section, and mass attenuation coefficients in the vicinity of absorption edges in the soft X-ray (Z= 30–36, Z= 60–89, E= 0.1 keV–10 keV), addressing convergence issues of earlier work.* Journal of Physical and Chemical Reference Data, 2000. **29**(4): p. 597-1056.
33. Goldstein, J.I., et al., *Scanning electron microscopy and X-ray microanalysis: a text for biologists, materials scientists, and geologists.* Plenum Press, New York, 1992.
34. Schreiber, T. and A. Wims, *Relative intensity factors for K, L and M shell x-ray lines.* X-Ray Spectrometry, 1982. **11**(2): p. 42-45.

3.8 Appendix

3.8.1 Appendix A

The derivation of the fluorescence correction equation from one differential slice to the other

The derivation of the fluorescence correction equation has been mentioned numerous times in the literature, but not all the details are given [6, 8, 15, 18, 23, 29]. In this appendix, all the details of the derivation are explained.

As shown in Figure 3.1, a primary X-ray X_b is generated at P_1, and it travels through multiple layers to P_2, where it is absorbed by element E_a and excites X-ray X_a. With knowledge of the generated primary intensity of X-ray X_b emitted from slice B [with mass depth from $(\rho z)_B$ to $(\rho z)_B + d(\rho z)_B$] , $I_{X_b,p}((\rho z)_B)$, the corresponding generated fluorescence X-ray intensity in slice A [with mass depth from $(\rho z)_A$ to $(\rho z)_A + d(\rho z)_A$], $I_{X_a,f}((\rho z)_A, (\rho z)_B)$, is calculated. The following factors are considered:

The fraction of the primary X-ray X_b that travels through the polar angle β to $\beta + d\beta$ and azimuthal angle $d\varphi$ is

$$I_1 = \frac{sin\beta d\beta d\varphi}{4\pi} I_{X_b,p}((\rho z)_B), \tag{3.A1}$$

where 4π is a full solid angle, the solution of the integral, $\int_0^{2\pi}\int_0^{\pi} sin\beta d\beta d\varphi$.

Among those X-rays, the fraction that travels through multiple layers arriving at P_2 and are not absorbed is

$$I_2 = I_1 \exp\left(-sec\beta\left[\sum_{i=n}^{m}(\rho s)_i\left(\frac{\mu}{\rho}\right)_i\right]\right), \tag{3.A2}$$

Some of the X-rays are absorbed by slice A with mass thickness $d(\rho z)_A$,

$$I_3 = I_2\left(1 - \exp\left(-\left(\frac{\mu}{\rho}\right)_m sec\beta d(\rho z)_A\right)\right). \tag{3.A3}$$

As $d(\rho z)_A$ approaches 0, using the first two terms of the Taylor expansion, $e^x \approx 1 + x$,

$$1 - \exp\left(-\left(\frac{\mu}{\rho}\right)_m sec\beta d(\rho z)_A\right) \approx \left(\frac{\mu}{\rho}\right)_m sec\beta d(\rho z)_A. \tag{3.A4}$$

From those X-rays, only the part that is absorbed by element E_a can ionize X-ray X_a:

$$I_4 = \frac{I_3 c_{E_a}(\mu/\rho)_{E_a}}{(\mu/\rho)_m}. \tag{3.A5}$$

The portion of the remaining radiation resulting in the certain line X-ray emission (X_a) is

$$I_5 = I_4 \cdot \frac{r_{X_a} - 1}{r_{X_a}} \cdot \omega_{X_a} p_{X_a}. \tag{3.A6}$$

The total fluorescence radiation generated from slice *A*, emitted by X-ray X_b generated from slice *B*, $I_{X_a,f}((\rho z)_A, (\rho z)_B)$ is calculated by integrating over β from 0 to π/2 (because the depth of layer *n* and layer *m* are settled) and over φ from 0 to 2π,

$$I_{X_a,f}((\rho z)_A, (\rho z)_B) = \int_0^{2\pi} \int_0^{\frac{\pi}{2}} I_5 d\beta \mathrm{d}\varphi. \tag{3.A7}$$

So, by combining equations (3.A1) to (3.A6) into equation (3.A7), the fluorescence equation is expressed as follows:

$$\begin{aligned} I_{X_a,f}((\rho z)_A, (\rho z)_B) &= c_{E_a} d(\rho z)_A \left(\frac{\mu}{\rho}\right)_{E_a} \frac{r_{X_a} - 1}{r_{X_a}} \omega_{X_a} p_{X_a} \\ &\cdot \int_0^{2\pi} \int_0^{\frac{\pi}{2}} tan\beta \exp\left(-sec\beta \left[\sum_{i=n}^{m} (\rho s)_i \left(\frac{\mu}{\rho}\right)_i\right]\right) d\beta \, d\varphi \, \frac{I_{X_b,p}((\rho z)_B)}{4\pi} \\ &= \frac{c_{E_a} d(\rho z)_A}{2} \left(\frac{\mu}{\rho}\right)_{E_a} \frac{r_{X_a} - 1}{r_{X_a}} \omega_{X_a} p_{X_a} \\ &\cdot \int_0^{\frac{\pi}{2}} tan\beta \exp\left(-sec\beta \left[\sum_{i=n}^{m} (\rho s)_i \left(\frac{\mu}{\rho}\right)_i\right]\right) d\beta \, I_{X_b,p}((\rho z)_B) \end{aligned} \tag{3.A8}$$

The integral over β is analytically solved by setting $x = sec\beta$, thus

$$tan\beta = \sqrt{x^2 - 1}, \tag{3.A9}$$

$$d\beta = \frac{dx}{x\sqrt{x^2 - 1}}. \tag{3.A10}$$

So,

$$\begin{aligned} I_{X_a,f}((\rho z)_A, (\rho z)_B) &= \frac{c_{E_a} d(\rho z)_A}{2} \left(\frac{\mu}{\rho}\right)_{E_a} \frac{r_{X_a} - 1}{r_{X_a}} \omega_{X_a} p_{X_a} \\ &\cdot \int_1^{\infty} \frac{1}{x} \exp\left(-x \left[\sum_{i=n}^{m} (\rho s)_i \left(\frac{\mu}{\rho}\right)_i\right]\right) dx \, I_{X_b,p}((\rho z)_B) \end{aligned} \tag{3.A11}$$

Since $\int_1^\infty 1/x \cdot \exp(-xt)dx$ is defined as $E_1(t)$ [or $-E_i(-t)$], the exponential integral [24] whose value can be directly obtained through the C++ library boost [25],

$$I_{X_af}((\rho z)_A, (\rho z)_B) = \frac{1}{2} c_{E_a} d(\rho z)_A \left(\frac{\mu}{\rho}\right)_{E_a} \frac{r_{X_a} - 1}{r_{X_a}} \omega_{X_a} p_{X_a} \left(E_1 \left[\sum_{i=n}^{m} (\rho s)_i \left(\frac{\mu}{\rho}\right)_i \right] \cdot I_{X_b,p}((\rho z)_B \right). \quad (3.A12)$$

The calculated fluorescence X-ray intensity above is the generated intensity. The emitted intensity, $I_{X_a,f,emit}((\rho z)_A, (\rho z)_B)$, that exits the sample and is detected by the EDS detector is calculated by,

$$I_{X_a,f,emit}((\rho z)_A, (\rho z)_B) = I_{X_a,f}((\rho z)_A, (\rho z)_B) \exp\left(-cec\psi \left[\sum_{i=0}^{m} (\rho s)_i \left(\frac{\mu}{\rho}\right)_i \right] \right). \quad (3.A13)$$

Table 3.3 gives the definitions of all symbols used in equations (3.A1) to (3.A13). Table 3.4 shows all the models used for each parameter.

Table 3.3 Symbols definitions

Parameter	Meaning
β	Polar angle
φ	Azimuthal angle
$(\rho s)_i$	The mass depth during which X-ray X_b travels in layer i
$\left(\frac{\mu}{\rho}\right)_i$	The mass absorption coefficient of X-ray X_b in layer i
$d(\rho z)_A$	The thin slice thickness of slice A where X-ray X_a is generated
$\left(\frac{\mu}{\rho}\right)_{E_a}$	The mass absorption coefficient of X-ray X_b absorbed by pure E_a
c_{E_a}	The weight fraction of element E_a in layer m
r_{X_a}	The jump ratio of the X-ray line X_a
ω_{X_a}	The fluorescence yield of the X-ray line X_a

p_{X_a}	The relative intensity of the X-ray line X_a
ψ	Take off angle

Table 3.4 Models used for each parameter

Mass absorption coefficient	MacChantler2005 [31, 32]
Absorption jump ratio	MacChantler2005 [31, 32]
Fluorescence yield	Goldstein1992 [33]
Relative line intensity	Schreiber & Wims1982 [34]

3.8.2 Appendix B

The derivation of the fluorescence correction when $\beta = \frac{\pi}{2}$ (when X-ray X_a and X-ray X_b are at the same differential slice)

When X-ray X_a and X-ray X_b are at the same differential slice, the equation derivation in Appendix A is not available because $cos\beta = 0$, which makes the absorption factor incalculable and changes the integral limit of β. The calculation needs to be performed numerically.

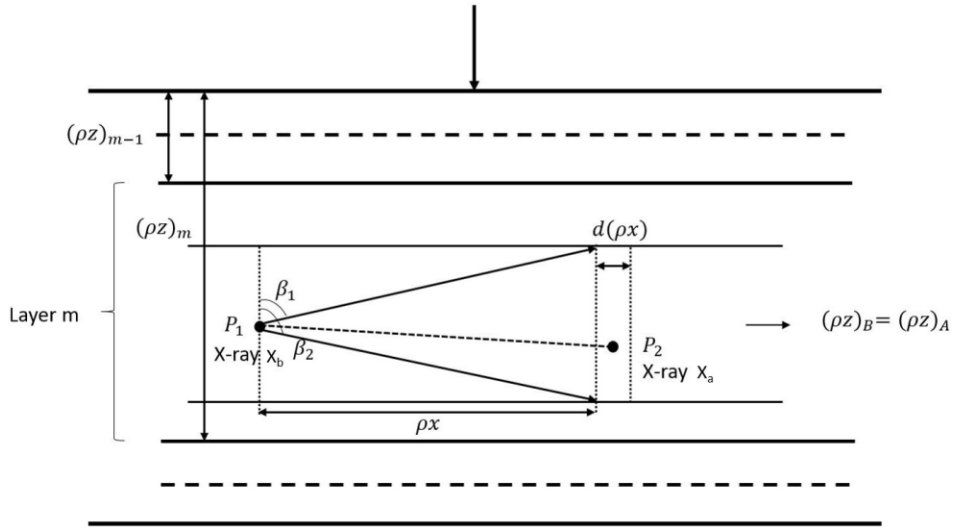

Figure 3.11 Schematic for the derivation of the secondary fluorescence correction when X-ray X_b and X-ray X_a are at the same differential slice.

As shown in Figure 3.11, P_1 and P_2 are at the same layer m and the same slice. The horizonal axis x is added. X-ray X_a that is generated from (ρx) to $(\rho x) + d(\rho x)$ in the polar angle β to $\beta +$

$d\beta$ and azimuthal angle $d\varphi$, $I_{X_a,f}(\rho x, \beta, \varphi)$ is calculated in a similar way with a derivation in Appendix A,

$$I_{X_a,f}(\rho x, \beta, \varphi) = \frac{sin\beta d\beta d\varphi}{4\pi} I_{X_b,p} \cdot \exp\left(-\frac{\rho x}{sin\beta}\left(\frac{\mu}{\rho}\right)_m\right) \cdot \left(\frac{\mu}{\rho}\right)_m \frac{d(\rho x)}{sin\beta} \cdot \frac{c_{E_a}\left(\frac{\mu}{\rho}\right)_{E_a}}{\left(\frac{\mu}{\rho}\right)_m} \cdot \frac{r_{X_a}-1}{r_{X_a}} \cdot \omega_{X_a} p_{X_a}. \quad (3.B1)$$

A triple integral is needed to calculate the total fluorescence intensity of X-ray X_a in this slice,

$$I_{X_a,f} = \int_{\rho x=0}^{\infty} \int_{\varphi=0}^{2\pi} \int_{\beta=\beta_1}^{\beta_2} I_{X_a,f}(\rho x, \beta, \varphi), \quad (3.B2)$$

where $\beta_1 = \arctan(2\rho x / d(\rho z)_A)$ and $\beta_2 = \pi - \beta_1$. Since X-ray fluorescence is the same when β is from β_1 to $\pi/2$ and when it is from $\pi/2$ to β_1,

$$I_{X_a,f} = \int_{\rho x=0}^{\infty} \int_{\varphi=0}^{2\pi} \int_{\beta=\beta_1}^{\pi/2} 2 I_{X_a,f}(\rho x, \beta, \varphi) \quad (3.B3)$$

Thus,

$$I_{X_a,f} = \frac{1}{2} c_{E_a}\left(\frac{\mu}{\rho}\right)_{E_a} \frac{r_{X_a}-1}{r_{X_a}} \omega_{X_a} p_{X_a} I_{X_b,p} \int_{\rho x=0}^{\infty} \int_{\beta=\beta_1}^{\pi/2} \exp\left[-\frac{\rho x}{sin\beta}\left(\frac{\mu}{\rho}\right)_m\right] d\beta d(\rho x). \quad (3.B4)$$

This double integral does not have an analytical solution. So, it is numerically solved in our program by setting the upper limit of the integral over ρx, ∞ as $(\rho x)_1$, the X-ray range, defined as the mass depth where 99% of X-rays are absorbed, i.e., $\exp(-(\rho x)_1(\mu/\rho)_m) = 0.01$.

3.8.3 Appendix C

PENEPMA input file for a Ni coating on an Fe substrate

TITLE Ni on Fe

>>>>>>>> Electron beam definition.

SENERG 10e3 [Energy of the electron beam, in eV]

SPOSIT 0 0 1 [Coordinates of the electron source]

SDIREC 180 0 [Direction angles of the beam axis, in deg]

```
SAPERT 0                                          [Beam aperture, in deg]
     .
>>>>>>>> Material data and simulation parameters.
MFNAME Ni.mat                                     [Material file, up to 20 chars]
MSIMPA 1e2 1e1 1e2 0.2 0.2 1e2 1e1                [EABS(1:3),C1,C2,WCC,WCR]
MFNAME Fe.mat                                     [Material file, up to 20 chars]
MSIMPA 1e2 1e1 1e2 0.2 0.2 1e2 1e1                [EABS(1:3),C1,C2,WCC,WCR]
     .
>>>>>>>> Geometry of the sample.
GEOMFN layer.geo                                  [Geometry definition file, 20 chars]
DSMAX  1 1.0e-5                                   [IB, Maximum step length (cm) in body IB]
DSMAX  2 1.0e-5                                   [IB, Maximum step length (cm) in body IB]
     .
>>>>>>>> Interaction forcing.
IFORCE 1 1 4 -5       0.9  1.0                   [KB,KPAR,ICOL,FORCER,WLOW,WHIG]
IFORCE 1 1 5 -250     0.9  1.0                   [KB,KPAR,ICOL,FORCER,WLOW,WHIG]
IFORCE 1 2 2  -10     1e-3 1.0                   [KB,KPAR,ICOL,FORCER,WLOW,WHIG]
IFORCE 1 2 3  -10     1e-3 1.0                   [KB,KPAR,ICOL,FORCER,WLOW,WHIG]
IFORCE 2 1 4 -5       0.9  1.0                   [KB,KPAR,ICOL,FORCER,WLOW,WHIG]
IFORCE 2 1 5 -7       0.9  1.0                   [KB,KPAR,ICOL,FORCER,WLOW,WHIG]
IFORCE 2 2 2  -10     1e-3 1.0                   [KB,KPAR,ICOL,FORCER,WLOW,WHIG]
IFORCE 2 2 3  -10     1e-3 1.0                   [KB,KPAR,ICOL,FORCER,WLOW,WHIG]
     .
>>>>>>>> Bremsstrahlung splitting.
IBRSPL 1 2                                                [KB,splitting factor]
IBRSPL 2 2                                                [KB,splitting factor]
     .
>>>>>>>> X-ray splitting.
IXRSPL 1 2                                                [KB,splitting factor]
IXRSPL 2 2                                                [KB,splitting factor]
     .
```

>>>>>>>> Emerging particles. Energy and angular distributions.

NBE 0 20e3 300 [E-interval and no. of energy bins]

NBANGL 45 30 [Nos. of bins for the angles THETA and PHI]

.

>>>>>>>> Photon detectors (up to 25 different detectors).

IPSF=0, do not create a phase-space file.

IPSF=1, creates a phase-space file.

PDANGL 5 15 0 360 0 [Angular window, in deg, IPSF]

PDENER 0.0 0.5e4 1000 [Energy window, no. of channels]

.

PDANGL 15 25 0 360 0 [Angular window, in deg, IPSF]

PDENER 0.0 0.5e4 1000 [Energy window, no. of channels]

.

PDANGL 25 35 0 360 0 [Angular window, in deg, IPSF]

PDENER 0.0 0.5e4 1000 [Energy window, no. of channels]

.

PDANGL 35 45 0 360 0 [Angular window, in deg, IPSF]

PDENER 0.0 0.5e4 1000 [Energy window, no. of channels]

.

PDANGL 45 55 0 360 0 [Angular window, in deg, IPSF]

PDENER 0.0 0.5e4 1000 [Energy window, no. of channels]

.

PDANGL 55 65 0 360 0 [Angular window, in deg, IPSF]

PDENER 0.0 0.5e4 1000 [Energy window, no. of channels]

.

PDANGL 65 75 0 360 0 [Angular window, in deg, IPSF]

PDENER 0.0 0.5e4 1000 [Energy window, no. of channels]

.

PDANGL 75 85 0 360 0 [Angular window, in deg, IPSF]

PDENER 0.0 0.5e4 1000 [Energy window, no. of channels]

.

```
>>>>>>>> Spatial distribution of x-ray emission events.
GRIDX  -1e-5 5e-5 60                    [X coords of the box vertices, no. of bins]
GRIDY  -3e-5 3e-5 60                    [Y coords of the box vertices, no. of bins]
GRIDZ  -6e-5 0.   60                    [Z coords of the box vertices, no. of bins]
XRLINE 26010300                         [X-ray line, IZ*1e6+S1*1e4+S2*1e2+S3]
      .
>>>>>>>> Job properties
RESUME dump1.dat                        [Resume from this dump file, 20 chars]
DUMPTO dump1.dat                        [Generate this dump file, 20 chars]
DUMPP  60                               [Dumping period, in sec]
      .
RSEED  -10 1                            [Seeds of the random-number generator]
REFLIN 26010300 1 1.5E-3                [IZ*1e6+S1*1e4+S2*1e2,detector,tol.]
NSIMSH 1.0e3                            [Desired number of simulated showers]
TIME   2.0e5                            [Allotted simulation time, in sec]
```

Chapter 4. Secondary fluorescence of 3D heterogeneous materials using a hybrid model

Chapter 3 demonstrated an approach to secondary fluorescence correction for bulk and multilayer materials. The approach was shown to be accurate and efficient. In this chapter, the approach was extended to apply to 3D heterogeneous materials by replacing thin layers with voxels. Examples of applications were shown for materials couples and spherical inclusions embedded inside matrices.

- This chapter has been published as: Y. Yuan*, H. Demers, X. Wang, R. Gauvin, Secondary Fluorescence of 3D Heterogeneous Materials Using a Hybrid Model, Microscopy and Microanalysis, 26 (2020) 484-496.

4.1 Abstract

In electron probe microanalysis (EPMA) or scanning electron microscopy (SEM), the Monte Carlo method is widely used for modeling electron transport within specimens and calculating X-ray spectra. For an accurate simulation, the calculation of secondary fluorescence is necessary, especially for samples with complex geometries. In this study, we developed a program, using a hybrid model that combines Monte Carlo simulation with an analytical model, to perform secondary fluorescence correction for 3D heterogeneous materials. The Monte Carlo simulation is performed using MC X-ray, a Monte Carlo program, to obtain the three-dimensional primary X-ray distribution, which becomes the input of the analytical model. The voxel-based calculation of MC X-ray enables the model to be applicable to arbitrary samples. We demonstrate the derivation of the analytical model in detail and present the three-dimensional X-ray distributions for both primary and secondary fluorescence to illustrate the capability of our program. Examples for non-diffusion couples and spherical inclusions inside matrices are shown. The results of our program are compared with experimental data from references and with results from other Monte Carlo codes. They are found to be in good agreement.

4.2 Introduction

MC X-ray [1], based on Win X-ray [2] and CASINO [3], is a Monte Carlo program for simulating electron trajectories and computing X-ray intensities. With a user-friendly graphical interface, one can easily set all the parameters of electron beam, detector, specimen, and physical models to simulate the experimental conditions. The specimen in the program is composed of various regions, defined by their geometries and compositions. The geometries are built from several basic shapes including spheres, cylinders, and boxes, as well as their sums or differences, which allow great flexibility in describing the specimen. Moreover, one can obtain the X-ray distribution in three-dimensional (3D) space for both characteristic and bremsstrahlung X-rays. However, one drawback of MC X-ray is the lack of the modeling of secondary fluorescence (SF), which has limited its application in some cases [4].

Primary X-rays are those produced by electron-beam ionization of atoms [5]. There are two types of primary X-rays: characteristic X-rays, which are produced by inner-shell transitions; and bremsstrahlung X-rays, which are generated through deceleration of beam electrons in the electric field of the specimen atoms. SF, on the other hand, is generated through the ionization of atoms by higher-energy X-rays, which can be either characteristic X-rays or bremsstrahlung X-rays [5]. Since X-rays can travel greater distances compared to electrons, SF may be generated at places far away from the primary interaction volume, which leads to errors in quantitative analysis or even qualitative analysis under some circumstances. SF is typically negligible for bulk materials. However, for materials with complex structures, it can be important [6]. Although SF corrections of bulk and multilayer materials for MC X-ray have been implemented [7], it has not been formulated or applied to materials with arbitrarily complex structures. This paper provides an accurate solution to this widely appreciated problem.

Currently, three approaches are adopted for SF calculation: analytical modeling, Monte Carlo simulation, and hybrid modeling that combines the two. Attempts have been made in the development of analytical models for SF correction for non-diffusion couples [8-12] and single particles [13]. The analytical models provide efficient calculations for SF. However, most of them either rely on some assumptions or only consider characteristic fluorescence. For example, Bastin et al. [9], Escuder et al. [12], and Henoc et al. [8] all assumed that primary radiation is emitted from a point source located at the surface of the specimen, without considering the X-ray

distribution in depth. The derivation of an analytical model relies strongly on the specimen structure; and it is not possible to find a general formula adapted to all structures.

Monte Carlo simulation, on the other hand, is capable of handling complex geometries due to the stochasticity of the simulation for electron and X-ray transport [14, 15]. Only two programs for electron microanalysis use the Monte Carlo method to simulate SF: DTSA-II [16] and PENEPMA [17]. DTSA-II adopts the fractional X-ray model for primary X-ray emission and adds SF by propagating primary X-ray intensity in a random direction until it is absorbed by photoionization, followed by relaxation with possible emission of secondary X-rays. With the utilization of a variance reduction technique, DTSA-II provides an efficient simulation. In contrast, PENEPMA simulates the coupled transport of electrons and photons, which means SF (or even higher order fluorescence) is naturally included. This generalization without any approximation requires high computational cost [16]. The results from this work will be compared with the simulation data from DTSA-II and PENEPMA.

Llovet et al. [18] first described a hybrid method for the fast calculation of SF of material couples. They obtained physical interaction parameters from PENELOPE and calculated SF using an analytical model. Following Llovet et al. [18], Yuan et al. [7] proposed a hybrid model which used MC X-ray to calculate the depth distribution of X-ray intensity and adopted an analytical model to calculate both characteristic and bremsstrahlung fluorescence. It can be applied to any bulk or multilayer materials. The hybrid method is more efficient than the Monte Carlo method and more accurate than analytical models since MC X-ray provides an accurate X-ray distribution in depth. Thus, the same strategy is used in this paper.

This paper develops a SF correction program using a hybrid model based on MC X-ray. The program can be applied to materials having arbitrary 3D heterogenous structures. In the following sections, the details of the correction method will be discussed and demonstrated using examples of couples with grain boundaries and spherical inclusions embedded in matrices. The results of our program will be compared with experimental data available in the literature and with results from other Monte Carlo codes including DTSA-II and PENEPMA, along with the semi-analytical data from Llovet et al. [18].

4.3 Method

It is difficult to develop a general analytical model adapted to all specimens because its derivation relies strongly on specimen structure. The voxel-based calculation of X-ray distribution in MC X-ray provides a solution. The simulated specimen is partitioned by a regular grid in 3D space and split into a number of arbitrarily small cuboids. Each of the cuboids is called a *voxel*, which represents the smallest unit of homogeneous structure used for electron scattering and X-ray generation. In other words, within each voxel, it is assumed that the volume is homogeneous, and all X-rays are generated from a point source, which is the center of the voxel in our model. Based on the two assumptions above, we can easily convert the structure of an arbitrary specimen into a voxel-based volume and calculate SF exclusively using the analytical model for voxels. In the following sections, the details of this model will be discussed from four perspectives: Monte Carlo simulation, estimation of the SF range, analytical modeling, and a computation reduction algorithm.

4.3.1 Monte Carlo simulation

The Monte Carlo simulation is performed using MC X-ray. Since the focus of this paper is SF correction, we mainly introduce the required output of parameters from MC X-ray. The most important data required for SF correction is the primary X-ray distribution in 3D space, and thus, we need the generated primary X-ray intensities (both characteristic and bremsstrahlung) of each voxel as well as the voxel's position represented by the 3D coordinates of its center. For the bremsstrahlung X-rays, the input parameter *Number of Energy Window* (*NW*) determines the energy of each window by $E_i = (i - 1/2)E_0/NW$, where E_0 is the beam energy and $0 < i \leq NW$ [2]. The number of voxels in the output is given by $LNx \times LNy \times LNz$, where LNx, LNy, and LNz represent *Layer Number* along axes X, Y and Z, respectively. The size of each voxel is determined by the primary X-ray range together with the *Layer Numbers*. More specifically, for given *Layer Numbers*, the dimension of the voxels increases with the primary X-ray range. Moreover, other simulation parameters for electron beam, specimen, and detector are also required. All the data above are input into our SF correction program for further calculations.

4.3.2 Estimation of the SF range

The first step of the SF calculation is to estimate the SF range. Since X-rays can travel greater distances compared to electrons, the X-ray-induced X-ray emission (fluorescence) has a much larger interaction volume than the electron-beam-induced X-ray emission (primary). For the primary X-ray data obtained from MC X-ray, all the voxels are located within the primary X-ray range. If the program only performs SF calculations for those voxels, the fluorescence intensity may be significantly underestimated. Therefore, in our model, the fictitious boundary for the SF calculation is extended from the primary X-ray range to the SF range, estimated as the distance where 99% of the primary X-rays are absorbed. To simplify the calculation, it is assumed that all primary X-rays are generated at the point where the electron beam strikes the sample. Note that this simplification is made only for the estimation of the SF range, not for the following calculations. For the characteristic SF, the travel distance of the characteristic X-ray is calculated. As for the bremsstrahlung SF, the bremsstrahlung X-ray with energy just higher than the excitation energy of the fluoresced X-ray is considered, which has the greatest possibility to be absorbed and to generate SF. The estimation of the SF range is a rough yet reasonable approximation because the SF range is typically an order of magnitude larger than the primary X-ray range. Moreover, for the voxels close to the SF calculation boundary, their contribution to SF intensity is small due to the fact that only a small fraction of primary X-rays successfully arrives at those voxels without being absorbed. Thus, the error in SF intensity resulted from the rough estimation of the SF range should be negligible.

The SF ranges along three axes X, Y, and Z can be the same or different depending on the specimen structure. The Z-axis is perpendicular to the specimen surface. For example, take the case of the characteristic fluorescence of the Fe Kα line for a Cu spherical inclusion embedded in an Fe matrix and exposed at the surface (see the sample structure in Figure 4.1), and the electron beam strikes on the top center of the Cu inclusion. To fluoresce Fe K X-rays, along the Z-axis the primary Cu Kα X-rays have to travel through the Cu inclusion to reach the Fe matrix. However, along the X- or Y-axis, the X-rays can directly enter the Fe matrix due to the point source assumption of the primary X-rays. Hence, with an increase in the inclusion size, the travel distance of the Cu Kα X-rays along the Z direction increases because of the enlarged Cu region in which the X-rays have a lower mass absorption coefficient than in the Fe matrix, resulting in an increase

in the SF range as shown in Figure 4.2. On the contrary, the SF ranges along the X- and Y-axes are the same due to the symmetry and remain constant despite the change of the inclusion size.

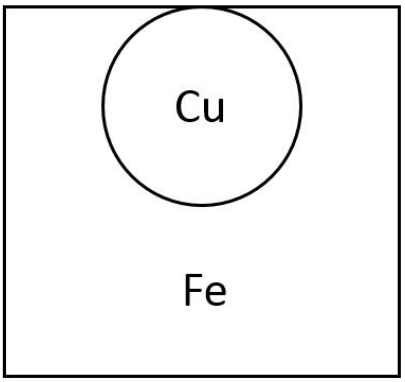

Figure 4.1 Sample structure for a Cu spherical inclusion embedded in an Fe matrix.

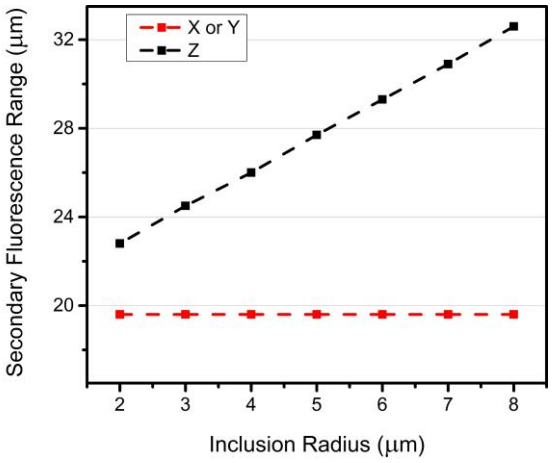

Figure 4.2 Variation of the SF range along X- or Y- and Z-axes relative to the inclusion radius for characteristic fluorescence of the Fe Kα line in the case of a Cu spherical inclusion embedded in an Fe matrix.

4.3.3 Analytical modeling

Following the estimation of the SF range, the generated SF intensity is calculated using analytical modeling. For the element of interest in each of the voxels, the generated SF intensity is computed by summing up the contributions of the primary X-rays from different voxels located within the primary X-ray range. The SF intensities of all the voxels are then summed up together to obtain the total intensity.

For specimens with curved boundaries, the simplification of the voxel-based volume with flat surfaces may introduce errors due to spatial sampling. However, the errors are negligible because the volume of the voxels located at the curved boundaries is relatively small compared to that of the whole SF range, and the errors can be minimized by diminishing the size of the voxel. We have reviewed the magnitude of this error and determined that it is negligible.

The analytical model used to perform the SF correction of voxels is an extension of the model used for multilayers [7], which is based on analytical models from previous research [6, 13, 19-22]. The derivation of the model is discussed below.

Take the SF calculation of voxel V_A fluoresced by the primary X-rays from voxel V_B as an example. Figure 4.3 shows the schematic of the derivation. The positions of voxel V_B and voxel V_A, represented by the 3D coordinates of their centers, are (x_B, y_B, z_B) and (x_A, y_A, z_A), respectively. The generated primary X-ray intensity of the X-ray X_B in voxel V_B is $I_{p,X_B}(V_B)$, and X_B can be either a characteristic or bremsstrahlung X-ray. To calculate the SF intensity of the characteristic X-ray line X_A generated in voxel V_A and ionized by X_B from voxel V_B, $I_{f,X_A}(V_A, X_{B,V_B})$, the following physical processes are considered.

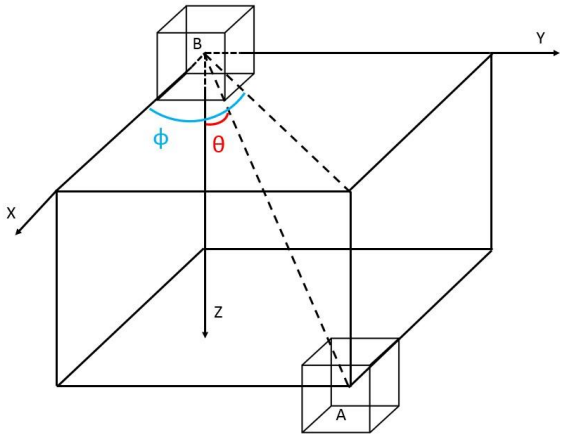

Figure 4.3 Schematic of the SF calculation for voxels.

Consider the fraction of the generated radiation of X-ray line X_B that travels toward voxel V_A in the direction between θ and $(\theta + d\theta)$ for the polar angle, and between φ and $(\varphi + d\varphi)$ for the azimuthal angle:

$$I_1 = I_{p,X_B}(V_B) \times \frac{sin\theta d\theta d\varphi}{\int_0^{2\pi}\int_0^{\pi} sin\theta d\theta d\varphi} = \frac{sin\theta d\theta d\varphi}{4\pi} I_{p,X_B}(V_B)\,, \tag{4.1}$$

where $\int_0^{2\pi}\int_0^{\pi} sin\theta d\theta d\varphi$ is the full solid angle in steradians, which equals 4π, and $sin\theta d\theta d\varphi$ is the solid angle toward voxel V_A, in which $sin\theta$ is calculated by

$$sin\theta = \frac{\sqrt{(x_A - x_B)^2 + (y_A - y_B)^2}}{\sqrt{(x_A - x_B)^2 + (y_A - y_B)^2 + (z_A - z_B)^2}}. \tag{4.2}$$

See Table 4.1 for the descriptions of the symbols.

Table 4.1 Description of symbols

Parameter	Meaning	Unit
θ	Polar angle	steradian
φ	Azimuthal angle	steradian
$\left(\frac{\mu}{\rho}\right)_{X_B}^{i}$	Mass absorption coefficient of X-ray X_B in voxel i	m^2/kg
ρ_i	Density of voxel i	kg/m^3
d_i	Travel distance within voxel i	m
c_{E_A}	Weight fraction of element E_A in voxel V_A	
$\left(\frac{\mu}{\rho}\right)_{X_B}^{E_A}$	Mass absorption coefficient of X-ray X_B absorbed by pure E_A	m^2/kg
r_{X_A}	Jump ratio for X-ray line X_A	
ω_{X_A}	Fluorescence yield for X-ray line X_A	
p_{X_A}	Relative intensity for X-ray line X_A	
dx, dy, dz	Voxel size along the X-, Y-, and Z-axes	m
ψ	Take-off angle	degree
Ω	Solid angle of the detector	steradian
ε_i	Detector efficiency for X-rays with energy i	
E_i	X-ray energy of i	keV

During the travel of X_B toward voxel V_A, some X-rays are absorbed and the remaining intensity that arrives at voxel V_A, I_2, is calculated considering the absorption in all the voxels through which X_B passes

$$I_2 = I_1 \exp\left(\sum_{path\, V_B - V_A} \left[-\left(\frac{\mu}{\rho}\right)^{i}_{X_B} \rho_i d_i\right]\right), \tag{4.3}$$

where $\sum_{path\, V_B - V_A} [-\left(\frac{\mu}{\rho}\right)^{i}_{X_B} \rho_i d_i]$ represents the summation over all voxels in the path from V_B to V_A.

The portion of the remaining radiation (I_2) absorbed by element E_A in voxel V_A is

$$I_3 = I_2\left(1 - \exp\left(-c_{E_A}\left(\frac{\mu}{\rho}\right)^{E_A}_{X_B} \rho_{V_A} d_{V_A}\right)\right), \tag{4.4}$$

where d_{V_A} is the travel distance in voxel V_A.

The fraction of I_3 that results in certain shell ionization is

$$I_4 = I_3 \frac{r_{X_A} - 1}{r_{X_A}}, \tag{4.5}$$

where r_{X_A} represents the jump ratio for X-ray line X_A. Among those X-rays, the part that results in X-ray generation of the line of interest (X_A) for element E_A is successfully fluoresced:

$$I_{f,X_A}(V_A, X_{B,v_B}) = I_4 \omega_{X_A} p_{X_A}. \tag{4.6}$$

Substituting equations (4.1) through (4.5) into equation (4.6), the fluorescence intensity is expressed as follows:

$$I_{f,X_A}(V_A, X_{B,v_B})$$

$$= \frac{\sin\theta\, d\theta d\varphi}{4\pi} I_{p,X_B}(V_B) \exp\left(\sum_{path\, V_B - V_A} \left(-\left(\frac{\mu}{\rho}\right)^{i}_{X_B} \rho_i d_i\right)\right) \times \tag{4.7}$$

$$\left(1-\exp\left(-c_{E_A}\left(\frac{\mu}{\rho}\right)_{X_B}^{E_A}\rho_{V_A}d_{V_A}\right)\right)\frac{r_{X_A}-1}{r_{X_A}}\omega_{X_A}p_{X_A}.$$

The calculations of $d\theta$ and $d\varphi$ are shown in Appendix A.

The SF intensity fluoresced by the primary X-rays generated from the same voxel cannot be calculated using the model above. Instead, a triple numerical integral is used. Please see Appendix B for more details.

The total X-ray fluorescence intensity of X_A in voxel V_A ionized by the primary X-rays generated from voxel V_B, $I_{f,X_A}(V_A,V_B)$ is calculated by summing up the contributions from all primary X-ray lines (both characteristic and bremsstrahlung) whose energies are higher than the excitation energy of X_A:

$$I_{f,X_A}(V_A,V_B)=\sum_{X_B}I_{f,X_A}(V_A,X_{B,v_B})\,. \tag{4.8}$$

To calculate the total fluorescence intensity of X_A in the whole specimen, a double summation for voxel V_B over voxels within the primary X-ray range and for voxel V_A over voxels within the SF X-ray range is needed:

$$I_{f,X_A}=\sum_{V_A}\sum_{V_B}I_{f,X_A}(V_A,V_B)\,. \tag{4.9}$$

The summation over voxel V_A starts from the calculations for the voxels within the primary X-ray range. The program then extends the calculation boundary by repeatedly adding a slice of voxels at the corresponding direction and performs the calculation for the added voxels until the boundary is extended to the SF range. Notice that the calculation is only performed if element E_A is present in voxel V_A.

All the intensities mentioned above are the generated intensities. To obtain the emitted intensity, the X-ray absorption along the direction paths is calculated:

$$I_{Emitted,X_A}=I_{Generated,X_A}\exp\left(-csc\psi\left[\sum_i\left(\frac{\mu}{\rho}\right)_{X_A}^{i}\rho_i d_i\right]\right), \tag{4.10}$$

where i represents all the voxels through which a given X-ray travels out of the sample in the direction of the take-off angle ψ. The detected X-ray intensity can be calculated by

$$I_{Detected,X_A} = I_{Emitted,X_A} \frac{\Omega}{4\pi} \varepsilon_{E_{X_A}} . \tag{4.11}$$

Table 4.2 shows the models for the physical parameters used in our program.

Table 4.2 Models for the physical parameters.

Mass absorption coefficient	Chantler2005 [23-25]
Absorption jump ratio	Chantler2005 [23-25]
Fluorescence yield	Goldstein et al. [26]
Relative line intensity	Schreiber & Wims [27]

4.3.4 Computation reduction algorithm

As the size of the computation boundary increases, there is also a dramatic increase in the number of voxels that require calculations. Considering the voxel-based volume as a multilayer shell structure in which each layer is composed of several slices of voxels along different directions, the SF calculation starts from the inner-most layer, which is the closest one to the primary beam, and extends to the outside layers as the extension of the boundary. If the structure is a cube, the number of voxels in the i^{th} layer is $i^3 - (i-1)^3$, which equals $3i^2 - 3i + 1$. For example, for the 10^{th} layer, the number of voxels is 271, whereas the value for the 20^{th} layer is 1,141, which shows an increase of more than a factor of 3. On the other hand, the SF intensity of each voxel becomes smaller as the calculation moves to the outside layers due to the increase of the travel distance for the primary X-rays and the decrease in solid angle. The result of the two effects is that the magnitude of the intensity becomes small compared to the computational time spent for the outside layers.

To reduce the computation load and at the same time minimize the loss in accuracy, an algorithm "SkipVoxel" was developed, which skips the computation for some voxels located in the enlarged region according to the solid angle. In this algorithm, $d\theta$ and $d\varphi$ of voxel V_A, which represent the size of the solid angle, are calculated taking the voxel on which the electron beam

strikes as the source of primary X-rays and are compared with those for voxels within the primary X-ray range. The smallest values of $d\theta$ and $d\varphi$ for voxels within the primary X-ray range are found and defined as $(d\theta)_{min}$ and $(d\varphi)_{min}$. The *Skip Value* for voxel V_A, SK_{V_A} is defined as the integer part of the ratio of $(d\theta)_{min} \times (d\varphi)_{min}$ and $(d\theta)_{V_A} \times (d\varphi)_{V_A}$. When the SF calculation for a new layer of voxels starts, layer L_i (i is the index number) for example, the minimum value of the *Skip Values* of the voxels in the last layer (layer L_{i-1}) is chosen to be the *Skip Value* of this new layer, which is written as SK_{L_i}. Then the following $(SK_{L_i} - 1)$ layers are skipped without performing the SF calculation. Next, the calculation for layer $L_{i+(SK_{L_i}-1)}$ is performed, after which the intensities for those skipped voxels are calculated using the linear interpolation method.

Figure 4.4 shows the *Skip Value* of voxels for a non-diffusion couple of Cu and Fe with a vertical boundary to calculate the SF intensity of the Fe Kα line at 20 keV. The specimen structure is shown in Figure 4.5. The boundary of Cu and Fe is a vertical plane with the coordinate $X = 0$, and the sample is homogeneous along the Y- and Z-axes. The distance between the electron beam and the vertical boundary is 3 μm. It is observed that the *Skip Value* increases with the increase of the distance between the voxel and the electron beam. Table 4.3 compares the SF intensities of the Fe $K\alpha_1$ line as well as the computation time with and without using "SkipVoxel" when 100,000 electrons were simulated. It is indicated that more than 83% of time is saved when the differences in the intensities are less than 0.1% for both emitted and generated intensities (bremsstrahlung and characteristic).

Table 4.3 Comparison of fluorescence intensities for the Fe $K\alpha_1$ line and computation time with and without "SkipVoxel".

	Characteristic Fluorescence intensity (photons/electron/sr)		Bremsstrahlung Fluorescence intensity (photons/electron/sr)		Computation time (min)
	Emitted	Generated	Emitted	Generated	
Without Skipping	1.743×10^{-6}	2.118×10^{-6}	6.803×10^{-7}	8.330×10^{-7}	201
Skipping	1.745×10^{-6}	2.120×10^{-6}	6.809×10^{-7}	8.337×10^{-7}	33
Difference (%)	0.091	0.090	0.080	0.079	83.58

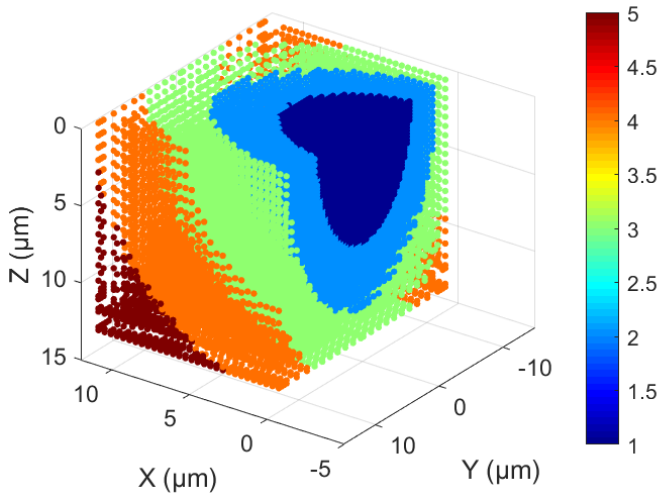

Figure 4.4 Skip Values of voxels for a non-diffusion couple of Fe and Cu to fluoresce Fe Kα line at 20 keV when the distance between the electron beam and the boundary is 3μm.

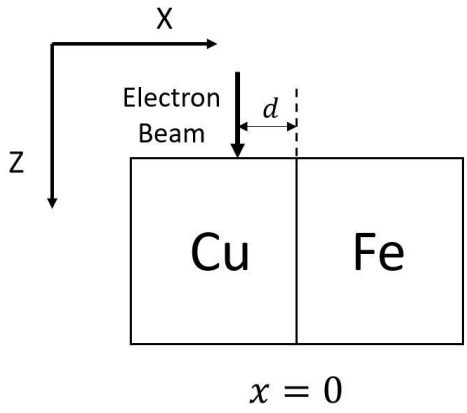

Figure 4.5 Specimen structure for a non-diffusion couple of Cu and Fe.

4.4 Results and discussion

4.4.1 Fe and Cu coupled with a vertical boundary

In order to assess the reliability of our program, an Fe and Cu non-diffusion couple was taken as an example. The parameter *d* is used to indicate the distance between the electron beam and the boundary. The simulation results presented in this paper were all measured at 40° take-off angle.

Figure 4.6 and Figure 4.7 show the simulation results for *d* of 1 μm and the beam energy 20 keV. In this case, most of the electrons interact with Cu in the left region (where X < 0 μm), and only a few electrons interact with Fe in the right region (where X > 0 μm) and emit Fe K-line X-

rays. Thus, the emitted primary X-ray intensity for the Fe Kα line (including $K\alpha_1$ and $K\alpha_2$), 6.45×10^{-10} photons/electron/steradian (photons·(e·sr)$^{-1}$), is much smaller than that for the Cu Kα line, 8.13×10^{-5} photons·(e·sr)$^{-1}$. However, some Cu Kα X-rays and bremsstrahlung X-rays might travel to the right region and fluoresce Fe Kα line X-rays. The SF X-ray intensities of Fe Kα for characteristic and bremsstrahlung are 4.05×10^{-6} and 1.90×10^{-6} photons·(e·sr)$^{-1}$, respectively, whose summation is more than 9,000 times greater than the primary X-ray intensity. Figure 4.6 shows the primary X-ray distribution in 3D space for a) Cu $K\alpha_1$ and b) Fe $K\alpha_1$ with voxel size $0.4 \times 0.4 \times 0.2\ \mu m$. Figure 4.7 a) displays the characteristic SF intensity distribution in 3D space for Fe $K\alpha_1$.The color of each point represents the X-ray intensities at the corresponding voxel in log scale with units of photons per electron per steradian. As the distance between the voxel and the electron beam increases, the fluorescence intensity decreases. By comparing Figure 4.6 a) and Figure 4.7 a), it is also shown that the characteristic SF has a much larger interaction volume and much lower intensities than the emitting X-rays (primary X-rays for Cu $K\alpha_1$ line). Figure 4.7 b)–d) present the cross-section views of the characteristic SF intensity distribution on three planes X = 0, Y = 0.2 μm, and Z = 0 μm, respectively. It is worth noticing that at the plane X = 0 (Figure 4.7 b), for deeper positions where Z > 2 μm, the SF intensity increases at first and then decreases as the voxel moves away from the plane Y = 0. A similar phenomenon is observed at the plane Y = 0.2 μm (Figure 4.7 c) as the X coordinate increases. This can be explained by the variation of d_{V_A}, the travel distance of X_B in voxel V_A, as the relative position of V_A and V_B changes. For example, for voxels on the plane X = 0, the travel distance of X_B within a certain voxel V_A increases with an increase in the azimuthal angle φ within a certain range. The travel distance in the voxel with coordinates (0, 0, and 4 μm) is smaller than that in the voxel (0, 5, and 4 μm) because the former one has an azimuthal angle close to 0, which results in a lower chance of secondary fluorescence according to equation (4.7).

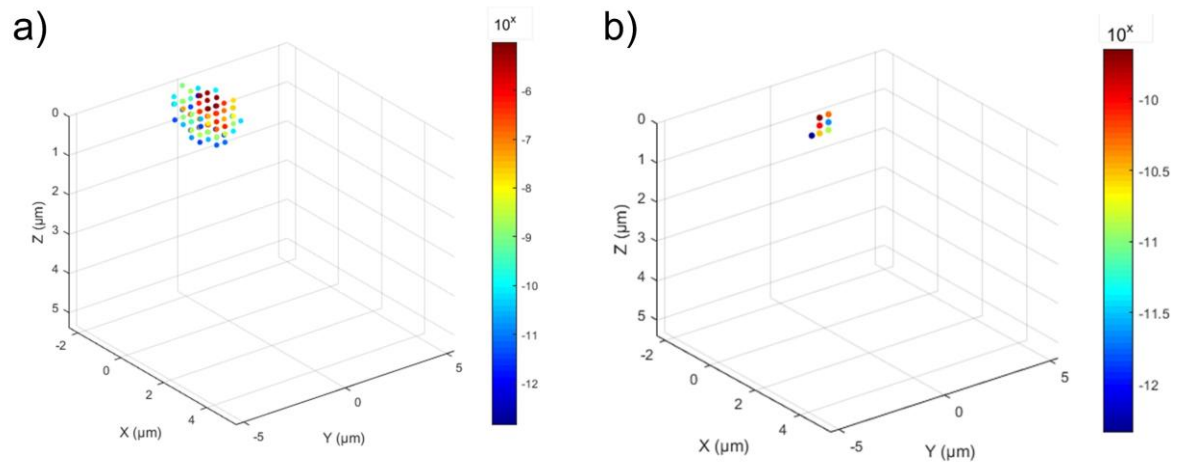

Figure 4.6 The X-ray intensity distribution in 3D space for the primary X-rays of a) Cu $K\alpha_1$ and b) Fe $K\alpha_1$. The intensity values are shown in 'log scale' with unit photons per electron per steradian.

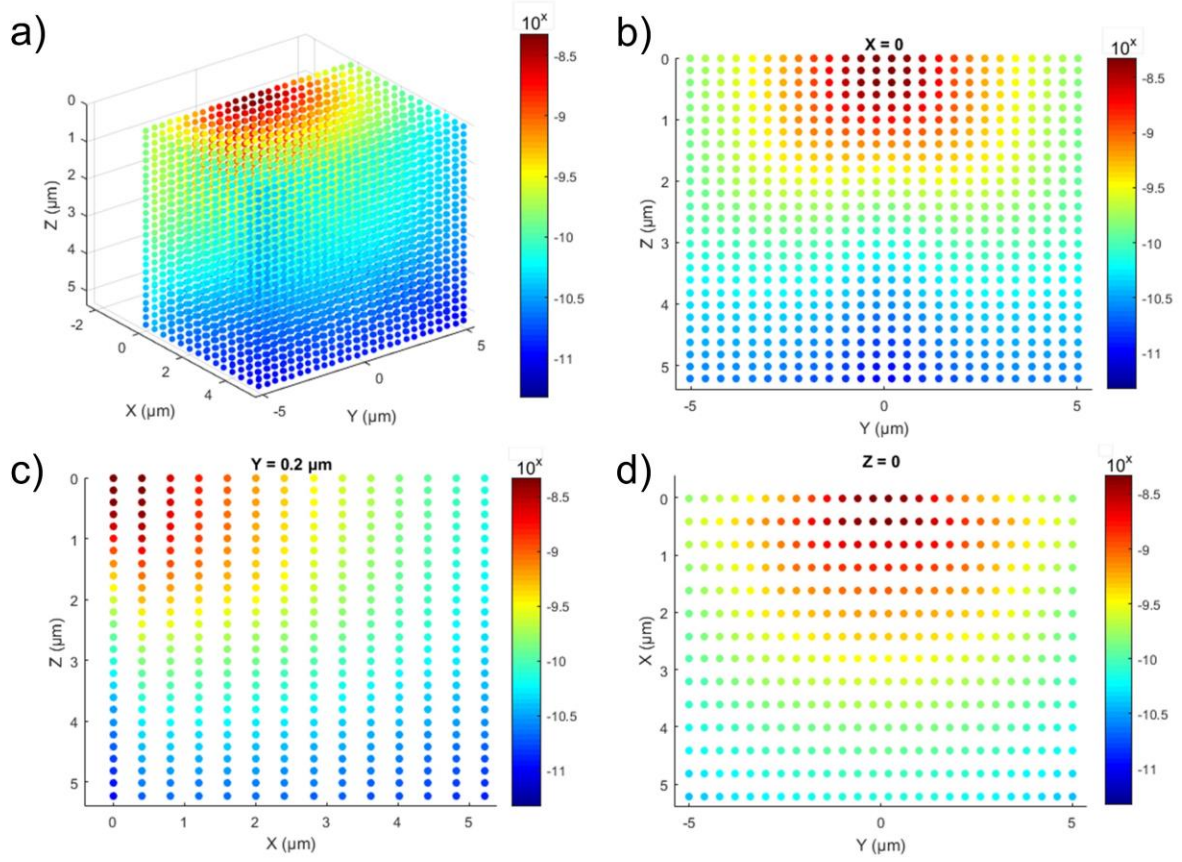

Figure 4.7 a) The X-ray distribution in 3D space for the characteristic SF intensity for the Fe $K\alpha_1$ line. The cross-section views of the characteristic SF intensity distribution on plane b) X = 0; c) Y = 0.2 μm; and d) Z = 0. The intensity values are shown in 'log scale' with unit photons per electron per steradian.

Figure 4.8 shows the variation of the k-ratio, the ratio of the emitted X-ray intensity of the target element measured in an unknown specimen and a standard, versus the distance between the electron beam and the boundary (at 20 keV). For all the results presented in this paper, we used pure element standards and included the fluorescence effect for the X-ray radiation. The results of this work were compared with experimental data from Valovirta et al. [28], semi-analytical modeling from Llovet et al. [18], and simulation results from Ritchie [16] and PENEPMA [17]. Figure 4.8 a) presents the results for the Fe Kα line when the electron beam strikes the Cu region, which includes the contributions of both characteristic and bremsstrahlung fluorescence, while Figure 4.8 b) presents the results for the Cu Kα line when the electron beam strikes the Fe region, which exclusively includes the bremsstrahlung fluorescence. As the distance *d* increases, the k-ratio decreases due to the reduction of the fraction of the primary X-rays that arrives at the left region [Fe for a) and Cu for b)]. Computation results of this work are found to be in good agreement (with relative differences smaller than 15%) with both experimental data from Valovirta et al. [28], and simulation data extracted from Llovet et al. [18] and PENEPMA. However, in Figure 4.8 b), slight differences are found between our results and the simulation data from Ritchie [16] with an average relative difference of 15.4%. The differences can be attributed to differences in the cross-section models of the two programs, which are listed in Table 4.4 [2, 29].

Table 4.4 Cross-section models used in MC X-ray, DTSA-II, and PENEPMA

	MC X-ray	DTSA-II	PENEPMA
Electron cross-section	Mott & Browning [30, 31]	NIST electron elastic-scattering cross-section database [32]	Numerical calculation from ELSEPA [33]
Characteristic X-ray cross-section	Casnati et al. [34]	Bote & Salvat [35]	Bote & Salvat [35]
Bremsstrahlung X-ray cross-section	Kirkpatrick & Wiedmann [36]	Seltzer & Berger [37]	Seltzer & Berger [37]

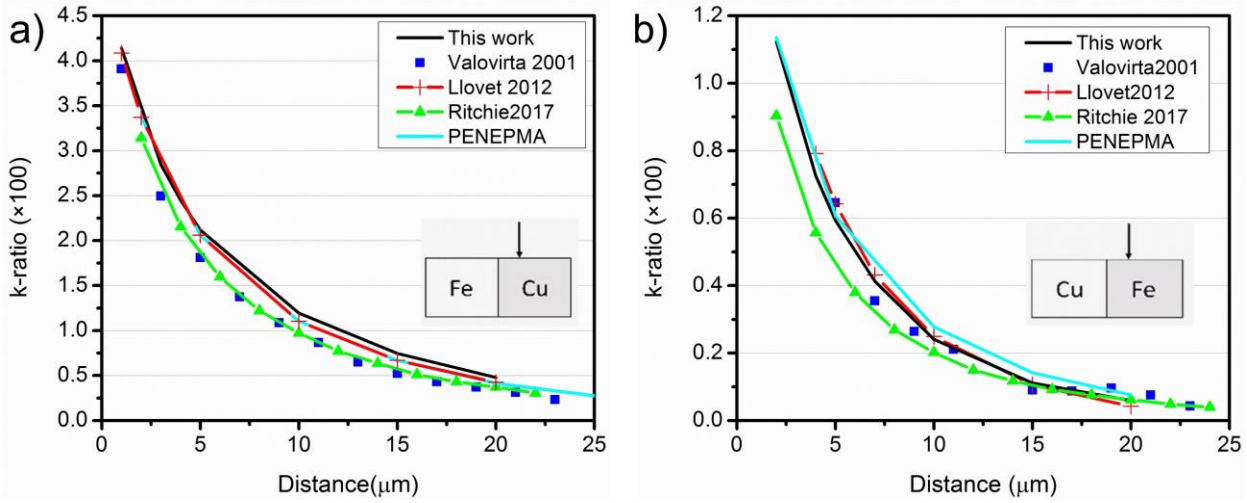

Figure 4.8 Variation of the k-ratio as the change of the distance between the electron beam and the boundary at 20 keV for a) Fe Kα line when the electron beam strikes the Cu region, and b) Cu Kα line when the electron beam strikes the Fe region.

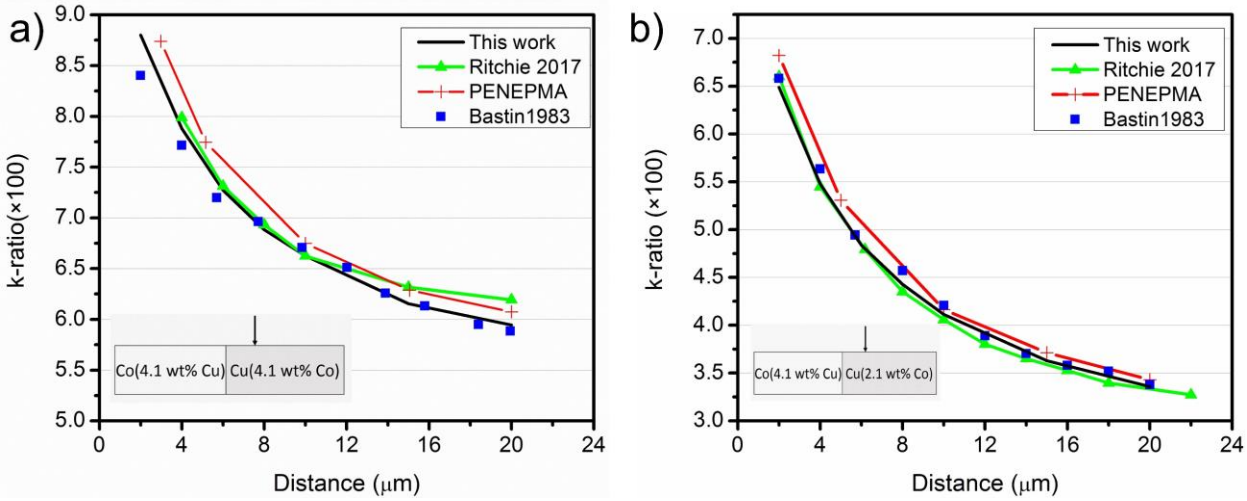

Figure 4.9 Variation of the k-ratio for the Co Kα line as a function of the distance between the electron beam and the boundary at 20 keV for a) a Cu matrix with 4.1 wt% Co coupled with a Co matrix with 4.1wt% Cu, and b) a Cu matrix with 2.1 wt% Co coupled with a Co matrix with 4.1 wt% Cu.

4.4.2 Cu and Co alloys coupled with a vertical boundary

To further validate our model, the SF intensities were calculated for a non-diffusion couple with two regions having the same elements but different compositions. Figure 4.9 displays the variation of the k-ratio for the Co Kα line as a function of the distance between the electron beam and the grain boundary at 20 keV. Figure 4.9 a) shows the case of a Cu matrix with 4.1 wt% Co coupled with a Co matrix with 4.1wt% Cu, while Figure 4.9 b) shows the case of a Cu matrix with

2.1 wt% Co coupled with a Co matrix with 4.1 wt% Cu. For both cases, the electron beam strikes the copper-rich region. Higher k-ratios for the Co Kα line are observed due to a higher weight fraction of Co in the region that the electron beam strikes. The simulation results of our program are compared with results from PENEPMA [17] and Ritchie [29], and analytical results from Bastin et al. [9]. As can be seen in Figure 4.9, there is a very good agreement between different simulation methods.

4.4.3 Cu inclusion embedded in an Fe matrix

In this section, we present results for the structure of a spherical inclusion embedded in a matrix. As displayed in Figure 4.1, a spherical Cu inclusion is embedded in an Fe matrix and attached to the surface, and the electron beam is positioned at the center of the Cu inclusion. The SF intensities were calculated for a Cu inclusion with a radius of 5 μm measured at 10 keV.

Figure 4.10 a) shows the electron trajectories of 200 electrons. The interaction volume has a radius of 0.3 μm, which is much smaller than the inclusion radius (5 μm), resulting in a small primary X-ray intensity for the Fe Kα line, 1.3% of that for the Cu Kα line. Thus, the Fe Kα line peak is barely seen in the simulated convolved spectrum without the fluorescence correction as shown in Figure 4.10 b) with a black solid line. However, because of the strong fluorescence of Fe, the simulated spectrum including fluorescence, as displayed in Figure 4.10 b) with red dots, shows the Fe Kα and Kβ peaks. When performing qualitative analysis for this spectrum, an analyst might interpret the Fe peaks as a trace constituent, while in fact it is produced by SF effects. This demonstrates the importance of SF both as an observed feature in an energy-dispersive spectrum, and of the need to perform simulation analysis.

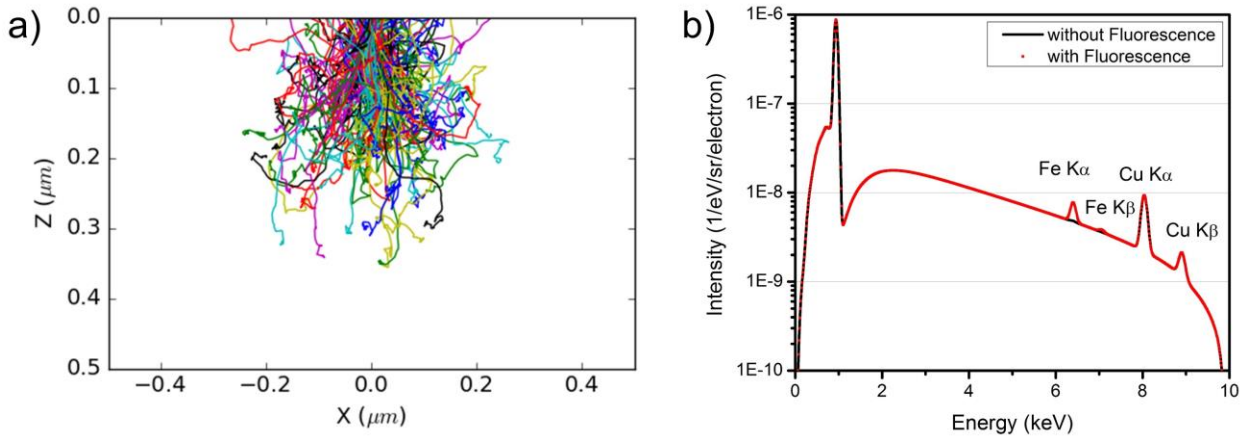

Figure 4.10 a) Electron trajectories of 200 electrons. b) Simulated spectra using MC X-ray with (red dots) and without (black solid line) the SF at 10 keV for a Fe matrix with a Cu inclusion embedded with a radius of 5 μm. The spectra were simulated with an energy channel width of 10 eV.

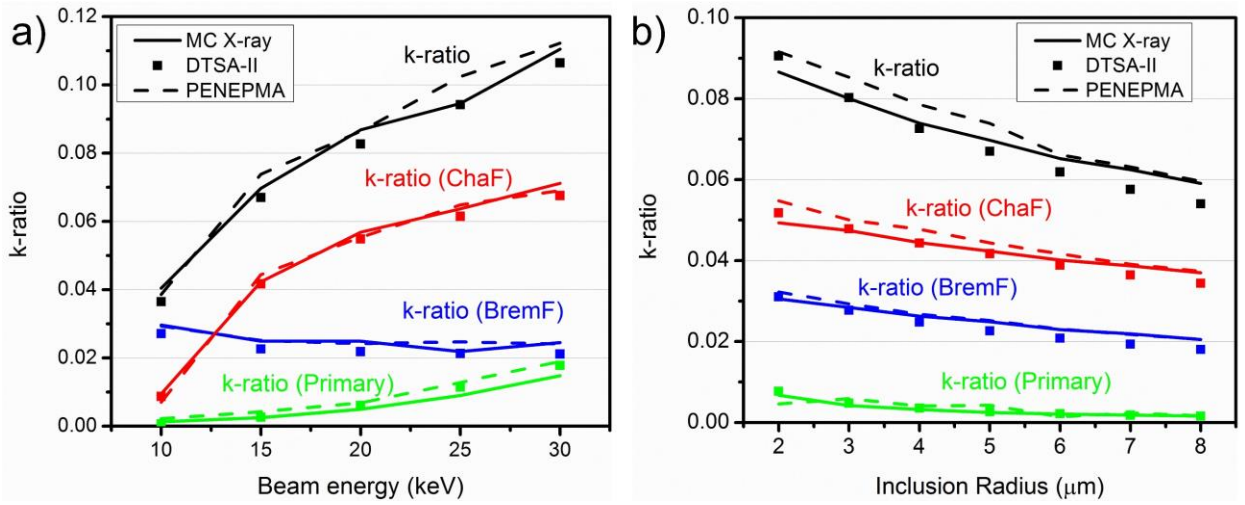

Figure 4.11 Variation of the k-ratios of the total (black), primary (green), characteristic fluorescence (red), and bremsstrahlung fluorescence (blue) for the Fe Kα line as functions of a) beam energy for a Cu spherical inclusion with a radius of 5μm and b) inclusion radius for 15 keV.

Figure 4.11 a) and b) show the variation of the k-ratios of the total (black), primary (green), characteristic fluorescence (red), and bremsstrahlung fluorescence (blue) for the Fe Kα line as a function of variable beam energy for a fixed inclusion radius of 5μm and of variable inclusion size for a fixed beam energy of 15 keV, respectively. The k-ratios of the primary, characteristic fluorescence, and bremsstrahlung fluorescence are the ratio of the primary, characteristic fluorescence, and bremsstrahlung fluorescence intensities of the specimen and the total intensity

of the standard, respectively. We observe good agreements of our simulation results with those from DTSA-II [16] and PENEPMA [17].

For both figures, the SF contribution is much higher than that of the primary X-rays. As shown in Figure 4.11 a), the k-ratio increases dramatically as the beam energy increases due to the enlarged interaction volume. When the beam energy is below 15 keV, the k-ratios of the bremsstrahlung fluorescence are higher than that of the characteristic fluorescence. However, as the beam energy increases, the characteristic fluorescence dominates. This is because the intensity of the Cu Kα line, which is the main source of the characteristic fluorescence, largely increases as the beam energy increases from 10 keV to 15 keV. Similar results are found for MC X-ray compared with DTSA-II and PENEPMA. In Figure 4.11 b), as the inclusion size increases, both the characteristic and bremsstrahlung fluorescence decrease since the emitting X-rays (Cu Kα line or bremsstrahlung X-rays) travel farther to enter the Fe region in order to fluoresce Fe X-rays. When the inclusion size is smaller than 5μm, we observe better agreement between MC X-ray and DTSA-II in comparison to between MC X-ray and PENEPMA. Conversely, as the inclusion radius increases above 5 μm, better agreement is observed with PENEPMA than DTSA-II. We attribute this to differences in physical models used in the different software algorithms as shown in Table 4.4.

4.4.4 Four Co inclusions embedded in a Cu matrix

To show the flexibility of our program in sample structure, an example of four Co spherical inclusions embedded in a Cu matrix is presented. Figure 4.12 shows the specimen structure in the X-Y plane, where *A* is the electron beam position with coordinates (0, 0, 0). The four Co spheres have coordinates of their centers at (1.5, 1.5, 1.5), (1.5, -1.5, 1.5), (-1.5, 1.5, 1.5), and (-1.5, -1.5, 1.5), respectively (unit in μm). The SF calculations were performed for various values of beam energy and inclusion radius. For all the setups presented in this section, the primary intensities for Co are 0 since the inclusions are outside the primary X-ray range. However, the Co Kα X-rays are still detected because of the fluorescence effect from both the Cu Kα X-rays and bremsstrahlung X-rays. Figure 4.13 shows the variation of the emitted X-ray intensities for the Co $K\alpha_1$ line as a function of beam energy for Co spherical inclusions with a radius of 500 nm and of inclusion radius at 15 keV. It is observed that the characteristic fluorescence intensities are greater than the bremsstrahlung fluorescence intensities for both figures. The strong characteristic fluorescence is

attributed to the strong absorption of Cu Kα X-rays in Co [25]. In Figure 4.13 a), as the beam energy increases, the SF intensity increases because of an increase in the emitting X-rays (both Cu Kα line and bremsstrahlung X-rays). In Figure 4.13 b), an increase of the SF intensity is shown with an increase in the inclusion radius due to the increased X-ray production as the volume of Co spheres increases.

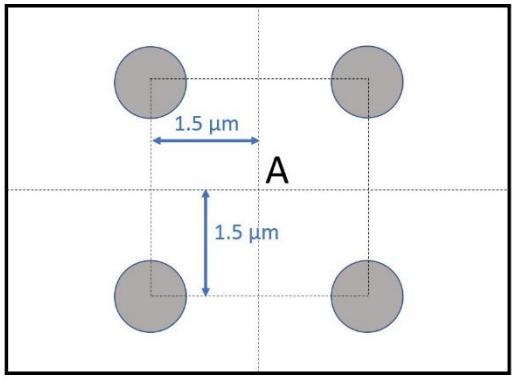

Figure 4.12 Specimen structure in the X-Y plane for four Co spherical inclusions embedded inside a Cu matrix. The white area represents the Cu matrix, and the gray areas represent the Co particles.

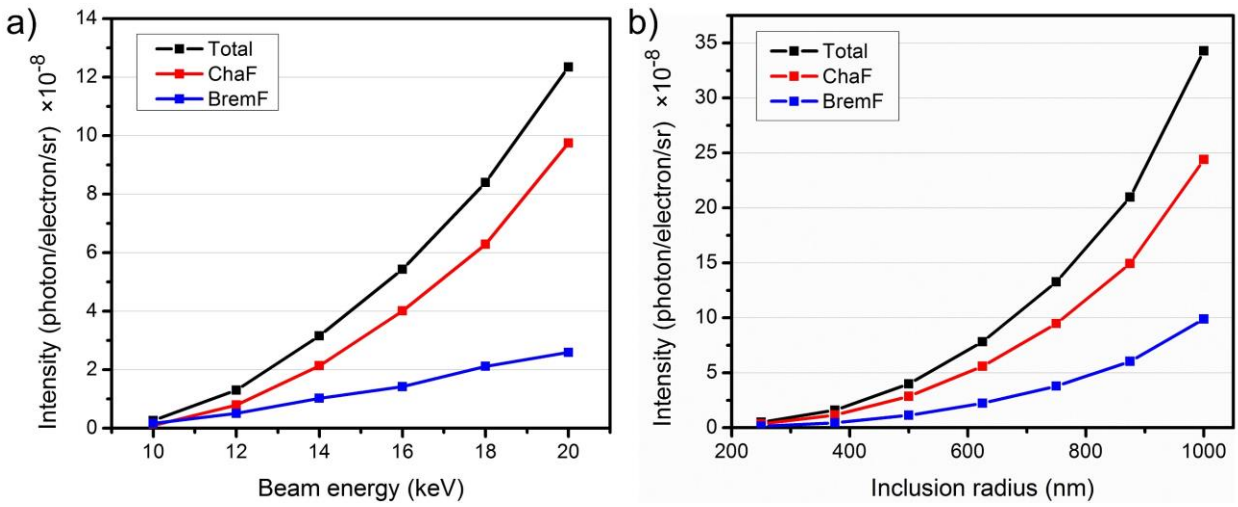

Figure 4.13 Variation of the emitted intensity for the Co $K\alpha_1$ line with the changes of a) beam energy for Co spherical inclusions with radius of 500 nm and b) inclusion radius at 15 keV.

4.5 Conclusion

In this work, a program was developed using a hybrid model which combines the Monte Carlo simulation and the analytical modeling to calculate SF intensities. The program can be applied to

materials with arbitrary 3D heterogeneous structures, and it includes the accurate calculation of both characteristic and bremsstrahlung fluorescence. An improvement in computation using "SkipVoxel" saves more than 80% of the simulation time with a less than 0.1% change in intensities by skipping the fluorescence calculation for some of the voxels and utilizing linear interpolation instead. Using the 3D intensity distribution of the primary X-rays obtained from MC X-ray, our program accurately computes the 3D distribution of the fluorescence X-rays. We have shown applications using material couples and embedded spherical inclusion structures and demonstrated very good agreement with experimental and analytical results from the previous studies and other Monte Carlo codes. MC X-ray combined with our fluorescence correction program provides accurate predictions of X-ray intensity for a diverse set of materials.

4.6 Acknowledgments

The authors acknowledge the financial support from McGill Engineering Doctoral Awards (MEDA).

4.7 References

1. Gauvin, R. and P. Michaud, *MC X-Ray, a new Monte Carlo program for quantitative X-ray microanalysis of real materials.* Microscopy and Microanalysis, 2009. **15**(S2): p. 488-489.
2. Gauvin, R., et al., *Win X-ray: A new Monte Carlo program that computes X-ray spectra obtained with a scanning electron microscope.* Microscopy and Microanalysis, 2006. **12**(1): p. 49-64.
3. Hovington, P., D. Drouin, and R. Gauvin, *CASINO: A new Monte Carlo code in C language for electron beam interaction—Part I: Description of the program.* Scanning, 1997. **19**(1): p. 1-14.
4. Yuan, Y., et al., *X-ray Emission From Thin Films on a Substrate-Experiments and Simulation.* Microscopy and Microanalysis, 2016. **22**(S3): p. 400-401.
5. Goldstein, J.I., et al., *Scanning electron microscopy and X-ray microanalysis*. 2017: Springer.
6. Cox, M., G. Love, and V. Scott, *A characteristic fluorescence correction for electron-probe microanalysis of thin coatings.* Journal of Physics D: Applied Physics, 1979. **12**(9): p. 1441.
7. Yuan, Y., et al., *Secondary Fluorescence Correction for Characteristic and Bremsstrahlung X-Rays Using Monte Carlo X-ray Depth Distributions Applied to Bulk and Multilayer Materials.* Microscopy and Microanalysis, 2019. **25**(1): p. 92-104.
8. Henoc, M., M.F. Maurice, and M.A. Zemskoff. *Phenomenes de fluorescence aux limites de phases*. in *Vth International Congress on X-Ray Optics and Microanalysis/V.*

Internationaler Kongreß für Röntgenoptik und Mikroanalyse/Ve Congrès International sur l'Optique des Rayons X et la Microanalyse. 1969. Springer.
9. Bastln, G., et al., *A correction procedure for characteristic fluorescence encountered in microprobe analysis near phase boundaries.* Scanning, 1983. **5**(4): p. 172-183.
10. Bastin, G., et al., *An iterative procedure for the correction of secondary fluorescence effects in electron-probe microanalysis near phase boundaries.* Spectrochimica Acta Part B: Atomic Spectroscopy, 1984. **39**(12): p. 1517-1522.
11. Myklebust, R.L. and D.E. Newbury, *Monte Carlo modeling of secondary x-ray fluorescence across phase boundaries in electron probe microanalysis.* Scanning, 1995. **17**(4): p. 235-242.
12. Escuder, J., et al. *Numerical correction for secondary fluorescence across phase boundaries in EPMA.* in *IOP Conference Series: Materials Science and Engineering*. 2010. IOP Publishing.
13. Armstrong, J.T. and P.R. Buseck, *A general characteristic fluorescence correction for the quantitative electron microbeam analysis of thick specimens, thin films and particles.* X-Ray Spectrometry, 1985. **14**(4): p. 172-182.
14. Llovet, X. and G. Galan, *Correction of secondary X-ray fluorescence near grain boundaries in electron microprobe analysis: Application to thermobarometry of spinel lherzolites.* American Mineralogist, 2003. **88**(1): p. 121-130.
15. Llovet, X., E. Valovirta, and E. Heikinheimo, *Monte Carlo simulation of secondary fluorescence in small particles and at phase boundaries.* Microchimica Acta, 2000. **132**(2): p. 205-212.
16. Ritchie, N.W., *Efficient Simulation of Secondary Fluorescence Via NIST DTSA-II Monte Carlo.* Microscopy and Microanalysis, 2017. **23**(3): p. 618-633.
17. Llovet, X. and F. Salvat, *PENEPMA: a Monte Carlo program for the simulation of X-ray emission in electron probe microanalysis.* Microscopy and Microanalysis, 2017. **23**(3): p. 634-646.
18. Llovet, X., et al., *Secondary fluorescence in electron probe microanalysis of material couples.* Journal of Physics D: Applied Physics, 2012. **45**(22): p. 225301.
19. Armigliato, A., A. Desalvo, and R. Rosa, *A Monte Carlo code including an X-ray characteristic fluorescence correction for electron probe microanalysis of a thin film on a substrate.* Journal of Physics D: Applied Physics, 1982. **15**(10): p. L121.
20. Youhua, H., H. Yuencai, and C. Jiaguang, *The calculation equations of characteristic fluorescence for multi-layer films.* Journal of Physics D: Applied Physics, 1988. **21**(7): p. 1221.
21. Waldo, R., *A characteristic x-ray fluorescence correction for thin-film analysis by electron microprobe.* Microbeam Analysis, 1991: p. 45.
22. Pfeiffer, A., C. Schiebl, and J. Wernisch, *Continuous fluorescence correction in electron probe microanalysis applying an electron scattering model.* X-Ray Spectrometry, 1996. **25**(3): p. 131-137.
23. Chantler, C.T., *Theoretical form factor, attenuation, and scattering tabulation for Z= 1–92 from E= 1–10 eV to E= 0.4–1.0 MeV.* Journal of Physical and Chemical Reference Data, 1995. **24**(1): p. 71-643.
24. Chantler, C.T., *Detailed tabulation of atomic form factors, photoelectric absorption and scattering cross section, and mass attenuation coefficients in the vicinity of absorption edges in the soft X-ray (Z= 30–36, Z= 60–89, E= 0.1 keV–10 keV), addressing*

convergence issues of earlier work. Journal of Physical and Chemical Reference Data, 2000. **29**(4): p. 597-1056.
25. Chantler, C.T., et al., *X-ray form factor, attenuation and scattering tables (version 2.1)*. 2005.
26. Goldstein, J.I., et al., *Scanning electron microscopy and X-ray microanalysis: a text for biologists, materials scientists, and geologists.* Plenum Press, New York, 1992.
27. Schreiber, T. and A. Wims, *Relative intensity factors for K, L and M shell x-ray lines.* X-Ray Spectrometry, 1982. **11**(2): p. 42-45.
28. Valovirta, E., et al. *EPMA of metal-metal diffusion couples at high temperature*. in *EMAS 2001–7th European Workshop on Modern Developments and Applications in Microbeam Analysis*. 2001. European Microbeam Analysis Society.
29. Ritchie, N.W., *Spectrum simulation in DTSA-II.* Microscopy and Microanalysis, 2009. **15**(5): p. 454-468.
30. Czyżewski, Z., et al., *Calculations of Mott scattering cross section.* Journal of Applied Physics, 1990. **68**(7): p. 3066-3072.
31. Browning, R., et al., *Empirical forms for the electron/atom elastic scattering cross sections from 0.1 to 30 keV.* Journal of Applied Physics, 1994. **76**(4): p. 2016-2022.
32. Powell, C.J., et al., *NIST Electron Elastic-Scattering Cross-Section Database, Version 4.0*. 2016.
33. Salvat, F., A. Jablonski, and C.J. Powell, *elsepa—Dirac partial-wave calculation of elastic scattering of electrons and positrons by atoms, positive ions and molecules.* Computer Physics Communications, 2005. **165**(2): p. 157-190.
34. Casnati, E., A. Tartari, and C. Baraldi, *An empirical approach to K-shell ionisation cross section by electrons.* Journal of Physics B: Atomic and Molecular Physics, 1982. **15**(1): p. 155.
35. Bote, D. and F. Salvat, *Calculations of inner-shell ionization by electron impact with the distorted-wave and plane-wave Born approximations.* Physical Review A, 2008. **77**(4): p. 042701.
36. Kirkpatrick, P. and L. Wiedmann, *Theoretical continuous X-ray energy and polarization.* Physical Review, 1945. **67**(11-12): p. 321.
37. Seltzer, S.M. and M.J. Berger, *Bremsstrahlung energy spectra from electrons with kinetic energy 1 keV–10 GeV incident on screened nuclei and orbital electrons of neutral atoms with Z= 1–100.* Atomic data and nuclear data tables, 1986. **35**(3): p. 345-418.

4.8 Appendix

4.8.1 Appendix A

Calculations of $d\theta$ and $d\varphi$

There are two geometry-related parameters which need to be calculated for different voxels, $d\theta$ and $d\varphi$. The parameter $d\theta$ is the angle between BA_1 and BA_2 and is expressed as follows (as shown in Figure 4.14):

$$d\theta = \theta_1 - \theta_2 \,, \tag{4.A1}$$

where

$$\theta_1 = \arctan\left(\frac{\sqrt{(x_A - x_B)^2 + (y_A - y_B)^2}}{|z_A - z_B| - \frac{dz}{2}}\right), \tag{4.A2}$$

$$\theta_2 = \arctan\left(\frac{\sqrt{(x_A - x_B)^2 + (y_A - y_B)^2}}{|z_A - z_B| + \frac{dz}{2}}\right). \tag{4.A3}$$

$d\varphi$ is calculated by (as shown in Figure 4.15 a and b)

$$d\varphi = 2 \times \arctan\left(\frac{\frac{d(A_3A_4)}{2}}{\sqrt{(x_A - x_B)^2 + (y_A - y_B)^2}}\right), \tag{4.A4}$$

where

$$d(A_3A_4) = \min\left(\frac{dx}{sin\varphi}, \frac{dy}{cos\varphi}\right), \tag{4.A5}$$

$$sin\varphi = \frac{dy}{\sqrt{(x_A - x_B)^2 + (y_A - y_B)^2}}, \tag{4.A6}$$

and

$$cos\varphi = \frac{dx}{\sqrt{(x_A - x_B)^2 + (y_A - y_B)^2}}. \tag{4.A7}$$

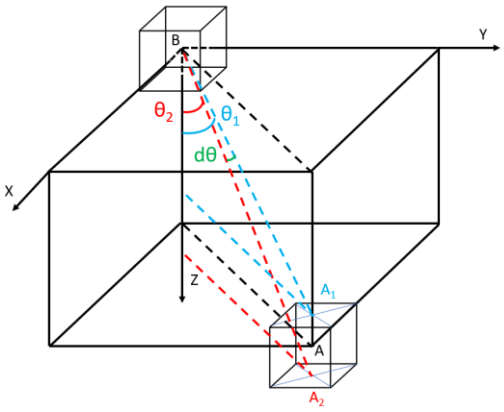

Figure 4.14 Schematic for the derivation of $d\theta$. Point B, A, A_1, and A_2 and angle $d\theta$, θ_1, and θ_2 lie on the same plane, which is perpendicular to the X-Y plane.

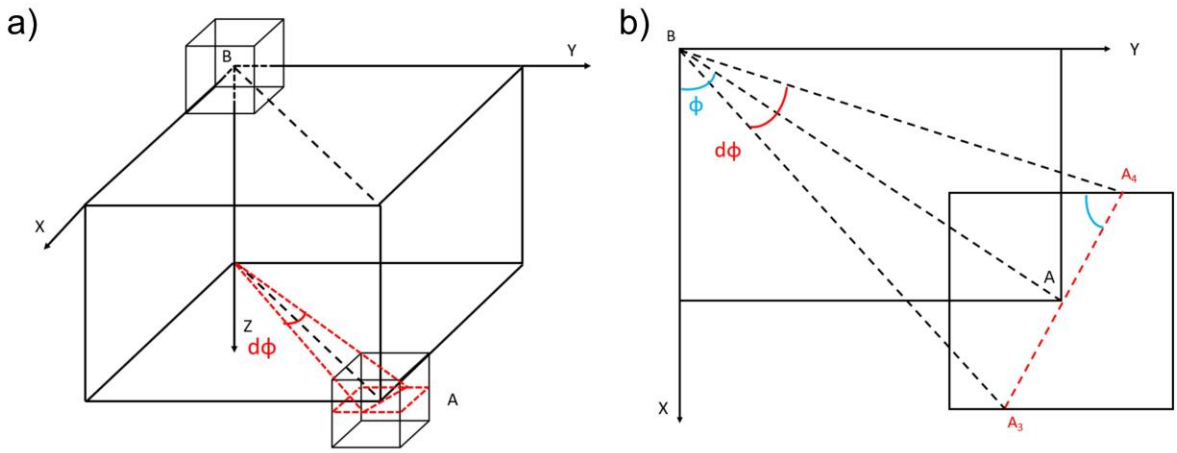

Figure 4.15 a) Schematic for the derivation of $d\phi$. The angle $d\phi$ lies within the X-Y plane. b) Schematic for the derivation of $d\phi$ on the X-Y plane.

Figure 4.16 a) and b) show the values of $d\theta$ and $d\varphi$ (in steradian) in 3D space, respectively, to calculate the SF intensity of the Fe Kα line for a non-diffusion couple of Fe and Cu at 20 keV and the distance between the electron beam and the grain boundary is 3 μm (see Figure 4.5 for the sample structure). The electron beam strikes the Cu region. The volume of each voxel is 0.032 μm^3 ($0.4 \times 0.4 \times 0.2\ \mu m$). The coordinates of each point in the figure represent the position of voxel V_A, and voxel V_B is the voxel where the electron beam hits. Since the calculation was only performed at the Fe region, data is shown only for voxels whose X coordinate is smaller than 0. The parameter $d\theta$ decreases as the voxel V_A moves away from voxel V_B, and $d\varphi$ does not change as the Z coordinate changes. The values of $d\theta$ and $d\varphi$ also depend on the size of the voxel. As shown in Figure 4.17, both two angles increase with an increase in the voxel volume.

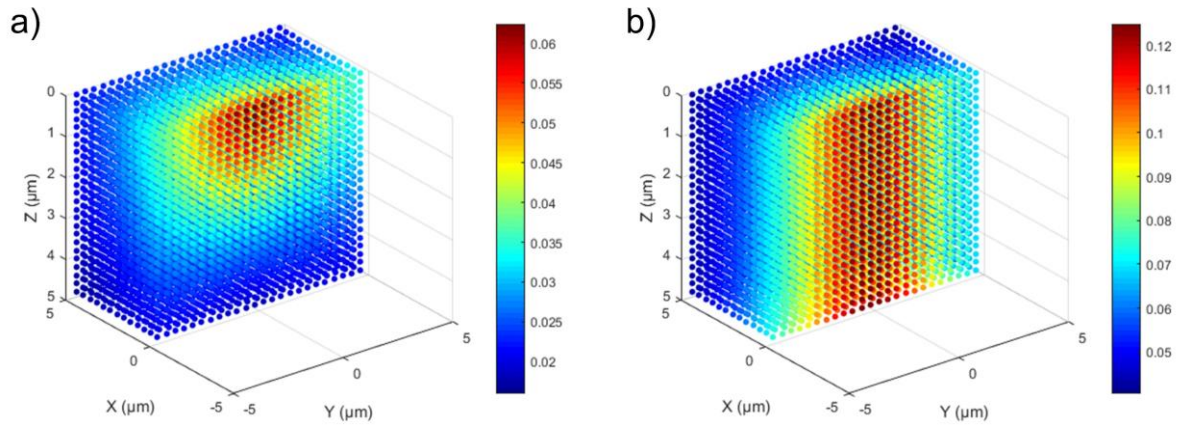

Figure 4.16 Values of a) $d\theta$ and b) $d\varphi$ for each voxel to calculate the SF intensity of Fe Kα line for a non-diffusion couple of Fe and Cu at 20 keV. The distance between the electron beam and the boundary is 3 μm and the electron beam strikes the Cu region.

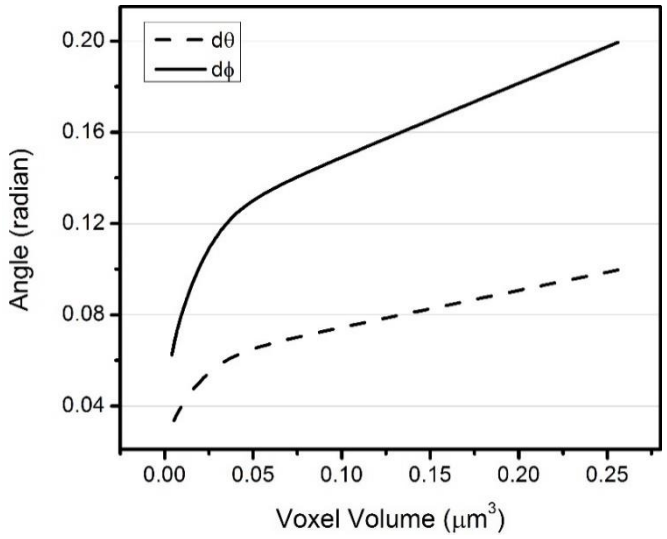

Figure 4.17 Variations of $d\theta$ and $d\varphi$ versus the voxel volume (Note that the side lengths along the X- and Y-axes are the same and are double the side length along the Z-axis).

4.8.2 Appendix B

Fluorescence correction from the same voxel

To calculate the SF intensity fluoresced by X-rays from the same voxel (as shown in Figure 4.18), a triple numerical integral is required. In this case, we only need to consider the fraction of X-rays which are absorbed before exiting the voxel. Assuming that the primary X-rays are generated at point A (the center of the voxel) and absorbed at point A' with the distance between s

and $s + ds$ in the direction with the polar angle θ and the azimuthal angle φ, based on equation (4.7), the following equation can be easily obtained:

$$I_{f,X_A}(V_A, X_{B,v_A}) = \frac{\sin\theta\, d\theta d\varphi}{4\pi} I_{p,X_B}(V_A) \exp\left(-\left(\frac{\mu}{\rho}\right)_{X_B}^{V_A} \rho_{V_A} s\right) \times \left(1 - \exp\left(-c_{E_A}\left(\frac{\mu}{\rho}\right)_{X_B}^{E_A} \rho_{V_A} ds\right)\right) \frac{r_{X_A} - 1}{r_{X_A}} \omega_{X_A} p_{X_A}. \tag{4.B1}$$

To obtain the total SF intensity, a triple integral over $d\theta$, $d\varphi$, and ds is performed as follows:

$$I_{f,X_A}(V_A, X_{B,v_A}) = I_{p,X_B}(V_A) \frac{1}{4\pi} \frac{r_{X_A} - 1}{r_{X_A}} \omega_{X_A} p_{X_A} \int_0^{2\pi} \int_0^{\pi} \int_0^{s_{max}} \sin\theta \exp\left(-\left(\frac{\mu}{\rho}\right)_{X_B}^{V_A} \rho_{V_A} s\right) \times \left(1 - \exp\left(-c_{E_A}\left(\frac{\mu}{\rho}\right)_{X_B}^{E_A} \rho_{V_A} ds\right)\right) d\theta d\varphi, \tag{4.B2}$$

where s_{max} is the maximum path length that an X-ray travels within voxel V_A starting from the center of V_A as a function of θ and φ. As ds gets close to 0, we have

$$1 - \exp\left(-c_{E_A}\left(\frac{\mu}{\rho}\right)_{X_B}^{E_A} \rho_{V_A} ds\right) \approx c_{E_A}\left(\frac{\mu}{\rho}\right)_{X_B}^{E_A} \rho_{V_A} ds. \tag{4.B3}$$

Substituting equation (4.B3) into equation (4.B2),

$$I_{f,X_A}(V_A, X_{B,v_A}) = I_{p,X_B}(V_A) \times \frac{1}{4\pi} c_{E_A}\left(\frac{\mu}{\rho}\right)_{X_B}^{E_A} \rho_{V_A} \frac{r_{X_A} - 1}{r_{X_A}} \omega_{X_A} p_{X_A} \times \int_0^{2\pi} \int_0^{\pi} \int_0^{s_{max}} \sin\theta \exp\left(-\left(\frac{\mu}{\rho}\right)_{X_B}^{V_A} \rho_{V_A} s\right) ds d\theta d\varphi. \tag{4.B4}$$

Because of the central symmetry of the voxel, equation (4.B4) can be written as follows:

$$I_{f,X_A}(V_A, X_{B,v_A}) = I_{p,X_B}(V_A) \frac{1}{4\pi} c_{E_A}\left(\frac{\mu}{\rho}\right)_{X_B}^{E_A} \rho_{V_A} \frac{r_{X_A} - 1}{r_{X_A}} \omega_{X_A} p_{X_A} \times \tag{4.B5}$$

$$8\int_0^{\pi/2}\int_0^{\pi/2}\int_0^{s_{max}} \sin\theta \exp\left(-\left(\frac{\mu}{\rho}\right)_{X_B}^{V_A}\rho_{V_A}s\right) dsd\theta d\varphi.$$

The triple integral $\int_0^{\pi/2}\int_0^{\pi/2}\int_0^{s_{max}} \sin\theta \exp\left(-\left(\frac{\mu}{\rho}\right)_{X_B}^{V_A}\rho_{V_A}s\right) dsd\theta d\varphi$ is solved numerically using a triple computational loop in our program.

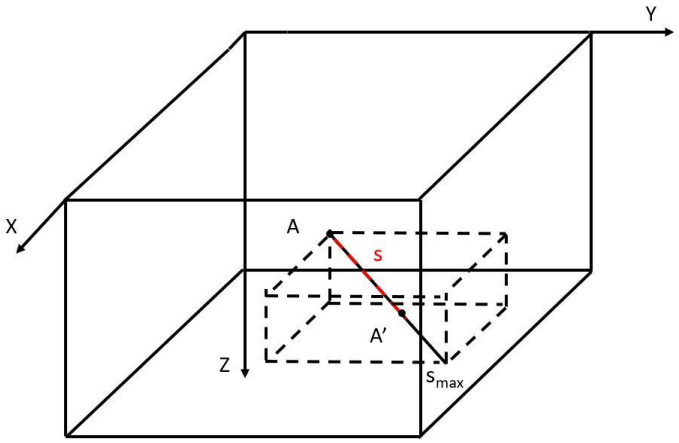

Figure 4.18 Schematic for the derivation of SF intensity from the same voxel. The primary X-rays are generated at point *A* (the center of the voxel) and absorbed at point *A′*.

Chapter 5. Inverse modeling for quantitative X-ray microanalysis applied to 2D heterogeneous materials

In Chapter 3 & Chapter 4, the developed secondary fluorescence correction program has significantly improved the accuracy of X-ray emission forward modeling using the Monte Carlo method, especially for heterogeneous materials. We can next focus on the inverse modeling algorithm. In this chapter, a novel inverse modeling algorithm was proposed to extract the compositional and structural information of an unknown specimen from a series of X-ray intensity measurements.

- This paper has been published as: Y. Yuan*, H. Demers, N. Brodusch, X. Wang, R. Gauvin, Inverse Modeling for Quantitative X-ray Microanalysis Applied to 2D Heterogeneous Materials, Ultramicroscopy, 219 (2020) 113117.

5.1 Abstract

Current quantitative X-ray microanalysis methods are only available for homogeneous materials. This paper presents a newly developed inverse modeling algorithm to determine both the structure and composition of two-dimensional (2D) heterogeneous materials from a series of X-ray intensity measurements under different beam energies and beam positions. It utilizes an iterative process of forward modeling to determine the optimal specimen to minimize the relative differences between the simulated and experimental characteristic X-ray intensities. The Monte Carlo method is used for the forward modeling to predict the X-ray radiation for a given specimen and experimental setup. Several examples of applications are presented for different types of samples with one-dimensional and two-dimensional structures, in which the simulated X-ray intensities from phantom samples are used as input. Most of the results obtained from our algorithm agree well with the phantom samples. Some discrepancies are found for the voxels located at deeper depths of the two-dimensional samples. And the discrepancies may be attributed to errors from the Monte Carlo simulations and from the variation of the X-ray range with beam energy. As a proof-of-concept work, this paper confirms the feasibility of our inverse modeling algorithm applied to 2D heterogeneous materials.

5.2 Introduction

The technique of energy dispersive spectroscopy (EDS) or wavelength dispersive spectroscopy (WDS) allows users to collect X-ray signals emitted through the interaction of the electron beam with the specimen and accurately measure their intensities with the help of scanning electron microscopy (SEM) or electron probe microanalysis (EPMA) [1]. Qualitative X-ray analysis can then be carried out using characteristic energies of X-ray lines of different elements to identify the elements present in an unknown specimen [2]. Furthermore, one can also perform quantitative X-ray microanalysis, i.e., calculating the concentrations of the constituent elements [3, 4].

One of the most common techniques of quantitative X-ray microanalysis, the k-ratio method, describes the relationship between the ratio of the characteristic X-ray intensities from an element of interest in the unknown and the standard sample and the ratio of the concentration of the element in the unknown and the standard sample (with matrix corrections) [2, 4, 5]. However, this method requires the same conditions of analysis for the unknown and the standard sample, which are not always achievable. Another emerging method is the f-ratio method, which uses the ratio of the characteristic X-ray intensity of the element of interest to the sum of the intensities of all the constituent elements with calibration factors for the calculation [6-9]. Although the same analysis conditions are not necessary, the calibration factors for different systems require further calculations. For the two above-mentioned methods and others which are currently available, one identical restriction is that they can only be applied to homogeneous samples, or, more precisely, samples that are homogeneous within the interaction volume [1].

For materials with complex structures such as multilayers and inclusions inside matrices, the characteristic X-ray intensity of the element of interest is relative to both the structure and composition of the specimen and cannot be simply expressed in a mathematical form. Therefore, the traditional quantitative X-ray microanalysis methods are not applicable. X-ray microanalysis inverse modeling is a methodology to extract the structural and compositional information of an unknown sample from a series of X-ray intensity measurements using EDS or WDS [10].

To understand the inverse modeling methodology, we must first explain the Monte Carlo method, which is currently the most important forward modeling approach to predict X-ray production with knowledge of the sample (both structure and composition) and experimental setup

[11, 12]. The Monte Carlo method uses random numbers to predict the outcome of an event [13]. In X-ray microanalysis, it is used to compute the travel direction and travel distance of an electron after each elastic collision event to obtain the whole electron trajectory in the solid sample. Furthermore, both characteristic and bremsstrahlung X-ray productions are calculated to obtain the full X-ray spectrum [14]. The method can be applied to arbitrary heterogenous samples, and the simulation results are found to agree well with experimental data [15-19].

Several Monte Carlo programs have been developed for X-ray microanalysis [14, 20-23]. One of them is MC X-ray [20]. A feature of MC X-ray is that it is scriptable using Python, which means that all the input parameters, including specimen and experimental parameters, can be modified using the script. In this way, a large number of simulations with various series of experiment setups can be easily performed with a single loop in the script. Moreover, the voxel-based specimen can be defined using several matrices representing the weight fractions of elements at different positions, making the sample structure and composition easy to modify. MC X-ray is used to perform the forward modeling in our work. One can also use other programs with the help of *pyMonteCarlo*, an open source code that runs various Monte Carlo programs using Python script [24].

Previous research has been conducted on one-dimensional (1D) and 2D inverse modeling. 1D inverse modeling is intended to estimate the thickness or composition of thin layers coated on substrates or multilayer samples. For example, methods have been developed to determine the thickness of a coating film on a substrate with prior knowledge of the compositions of both the coating and the substrate [25-28]. One can first perform a series of Monte Carlo simulations or analytical calculations using depth distribution models [$\phi(\rho z)$] for various film thicknesses and beam energies to get the calibration curves of the k-ratio, and then use the experimental k-ratios to find the correct film thickness. Several programs have been developed to calculate the composition and film thickness simultaneously [29-32]. For example, a commercial software AZtec LayerProbe is available for the analysis of both thin films and multilayers using a single beam energy when the possible sample structure is known [30]. Some of the developed programs can even deal with the problem of common elements in different layers, like *Strata* [32] and *XFilm* [31]. Since both *Strata* and *XFilm* use $\phi(\rho z)$ curves to calculate the X-ray emissions of a given specimen, the

accuracy of the estimated composition and film thickness greatly depends on the accuracy of the $\phi(\rho z)$ model.

2D inverse modeling is more difficult because 2D materials have more complex structures than 1D materials, bringing difficulties to the analytical calculation of X-ray emission. Current 2D inverse modeling algorithms all use the Monte Carlo method to simulate X-ray emission. A specific problem can be solved only when the structure or the possible compositions for different regions of the sample are known in advance. For example, Ro et al. [12] estimated the thickness of carbon layers coated on glass particles with known composition by comparing the simulated C/O X-ray intensity ratios with the experimental one. Gauvin et al. [33] computed the calibration curves to determine the depth and size of spherical manganese sulfide (MnS) inclusions embedded in an iron (Fe) matrix. Wagner et al. [10] developed a more general model, which uses the simulated annealing method to extract structural information from a set of X-ray intensity measurements under different beam energies and beam positions for arbitrary 2D and 1D structures. However, this method can only be implemented when possible compositions of the specimen are known.

With respect to the samples with three-dimensional (3D) structures, people typically use a technique that combines focused ion beam (FIB) and SEM-EDS to perform 3D quantitative X-ray microanalysis by serially sectioning the specimen and performing EDS mapping for each slice [34-36]. However, this technique is destructive. Overall, it is necessary to propose a non-destructive method that can be generally applied to 2D and 3D inverse modeling to simultaneously extract the structural and compositional information of an unknown sample.

In this work, we introduce a new inverse modeling algorithm for quantitative X-ray microanalysis of heterogeneous materials. As a proof-of-concept prototype, the developed algorithm is currently applicable to 2D and 1D heterogeneous materials.

5.3 Methods

Our inverse modeling algorithm uses iterations of forward modeling, which is implemented through a Monte Carlo program, MC X-ray, to find the optimal structure and composition of an unknown sample to minimize the relative differences between the simulated and experimental X-ray intensities.

5.3.1 Voxel-based 2D sample structure

The 2D inverse modeling assumes that the 2D heterogeneous samples are homogeneous along the Y-axis and heterogeneous along the X- and Z-axes. The coordinate system is defined in the way that the surface of the specimen is on the X-Y plane and the direction perpendicular to the specimen's surface is the Z direction (the direction that points inside the specimen is the positive direction of Z). As shown in Figure 5.1 b), the whole sample is split into small cuboids, which are infinite along the Y-axis. Each cuboid is called a voxel, representing the smallest homogeneous structure within the sample. The sample is also assumed to be infinite along the X-axis and positive direction of the Z-axis, and the composition for the extended area is the same as that of the nearest voxel. By changing the size and composition of each voxel randomly, arbitrary 2D materials can be simulated. Figure 5.2 shows the cross-section views of some examples of the sample structure on the X-Z plane. Figure 5.2 a) presents a simulated multilayer sample, in which each region with the same color represents a thin layer. Figure 5.2 b) uses the red voxels to represent grain boundaries and yellow voxels to represent grains. Furthermore, when some of the voxels on the surface are left empty, the fracture surface can be displayed as shown in Figure 5.2 c). The voxel-based sample structure may have some limitations when dealing with samples with smooth concentration gradient due to the abrupt boundary assumption. In an ideal situation, the limitations can be minimized by choosing a small voxel size because, in principle, any smooth gradient can be described in a discrete form as long as the step size is small enough. Further research is needed to understand the tolerance of our inverse modeling algorithm to such kind of samples, and this will be conducted in the future.

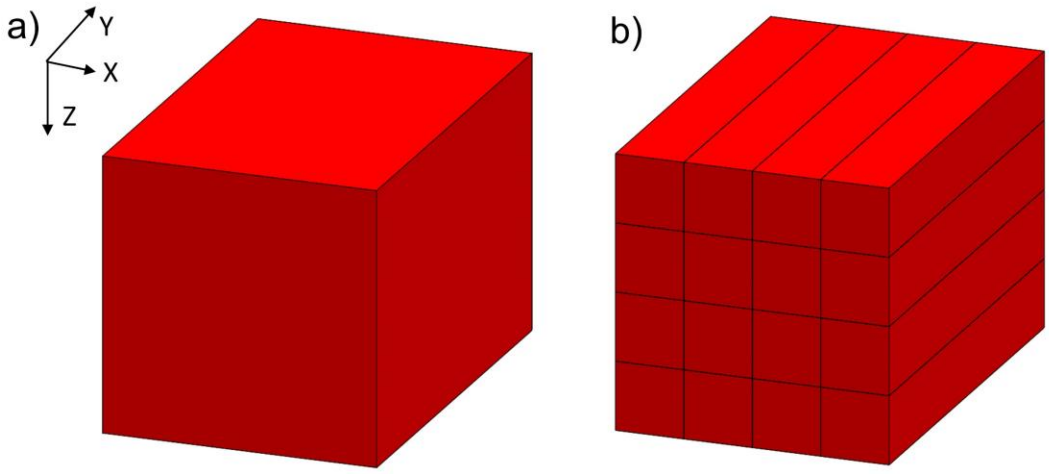

Figure 5.1 Voxel-based sample structure, a) the sample; b) the sample is split into small cuboids, which are homogeneous along the Y-axis and heterogeneous along the X- and Z-axes.

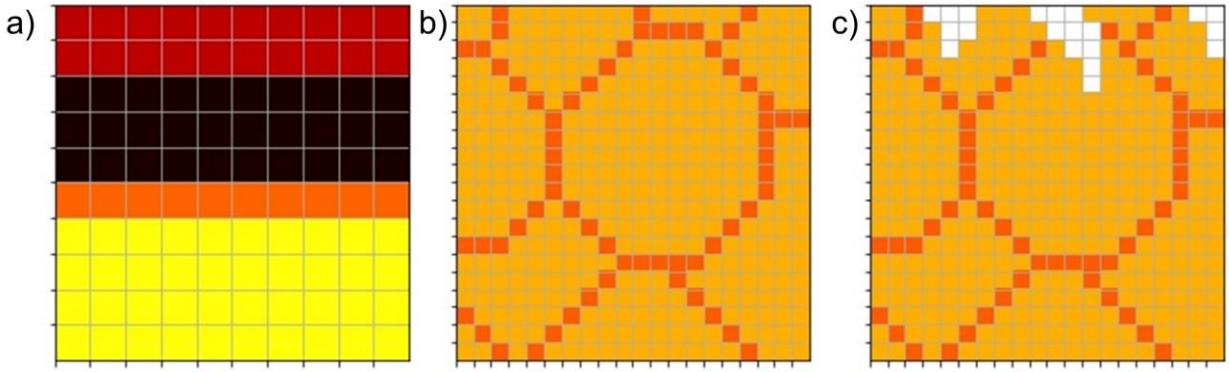

Figure 5.2 Examples of sample structure simulated using cuboids on the X-Z plane. a) Multilayer, b) grain boundaries, and c) fracture surface. Each color represents a certain composition.

5.3.2 Forward modeling using MC X-ray

MC X-ray is scriptable in Python, which facilitates running a batch of simulations. The structure and composition of a voxel-based 2D specimen can be expressed as a 3D matrix $\boldsymbol{C}$, which is composed of a series of two-dimensional matrices, whose sizes are equal to the number of voxels, representing the weight fraction of each element. For example, $\boldsymbol{C}(l,i,j)$ denotes the weight fraction of element A_l for the voxel located at the i^{th} row and the j^{th} column. In the following text, $\boldsymbol{C}$ is used to represent the specimen directly.

In each iteration, MC X-ray is used to simulate the emitted X-ray intensities for a new generated specimen ***C***. For a known specimen ***C***, the simulated X-ray intensity for a certain characteristic X-ray line and a specific experimental setup (with two variables: beam energy and beam position) is given by:

$$I_{sim}(X_A, E_0, P_X) = MC(\boldsymbol{C}, X_A, E_0, P_X, S), \tag{5.1}$$

where MC denotes the Monte Carlo simulation, X_A is the characteristic X-ray line of a certain element *A*, E_0 is the beam energy, P_X is the beam position along the X-axis, and S represents other fixed experimental parameters; for example, solid angle and take-off angle. Since the specimen is homogeneous along the Y-axis, the beam position along the Y-axis does not affect the X-ray radiation. Thus only P_X is considered. In addition, the X-ray emission range, R_X, which is defined as the depth where 98% of the emitted characteristic X-rays (including absorption) are generated, is also output from MC X-ray. For the results presented in this paper, the electron number of 1,000 was used for the forward modeling.

5.3.3 Problem to solve

For a given specimen ***C***, the absolute value of the relative difference between the simulated and experimental characteristic X-ray intensities is expressed as follows:

$$|d_r(X_A, E_0,\ P_X)| = \left|\frac{I_{sim}(X_A, E_0,\ P_X) - I_{exp}(X_A, E_0,\ P_X)}{I_{exp}(X_A, E_0,\ P_X)}\right|, \tag{5.2}$$

where $I_{exp}(X_A, E_0,\ P_X)$ is the experimental intensity of the characteristic X-ray line X_A at the beam energy E_0 and beam position P_X.

The purpose of the inverse modeling is to find a specimen ***C*** to minimize the absolute values of relative differences between the simulated and experimental X-ray intensities $|d_r|$ for a series of measurements under different beam energies and beam positions.

5.3.4 Algorithm of the inverse modeling

The composition information along the Z- and X-axes is extracted from the measurements under varying beam energies and varying beam positions, respectively. The composition of each voxel of the sample is optimized by iteratively comparing the simulated and experimental X-ray

intensities for the corresponding beam energy and beam position and updating the composition accordingly. The corresponding beam energy is determined according to the X-ray emission range, R_X, obtained from MC X-ray.

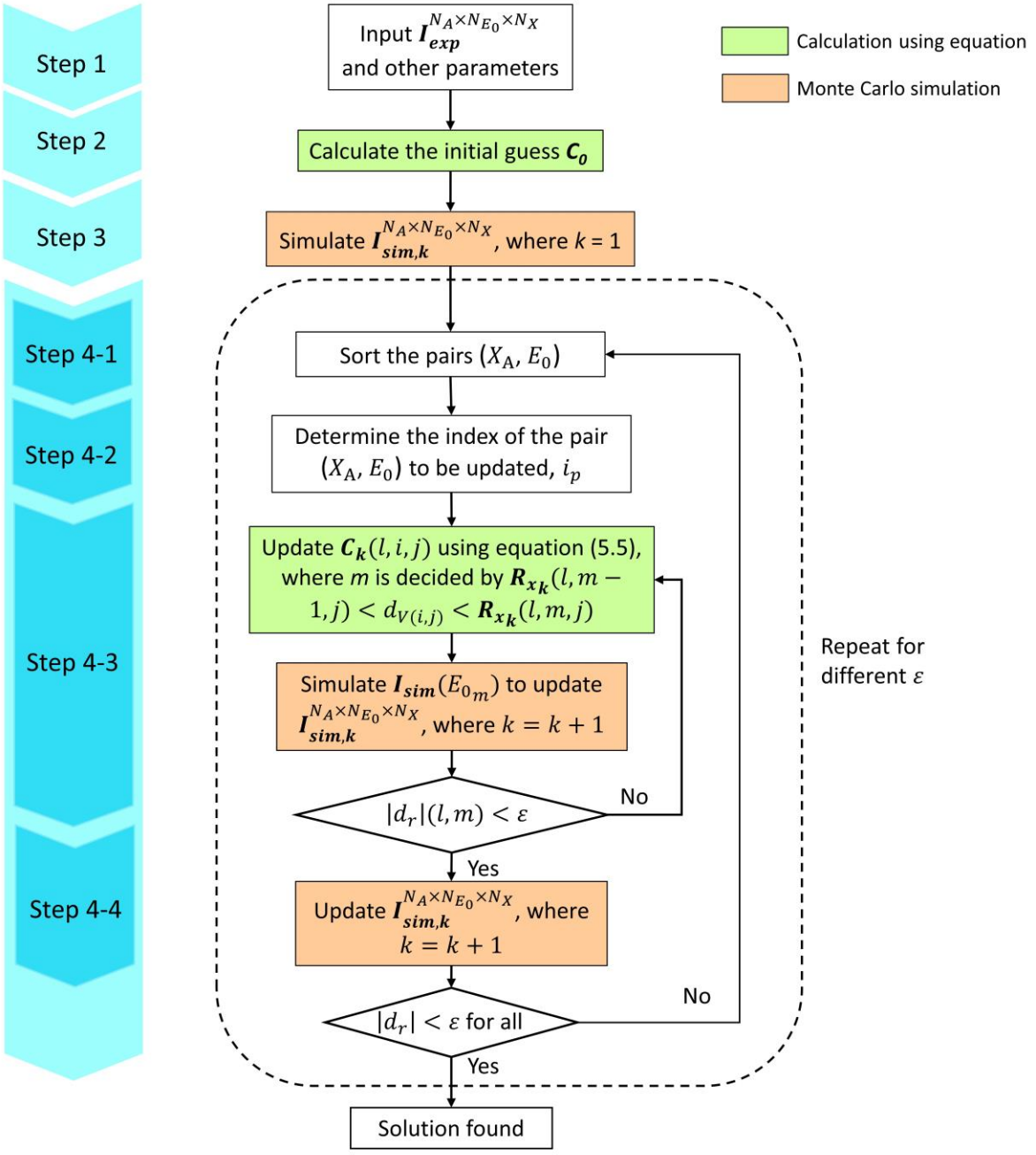

Figure 5.3 Flowchart for the inverse modeling algorithm

The process of the inverse modeling algorithm will be introduced in the following four steps. A flowchart of the algorithm is presented in Figure 5.3.

Step 1: Input parameters

The input parameters include experimental data and other parameters. The experimental data is obtained through a series of EDS or WDS measurements under different beam energies and beam positions and input into our algorithm as a 3D matrix $\boldsymbol{I}_{\boldsymbol{exp}}^{N_{X_A} \times N_{E_0} \times N_{P_X}}$, where $N_{X_A} \times N_{E_0} \times N_{P_X}$ is the matrix size, and N_{X_A}, N_{E_0}, and N_{P_X} are the number of the X-ray lines, the beam energies, and the beam positions, respectively. $\boldsymbol{I}_{\boldsymbol{exp}}(l, m, n)$ is used to represent the experimental X-ray intensity for the X-ray line X_{A_l} with a beam energy of E_{0_m} for the beam position P_{X_n}, where *l*, *m*, and *n* are the index of the X-ray line, the beam energy, and the beam position, respectively, and $0 < l \leq N_{X_A}$, $0 < m \leq N_{E_0}$, and $0 < n \leq N_{P_X}$. The lists of the X-ray lines, beam energies, and beam positions are also required, and the beam energies and beam positions are sorted from small to large. We typically choose only one X-ray line for each element so that the number of X-ray lines is equal to the number of elements.

Other input parameters include the voxel's side length along the Z-axis (L_Z), the number of voxels along the Z-axis (N_Z), and the initial error tolerance ε. Note that the voxel's side length along the X-axis (L_X), the number of voxels along the X-axis (N_X), and their positions are determined directly by the beam positions in the way that the X coordinates of the voxels' centers equal the beam positions, and N_X equals the number of the beam positions.

The input parameters including the voxel's side length along the Z-axis, beam energies, and beam positions, greatly influence the accuracy and the smallest feature that could be distinguished of the final solution $\boldsymbol{C}$, and different parameters correlate with each other. We have not found an appropriate algorithm to determine the optimal input parameters. However, the effects of the input parameters will be discussed in the results and discussion section, which may be helpful to users.

Step 2: Initialize *C*

The initial guess of the specimen $\boldsymbol{C_0}$ is calculated using the k-ratio method without correction factors, written as $c_{unk} = k \times c_{stan}$, where *k* is the k-ratio, the intensity ratio of the characteristic X-ray line in the unknown and standard sample, and c_{unk} and c_{stan} are the concentrations of the

element of interest in the unknown and standard sample. The concentration of a certain element of a certain voxel $\mathbf{C_0}(l,i,j)$ is initialized using the experimental X-ray intensity $\boldsymbol{I_{exp}}(l,m,j)$, which is obtained at the beam position that has the same X coordinate as the voxel's center and under the beam energy, which corresponds to the X-ray emission range that is just greater than the Z coordinate of the voxel. It is expressed as follows:

$$\boldsymbol{C_0}(l,i,j) = \frac{\boldsymbol{I_{exp}}(l,m,j)}{I_{stan}(l,m)} c_{stan}(l), \tag{5.3}$$

where *m* satisfies the condition $R_x(l,m-1) < d_{V(i,j)} < R_x(l,m)$, in which $d_{V(i,j)}$ is the depth of the voxel *V(i, j)*, represented by the Z coordinate of the voxel's center, $R_x(l,m-1)$ and $R_x(l,m)$ are the X-ray range of the X-ray line X_{A_l} in the standard for the *(m-1)*th beam energy and the *m*th beam energy, respectively, $\boldsymbol{C_0}(l,i,j)$ is the weight fraction of the element A_l for the voxel *V(i, j)*, $I_{stan}(l,m)$ is the X-ray intensity of the X-ray line X_{A_l} in the standard under the beam energy E_{0_m}, and $c_{stan}(l)$ is the weight fraction of element A_l in the standard. X_{A_l} is the X-ray line of the element A_l. The X-ray intensities of the standard sample can be obtained through either experiments or simulations. But in this work, all measurements of the standard samples were conducted through Monte Carlo simulation. Normally, pure bulk sample is used as standard, in which the concentration of the target element is 1.

The composition of each voxel is then normalized, written as follows:

$$\boldsymbol{C_0}(l,i,j) = \frac{\boldsymbol{C_0}(l,i,j)}{\sum_{z=1\ to\ N_A} \boldsymbol{C_0}(z,i,j)}, \tag{5.4}$$

where N_A is the number of elements in the unknown sample.

In this step, the algorithm tries to get an initial guess close to the final solution to decrease the number of iterations taken for the optimization.

Step 3: Update the simulated X-ray intensities

Following the initialization of $\boldsymbol{C}$, Monte Carlo simulations are performed for all the beam energies and beam positions for the specimen $\boldsymbol{C_0}$ to obtain the simulated X-ray intensities $\boldsymbol{I}_{\boldsymbol{sim,k}}^{N_{X_A} \times N_{E_0} \times N_{P_X}}$ and X-ray ranges $\boldsymbol{R}_{\boldsymbol{x,k}}^{N_{X_A} \times N_{E_0} \times N_{P_X}}$, where *k* is defined as the number of times that

the forward modeling is performed to monitor the variation of simulated X-ray intensities. k is equal to 1 in this step.

Step 4: Optimize *C* for a certain ε

Step 4 is composed of iterations of four sub-steps (step 4-1 to step 4-4).

Step 4-1: *Sort the pairs of* (X_A, E_0)

The pairs of the X-ray line and the beam energy (X_{A}, E_0) are sorted by the average X-ray emission range of different beam positions from small to large, and the average X-ray emission range is calculated using $R_{x,k,ave}(X_{\mathrm{A}_l}, E_{0_m}) = \sum_{n=1}^{N_{P_X}} \boldsymbol{R_{x,k}}(l,m,n)\,/N_{P_X}$. The purpose of this step is to make sure that the optimization starts from the pairs with smaller X-ray ranges, which corresponds to the voxels located at shallower depths, considering the great effect of those voxels on the X-ray emission of the voxels located at deeper depths.

Step 4-2: *Determine the pair to be updated*

According to the sorted pairs of (X_{A}, E_0), the index of the pair that will be updated i_p is determined to satisfy two conditions. The first condition is that, for all the pairs $(X_{\mathrm{A}}, E_0)_i$ with index $i < i_p$, the absolute values of their relative differences between the simulated and experimental X-ray intensities ($|d_r|$) are all smaller than ε. The second condition is that, for the pair that is chosen to be updated $(X_{\mathrm{A}}, E_0)_{i_p}$, not all of the $|d_r|$ values are smaller than ε.

Step 4-3: *Update* ***C*** *for the pair* $(X_A, E_0)_{i_p}$

For the chosen pair $(X_{\mathrm{A}}, E_0)_{i_p}$, the concentrations of the element A_l for some chosen voxels are updated using the following equation (l and m are the index of the X-ray line and the beam energy for $(X_{\mathrm{A}}, E_0)_{i_p}$):

$$\boldsymbol{C_k}(l,i,j) = \boldsymbol{C_{k-1}}(l,i,j)\,\frac{\boldsymbol{I_{exp}}(l,m,j)}{\boldsymbol{I_{sim,k}}(l,m,j)}, \tag{5.5}$$

where j is for all the beam positions, i.e., $0 < j \le N_{P_X}$, and i is selected accordingly to satisfy the condition $\boldsymbol{R_{x,k}}(l,m-1,j) < d_{V(i,j)} < \boldsymbol{R_{x,k}}(l,m,j)$, where $\boldsymbol{R_{x,k}}(l,m-1,j)$ and $\boldsymbol{R_{x,k}}(l,m,j)$ are

the simulated X-ray emission range of the X-ray line X_{A_l} for the k^{th} forward modeling for the beam position P_{X_j} when the beam energy is $E_{0_{m-1}}$ and E_{0_m}, respectively.

The compositions are then normalized for the modified voxels using the following equation:

$$\boldsymbol{C_k}(y,i,j) = \frac{\boldsymbol{C_{k-1}}(y,i,j)}{\boldsymbol{C_k}(l,i,j) + \sum_{z=1\ to\ N_A}^{excep\ l} \boldsymbol{C_{k-1}}(z,i,j)} \tag{5.6}$$

and,

$$\boldsymbol{C_k}(l,i,j) = \frac{\boldsymbol{C_k}(l,i,j)}{\boldsymbol{C_k}(l,i,j) + \sum_{z=1\ to\ N_A}^{excep\ l} \boldsymbol{C_{k-1}}(z,i,j)}, \tag{5.7}$$

where y represents the index of other elements, whose concentrations are not changed, ranging from 1 to N_A except l.

With this new generated solution $\boldsymbol{C_k}$, the forward modeling is implemented again to get the updated intensity matrix. Since, in this step, only the $|d_r|$ values for the beam energy E_{0_m} are used, the forward modeling is only performed for E_{0_m} to save simulation time. The number of times that the forward modeling is performed k increases by 1. And the absolute values of the relative differences for the X-ray line X_{A_l} at E_{0_m}, $|d_r(l,m,j)|$, are calculated for all beam positions. If any of the values is larger than the error tolerance ε, step 4-3 is repeated. Otherwise, we move on to step 4-4.

Step 4-4: *Update the simulated X-ray intensities*

This step is similar to step 3. The Monte Carlo simulations are performed for all the beam energies and beam positions to update the simulated X-ray intensities $\boldsymbol{I}_{\boldsymbol{sim,k}}^{N_{X_A}\times N_{E_0}\times N_{P_X}}$ and X-ray ranges $\boldsymbol{R}_{\boldsymbol{x,k}}^{N_{X_A}\times N_{E_0}\times N_{P_X}}$. k increases by 1.

Sub-steps 4-1 to 4-4 are repeated until the absolute values of the relative differences $|d_r(X_A, E_0, P_X)|$ for all the X-ray lines, beam energies, and beam positions are smaller than ε, which means that the optimization for the error tolerance ε is finished.

Step 4 is repeated multiple times during which the error tolerance ε is successively decreased until the convergence cannot be obtained. The minimum error tolerance with which the convergence can be obtained is written as ε_{min}. Decreasing ε successively helps save simulation time because, instead of spending a lot of time for the first several rows of voxels (the case for a small ε), our algorithm finds a rough answer first (for a large ε) and then converges to the real specimen slowly. This is especially important considering the complex effect of voxels among each other, i.e., the compositions of the voxels located at deeper depths influence the X-ray emission of the voxels located at shallower depths through backscattered electrons, and on the other hand, the compositions of the voxels located at shallower depths influence the X-ray emission of the voxels located at deeper depths by changing the direction and energy of the incident electrons that travel through. Though any value ranging from 0% to 20% can be chosen as ε, it is recommended to start with a value larger than 10%, and then decrease it by 15 to 25% for each iteration.

As a proof-of-concept work, the developed algorithm can only be applied to 2D and 1D heterogeneous materials. But in principle, the algorithm can be extended to 3D heterogeneous materials by extracting the composition information along the Y-axis in the same way as that along the X-axis. Specifically, the required experimental data is acquired through mapping instead of line scan, and the lateral information is extracted by changing the beam position on the X-Y plane.

5.3.5 One simple example

In this section, the inverse modeling algorithm is further presented through an example. A sample structure with 9×9 voxels is designed, which is composed of two elements: Al and Cu. The phantom image of the sample structure is shown in Figure 5.4. It consists of a matrix of 98 wt% Al and 2 wt% Cu (light yellow region) and an Al_2Cu precipitate embedded in the center (red region). The voxel size of the phantom sample on the X-Z plane is 200×200 nm.

Step 1: Input parameters

The blue arrows shown in Figure 5.4 represent the beam positions to perform a line scan along the X-axis with an interval of 200 nm. The line scan was repeated 11 times for varying beam energies ranging from 10 keV to 20 keV with an interval of 1 keV. The simulated X-ray intensities for both the Al Kα line and Cu Kα line (as shown in Figure 5.5) were taken as the "experimental

data" to input, and the predicted composition was compared with the reference value to test the validity of our algorithm. The voxel size along the Z-axis is 200 nm, and the number of voxels along the Z-axis is 9.

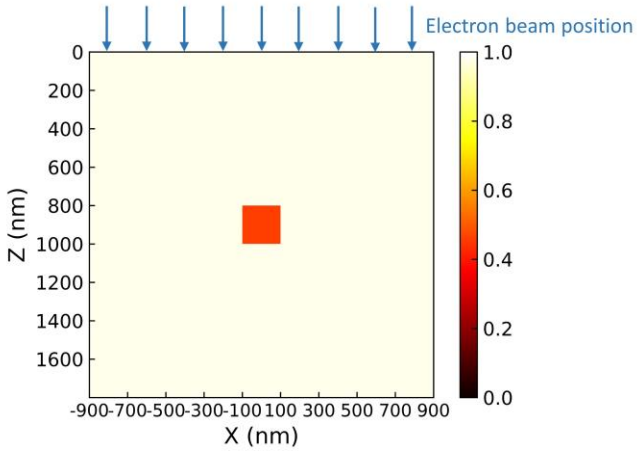

Figure 5.4 Al weight fraction distribution on the X-Z plane of the designed sample structure consisting of a matrix of 98 wt% Al and 2 wt% Cu and an Al_2Cu precipitate embedded in the center.

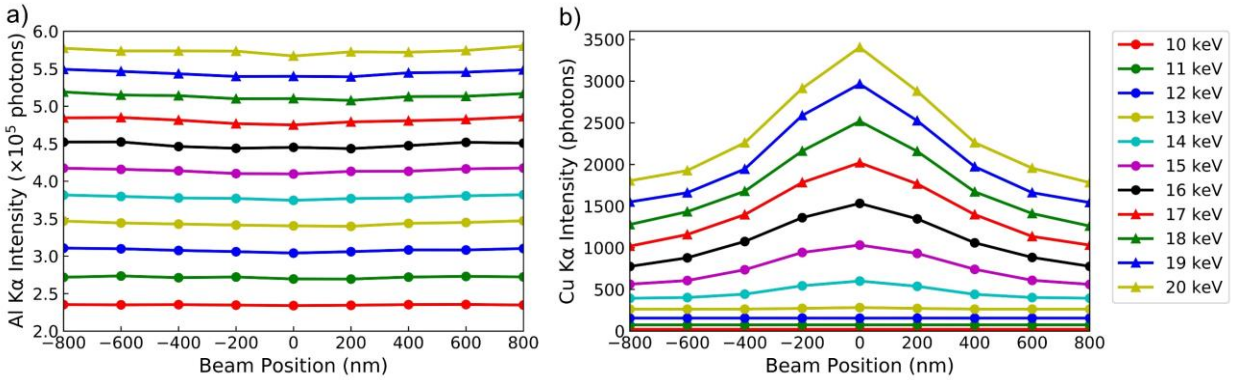

Figure 5.5 Input X-ray intensities for the a) Al Kα line and b) Cu Kα line under varying beam energies ranging from 10 keV to 20 keV with an interval of 1 keV and for 9 different beam positions. a) and b) have the same legend.

Step 2: Initialize *C*

The inverse modeling starts with the initialization of the specimen ***C***. Figure 5.6 a) shows the Al weight fraction distribution for the initial guess of the specimen ***C***. Since the initialization simply takes the k-ratio as the weight fraction without considering the matrix correction, the initial guess has a strong bias and differs significantly from the designed structure. Slight differences in composition are found among the voxels of the initial guess. For example, the weight fraction of

Al is 0.983 for the voxel with coordinates X = 0 and Z = 100 nm, while that is 0.961 for the voxel with coordinates X = 0 and Z = 1700 nm.

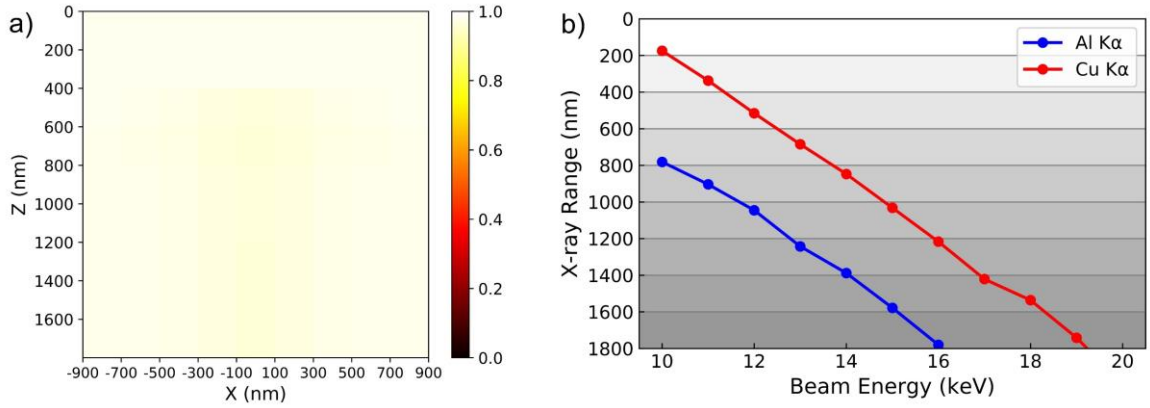

Figure 5.6 a) Al weight fraction distribution on the X-Z plane for the initial guess of the specimen C b) X-ray emission ranges for the Cu Kα line and Al Kα line under different beam energies at beam position X = 0 for the initial guess.

Step 3: Update the simulated X-ray intensities

MC X-ray was used to perform Monte Carlo simulations for all beam energies and beam positions to obtain the simulated X-ray intensities and X-ray ranges. Figure 5.6 b) shows the simulated X-ray ranges for both the Cu Kα line and the Al Kα line under different beam energies when the electron beam is at X = 0. The horizontal lines and different colors in the background indicate voxels at different depths. It is observed that the X-ray ranges increase as the beam energy increases, and the X-ray ranges of the Cu Kα line are smaller than that of the Al Kα line since Cu Kα has a higher excitation energy.

Step 4: Optimize *C* for a certain ε

The initial error tolerance ε was set to be 12% in this case. The pairs of the characteristic X-ray line and beam energy (X_A, E_0) were sorted according to their X-ray ranges in the specimen $\boldsymbol{C}_0$, which were obtained from MC X-ray (step 4-1). As shown in Figure 5.6 b), the optimization started from the pair (Cu Kα line, 10 keV), which has the smallest X-ray range (around 180 nm), by letting the index of the pair i_p equal 1. Its X-ray range corresponds to the voxels at the first row with a depth ranging from 0 to 200 nm. And the Cu weight fractions of those voxels were updated by comparing the simulated and experimental X-ray intensities of the Cu Kα line at 10 keV using equation (5.5) and then normalized.

The tested beam energy E_{0_t} for the forward modeling is defined as E_{0_m}, the beam energy of the pair (X_{A}, E_0) for the step 4-3 and as the highest beam energy (20 keV in this case) for the step 3 and step 4-4. The average of the absolute values of the relative differences between the simulated and experimental X-ray intensities for a certain X-ray line and a certain beam energy $\left|d_r\left(X_{\mathrm{A}_l}, E_{0_m}\right)\right|_{ave}$ is calculated using the following equation:

$$\left|d_r\left(X_{\mathrm{A}_l}, E_{0_m}\right)\right|_{ave} = \frac{1}{N_{P_X}} \sum_{P_X} \left|d_r\left(X_{\mathrm{A}_l}, E_{0_m}, P_X\right)\right|, \tag{5.8}$$

where N_{P_X} is the number of beam positions, and $\sum_{P_X} \left|d_r\left(X_{\mathrm{A}_l}, E_{0_m}, P_X\right)\right|$ represents the sum over all the beam positions. Figure 5.7 presents the variations of E_{0_t} and $\left|d_r(Cu\ K\alpha, E_{0_m})\right|_{ave}$ relative to the number of times that the forward modeling is performed k. Only data for $k > 1$ is shown because E_{0_m} was not determined yet when $k = 1$. Since the phantom sample is a two-element system, the accurate prediction of the weight fraction of one element would result in the accurate prediction for both elements. Thus, the pairs with the Al Kα line were never chosen to be updated in the step 4-2, and only the values of $|d_r|_{ave}$ for the Cu Kα line need to be presented.

In Figure 5.7, the first two iterations ($k = 2, 3$) are the iterations of step 4-3 for the first pair (Cu Kα line, 10 keV), in which the tested beam energy stays at 10 keV and $|d_r|_{ave}$ goes down dramatically. When $k = 4$, the optimization for the pair (Cu Kα line, 10 keV) is finished because all $|d_r|$ values for the Cu Kα line at 10 keV are smaller than ε (12%), and the forward modeling is performed for all beam energies (step 4-4), which results in an increase in the tested beam energy to 20 keV. All sudden increases of the tested beam energy to 20 keV in Figure 5.7 indicate the performance of step 4-4. Following step 4-4, step 4-1 to step 4-4 are repeated for other pairs whose $|d_r|$ values are larger than ε. The iterations move on to the pair (Cu Kα, 13 keV) at $k = 5$. Under some circumstances, the pair that has been optimized may be chosen again. For example, when $k = 51$, 16 keV is chosen as the tested beam energy after it has been optimized from $k = 33\ to\ 43$. This is because the composition changes of the voxels at 17 keV ($k = 45\ to\ 51$) have impact on the X-ray emission of 16 keV. Another reason is that the results of the Monte Carlo simulations for the same specimen might be different because of the stochastic nature of the Monte Carlo method. It is also observed that the iteration still proceeds after $k = 17$ although $|d_r|_{ave}$ is smaller than 12% as some of the $|d_r|$ values are still greater than 12% despite the small value of $|d_r|_{ave}$.

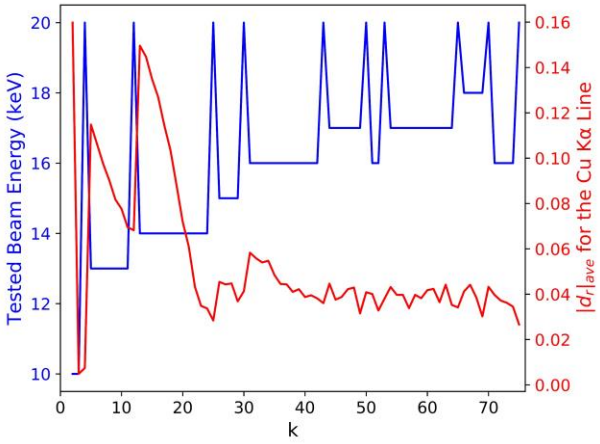

Figure 5.7 Variation of the tested beam energy(blue) and the $|d_r|_{ave}$ for the Cu Kα line and E_{0_m} (red) as the change of the number of times that the forward modeling is performed k when ε = 12%.

The resulting Al weight fraction distribution when ε =12% is presented in Figure 5.8 a), which shows that the voxels located in the center of the specimen have a slightly lower concentration of Al compared with the rest voxels.

Iterations of step 4

Based on the result of ε =12%, the optimization process (step 4) was repeated for a reduced error tolerance ε = 7% and then for ε = 1.5%. As shown in Figure 5.8 b), the result for ε = 7% better shows the feature in the center with a much lower Al weight fraction, which is more similar to the phantom image than the result of ε = 12% (Figure 5.8 a). The optimization for ε = 1.5% (Figure 5.8 c) failed to converge for high beam energies since the conditions were not satisfied after over 500 iterations. The reason will be discussed in section 5.4.4. The iteration was, therefore, performed again for an error tolerance of 7% based on the result of ε = 1.5%, and the final result is shown in Figure 5.8 d). Although the same error tolerance was used, Figure 5.8 b) and d) show slight differences as a result of different initial states of step 4 (Figure 5.8 a) for Figure 5.8 b), and Figure 5.8 c) for Figure 5.8 d), respectively).

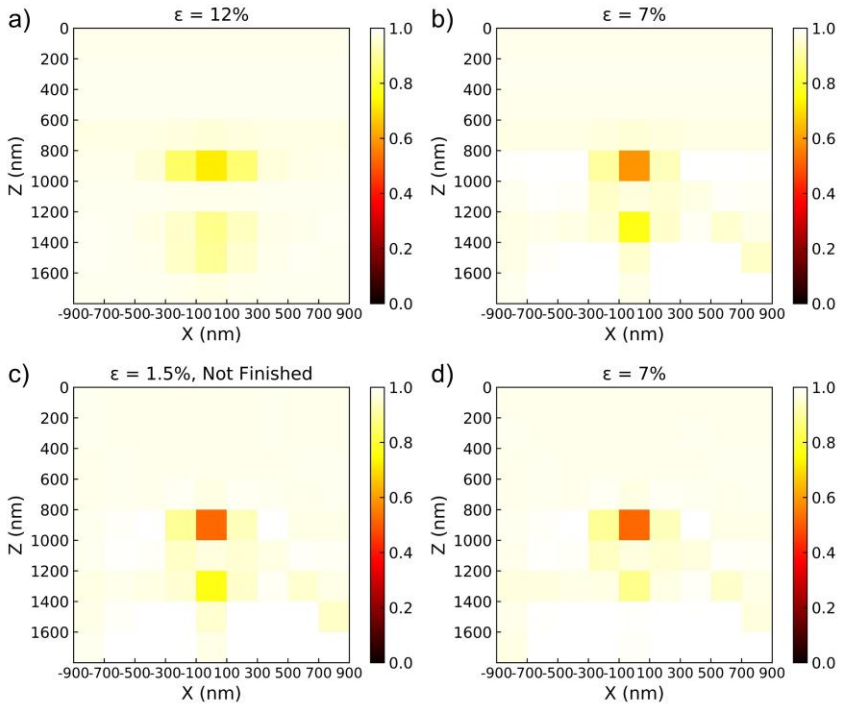

Figure 5.8 Evolution of the inverse modeling output (Al weight fraction distribution on the X-Z plane) with the iterations of step 4. The values of ε for different iterations are a) ε = 12%; b) ε = 7%; c) ε = 1.5%; and d) ε = 7%.

5.3.6 Clustering algorithm

It is observed in Figure 5.8 that the voxels with the same composition in the designed structure might end up with slightly different weight fractions. This is due to several reasons. First, during the optimization, not only the actual information of the specimen is fitted but also the noise contained in the input data. Secondly, the results from Monte Carlo simulation vary slightly even for an identical sample and experimental setup (refer to section 5.4.4). To provide a suggestion on the specimen segmentation according to the voxels' compositions, we use the K-means algorithm to perform clustering for all the voxels despite the voxel position [37]. Note that the clustering algorithm itself does not retrieve extra information, and the reconstructed data with and without clustering have the same merit. The clustering algorithm only enhances the apparent information so that users can take it as reference to recognize the main components of the specimen. More details about the algorithm can be found in Appendix.

In real applications, it is recommended to use the clustering algorithm only when it is known that there are discrete regions of homogeneous composition within the specimen, for example, in the case when a specimen has been fabricated in layers, or there are uniform inclusions with sharp boundaries.

The K-means algorithm was applied to the inverse modeling result shown in Figure 5.8 d), and the resulting Al weight fraction distribution is presented in Figure 5.9. Using the clustering algorithm, two clusters representing the precipitate and matrix are successfully distinguished. Please refer to Appendix for the determination of the number of clusters, *K*. For the matrix, the estimated Al weight fraction is 97.93%, which is smaller than the reference value (98%) with a difference of 0.07%. The precipitate in the center has 52.08% Al, which is higher than the reference value (45.9%) with a difference of 6.18%.

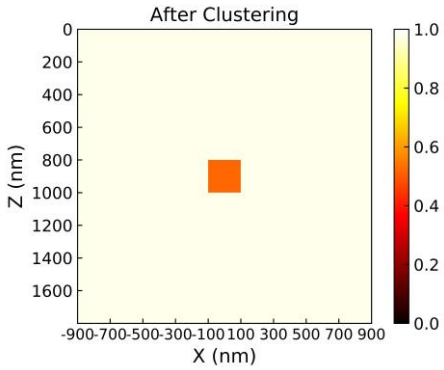

Figure 5.9 Al weight fraction distribution on the X-Z plane after clustering for the result shown in Figure 5.8 d).

5.4 Results and discussion

In this section, we examined the performance of our algorithm when applied to some types of sample where the structures are known but the extent and composition are unknown. In section 5.4.1, tests on 1D samples along the X-axis are presented and the effects of the input parameters including beam energy and beam positions are discussed. Section 5.4.2 shows two examples of 1D samples along the Z-axis: a multilayer sample and a thin film coated on a substrate. And section 5.4.3 presents several examples of 2D inverse modeling. Following the examples of applications, the sources of errors are analyzed in section 5.4.4. Notice that for the results presented, the clustering algorithm was not applied unless stated otherwise. Unfortunately, we have not been able

to develop and test any strategy to analyze a completely unknown sample. But this will be the goal for future work.

5.4.1 1D inverse modeling along the X-axis

Inverse modeling at 10 keV

The first phantom sample is an Al-Cu compound with a vertical sandwich structure. The structure of the phantom sample on the X-Z plane is presented in Figure 5.10 a), in which a 200 nm width Al_2Cu feature (region 2) is placed in between two regions (region 1 and region 3), composed of 98 wt% Al and 2 wt% Cu. The center of the phantom sample is at X = 0. Since the phantom sample is homogeneous along the Z-axis, measurement is only needed for one beam energy. To recognize the feature along the X-axis, three beam positions were selected: -200 nm, 0, and 200 nm. Figure 5.10 b) presents the predicted Al weight fraction when the beam energy is 10 keV and ε_{min} = 1%. The inverse modeling algorithm successfully estimates the compositions of the three regions: 98 wt%, 45.9 wt%, and 98 wt% Al, respectively, which are the same as the reference values.

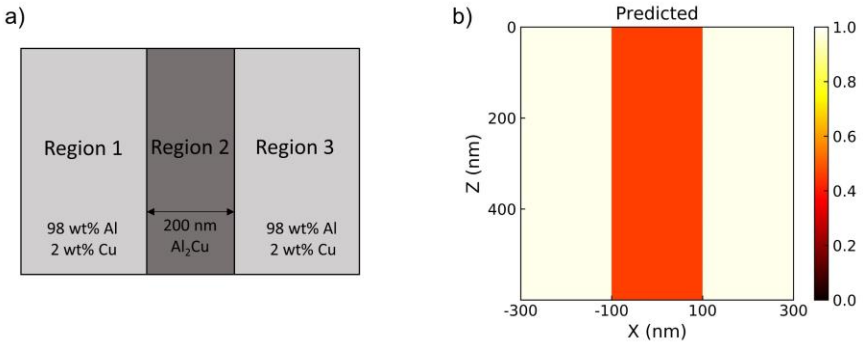

Figure 5.10 a) Phantom sample on the X-Z plane, b) Predicted Al weight fraction distribution on the X-Z plane

Effect of the beam energy

The effect of the beam energy was investigated when other parameters were kept the same as in the last section. Table 5.1 compares the predicted Al weight fractions of the three regions, number of times that the forward modeling is performed (k), and X-ray range of the Cu Kα line when the electron beam is at X = 0 under different beam energies. At 10 keV, the predicted compositions of the three regions are the same as the reference values. However, as the beam energy increases, the Al weight fraction of region 2 is marginally larger, while the weight fractions

for the other two regions are smaller than the reference values. And k also increases dramatically. These changes are due to the increase in the X-ray range as the beam energy increases.

The voxel size along the X-axis, determined by the beam positions, represents the expected lateral resolution of the inverse modeling. In this case, the value is 200 nm. On the other hand, the real or achievable lateral resolution is determined by the X-ray emission range, which mostly depends on the beam energy for a given specimen. Although the X-ray range varies for different elements or X-ray lines, the smallest X-ray range, typically for the X-ray line with the highest excitation energy (Cu Kα line in this case), is considered as the real resolution. At 10 keV, the X-ray range for the Cu Kα line is 111 nm (as shown in Table 5.1), which is smaller than the expected resolution. Under the circumstance, all the Cu Kα signals at a certain beam position are emitted from the same region, which makes the compositions easy to converge. However, at 15 keV, the X-ray range for the Cu Kα line (837 nm) is much larger than the expected resolution, indicating that the Cu X-ray signals from all three regions are collected for each beam position. Therefore, the composition of a certain region is also affected by the other two regions. As a result, the predicted Al weight fraction for region 2 is larger than the reference value, and that for region 1 and region 3 are smaller.

Table 5.1 Comparison of the predicted Al weight fractions, number of times that the forward modeling is performed (k), and X-ray range for the Cu Kα line at X = 0 under different beam energies

Beam energy (keV)	**Region1**	**Region2**	**Region3**	***k***	**X-ray range for Cu Kα (nm)**
10	0.980	0.459	0.980	160	111
15	0.976	0.461	0.976	440	837
20	0.976	0.464	0.980	1000	1809
Reference value	0.980	0.459	0.980	N/A	N/A

Normally, it is recommended to choose the beam energy for which the real resolution is smaller than the expected resolution. The real resolution can be estimated using the Monte Carlo simulations. For 2D inverse modeling in which a series of beam energies are used, one should make sure that the above criterion is satisfied at least for the lowest beam energy.

Effect of the beam positions

When handling unknown samples, the chosen voxel size (beam position interval) might not be equal to the feature size. To investigate the effect of the voxel size and voxel positions, which are determined by the beam positions, four inverse modeling setups were selected and compared for the same phantom sample as shown in Figure 5.10 a):

1) 3 voxels each with a width of 600 nm, and the X coordinate of the center voxel is 0.

2) 9 voxels each with a width of 200 nm, and the X coordinate of the center voxel is 0.

3) 18 voxels each with a width of 100 nm, and the X coordinates of the center two voxels are -50 and 50 nm, respectively.

4) 19 voxels each with a width of 100 nm, and the X coordinate of the center voxel is 0.

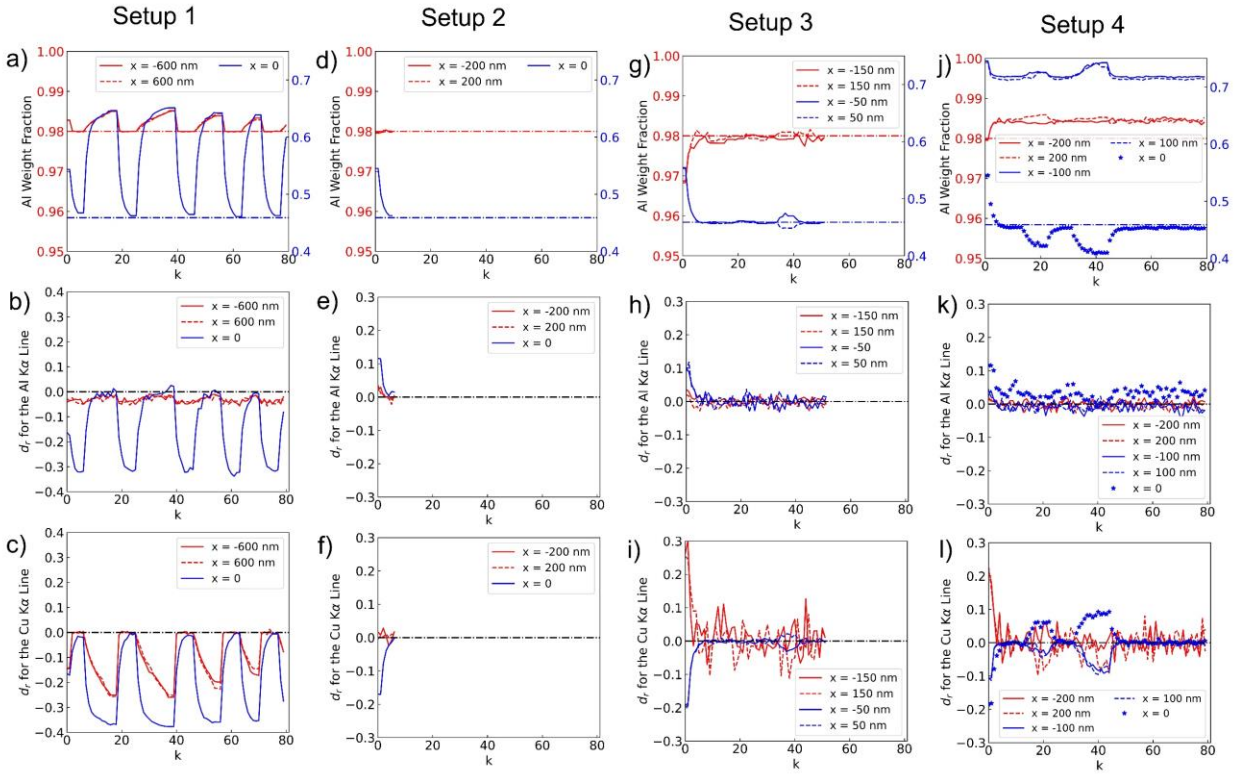

Figure 5.11 Variations of the Al weight fraction, relative difference in X-ray intensity (d_r) for the Al Kα line and Cu Kα line relative to the number of times that the forward modeling is performed, k ,for four different setups with voxel size and voxel number as follows: setup 1:600 nm × 3 (a, b, and c), setup 2: 200 nm× 9 (d, e, and f), setup 3: 100 nm× 18 (g, h, and i), and setup 4: 100 nm × 19 (j, k, and l) at 10 keV for the same phantom sample. Horizontal lines in a), d), g), and j) represent the reference value of the Al weight fraction. And the black horizontal lines show the relative difference, $d_r = 0$. Each curve represents the results for a certain voxel, marked by its position (the X coordinate of the voxel's center) in the legend.

The beam energy of 10 keV was used, and the error tolerance was set to be 2%. As shown in Figure 5.11, each column represents the results for a certain setup, and three rows present the variation of Al weight fraction, the relative difference in X-ray intensity for the Al Kα line, and the relative difference for the Cu Kα line, respectively, relative to *k*, ranging from 0 to 80.

Setup 1, 2, and 3 present the case when the selected voxel size is larger than, equal to, and smaller than the feature size, respectively. When the selected voxel size is the same as the feature size (setup 2), the Al weight fractions converge to the reference values within ten times of forward modeling (Figure 5.11 d, e and f). For setup 1 with a larger selected voxel size, the Al weight fractions rise and fall in cycles as shown in Figure 5.11 a). This is because that d_r for the Al Kα line and Cu Kα line can not converge to 0 simultaneously (as shown in Figure 5.11 b and c), especially for the voxel with X = 0 (blue lines). The inverse modeling for setup 1 proceeds until $k = 500$, during which the weight fractions of Al and Cu never converge simultaneously. For the case with a smaller selected voxel size (setup 3), as presented in Figure 5.11 g), the total number of times that the forward modeling is performed, 52, is much greater than that for setup 2. This is due to that the selected voxel size 100 nm is smaller than the X-ray range at 10 keV which has been discussed in section 5.4.1, and more X-ray intensities need to be fitted because of the increase in the number of voxels in comparison to setup 2 (18 voxels instead of 9 voxels).

Setup 4 differs from setup 3 in the voxel position. In setup 4, two voxels cross the boundaries between different regions of the phantom sample: X = -100 nm and X = 100 nm. The Al weight fractions of those two voxels gradually converge to the average Al weight fraction of the two crossed regions (72 wt% around) as presented in Figure 5.11 j). The relative differences of both the Al Kα line (Figure 5.11 k) and the Cu Kα line (Figure 5.11 l) vary to a larger extent than that for setup 3, and it is, therefore, hard to make all the absolute values of $d_r$smaller than 2%.

In summary, to converge, the selected voxel size along the X-axis has to be smaller than the expected resolution and feature size. Although the effect of features not aligning on voxel boundaries has been briefly discussed, its consequences can be more complicated in real applications, and further investigation is needed in the future.

5.4.2 1D inverse modeling along the Z-axis

Multilayer sample

The inverse modeling was implemented for a multilayer phantom sample with four thin layers on a substrate, and the thicknesses of the four layers from top to bottom are 400, 200, 200 and 400 nm, respectively. The Al weight fraction distribution of the phantom sample is shown in Figure 5.12 a) in which the red regions represent Al_2Cu and the light yellow regions represent the matrix with 98 wt% Al and 2 wt% Cu. Since the sample is homogeneous along the X- and Y-axes, only one beam position is needed.

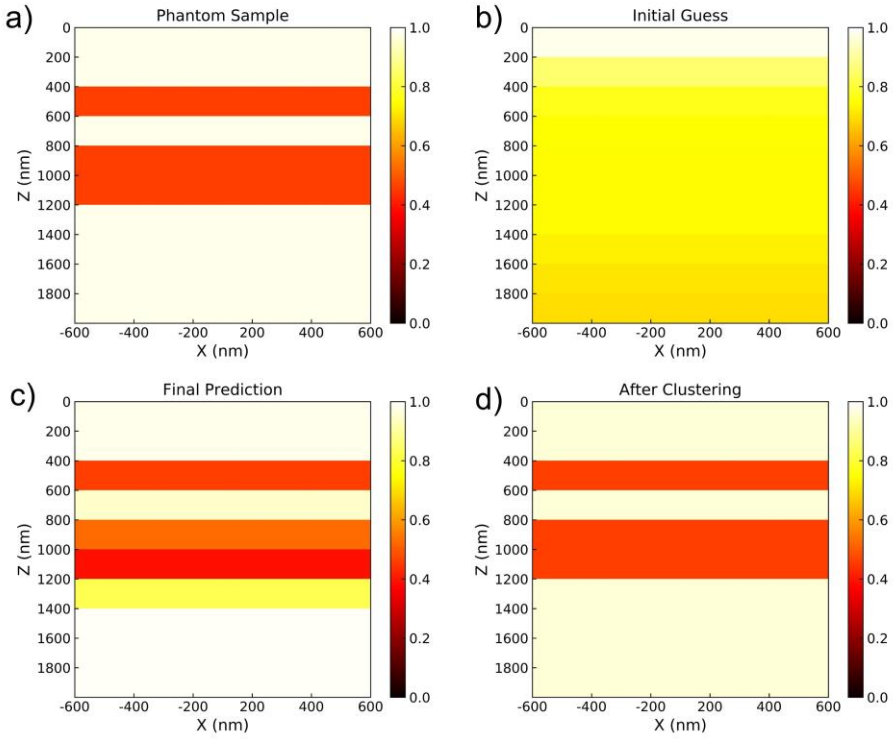

Figure 5.12 Al weight fraction distribution for a) phantom sample, b) initial guess, c) final prediction before clustering, d) final prediction after clustering.

For the inverse modeling, a voxel size along the Z-axis of 200 nm and beam energies ranging from 10 keV to 19 keV with an interval of 1 keV were used. ε_{min} is 2%. Figure 5.12 b) presents the Al weight fraction distribution of the initial guess, in which none of the layers are identified correctly. After the optimization process, as shown in Figure 5.12 c), four layers and the substrate are successfully recognized. However, for most of the layers, the compositions of the first row of voxels in that layer slightly deviate from the reference values and tend to be close to the compositions of the voxels located above them. A possible reason is that, for the voxels located at

deeper depth, only a small portion of the total emitted X-rays is generated from the voxel itself, and the rest is from the voxels located at shallower depths, which brings difficulties to the estimations of their compositions. The voxels were successfully classified into two clusters using the clustering algorithm (Figure 5.12 d). The predicted Al weight fraction is 45.72 wt% for the second and fourth layers, and 95.86 wt% for the rest.

A thin Fe-oxide layer on a steel substrate

The inverse modeling algorithm can also handle multi-elements system, i.e., system with more than two elements. We created a phantom sample with a simplified steel substrate with 95 wt% Fe and 5 wt% C, coated by a 50 nm Fe-oxide layer with 70 wt% Fe and 30 wt% O. The weight fraction distributions of Fe, O, and C for the phantom sample are presented in Figure 5.13 a), b), and c), respectively. One difficulty in the inverse modeling of this phantom sample is that the Fe oxide layer is so thin that it requires an improved resolution along the Z-axis. Therefore, lower beam energies were used ranging from 2 keV to 9 keV with an interval of 1 keV. Accordingly, the X-ray line with a lower excitation energy, Fe Lα line, was considered instead of the Fe Kα line.

Figure 5.13 d), e), and f) present the result of the inverse modeling when the voxel size along the Z-axis is 50 nm and ε_{min} is 10%. The thin oxidation layer is found to be in a perfect match with the phantom sample. For slices in the substrate, slight variations are observed. The composition after clustering is shown in Figure 5.13 g), h), and i). Two clusters were successfully found with compositions of 68.79 wt% Fe and 31.21 wt% O for the oxidation layer, and 95.38 wt% Fe, 4.16 wt% C, and 0.46 wt% O for the substrate.

Figure 5.14 a) shows the variations of the tested beam energy and $|d_r|_{ave}$ for the Fe Lα line and E_{0_m} relative to the number of times that the forward modeling is performed *k*. It is observed that the tested beam energy starts from 2 keV and gets larger as *k* increases. Figure 5.14 b) presents the result of the same phantom sample when an increased voxel thickness 100 nm was used. Since the voxel size is larger than the feature size, convergence cannot be achieved and the tested beam energy changes from 2 keV to 3 keV and comes back to 2 keV repeatedly. It is concluded that, in order to converge, the voxel size must be smaller than the feature size.

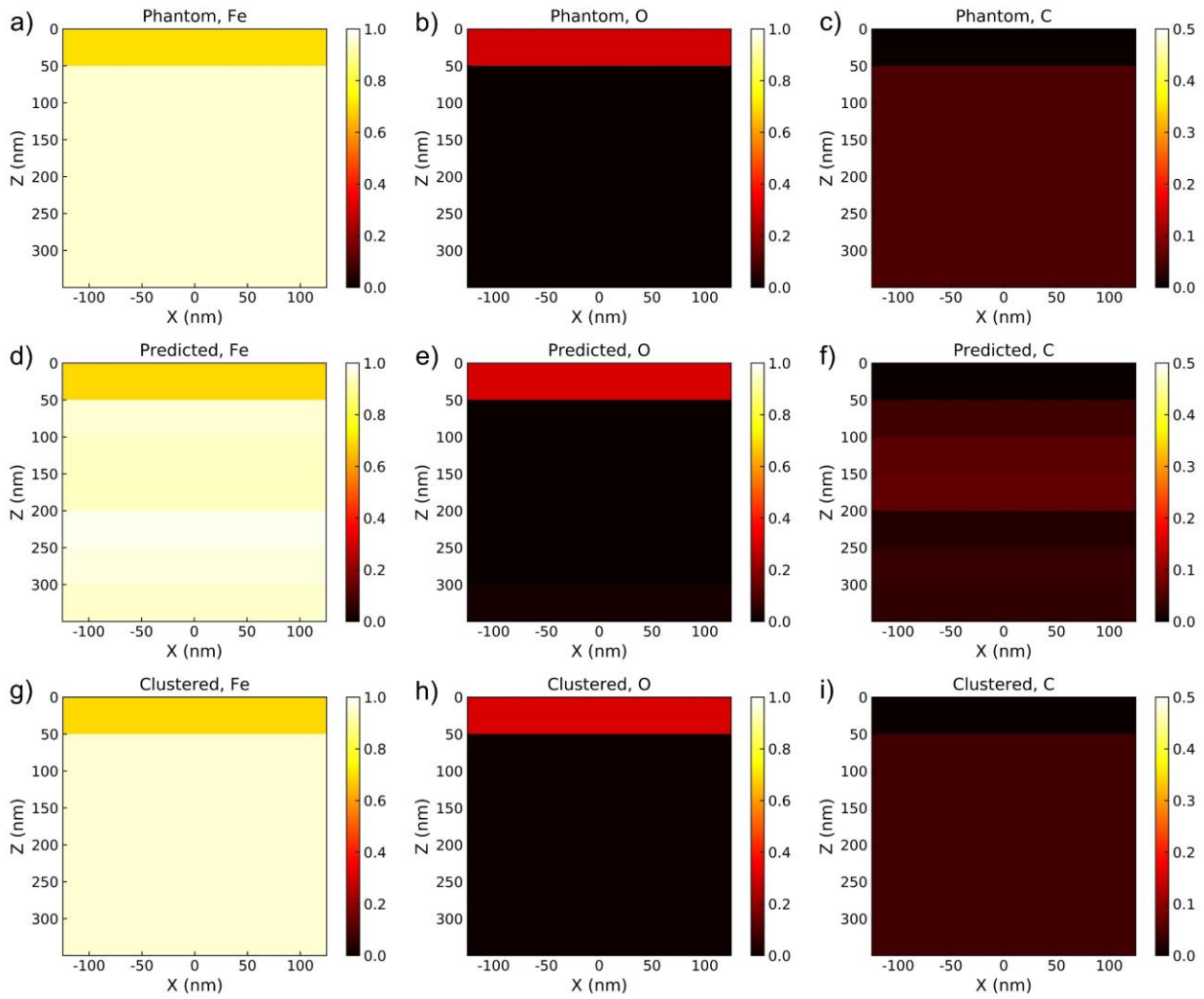

Figure 5.13 Weight fraction distributions of Fe, O and C for the phantom sample (a, b, and c), and predicted results before (d, e, and f) and after (g, h, and i) clustering.

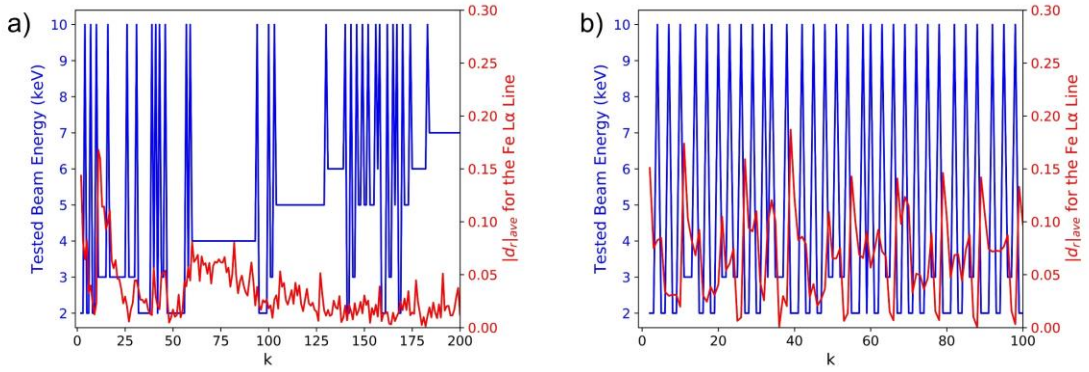

Figure 5.14 Variations of the tested beam energy (blue curve) and the $|d_r|_{ave}$ for the Fe Lα line and E_{0_m} (red curve) as the change of the number of times that the forward modeling is performed *k* for different voxel size along the Z-axis a) 50 nm and b) 100 nm.

5.4.3 2D inverse modeling

Four 2D phantom samples of Al-Cu compound were investigated for the structure of a particle embedded in a matrix with different size and depth. The first column of Figure 5.15 presents the Al weight fraction distribution of the four phantom samples on the X-Z plane, in which the light yellow area represents the matrix (98 wt% of Al and 2 wt% Cu), and the red area represents Al_2Cu precipitate (45.9 wt% Al and 54.1 wt% Cu). The precipitates for the 1st, 2nd, and 4th phantom samples are at the same depth with an increased size, and the precipitates for the 2nd and 3rd samples are with the same size but at different depths. For the inverse modeling, the input X-ray intensity data was acquired for 10 beam positions. The voxel size was set to be 200 × 200 nm, and the voxel number was 10 × 10. The beam energies and the minimum error tolerance are listed in Table 5.2.

Table 5.2 Inverse modeling parameters used for four phantom samples

Sample	1st	2nd	3rd	4th
Beam energies (keV) (1 keV interval)	From 10 to 16	From 10 to 20	From 10 to 19	From 10 to 21
Minimum Error tolerance	5%	8%	10%	10%

The predicted specimens before and after clustering are presented in the second and third columns of Figure 5.15, respectively. The inverse modeling of the 1st sample (Figure 5.15 c) shows the best result, in which all the voxels of the precipitate were recognized, and close compositions with the phantom sample were found for both the matrix and the precipitate. For the result of the 2nd sample, as shown in Figure 5.15 f), several voxels located at the center of the precipitate were mistakenly classified as matrix, and two voxels of matrix right below the precipitate were classified as precipitate. A similar phenomenon was found for the 3rd (Figure 5.15 i) and the 4th (Figure 5.15 l) samples, that the top half area of the precipitate was successfully recognized while some voxels located at the bottom of the precipitate were mistakenly classified. Besides, for the area of the matrix right below the precipitate, the predicted Al weight fractions are slightly lower than the reference value. In general, for the results of 2D inverse modeling, in terms of the structure, the top half of the boundaries between the matrix and the precipitate matches well with the phantom sample, while the prediction for the bottom half needs to be improved. As for the composition, the predicted weight fractions of the red area (recognized as precipitate) agree well with the reference value. The predicted Al weight fractions for the 1st to the 4th samples are 46.10%, 40.49%, 44.74%,

and 44.05%, respectively. And the Al weight fractions of the matrix are lower than the reference value. For some voxels located at deeper depths, large deviations were found.

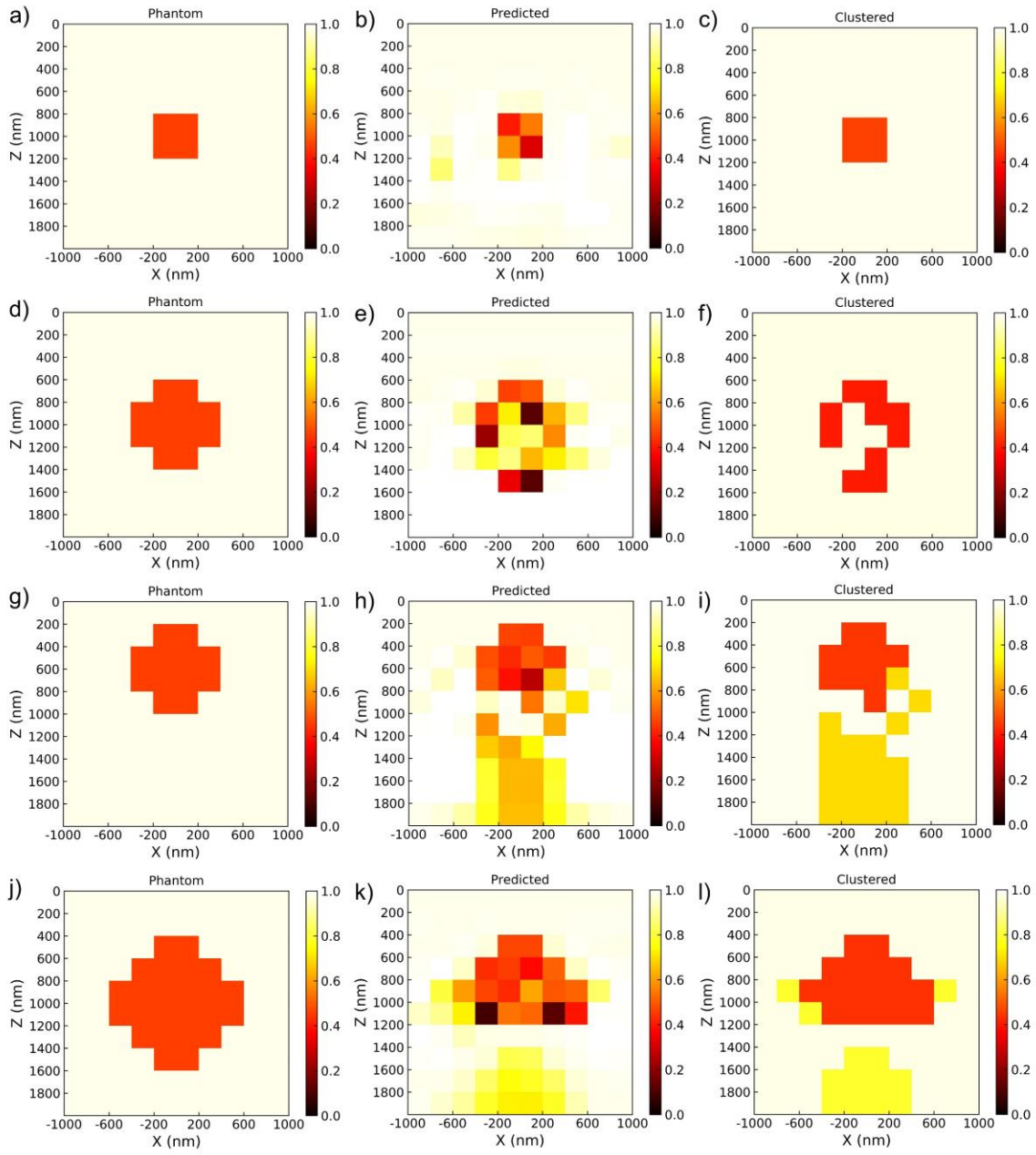

Figure 5.15 Al weight fraction distribution for phantom sample, predicted structure before and after clustering from left to right for four samples (a, b, c for the 1st; d, e, f for the 2nd; g, h, i for the 3rd; and j, k, l for the 4th sample). The red voxels represent the Al_2Cu precipitate and the light-yellow voxels represent the matrix with 98 wt% Al and 2 wt% Cu.

5.4.4 Sources of errors

Error from forward modeling

One of the sources of errors of the inverse modeling algorithm is from the forward modeling implemented by MC X-ray. Because of the stochastic nature of the Monte Carlo simulation, the simulated X-ray intensities for the same specimen and experimental setup might be different when the simulation is performed several times. If the selected error tolerance ε is smaller than the relative variation of the Monte Carlo simulation, the solution might be hard to find.

The variation of the simulated X-ray intensities for the same specimen and experimental setup depends on many factors, and one of the most important factors is the simulated electron number. Figure 5.16 presents the average and standard deviation of the emitted X-ray intensities for the Al Kα line and Cu Kα line relative to the electron number when the simulation is repeated 10 times for each electron number. The specimen is shown in Figure 5.4. The beam energy is 15 keV, and the beam position is X = 0. It is shown that the standard deviation decreases as the electron number increases. The values of the relative standard deviation, which is the ratio of the standard deviation to the average, are also listed in Table 5.3. When the electron number is 1,000, the relative standard deviation for the Cu Kα line is 2.46%, which is larger than the error tolerance used in Figure 5.8 c), 1.5%. This can explain why the optimization for the error tolerance of 1.5% fails. The relative standard deviation of X-ray intensity may be used to determine the optimal error tolerance by choosing the value that is slightly higher than the relative standard deviation.

Table 5.3 also presents the average simulation time taken for different electron numbers. The simulations were performed using a computer with Windows® 7, 16 GB RAM, and Intel® Core ™ i7-970 processor. Note that the presented simulation time is for a single simulation, and the overall computation time for analysis depends also on the number of beam positions, the number of beam energies, and the number of iterations. A trade-off between the simulation time and accuracy in the inverse modeling is observed. For example, when the electron number changes from 1,000 to 5,000, the simulation time increases by more than 2.5 times while the standard deviation decreases by 38% (average for the Al Kα line and Cu Kα line). For the simulations presented in this paper, an electron number of 1,000 was chosen. An improvement might be obtained by increasing the electron number as the error tolerance decreases with iterations.

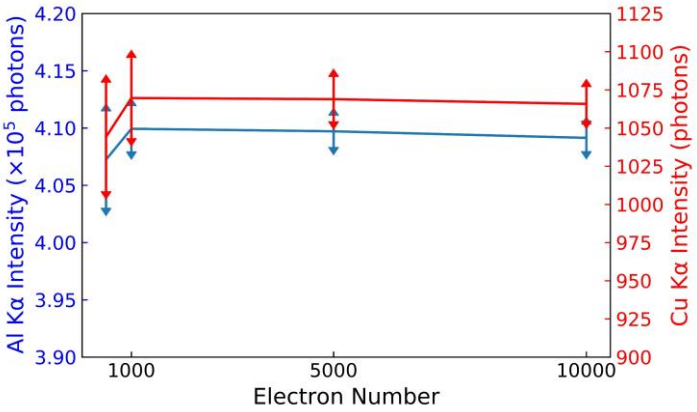

Figure 5.16 Variation of the average X-ray intensity and standard deviation of X-ray intensity for the Al Kα line and Cu Kα line relative to the electron number at 15 keV and beam position X = 0 for the sample shown in Figure 5.4 (the simulation is repeated 10 times for each electron number).

Table 5.3 Average time taken and relative standard deviations for different electron numbers

Electron number	500	1,000	5,000	10,000
Average time (s)	18	26	92	169
Relative standard deviation for the Al Kα line	1.03%	0.48%	0.33%	0.28%
Relative standard deviation for the Cu Kα line	3.41%	2.46%	1.36%	1.04%

Error from the change of X-ray range

Another important source of errors comes from the increase in X-ray range as the beam energy increases due to the limitation of the algorithm. This has been mentioned in section 5.4.1. Figure 5.17 compares the contributions of each voxel to the emitted X-ray signals of the Cu Kα line at different beam energies when beam position is X = 0 for the sample shown in Figure 5.4. At 10 keV, more than 90% of the X-ray signals are generated from the targeted voxel, making it easy to converge. When the beam energy is increased in order to compute the compositions of the voxels located in deeper depths, the X-ray emission range also increases. As shown in Figure 5.17 b), the X-ray intensity at 13 keV is used to determine the Cu weight fraction of the targeted voxel, which is marked with a red box. The algorithm assumes that the discrepancy between the simulated and "experimental" X-ray intensity at 13 keV completely results from the wrong composition of the

targeted voxel. However, both the voxels with coordinates (-200, 700) and (200, 700) nm contribute to the X-ray intensity, which undoubtedly brings difficulties to the optimization. It is even worse for 16 keV. In Figure 5.17 c), the contribution of the targeted voxel (marked with a red box) is only 0.53% because of the high Cu concentration of the voxel right on the top of the targeted voxel. Both the small contribution of the targeted voxel and the influences from the neighboring voxels make it difficult to determine the composition. Furthermore, it is possible that various combinations of compositions for different voxels might lead to identical X-ray intensities, which means that there may be more than one solution of the specimen for the same experimental data.

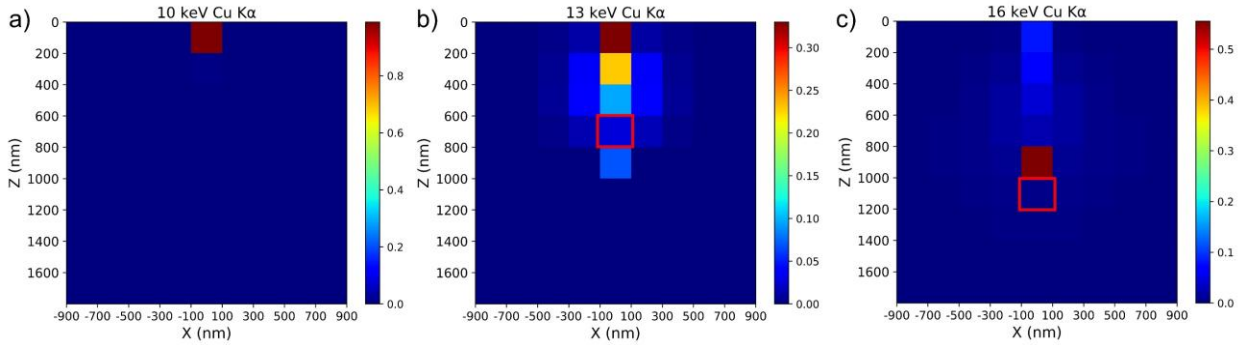

Figure 5.17 Contributions of each voxel to the emitted X-ray signals for the Cu Kα line under different beam energies a) 10 keV, b) 13 keV, and c) 16 keV for the sample shown in Figure 5.4.

Error from experimental measurement

In real applications, experimental measurements may also bring some inaccuracies to the inverse modeling. For example, the inaccuracy in beam position resulted from the specimen drift and switch of the primary beam energy [10], and the inaccuracy in the measured X-ray intensities due to errors related to the EDS detector system and data processing. Further investigation is needed to study the effects of those factors.

5.5 Limitations and possibilities

This newly proposed inverse modeling algorithm still has some limitations. For example, the errors from MC X-ray and from the change of X-ray emission range with beam energy limit its application for the voxels located in deeper depths; the variations of the input parameters have great impact on the accuracy and the smallest feature that can be distinguished of the result. Moreover, the practicality of this algorithm needs to be further tested and discussed regarding the

computation time, determination of experimental parameters, the precision of the voxel composition to ensure convergence, etc.

However, as a proof-of-concept work, this work is a successful attempt to extract structural and compositional information from a series of EDS/WDS measurements under different beam energies and beam positions. We hope that this work will encourage people in the community to explore more on the extraction of hidden information from the acquired experimental data. Some more advanced studies about this inverse modeling algorithm can be conducted in the future: using both the K-line and L-line simultaneously for the optimization to improve its accuracy; applying deep learning to the simulated data generated during the iterations to find out the relationship between the specimen and simulated X-ray intensities; etc.

5.6 Conclusion

In this paper, we developed an inverse modeling algorithm for determining the structure and composition of an unknown sample from a series of EDS/WDS experimental measurements at different beam energies and beam positions. The algorithm can be applied to arbitrary 2D heterogeneous materials by extracting the information along the X- and Z-axes through measurements under different beam positions and beam energies. It utilizes an iterative process of forward modeling to find the optimal composition of each voxel of the specimen to minimize the relative differences between the simulated and experimental X-ray intensities. A clustering algorithm was implemented for the result of the inverse modeling to smooth the reconstructed data and provide a suggestion on the voxel clustering. The algorithm was successfully applied to a phantom sample of an Al_2Cu precipitate embedded in a matrix of 98 wt% Al and 2 wt% Cu, in which the area of the precipitate and matrix were distinguished, and close compositions with the reference values were found.

Tests were performed for a 1D sample along the X-axis to recognize a 200 nm width Al_2Cu feature from the matrix. The effects of the input parameters including beam energy and beam positions were investigated. It was shown that to converge, the voxel size must be smaller than the feature size, and a more accurate result can be obtained when the X-ray emission range under the chosen beam energy is smaller than the voxel size. We have also shown that the algorithm works well for a multilayer sample and a 50 nm thin film coated on a substrate.

Four 2D phantom samples of Al-Cu were presented for precipitates of different sizes and positions embedded in matrices. Accurate compositions were found for the top half area of the precipitates, while some discrepancies were shown for the bottom half. Three sources of errors were discussed: the errors from forward modeling, from the increased X-ray range with beam energy, and from experimental measurement.

Overall, we have shown the feasibility of our inverse modeling algorithm applied to 2D heterogeneous materials for quantitative electron-induced X-ray analysis when appropriate input parameters including beam positions, beam energies, and voxel size are chosen.

5.7 Acknowledgements

The authors acknowledge financial support from McGill Engineering Doctoral Award (MEDA).

5.8 References

1. Goldstein, J.I., et al., *Scanning electron microscopy and X-ray microanalysis*. 2003: Springer.
2. Scott, V.D., G. Love, and S.J.B. Reed, *Quantitative electron-probe microanalysis*. 1995.
3. Castaing, R., *Application of electron probes to local chemical and crystallographic analysis.* Ph. D. Thesis (University of Paris), 1951.
4. Goldstein, J.I., *Principles of thin film X-ray microanalysis*, in *Introduction to Analytical Electron Microscopy*. 1979, Springer. p. 83-120.
5. Reed, S.J., *Electron probe microanalysis*, in *Microprobe techniques in the earth sciences*. 1995, Springer. p. 49-89.
6. Teng, C., Y. Yuan, and R. Gauvin, *The f-ratio quantification method applied to standard minerals with a cold field emission SEM/EDS.* Talanta, 2019.
7. Brodusch, N., H. Demers, and R. Gauvin, *Field emission scanning electron microscopy: New perspectives for materials characterization*. 2017: Springer.
8. Horny, P., *Development of a quantification method for X-ray microanalysis with an electron microscope*. 2006: McGill University Libraries.
9. Horny, P., et al., *Development of a new quantitative X-ray microanalysis method for electron microscopy.* Microscopy and Microanalysis, 2010. **16**(6): p. 821-830.
10. Wagner, H.W., et al., *Electron probe microanalysis inverse modeling.* Nuclear Instruments and Methods in Physics Research Section B: Beam Interactions with Materials and Atoms, 2001. **184**(3): p. 450-457.
11. Ritchie, N.W., *A new Monte Carlo application for complex sample geometries.* Surface and Interface Analysis: An International Journal devoted to the development and application of techniques for the analysis of surfaces, interfaces and thin films, 2005. **37**(11): p. 1006-1011.

12. Ro, C.-U., et al., *A Monte Carlo program for quantitative electron-induced X-ray analysis of individual particles.* Analytical Chemistry, 2003. **75**(4): p. 851-859.
13. Joy, D.C., *Monte Carlo modeling for electron microscopy and microanalysis*. Vol. 9. 1995: Oxford University Press.
14. Gauvin, R., et al., *Win X-ray: A new Monte Carlo program that computes X-ray spectra obtained with a scanning electron microscope.* Microscopy and Microanalysis, 2006. **12**(1): p. 49-64.
15. Echlin, P., et al., *Advanced scanning electron microscopy and X-ray microanalysis*. 2013: Springer Science & Business Media.
16. Gauvin, R., *Quantitative X-ray microanalysis of heterogeneous materials using Monte Carlo simulations.* Microchimica Acta, 2006. **155**(1-2): p. 75-81.
17. Love, G., M. Cox, and V. Scott, *A simple Monte Carlo method for simulating electron-solid interactions and its application to electron probe microanalysis.* Journal of Physics D: Applied Physics, 1977. **10**(1): p. 7.
18. Ding, Z.J., R. Shimizu, and K. Obori, *Monte Carlo simulation of x-ray spectra in electron probe microanalysis: Comparison of continuum with experiment.* Journal of applied physics, 1994. **76**(11): p. 7180-7187.
19. Murata, K., M. Kotera, and K. Nagami, *Quantitative electron microprobe analysis of thin films on substrates with a new Monte Carlo simulation.* Journal of applied physics, 1983. **54**(2): p. 1110-1114.
20. Gauvin, R. and P. Michaud, *MC X-Ray, a new Monte Carlo program for quantitative X-ray microanalysis of real materials.* Microscopy and Microanalysis, 2009. **15**(S2): p. 488-489.
21. Drouin, D., et al., *CASINO V2. 42—a fast and easy-to-use modeling tool for scanning electron microscopy and microanalysis users.* Scanning: The Journal of Scanning Microscopies, 2007. **29**(3): p. 92-101.
22. Llovet, X. and F. Salvat, *PENEPMA: a Monte Carlo program for the simulation of X-ray emission in electron probe microanalysis.* Microscopy and Microanalysis, 2017. **23**(3): p. 634-646.
23. Ritchie, N.W., *Spectrum simulation in DTSA-II.* Microscopy and Microanalysis, 2009. **15**(5): p. 454-468.
24. Pinard, P.T., et al., *pyMonteCarlo: A common programming interface for running identical simulations using different Monte Carlo programs.* Microscopy and Microanalysis, 2013. **19**(S2): p. 822-823.
25. Giurlani, W., M. Innocenti, and A. Lavacchi, *X-ray Microanalysis of Precious Metal Thin Films: Thickness and Composition Determination.* Coatings, 2018. **8**(2): p. 84.
26. Ng, F., et al., *Metallic thin film depth measurements by X-ray microanalysis.* Applied surface science, 2006. **252**(11): p. 3972-3976.
27. Campos, C.S., et al., *Thickness determination of ultra-thin films on Si substrates by EPMA.* Microchimica Acta, 2004. **145**(1-4): p. 13-17.
28. Youhua, H., *The calculation method of mass thickness of multi-layer films by Monte Carlo simulation and iteration.* Journal of Physics D: Applied Physics, 1990. **23**(11): p. 1420.
29. Waldo, R., *An iteration procedure to calculate film compositions and thicknesses in electron-probe microanalysis.* Microbeam Analysis, 1988: p. 310-314.

30. Statham, P. *Feasibility of x-ray analysis of multi-layer thin films at a single beam voltage*. in *IOP Conference Series: Materials Science and Engineering*. 2010. IOP Publishing.
31. Llovet, X. and C. Merlet, *Electron probe microanalysis of thin films and multilayers using the computer program XFILM.* Microscopy and Microanalysis, 2010. **16**(1): p. 21-32.
32. Pouchou, J. and F. Pichoir, *Electron probe X-ray microanalysis applied to thin surface films and stratified specimens.* Scanning Microscopy International(USA), 1992: p. 167-190.
33. Gauvin, R., G. L'Espérance, and S. St-Laurent, *Quantitative x-ray microanalysis of spherical inclusions embedded in a matrix using a SEM and Monte Carlo simulations.* Scanning, 1992. **14**(1): p. 37-48.
34. Burdet, P., S.A. Croxall, and P.A. Midgley, *Enhanced quantification for 3D SEM–EDS: using the full set of available X-ray lines.* Ultramicroscopy, 2015. **148**: p. 158-167.
35. Burdet, P., C. Hébert, and M. Cantoni, *Enhanced quantification for 3D energy dispersive spectrometry: Going beyond the limitation of large volume of X-ray emission.* Microscopy and Microanalysis, 2014. **20**(5): p. 1544-1555.
36. Schaffer, M., et al., *Automated three-dimensional X-ray analysis using a dual-beam FIB.* Ultramicroscopy, 2007. **107**(8): p. 587-597.
37. Jain, A.K. and R.C. Dubes, *Algorithms for clustering data*. Vol. 6. 1988: Prentice hall Englewood Cliffs, NJ.
38. Jain, A.K., *Data clustering: 50 years beyond K-means.* Pattern recognition letters, 2010. **31**(8): p. 651-666.
39. Thorndike, R.L., *Who belongs in the family?* Psychometrika, 1953. **18**(4): p. 267-276.
40. Bholowalia, P. and A. Kumar, *EBK-means: A clustering technique based on elbow method and k-means in WSN.* International Journal of Computer Applications, 2014. **105**(9).
41. Rousseeuw, P.J., *Silhouettes: a graphical aid to the interpretation and validation of cluster analysis.* Journal of computational and applied mathematics, 1987. **20**: p. 53-65.

5.9 Appendix

The details of the clustering algorithm are explained in this section. Assume that $X = \{x_i\}, i = 1, \dots, n$ is the set of n d-dimensional points to be clustered into a set of K clusters, $CL = \{cl_k, k = 1, \dots, K\}$ [38]. In our case, n is the number of voxels in the specimen, x_i is a d-dimensional point in which each value represents the weight fraction of a certain element despite the voxel position, and K is the number of different compositions in the specimen. Since the composition is normalized each time the specimen $\boldsymbol{C}$ is updated, which means that the sum of the weight fractions of all elements for a certain voxel is always 1, we only need to know the weight fractions of $(N_{element} - 1)$ elements, where $N_{element}$ is the number of elements that are present in

the specimen. Thus, d equals ($N_{element} - 1$). The basic idea of the K-means algorithm is to find a partition to minimize the squared error between the centroid of a cluster and the points in the cluster, also known as cost function, which is written as follows [38]:

$$J(CL) \equiv \frac{1}{n}\sum_{k=1}^{K}\sum_{x_i \epsilon cl_k} \|x_i - \mu_k\|^2 \tag{5.9}$$

where μ_k is the centroid of the cluster cl_k, which is defined by the mean of points assigned to the cluster cl_k. The procedure of the K-means algorithm is as follows [37]:

1. Randomly initialize K cluster centroids; Repeat step 2 and step 3 until the cluster membership stabilizes.
2. Generate a new partition by assigning each point to its closest cluster centroid.
3. Compute the new cluster centroids.

To choose the number of clusters *K*, the elbow method is used [39]. The basic principle of the elbow criterion [40] is that one should choose a number of clusters so that adding another cluster doesn't yield much better improvement in the cost function after training. Specifically, the variation of the cost function after training, $J(CL)$, is calculated as the increase of the number of clusters *K* starting with 1. At some values of *K*, the cost drops dramatically, and it reaches a plateau when *K* is further increased. This is the value *K* one wants to choose. One can also use other methods to determine the number of clusters [41]. Figure 5.18 presents the curve of the cost function after training as the variation of the number of clusters *K* for the result shown in Figure 5.8 d). According to the elbow criterion, the value of *K* =2 is chosen as the best number of clusters.

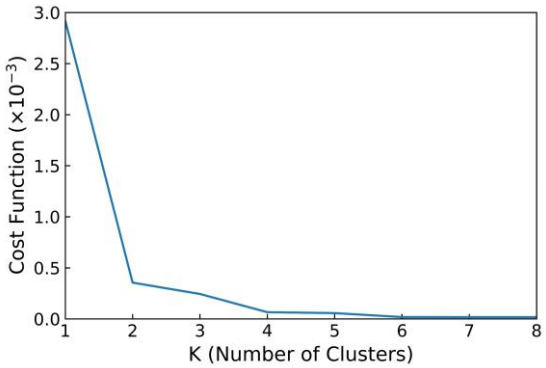

Figure 5.18 Variation of the cost function after training as the change of *K* (the number of clusters).

Chapter 6. Extraction of 3D quantitative maps using EDS-STEM tomography and HAADF-EDS bimodal tomography

In this chapter, we further explored the quantitative X-ray microanalysis of heterogeneous materials at the nanoscale by using electron tomography. A quantification approach was proposed to quantify the 3D elemental maps reconstructed using EDS-STEM tomography and HAADF-EDS bimodal tomography (HEBT). The approach was successfully applied to both simulated and experimental datasets.

- This paper has been published as: Y. Yuan*, K. E. MacArthur, S. M. Collins, N. Brodusch, F. Voisard, R. E. Dunin-Borkowski, R. Gauvin, Extraction of 3D Quantitative Maps using EDS-STEM Tomography and HAADF-EDS Bimodal Tomography, Ultramicroscopy, 220 (2021) 113166.

6.1 Abstract

Electron tomography has been widely applied to three-dimensional (3D) morphology characterization and chemical analysis at the nanoscale. A HAADF-EDS bimodal tomographic (HEBT) reconstruction technique has been developed to extract high resolution element-specific information. However, the reconstructed elemental maps cannot be directly converted to quantitative compositional information. In this work, we propose a quantification approach for obtaining elemental weight fraction maps from the HEBT reconstruction technique using the physical parameters extracted from a Monte Carlo code, MC X-ray. A similar quantification approach is proposed for the EDS-STEM tomographic reconstruction. The performance of the two quantitative reconstruction methods, using the simultaneous iterative reconstruction technique, are evaluated and compared for a simulated dataset of a two-dimensional phantom sample. The effects of the reconstruction parameters including the number of iterations and the weight of the HAADF signal are discussed. Finally, the two approaches are applied to an experimental dataset to show the 3D structure and quantitative elemental maps of a particle of flux melted metal-organic framework glass.

6.2 Introduction

Electron tomography is a technique that characterizes the three-dimensional (3D) structure of a typically nanoscale object from a tilt series of two-dimensional (2D) projections [1] and has been widely used in biological science [2, 3] and materials science [4]. Different image modes are available for electron tomography. The scanning transmission electron microscope (STEM) high-angle annular dark-field (HAADF) image is typically used for most cases in the field of material science to minimize the diffraction contrast that dominates in low-angle scattering which is the case for conventional bright-field (BF) or dark-field (DF) images of crystalline materials [5]. The intensity of the HAADF-STEM signal is strongly dependent on the atomic number and the projected thickness. HAADF tomography is thus sensitive to 3D chemical composition information. One disadvantage of HAADF tomography is that it only contains the accumulated information of all elements, which means the structures with different compositions but similar average atomic numbers cannot be distinguished. On the other hand, energy dispersive spectroscopy (EDS) STEM tomography can be used to extract element-specific distribution maps, and it has been applied to a wide range of materials including bimetallic nanoparticles [6], metallurgical samples [7], and semiconductor nanowires [8]. However, in comparison to HAADF-STEM tomography, it has poor signal-to-noise ratio (SNR) because of low count rates associated with the low probability of X-ray emission and the poor signal collection efficiency of available X-ray detectors [9, 10].

HAADF/ADF-STEM images have been used in EDS-STEM tomography for object contour determination [11], absorption correction [12], and shadowing effect correction [13]. Zhong et al. [14] proposed a HAADF-EDS bimodal tomographic (HEBT) reconstruction technique that uses HAADF-STEM and EDS-STEM simultaneously to extract 3D elemental maps. The technique links the HAADF image and EDS maps through response ratio factors using a linear relationship, i.e., the HAADF image is a weighted summation of the EDS maps of different elements. Using this technique, the element-specific features of EDS maps are extracted while also preserving the high SNR of the HAADF image. It has been successfully applied to the characterization of a nanowire device [15]. Nevertheless, it is not straightforward to obtain quantitative compositional information from the reconstructed intensities. To obtain the 3D elemental weight/atomic fraction maps, a quantification method needs to be applied.

There are currently three approaches to the quantification of EDS-STEM images: the Cliff-Lorimer method [16], the ζ-factor method [17], and the partial cross-section method [10]. The Cliff-Lorimer method connects the weight fractions, C_A and C_B, of two constituent elements *A* and *B* to their detected characteristic X-ray intensities, I_A and I_B using the following equation [16]:

$$\frac{C_A}{C_B} = k_{AB}\frac{I_A}{I_B}, \tag{6.1}$$

where k_{AB} is the Cliff-Lorimer factor (*k*-factor), which can be estimated using theoretical calculations or experiments [17]. The theoretical calculation of k-factors is fast but gives rise to relatively high systematic errors ($\pm 10\% - 20\%$ for the quantification of 2D elemental map) [17, 18], while the experimental determination is accurate with relative errors around $\pm 1\%$ but is often complicated and time-consuming [17]. An improved quantitative approach, the ζ-factor method, gives the relationship between the detected X-ray intensity of element *A*, I_A and the mass thickness ρt (ρ and t are the specimen density and thickness) as follows [17]:

$$\rho t = \zeta_A \frac{I_A}{C_A D_e}, \tag{6.2}$$

where ζ_A is the ζ-factor and D_e is the total electron dose. The ζ-factor method shows great advantages in absorption correction, spatial resolution calculation, etc. because it refines the thickness information. Moreover, the experimental determination of the ζ-factor is easier as it can be performed using single element standards.

A further, recently emerging approach uses EDS partial cross-sections to quantify X-ray counts in an absolute manner [10, 19]. The EDS partial cross-section of a single atom of element *A* is determined from a pure element standard using the following equation:

$$\sigma_{par}^{A} = \frac{I_A}{D_e n_A t}, \tag{6.3}$$

where $n_A t$ is the atom density per unit area in atoms/m^2, in which n_A is the atom volume density and t is the thickness. Although this approach is based on the ζ-factor method, the implementation of this approach is simpler because it is on an absolute scale [19]. A similar quantification method to the ζ-factor method and partial cross-section is used in our calculation, although here the correction factor is determined through physical models instead of experiments.

The main objective of this paper is to present a quantification method using theoretical cross-sections to obtain 3D elemental maps from both EDS-STEM tomography and HEBT through the simultaneous iterative reconstruction technique (SIRT). The effects of the reconstruction parameters are also studied in this work. Using a 2D phantom sample, the image qualities of the direct reconstructed maps and the quantified maps are investigated and compared for EDS-STEM tomography and HEBT. Both techniques are then applied to an experimental dataset of a particle of flux melted metal-organic framework glass, denoted a_g[(ZIF-67)$_{0.2}$(ZIF-62)$_{0.8}$], where a_g refers to amorphous glass structure, ZIF-67 and ZIF-62 refer to two compositionally distinct zeolitic imidazolate frameworks, and the subscripts refer to the relative fraction in the bulk glass. The synthesis and traditional quantitative EDS tomography of the glass particle have been explicitly described in previous reports [20, 21]. Here we look specifically at the implementation and results from the quantified HEBT reconstruction.

6.3 Methods

The following calculations are based on the thin film approximation, which means that the absorption and secondary fluorescence are negligible, as is the multiple scattering of the incident electrons. The quantifications of the EDS-STEM tomographic and HEBT reconstructions and the simulation of the HAADF and EDS signals using MC X-ray [22] will be introduced in this section.

6.3.1 Quantification of the EDS-STEM tomographic reconstruction

The measured characteristic intensity of a certain X-ray line of element *A* from a thin film is expressed using the equation [23]:

$$I_A = N_V \frac{\sigma_{ion}^A \omega_A p_A}{M_A} C_A \rho t D_e \left(\frac{\Omega}{4\pi}\right) \varepsilon_A \,, \tag{6.4}$$

where N_V is Avogadro's number, $\sigma_{ion}^A$is the ionization cross-section, ω_A is the fluorescence yield, p_A is the relative intensity, M_A is the atomic weight, Ω is the detector solid angle, and ε_A is the detector efficiency. To better demonstrate the relationship between the X-ray intensity and the weight fraction, equation (6.4) can be written as follows,

$$I_A = n f_A C_A \rho t, \tag{6.5}$$

where n is a constant for a certain measurement and f_A is an element-specific factor, which are calculated as follows:

$$n = N_V D_e \left(\frac{\Omega}{4\pi}\right), \tag{6.6}$$

$$f_A = \frac{\sigma_{ion}^A \omega_A p_A \varepsilon_A}{M_A}. \tag{6.7}$$

In electron tomography, for a heterogeneous sample, the measured characteristic X-ray intensity for a single measurement of the projection image can be expressed in an integral form along the electron trajectory inside the sample, t',

$$I_A = n f_A \int C_A(t')\rho(t')d(t'). \tag{6.8}$$

The continuous line integral can be replaced by a discrete ray-sum [14]:

$$I_A = n f_A \sum_{j=1}^{N} w_j C_{A,j} \rho_j \,, \tag{6.9}$$

where w_j is determined by the volume intersected between the electron beam and the j^{th} voxel [24]. N is the number of voxels in the specimen for the reconstruction.

For EDS-STEM tomography, multiple measurements are performed for various beam positions and tilt angles. The number of measurements, M, equals the product of the number of tilt angles and the number of beam positions. For a certain element A, the X-ray intensity for the i^{th} measurement, $I_{A,i}$ can be expressed as follows:

$$I_{A,i} = n f_A \sum_{j=1}^{N} w_{ij} C_{A,j} \rho_j \,. \tag{6.10}$$

The tomography reconstruction is often formulated as a least square minimization,

$$\boldsymbol{X}_A^* = \underset{X_A}{\operatorname{argmin}} \, ||\boldsymbol{I}_A - \boldsymbol{W}\boldsymbol{X}_A||_2^2 \,, \tag{6.11}$$

where $\boldsymbol{I}_A \in \boldsymbol{R}^M$ is the X-ray intensity matrix, $\boldsymbol{W} \in \boldsymbol{R}^{M \times N}$ is the projection matrix, and $\boldsymbol{X}_A \in \boldsymbol{R}^N$ is the reconstruction quantity. According to equation (6.10), we know that the reconstructed quantity for the j^{th} voxel, $\boldsymbol{X}_{A,j} = n f_A C_{A,j} \rho_j$. Since the sum of the weight fractions of the constituent elements for a certain voxel is always one, i.e., $\sum_{A=1}^{k} C_{A,j} = 1$, where k is the number of elements, using a similar calculation to the ζ-factor method, considering that the solid angle is the same for all the elements, we have

$$C_{A,j} = \frac{\boldsymbol{X}_{A,j}/f_A}{\sum_{A=1}^{k} \boldsymbol{X}_{A,j}/f_A}. \tag{6.12}$$

According to the definitions, the partial cross-section can be calculated using the factor f_A by $\sigma_{par}^{A} = f_A \cdot \Omega/4\pi \cdot M_A$.

SIRT is used to solve the least square problem [25]. SIRT updates the reconstructed values at each iteration using the data from all the projections simultaneously [26]. Its primary advantage is a reduced sensitivity to noise or other errors in under-sampled experimental data [27]. Unfortunately, it has the semi-convergence property, that the error initially decreases but starts to increase after some iterations when dealing with noisy data [28]. In this work, a non-negativity constraint was applied to SIRT algorithm by setting individual negative voxels to zero in each iteration since the reconstructed values should always remain non-negative [29].

The normalization in equation (6.12) may magnify the noise of the reconstructed map by changing a small value to one. Therefore, prior to this normalization, a thresholding was performed in order to define the voxels within the particle, that any intensities smaller than the threshold were set to zero based on the summation of all the elemental maps of $\boldsymbol{X}_{A,j}/f_A$. The exact threshold value was determined using a modified edge spread function (ESF) fitting approach [21]. The approach calculates the particle volume for a series of threshold values, and the variation of the threshold relative to the particle volume can be fitted using the ESF. Therefore, the smallest gradient of the particle volume over the threshold corresponds to the most appropriate threshold value. The same process was applied to the quantification of the HEBT reconstruction. For both the EDS-STEM and HEBT reconstruction, the thresholding step was applied after the reconstruction process as a post-processing step for the purpose of visualizing and interpreting the quantification within the volume of the particle.

6.3.2 Quantification of the HEBT reconstruction

It is worth noticing that HEBT can be applied only when two conditions are satisfied: first, both the HAADF and EDS data fulfill the projection requirement, that the signal is a monotonic function of the thickness and composition [30], and secondly, the HAADF signals are the weighted sum of the EDS signals for all the elements present [31].

The HAADF-STEM signal I^H is the number of electrons that are scattered at high angles and can be expressed as the sum of the scattered electrons by each element present in the specimen [14]:

$$I^H = D_e^H N_v \sum_{A=1}^{k} \sigma_{ela}^A \frac{\int C_A(t')\rho(t')d(t')}{M_A}, \tag{6.13}$$

where D_e^H is the electron dose for HAADF measurement, A is the index of the constituent element, k is the number of elements in the specimen, σ_{ela}^A is the elastic scattering cross-section, and $C_A(t')$ is the weight fraction of element A at t'. It can be written in the same form as equation (6.9):

$$I^H = D_e^H N_v \sum_{A=1}^{k} z_A \sum_{j=1}^{N} w_{ij} C_{A,j} \rho_j \,, \tag{6.14}$$

where $z_A = \sigma_{ela}^A / M_A$.

The HEBT reconstruction technique proposed by Zhong et al. [14] links the HAADF signals with the EDS signals using a response ratio factor r_A:

$$I^H = \sum_{A=1}^{k} r_A I_A \tag{6.15}$$

and,

$$r_A = \frac{D_e^H N_v z_A}{n f_A}. \tag{6.16}$$

Since the value of r_A might differ for various instruments or experimental setups, it is typically estimated using the measured intensities I^H and I_A through linear regression. The reconstruction using HEBT aims to minimize the least square of the measured and estimated signals (see [14] for more details),

$$\boldsymbol{X^b}^* = \underset{X^b}{\operatorname{argmin}} \, ||\boldsymbol{I^b} - \boldsymbol{W^b X^b}||_2^2 \tag{6.17}$$

where $\boldsymbol{I^b} = \begin{pmatrix} (1-\alpha) r_1 \boldsymbol{I}_1 \\ \vdots \\ (1-\alpha) r_A \boldsymbol{I}_e \\ \vdots \\ (1-\alpha) r_k \boldsymbol{I}_k \\ \alpha \boldsymbol{I}^H \end{pmatrix}$, $\boldsymbol{W^b} = \begin{pmatrix} (1-\alpha)\boldsymbol{W} & \dots & \emptyset & \dots & \emptyset \\ \vdots & \dots & \vdots & \dots & \vdots \\ \emptyset & \dots & (1-\alpha)\boldsymbol{W} & \dots & \emptyset \\ \vdots & \dots & \vdots & \dots & \vdots \\ \emptyset & \dots & \emptyset & \dots & (1-\alpha)\boldsymbol{W} \\ \alpha \boldsymbol{W} & \dots & \alpha \boldsymbol{W} & \dots & \alpha \boldsymbol{W} \end{pmatrix}$,

and $\boldsymbol{X^b} = \begin{pmatrix} \boldsymbol{X_1^b} \\ \vdots \\ \boldsymbol{X_A^b} \\ \vdots \\ \boldsymbol{X_k^b} \end{pmatrix}$, where $\boldsymbol{X_A^b} \in \boldsymbol{R}^N$, in which $X_{A,j}^b = z_A C_{A,j} \rho_j$, and α is the balance factor between the HAADF and EDS terms, which indicates the weight of the HAADF term ($0 < \alpha < 1$).

With the reconstructed quantity $\boldsymbol{X^b}$, the composition of element *A* for the j^{th} voxel can be calculated as follows:

$$C_{A,j} = \frac{X_{A,j}^b / z_A}{\sum_{A=1}^{k} X_{A,j}^b / z_A}. \tag{6.18}$$

6.3.3 Forward modeling using MC X-ray

The required physical parameters for the quantification including scattering and ionization cross-sections are extracted from MC X-ray [22], a Monte Carlo program for simulating electron trajectories within the solid and computing X-ray emissions. The physical models used for calculating those parameters are shown in Table 6.1. And the extracted physical parameters used in this work are listed in Table 6.2.

MC X-ray [22] was used to calculate the simulated HAADF and EDS signals from a phantom sample. The quantification processes using both EDS-STEM tomography and HEBT were applied to the simulated signals, and the reconstructed images (both before and after quantification) were compared with the phantom sample to assess the accuracy of each process. The HAADF detector inner collection angle used in MC X-ray for high angle and low angle are 611 and 94 mrad, respectively.

Table 6.1 Physical models used in MC X-ray [22]

Physical parameters	Physical models
Elastic scattering cross-section	Mott & Browning 1991 [32]
Ionization cross-section	Bote 2009 [33]
Fluorescence yield	Perkins et al. 1991 [34]
Relative intensity	Perkins et al. 1991 [34]

Table 6.2 Physical parameters extracted from MC X-ray

X-ray line	Ag Lα	Au Mα	Co Kα	Zn Kα
Incident beam energy (keV)	100		80	
Elastic scattering cross section (barn)	9.90×10^{6}	1.98×10^{7}	5.59×10^{6}	6.51×10^{6}
Ionization cross section (barn)	2.44×10^{3}	7.46×10^{3}	420	302
Fluorescence yield	0.057	0.030	0.369	0.466
Relative intensity	0.816	0.999	0.891	0.890

6.4 Results and discussion

6.4.1 A 2D phantom sample

Input

To assess the accuracy of the proposed quantification approaches, a 2D phantom sample of an alloyed Ag-Au nanoparticle, a slice on the X-Z plane, was created. The weight fractions of Ag and Au are presented in Figure 6.1. The phantom sample has a core-shell structure, in which the composition of the core is 80 wt% Au and 20 wt% Ag, while the shell has 20 wt% Au and 80 wt% Ag.

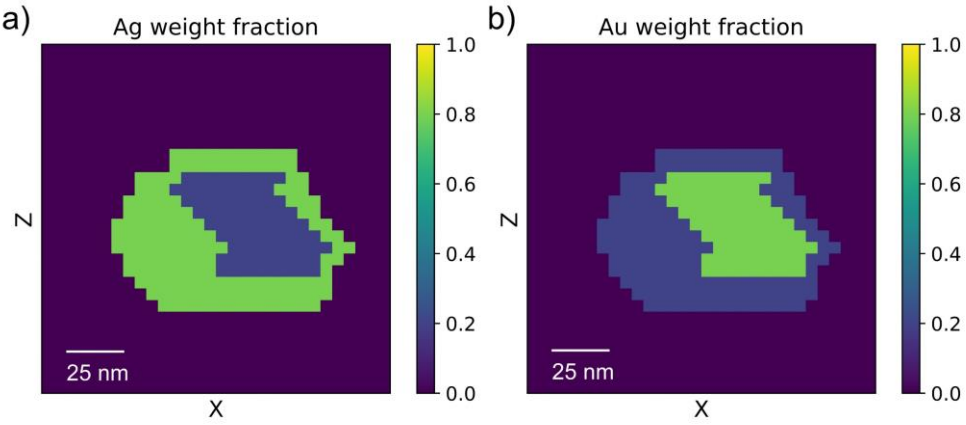

Figure 6.1 Weight fractions of a) Ag and b) Au for the phantom sample: a slice of Ag-Au alloyed particle with a core-shell structure. Core: 80 wt% Au and 20 wt% Ag; Shell: 20 wt% Au and 80 wt% Ag.

Simulations were performed using MC X-ray at 100 keV for 97 beam positions from -72 to 72 nm with a step size of 1.5 nm and 31 tilt angles from -75° to 75° with a step size of 5°. The HAADF sinogram (as presented in Figure 6.2 a) was obtained with a simulated electron number of 100,000 per pixel, which corresponds to an electron fluence of 444 e/A^2 (electrons per square angstrom). Pixels along the horizontal and vertical axes represent the signals for varying beam positions and varying tilt angles, respectively. To mimic reasonable experimental conditions, an acquisition time of 0.5 s for each pixel and a beam current of 100 pA were used, indicating an electron number of 3.12×10^8 per pixel, which corresponds to an electron fluence of 1.39×10^6 e/A^2. Since the experimental EDS signals follow a Poisson distribution [35], Poisson noise was applied to the simulated EDS sinograms, and the resulting sinograms of the Ag Lα line and Au Mα line are shown in Figure 6.2 b) and c), respectively.

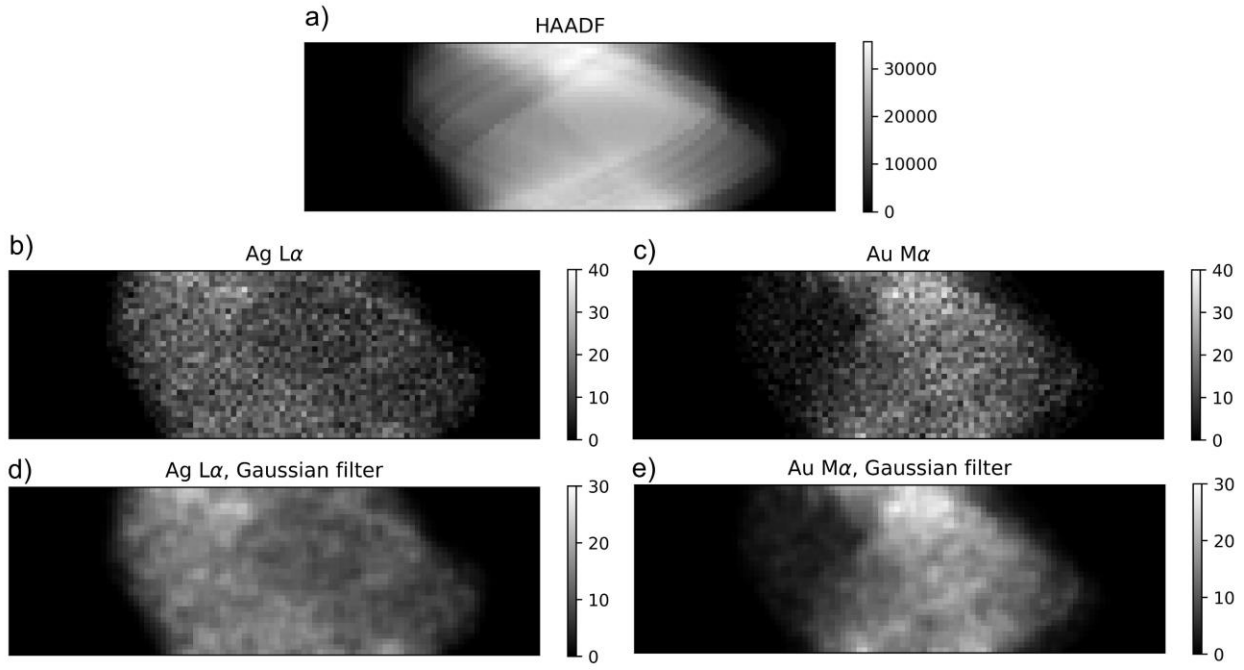

Figure 6.2 Sinograms of a) HAADF, b) EDS for the Ag Lα line, c) EDS for the Au Mα line, d) EDS for the Ag Lα line adding a Gaussian filter, and e) EDS for the Au Mα line adding a Gaussian filter. Pixels along the horizontal and vertical axes represent the signals for varying beam positions and varying tilt angles, respectively.

Before performing the tomography reconstruction, a Gaussian filter with a standard derivation of 0.8 was applied to the EDS elemental maps as a denoise process to improve the SNR. It was implemented using the multidimensional Gaussian filter function in Python library SciPy [36]. The EDS sinograms with Gaussian filter are presented in Figure 6.2 d) and e). For both EDS-STEM

tomography and HEBT, the EDS sinograms with Gaussian filter were used as input. And the original HAADF sinogram was used for HEBT.

EDS-STEM tomographic reconstruction

The EDS-STEM tomographic reconstruction was first performed using SIRT for the sinograms shown in Figure 6.2 d) and e). The reconstructed images were computed for different numbers of iterations, n = 20, 50 and 100, to investigate its effect. The reconstructed images of the quantity $\boldsymbol{X}_A$ for Ag and Au are presented in Figure 6.3. Note that the quantity $\boldsymbol{X}_A$ is not on an absolute scale. For Ag after 20 iterations (as shown in Figure 6.3 a), the core-shell structure can be distinguished, in which the intensity of Ag is higher in the shell than the core. However, the boundaries between the core and shell as well as between the object and background are blurry. When n increases to 50 (Figure 6.3 b), the contrast is improved, and the boundaries become clearer. At a higher n, however, an increased noise is observed (Figure 6.3 c) because of the over-fitting problem. As for Au, similarly, an increased noise is presented with an increase in n (as shown in Figure 6.3 d, e, and f). For all three numbers of iterations, the shape of the core with an increased Au intensity is well-preserved, while part of the boundaries is not correctly recognized. For example, several pixels in the bottom of the shell are recognized as background, which is due to the low SNR and large tilt angle increment (5° for this case) of the projection images and the relatively low concentration of Au in the shell.

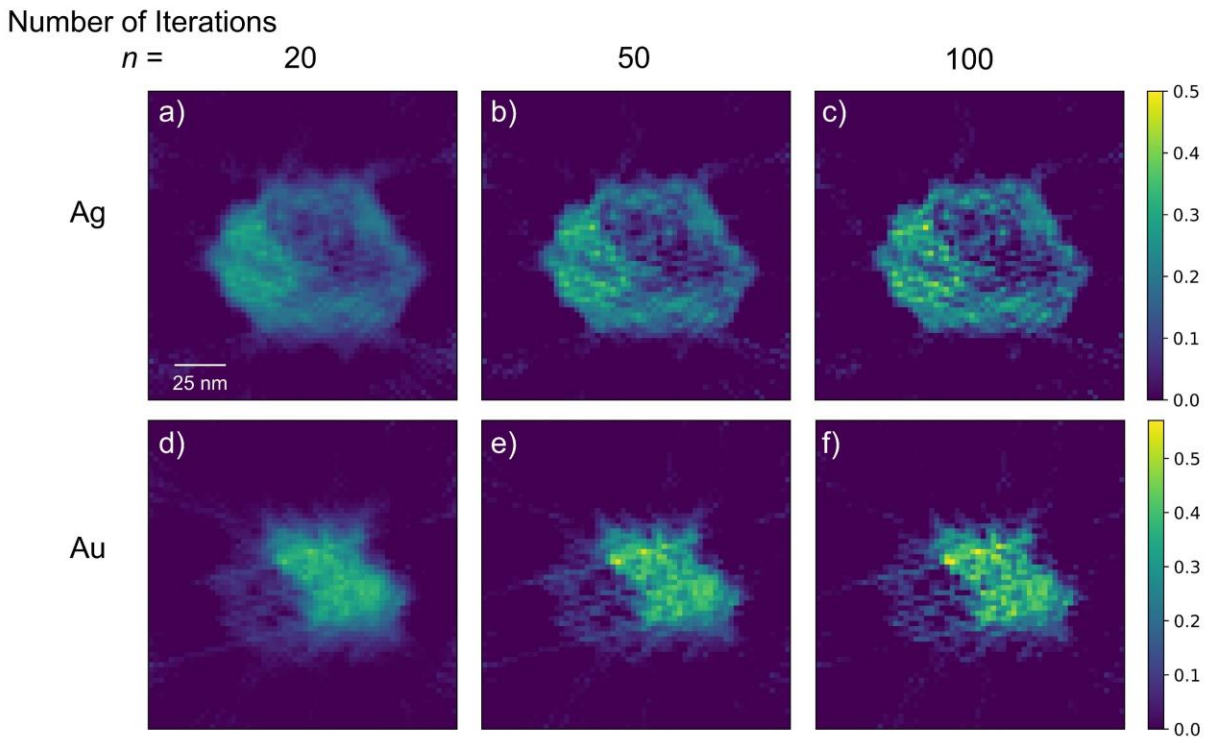

Figure 6.3 Ag and Au element maps reconstructed using SIRT through EDS-STEM tomography when the number of iterations n = 20, 50, and 100, respectively. a), b), and c) are on the same intensity scale, and d), e), f) are on the same intensity scale.

To better assess the quality of the reconstructed image, two types of image quality metrics are calculated: structural similarity index (SSIM) and mean squared error (MSE). SSIM [37] evaluates the structural similarity between two images considering three components: luminance, contrast, and structure. Since the intensities of the reconstructed images are not on the same scale with the reference image (phantom sample), only the structure component is compared. The structure component, s, of two signals $\boldsymbol{x}$ and $\boldsymbol{y}$ (with the same size) are calculated as follows [37]:

$$s(\boldsymbol{x}, \boldsymbol{y}) = \frac{\sigma_{xy} + C}{\sigma_x \sigma_y + C}, \tag{6.19}$$

where

$$\sigma_{xy} = \frac{1}{N-1} \sum_{i=1}^{N} (x_i - \mu_x)(y_i - \mu_y), \tag{6.20}$$

$$\sigma_x = \left(\frac{1}{N-1}\sum_{i=1}^{N}(x_i - \mu_x)^2\right)^{1/2}, \tag{6.21}$$

$$\sigma_y = \left(\frac{1}{N-1}\sum_{i=1}^{N}(y_i - \mu_y)^2\right)^{1/2}, \tag{6.22}$$

and C is a factor to avoid instability when $\sigma_x\sigma_y$ is very close to zero, N is the size of $\boldsymbol{x}$ and $\boldsymbol{y}$, μ_x and μ_y are the average intensity of $\boldsymbol{x}$ and $\boldsymbol{y}$. C is set to zero in our calculations but still included in equation (6.19) for consistency with common implementations. An SSIM value that is close to one means better structural similarity than for a value close to zero. MSE is the average of the squares of the errors between two signals. MSE between the direct reconstructed image $\boldsymbol{X}_A$ and the reference image (Figure 6.1 a and b) is computed using a scaling factor since they are in different scales, and the scaling factor is chosen to minimize the MSE. For the quantified weight fraction maps, MSE is calculated directly without scaling.

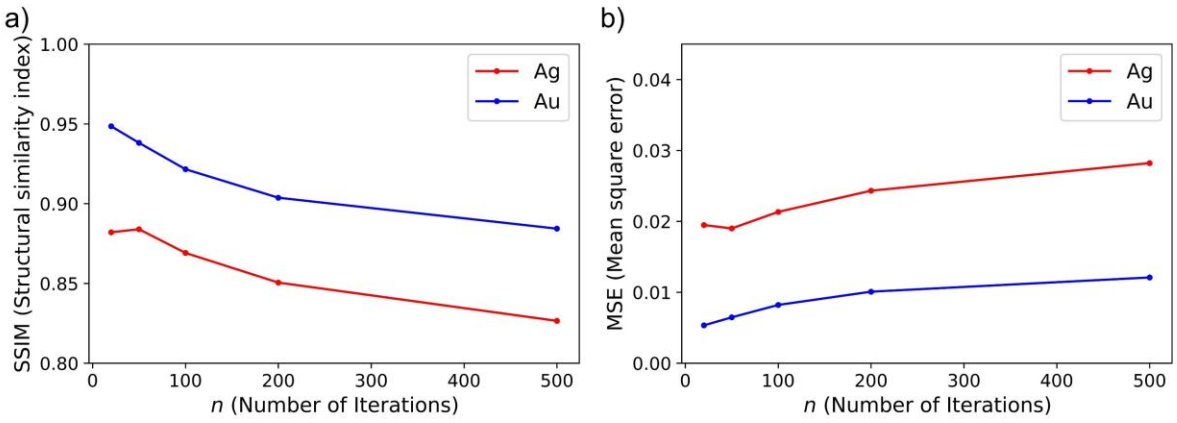

Figure 6.4 Variation of a) SSIM and b) MSE relative to *n*, the number of iterations for the EDS-STEM tomographic reconstruction.

Figure 6.4 shows the variations of a) SSIM and b) MSE relative to the number of iterations for the reconstructed images obtained using the EDS-STEM tomographic reconstruction. For both metrics, a better image quality for Au is found than for Ag. This difference is likely due to the slightly higher X-ray intensities of the Au Mα line (as shown in Figure 6.2 d and e), which means lower noise from the sinogram. Alternatively, the higher contrast between the shell and the background for Ag than for Au may impair the image quality for Ag to a greater extent due to an imperfect boundary. As *n* increases, the image quality for Ag initially improves but then starts to fall off after 50 iterations, whilst for Au this drop off occurs after only 20 iterations. This is

consistent with what we can observe qualitatively in Figure 6.3. Therefore, the approximately optimal value for the number of iterations for Ag and Au are 50 and 20, respectively.

From the reconstructed images of $\boldsymbol{X}_A$, Figure 6.3, the true weight fractions of Ag and Au were computed using equation (6.12). The computed weight fraction maps for different numbers of iterations are presented in Figure 6.5. In general, the core and shell are well segmented, and the compositions of both regions are close to the reference values. The boundary between the object and the background appears sharper after quantification primarily because the noise outside the object is removed by the thresholding step. The image quality of the quantitative element maps as shown in Figure 6.6 is thus slightly improved relative to the image quality of $\boldsymbol{X}_A$. The quantification process to a certain extent neutralizes the difference between the intensities of Ag and Au, making the relatively sharp boundary between the core and shell (as shown in Figure 6.3 a and d) become a 'belt-like' region (Figure 6.5 a and b) when the number of iterations is 20. The variation of the image quality relative to the number of iterations (Figure 6.6) presents a similar trend as that for the images of $\boldsymbol{X}_A$ (Figure 6.4).

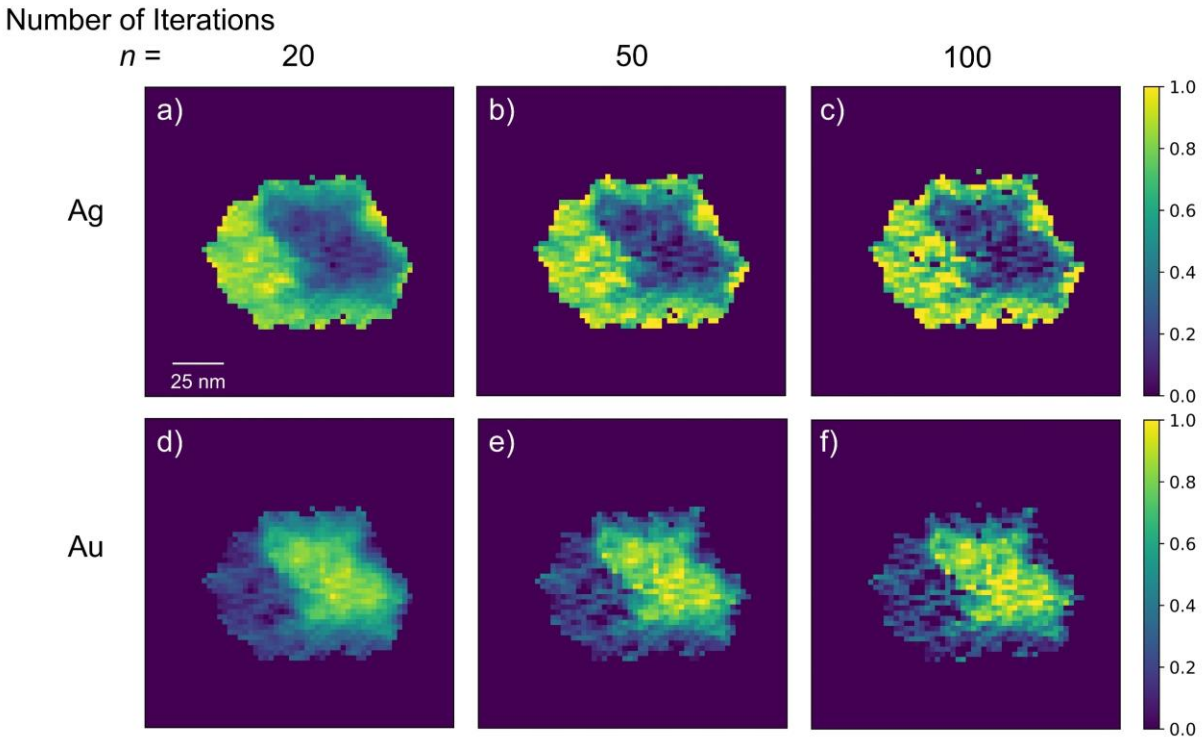

Figure 6.5 Quantitative elemental maps (weight fraction) of Ag and Au for different numbers of iterations, n = 20, 50, and 100. All figures are on the same intensity scale.

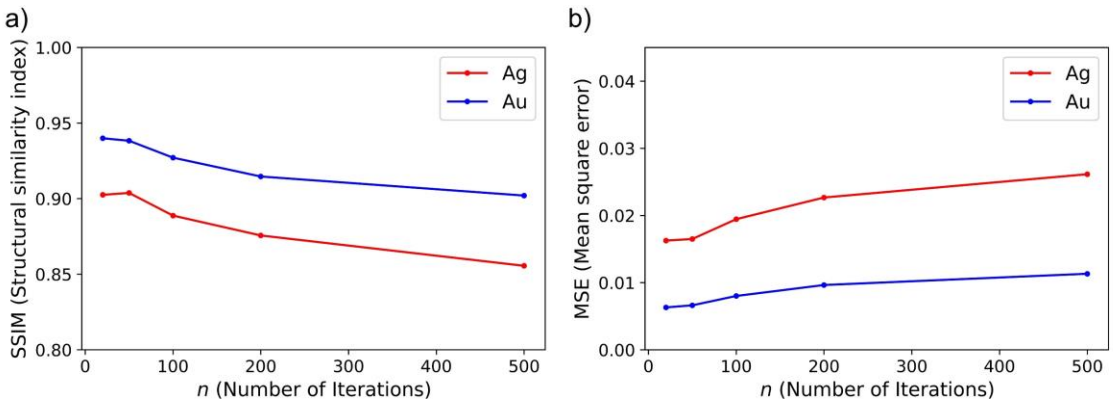

Figure 6.6 Variation of a) SSIM and b) MSE for the reconstructed weight fraction maps from EDS-STEM tomography as a function of *n*, the number of iterations.

HEBT reconstruction

In this section, results obtained using the HEBT reconstruction are presented. Figure 6.7 shows the reconstructed Z-contrast image from the HAADF-STEM sinogram after 50 iterations. Compared with the reconstructed elemental maps shown in the last section, the boundaries between the object and background as well as between the core and shell can be distinguished clearly, and there is notably higher contrast. It also shows an excellent agreement with the input phantom structure. Therefore, it is reasonable to assume the HEBT reconstruction has some advantages over the EDS-STEM tomographic reconstruction as it incorporates the HAADF signal.

The response ratio factors r_{Ag} and r_{Au} were calculated using the gradient descent method [38] to link the HAADF-STEM and EDS-STEM images by a linear relationship. The calculated r_{Ag} and r_{Au} are 805 and 987, respectively, with a coefficient of determination R^2 of 0.982, indicating that more than 98% of the measured data can be explained by the linear model.

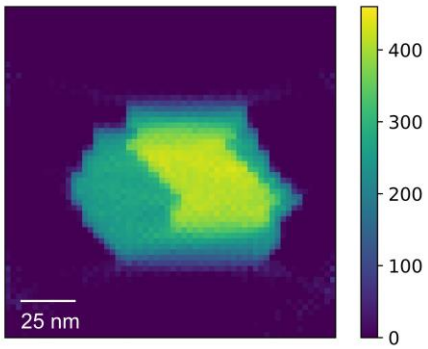

Figure 6.7 Reconstructed Z-contrast image from HAADF-STEM tomography after 50 iterations using SIRT.

Two parameters affect the HEBT reconstruction process: n, the number of iterations and α, the weight of the HAADF signal. We performed the HEBT reconstruction for different n: 100, 200, and 500, and varying α, ranging from 0 to 1. Note that the number of iterations required for the HEBT reconstruction is much larger than that for the EDS-STEM tomographic reconstruction due to the increased data volume. For the EDS-STEM tomographic reconstruction, the input data is the EDS sinogram for a certain X-ray line with a pixel size of M, while for the HEBT reconstruction, the input data is the EDS sinograms for all the X-ray lines of the elements present and the HAADF sinograms, with a total size of $M \times (k + 1)$, where k is the number of elements present in the specimen. Therefore, more data needs to be optimized for the HEBT reconstruction, requiring an increased number of iterations. Several numbers of iterations smaller than 100 were also tested, however they demonstrated far worse quality than the results presented here. The qualities of the reconstructed images for the quantity $\boldsymbol{X^b}$ are evaluated, taking Figure 6.1 as reference images.

The variations of SSIM and MSE are shown in Figure 6.8 a) and b), respectively, as a function of α for different n. A better image quality of Au is observed compared with Ag, which is similar to the results from EDS-STEM tomography. For each number of iterations, the image quality is first improved as α increases, and then deteriorates after reaching the best. To better investigate the effect of α, the weight of the HAADF signal, we present the reconstructed images for α = 0.7, 0.8, and 0.9 after 200 iterations in Figure 6.9. As α changes from 0.7 to 0.8, the noise level appears suppressed since the low noise HAADF data dominates more. As it continues increasing to 0.9, though with less noise, the boundary between the shell and core becomes blurry, and the contrast deteriorates. Figure 6.18 presents the intensity profiles across the boundary for the elemental maps shown in Figure 6.9 to better observe the variation of the boundary with α. The variation is because as α increases, the EDS-STEM terms contribute less, which makes the optimization process to minimize the residuals of the EDS-STEM terms inefficient. If the residual of the HAADF-STEM term has been minimized while those for the EDS-STEM terms remain large, the back projection from the HAADF-STEM image will appear in the reconstructed elemental maps. Therefore, in this case, the reconstructed elemental maps of both Ag and Au become similar to the image from the HAADF-STEM reconstruction (Figure 6.7), showing worse contrast.

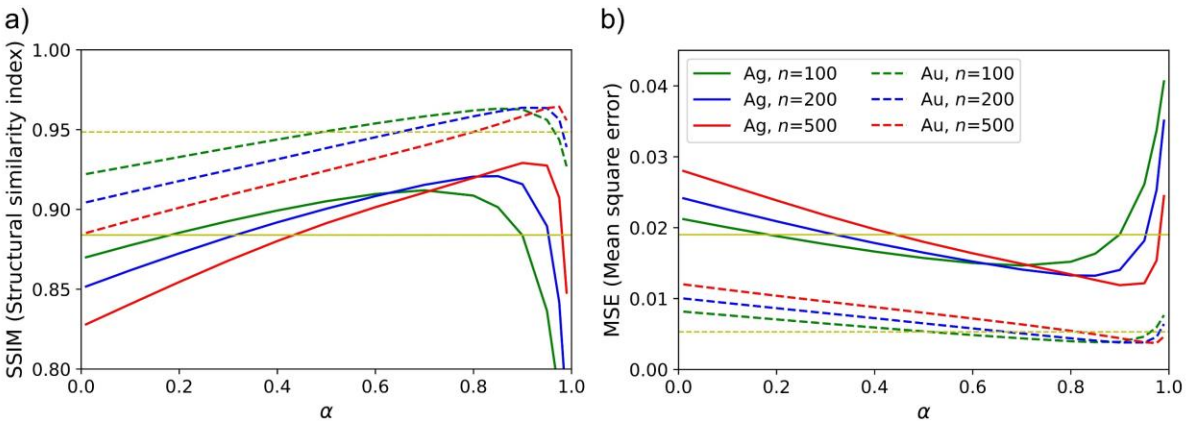

Figure 6.8 Variation of a) SSIM and b) MSE of Ag and Au as a function of α, the weight of the HAADF signal, for different n: 100 (green), 200 (blue), and 500 (red) for the direct reconstructed maps using HEBT. Solid lines represent the data for Ag, and dashed lines represent the data for Au. The yellow horizontal lines indicate the best image quality obtained using the EDS-STEM tomographic reconstruction.

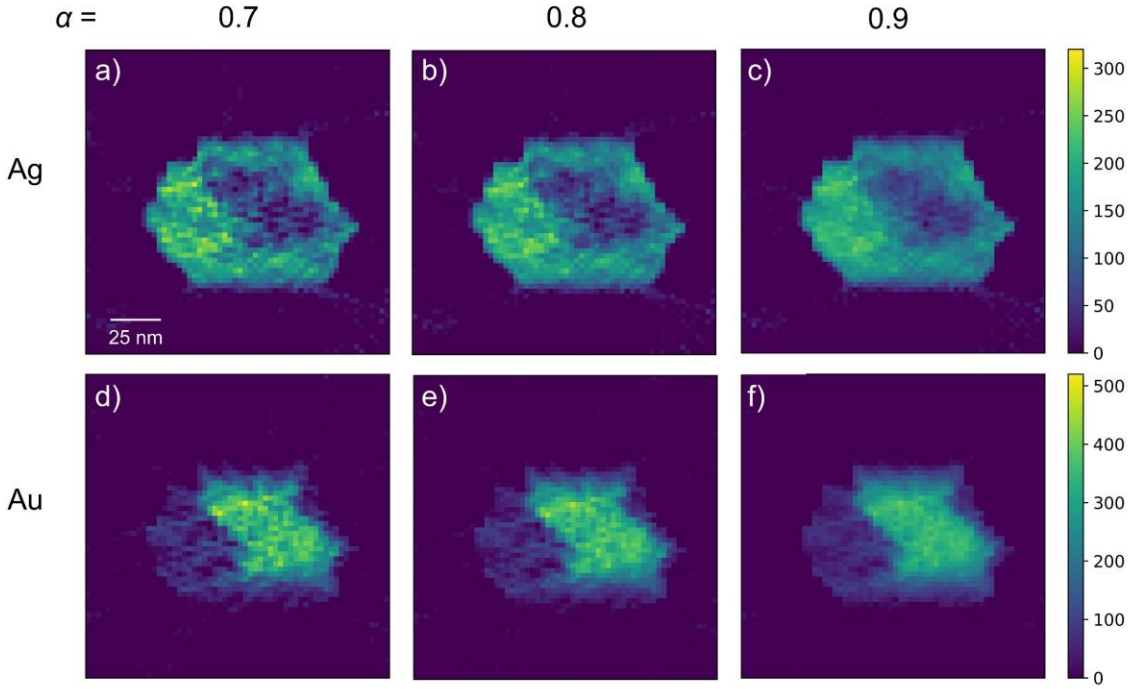

Figure 6.9 Elemental maps directly reconstructed using HEBT for Ag and Au for different α, the weight of the HAADF signal: 0.7, 0.8, 0.9 after 200 iterations. a), b), and c) are on the same intensity scale, and d), e), and f) are on the same intensity scale.

As n increases, the image quality typically improves before subsequently deteriorating due to the overfitting problem. Just as shown in Figure 6.10 d) e) and f), the Au elements map shows an improved contrast when n increases from 50 to 200. However, upon increasing to 500 iterations,

the noise begins to dominate again. The approximately optimal value of n is thus found to be 200. The optimal value of n changes as α increases. As shown in Figure 6.8, the approximately optimal value of n for Ag is 100 when α is smaller than 0.6, and the value changes to 200 when α is between 0.6 and 0.8. An optimal value around 500 is found for α larger than 0.8. This results from the inefficiency of the optimization process for the EDS-STEM terms as α increases. An increased number of iterations is required to reduce the appearance of the back projection of the HAADF-STEM image in the reconstructed elemental maps in the case when the residual of the HAADF-STEM term is minimized and those for the EDS-STEM terms remain large.

The horizontal yellow lines in Figure 6.8 represent the best reconstruction image quality obtained using the EDS-STEM tomographic reconstruction to be compared with the HEBT reconstruction. The best image quality is obtained when n=50 for Ag (yellow solid line) and 20 for Au (yellow dashed line). For both Ag and Au, the HEBT tomographic reconstruction shows better images under most circumstances as long as α is larger than 0.5. The element maps for Ag demonstrate a greater improvement in image quality compared to Au possibly due to the fact that the image quality of Ag is more sensitive to the change in the boundary resulting from higher contrast between the shell and the background. When comparing the reconstructed images from EDS-STEM tomography (Figure 6.3) with that of HEBT (Figure 6.9 and Figure 6.10), one improvement that stands out is that the boundary between the object and the background is defined more clearly for HEBT (see Figure 6.19 for the comparison of the intensity profiles across the boundary). This is primarily a benefit of the high SNR of the HAADF sinogram. Within the object, the segmentation of the core and shell relies partly on the choice of the reconstruction parameters like n and α.

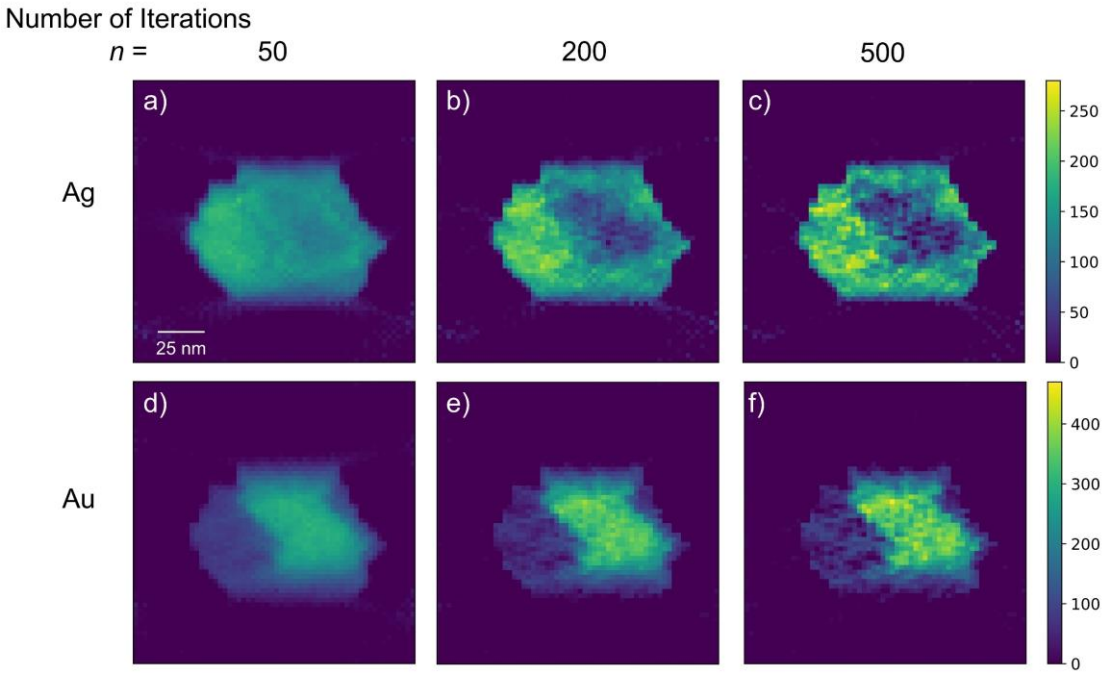

Figure 6.10 Elemental maps for Ag and Au directly reconstructed using HEBT for different *n*, the number of iterations: 50, 200, and 500 when α=0.9 (α is the weight of the HAADF signal). a), b), c) are on the same intensity scale, and d), e), f) are on the same intensity scale.

From the reconstructed images of $\boldsymbol{X^b}$, the quantitative elemental maps of Ag and Au were calculated using equation (6.18). The quantitative elemental maps of Figure 6.9 and Figure 6.10 are shown in Figure 6.11 and Figure 6.12, respectively. Similar effects of *n* and α are observed as previously seen in the reconstructed images of $\boldsymbol{X^b}$. For the same number of iterations, an increase in α can reduce the level of noise but simultaneously results in a blurring of the boundary between the core and shell (see Figure 6.20 for the intensity profiles of the elemental maps shown in Figure 6.11). For a constant α, an increase in *n* initially improves the contrast but subsequently brings more noise at higher α due to the over-fitting problem.

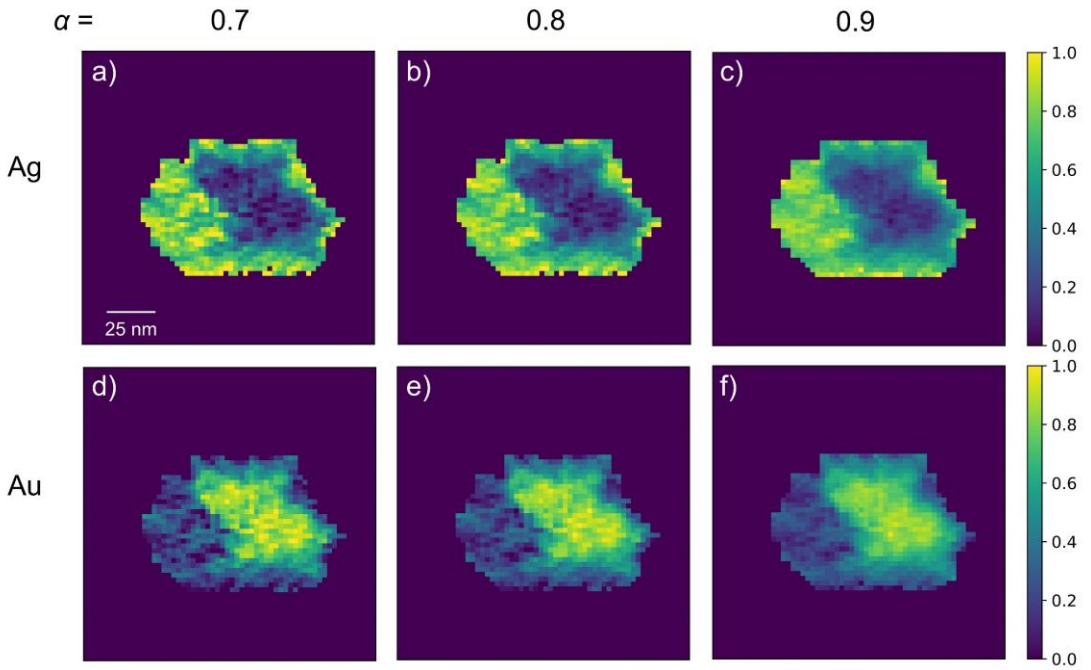

Figure 6.11 Quantitative elemental maps of Ag and Au (weight fraction) from HEBT for different α, the weight of the HAADF signal: 0.7, 0.8, 0.9 after 200 iterations. All figures are on the same intensity scale.

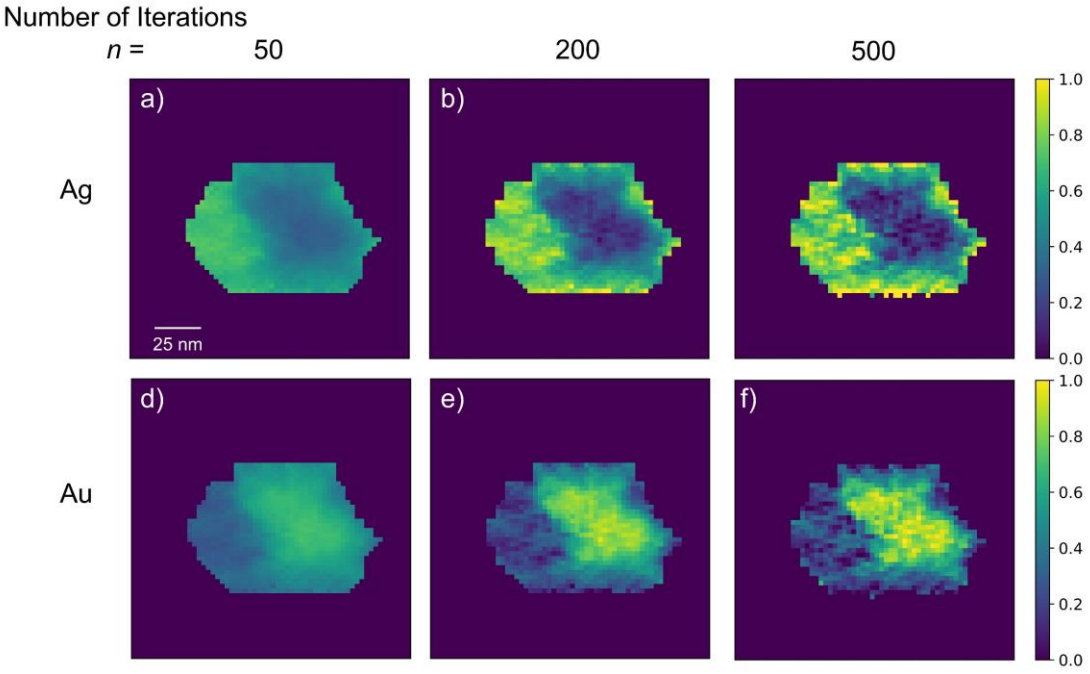

Figure 6.12 Quantitative elemental maps of Ag and Au (weight fraction) from HEBT for different *n*, the number of iterations: 50, 200, and 500 with α=0.9 (α is the weight of the HAADF signal). All figures are on the same scale.

The variations of SSIM and MSE as a function of α for the quantitative elemental maps are presented in Figure 6.13 for different *n*. The yellow horizontal lines correspond to the best image quality obtained from the quantification of the EDS-STEM tomographic reconstruction (solid line for Ag and dashed line for Au). The quality of the Ag elemental map is greatly improved by the well-determined object boundary. However, the quality of the Au elemental map is at a comparable level with the Au map before quantification. The different effect on Ag and Au is intrinsic, i.e., because the particle contains higher Ag content in the shell (80 wt%) and it therefore should demonstrate a higher contrast in the quantified composition map. The unusual fluctuation of the two metrics with α results from the threshold determination to define the particle volume, because this was done independently via the ESF method each time.

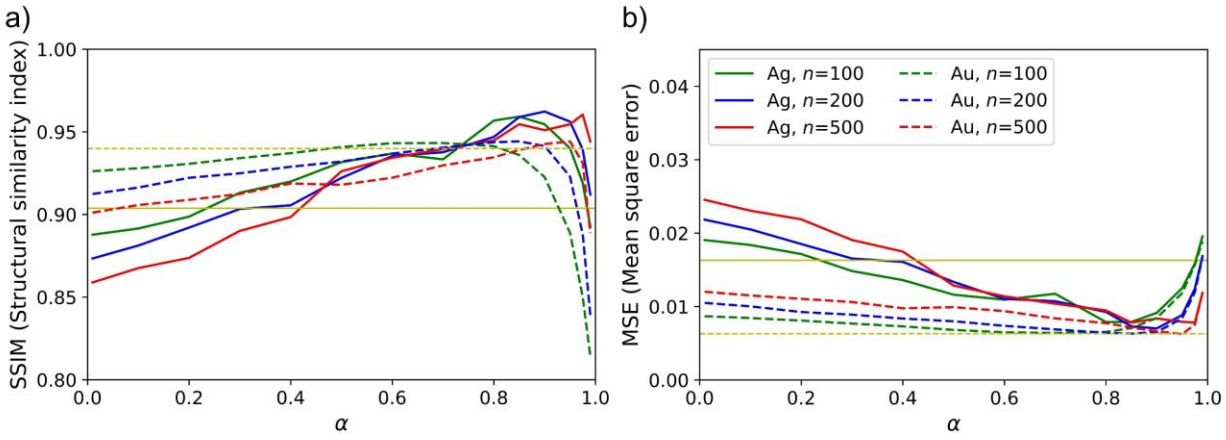

Figure 6.13 Variation of a) SSIM and b) MSE as a function of α for different *n*: 100 (green), 200 (blue), and 500 (red) for the quantitative elemental maps obtained using HEBT. Solid lines represent the data for Ag, and dashed lines represent the data for Au. The yellow horizontal lines indicate the best image quality obtained using the EDS-STEM tomographic reconstruction.

6.4.2 A particle of flux melted metal-organic framework glass

The two reconstruction techniques and quantification processes were next applied to 3D characterisation of a real experimental dataset obtained from a multicomponent zeolitic imidazolate framework (ZIF) glass: the a_g [(ZIF-67)$_{0.2}$(ZIF-62)$_{0.8}$] flux melted glass.

Specimen and experimental data

ZIFs, a subcategory of metal-organic framework, are composed of tetrahedral metal nodes connected by imidazolate-based organic ligands [39]. a_g [(ZIF-67)$_{0.2}$(ZIF-62)$_{0.8}$] is generated through the melting of ZIF-67 [Co(mlm)$_2$, mlm: 2-methylimidazolate, $C_4H_5N_2^-$] mixed with ZIF-

62 [$Zn(lm)_{1.75}(blm)_{0.25}$, lm: imidazolate, $C_3H_3N_2^-$, and blm: benzimidazolate, $C_7H_5N_2^-$] and brought to above the melting point of ZIF-62 [20]. The subscripts, 0.2 and 0.8, refer to the weight fraction of each component, and a_g refers to melt quenched glass. For additional details of the synthesis and previous EDS tomography analysis of this sample, refer to [20] and [21], respectively.

The experimental maps were acquired on a Thermo Fisher 80-200 keV probe corrected Titan with a four quadrant Super-X EDS detector operating at 80 keV. The EDS spectrum image data sets were acquired for different tilt angles ranging from -72° to 54° with a tilt increment of around 9°. For each tilt angle, an ADF image was simultaneously obtained using a Fischione HAADF detector. ADF images have been proved to satisfy the projection requirement, that the signal is a monotonic function of the thickness in a prior report [21]. It is, therefore, reasonable to use this signal in conjunction with EDS for a HEBT reconstruction. Please refer to reference [21] for more details about the experimental setup.

EDS maps were recorded with a pixel size approximately equal to the beam diameter, and then subsequently re-binned to make sure that each pixel contains enough X-ray counts. Both the EDS spectrum images and ADF images (required to have the same size as EDS maps) were re-binned to half of their original number of pixels in both spatial dimensions. The pixel size after re-binning is 2.74 × 2.74 nm. For the acquired EDS spectra, the background was subtracted, and the intensities of the peak of the C, N, Co, and Zn Kα line were integrated respectively to generate EDS maps using HyperSpy [40], an open source Python library. The ADF images and EDS maps for the same tilt angle were aligned by aligning the center of mass of ADF image with the elemental map of N. To reduce the shadowing effect, the total signals of a tilt series EDS maps for a certain element were normalized to the same value [41]. The in-plane alignment and tilt-axis shift and rotation were then performed for both ADF and EDS images. Figure 6.14 shows the processed ADF and EDS images of the C, N, Co and Zn Kα line for tilt angles: -45°, 0°, and 45°.

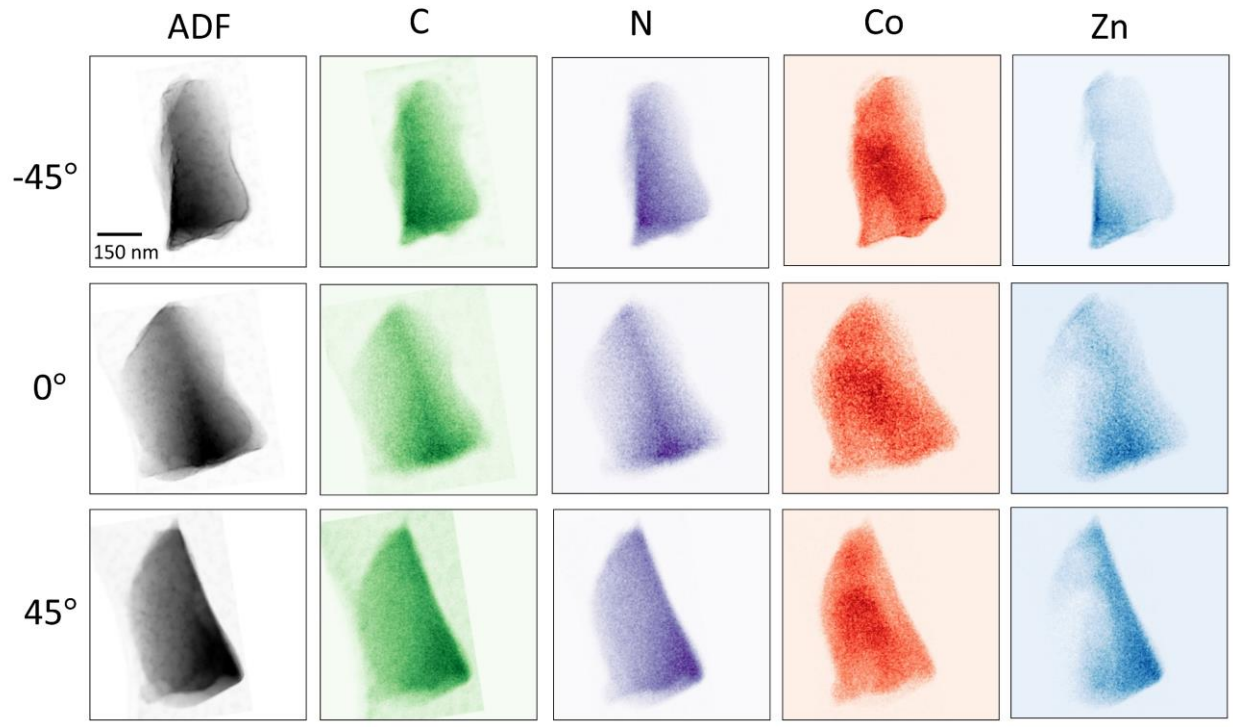

Figure 6.14 ADF and EDS maps for the C, N, Co, and Zn Kα line for tilt angles of -45°, 0°, and 45° . Note the presence of the carbon support film is visible in both the ADF maps and the EDS maps for the C Kα line, and the ADF maps are presented here on an inverted intensity scale.

Tomographic reconstruction

Since the weight fraction of H is relatively small for both components (4.6 wt% in ZIF-67 and 3.1 wt% in ZIF-62), the contribution of H to the elastic scattering of electrons, i.e., HAADF signals is ignored. Therefore, only four elements: C, N, Co, and Zn are considered for the HEBT reconstruction.

The HEBT reconstructions were performed for around 260 slices with $\alpha = 0.8$ and n = 100. The computed response factors for the four elements are $r_C = 1921$, $r_N = 3792$, $r_{Co} = 5179$, and $r_{Zn} = 6502$ with a coefficient of determination $R^2 = 0.92$. The reconstructed elemental maps are compared with the results from the EDS-STEM tomographic reconstruction in Figure 6.15, which presents the 2D reconstructed images for slice number 70, 130, and 190.

For both EDS-STEM tomography and HEBT, no clear boundaries between the Zn-rich and Co-rich components is observed. Instead, the interface displays the diffusion of the two components resulting in a region comprised of both Co and Zn, consistent with what has been

presented in prior reports [20, 21]. Moreover, a higher intensity of Co and little intensity of Zn are shown in the upper-left region of the particle, likely referring to remnant pure single-phase ZIF-67. Meanwhile the bottom of the particle, displaying high Zn intensity and an apparent absence of Co, likely contains a region corresponding to pure ZIF-62 domain. As we increase of the slice number from 70 to 190, the cross-sectional area of the particle increases.

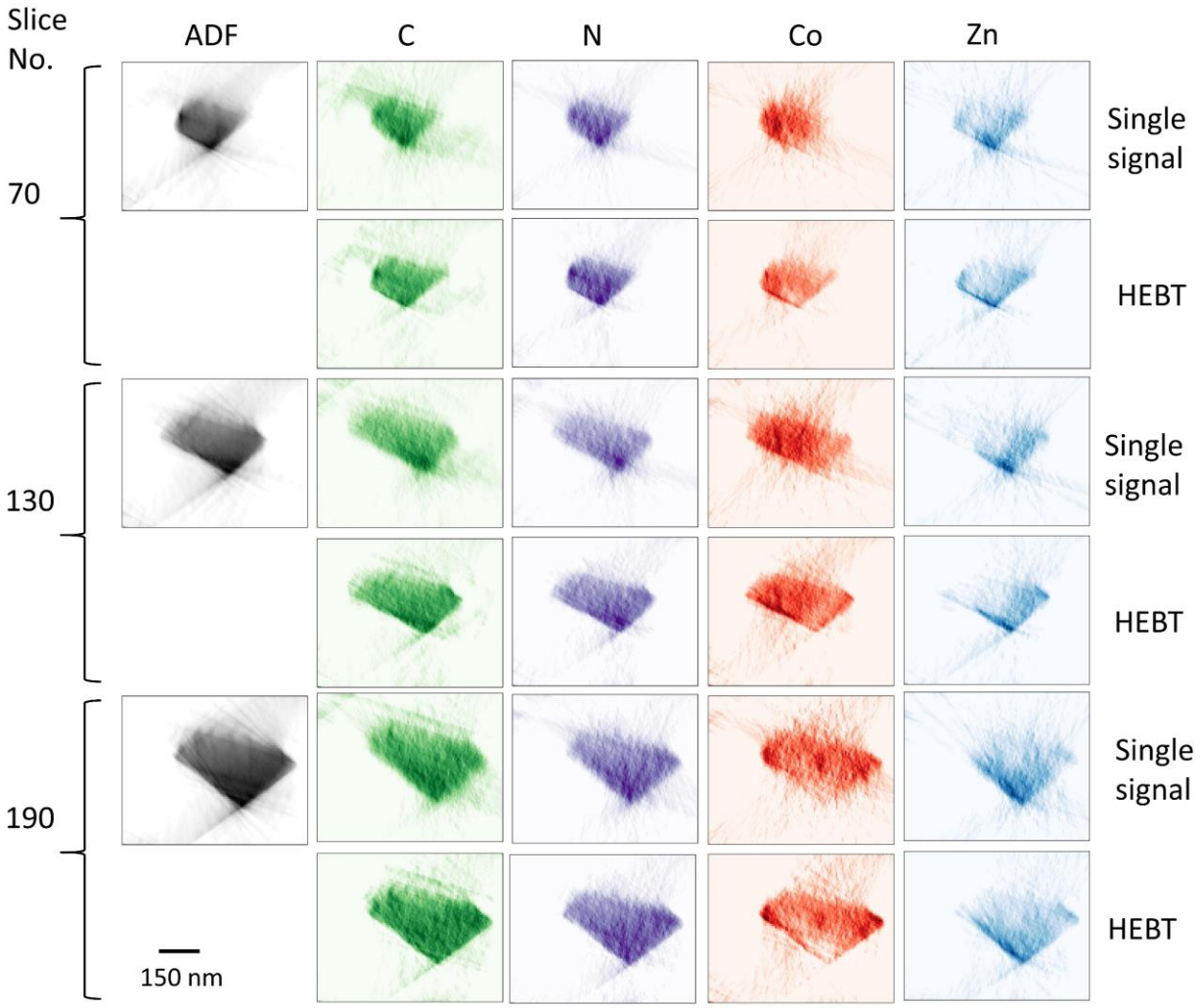

Figure 6.15 Reconstructed elemental maps for xz orthoslice (the cross-section view in/out of the paper for the maps shown in Figure 6.14) using the traditional single signal tomography reconstruction and HEBT reconstruction for three slices: no. 70, 130, and 190.

Compared with the EDS-STEM tomographic reconstruction, the HEBT reconstruction, in most cases, displays clearer boundaries and a better contrast. For example, for the Co element map at slice no.190, noise shows in the bottom-right region outside the particle for the EDS-STEM

tomographic reconstruction, while it is mostly absent in the reconstructed map from HEBT, making the blurry boundary between the particle and the background much sharper.

Some slight discrepancies in the shape of the particle between the two reconstruction techniques are observed. For example, for slice no.70, a "stripe-like" region along the bottom-right side in the HEBT reconstruction is missing in the elemental maps of the EDS-STEM tomographic reconstruction. This might be due to the misalignment between the ADF images and EDS maps considering that ADF images have only one frame, while EDS spectrum images were acquired as a summation over multiple frames with drift correction.

Quantification

The reconstructed images were then quantified using the physical parameters acquired from MC X-ray. Considering that the X-ray intensities of the C and N Kα lines extracted from the spectra can be inaccurate because of the poor background simulation at low energies, presence of the carbon support film underneath the particle, and possible enhancement in the absorption effects [21], C and N were not included in the quantification. We use the weight ratios of Zn and Co to the total weight of Zn and Co [Zn/ (Zn + Co) and Co/ (Zn +Co)] to indicate the quantities of Zn and Co, respectively. The HEBT quantification factors for Co and Zn are $z_{Co} = 9.49 \times 10^4\ b \cdot mol/g$ and $z_{Zn} = 9.96 \times 10^4\ b \cdot mol/g$, where b is the symbol of barn. And the EDS-STEM quantification factors are $f_{Co} = 2.25\ b \cdot mol/g$ and $f_{Zn} = 1.84\ b \cdot mol/g$. According to the definitions of the partial cross-section σ_{par}^{A} and the EDS quantification factor f_A, we have $\sigma_{par}^{Co}/\sigma_{par}^{Zn} = (f_{Co} \cdot M_{Co})/(f_{Zn} \cdot M_{Zn})$. In comparison to the partial cross-section ratio of $\sigma_{par}^{Co}/\sigma_{par}^{Zn} = 1.08$, determined experimentally by Collins et al. [21], our calculation obtains a close value of $(f_{Co} \cdot M_{Co})/(f_{Zn} \cdot M_{Zn})$, 1.10, which indicates the reliability of our model.

Figure 6.16 presents the absolute weight fraction of Co and Zn for three slices using the two different reconstruction techniques. Similar features as observed in Figure 6.15 are shown in Figure 6.16, that high Co concentration is found in the upper-left region, and high Zn concentration in the bottom-right region. Even though the same threshold determination method was used, the HEBT reconstruction shows smoother boundaries and a more similar shape to the reconstructed images before quantification as observed in Figure 6.15 than the EDS-STEM tomographic reconstruction. Again, small discrepancies in the shape might result from the misalignment between the ADF images and EDS maps.

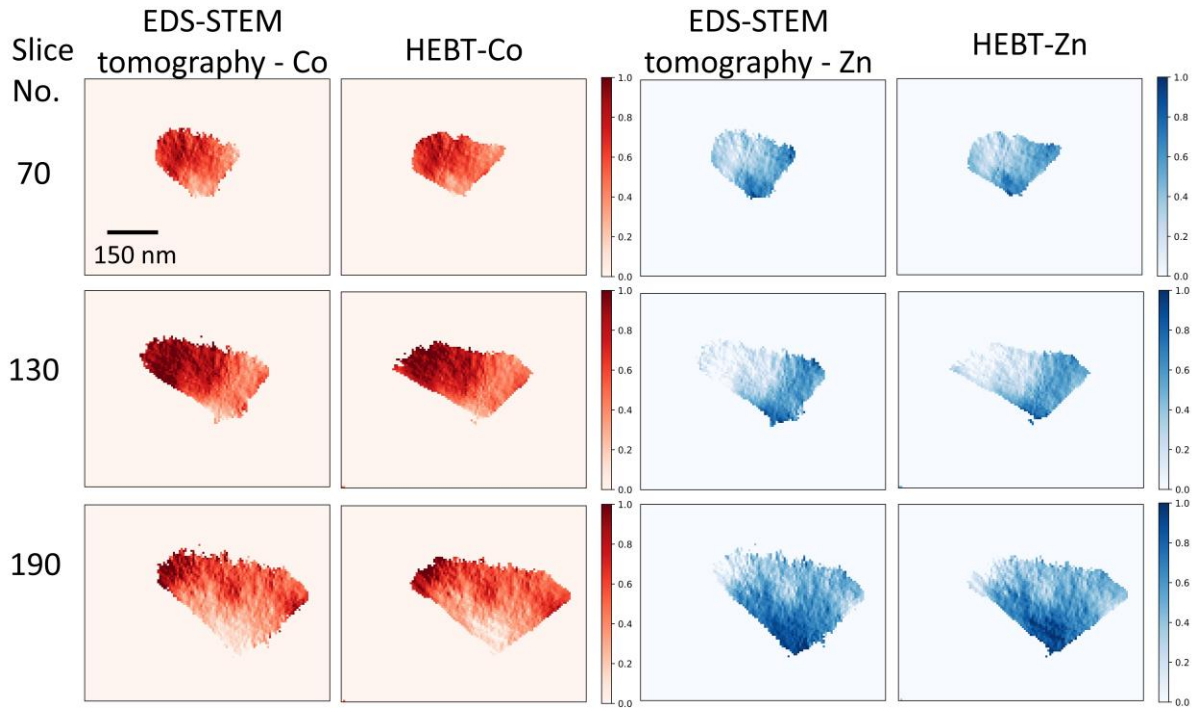

Figure 6.16 Weight fraction maps of Co and Zn [Co/(Co + Zn) and Zn/(Co + Zn)] using the EDS-STEM tomographic and HEBT reconstruction for slice no. 70, 130, and 190 (cross-section view on the xz plane).

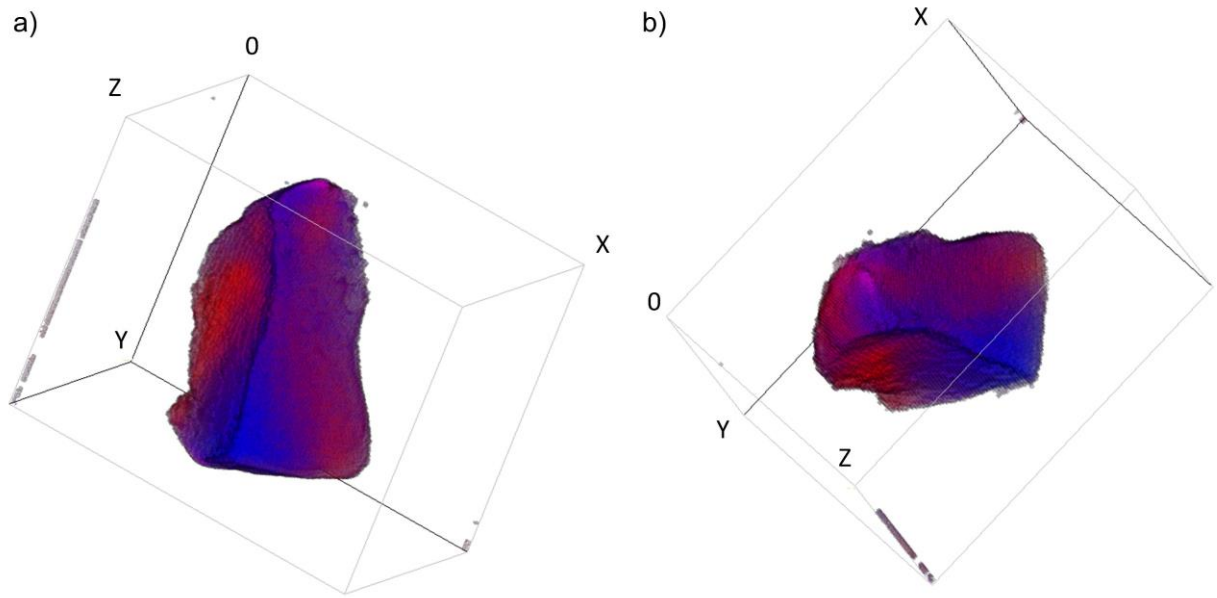

Figure 6.17 3D volume rendering of the flux melted particle using the HEBT reconstruction. Red represents Co, and blue represents Zn.

Figure 6.17 presents a 3D volume rendering of the flux melted particle obtained using the quantification of the HEBT reconstruction, which provides a complete view to observe the 3D morphology and diffusion of the Co-rich domain (red) and Zn-rich domain (blue) in the particle.

6.5 Conclusion

We have proposed a new quantification approach combining the physical parameters acquired from MC X-ray with tomographic reconstruction to characterize 3D elemental distribution of nanostructures quantitatively. Two types of tomographic reconstruction were investigated using the simultaneous iterative reconstruction technique (SIRT): the traditional EDS-STEM tomographic reconstruction and HAADF-EDS bimodal tomographic (HEBT) reconstruction. The two types of reconstruction technique and the corresponding quantification approaches were applied to a simulated dataset of a 2D phantom sample of a Ag-Au nanoparticle and an experimental dataset of a particle of flux melted metal-organic framework glass.

Using the simulated dataset of a 2D phantom sample (a single slice), the effects of the reconstruction parameters were investigated through two types of image quality metrics: SSIM and MSE. For both EDS-STEM tomography and HEBT, the quality of the reconstructed image is initially improved as a function of the number of iterations, before falling off at higher values due to the over-fitting problem. A similar trend was observed for α, the weight of the HAADF signal, in the HEBT reconstruction. Moreover, as α increases, the approximately optimal value for the number of iterations increases since the optimization becomes less efficient as α increases. In general, with appropriate reconstruction parameters, HEBT shows a better contrast and a reduced noise level compared with EDS-STEM tomography. The quantified elemental maps obtained from the HEBT reconstruction also present a better similarity and lower errors in comparison to the reference images when compared to that from the EDS-STEM tomographic reconstruction.

The quantification approaches of both reconstruction techniques were successfully applied to an experimental dataset of a particle of flux melted metal-organic framework glass, displaying the quantified 3D elemental distribution of Co and Zn. The diffusion of the Co-rich domain and Zn-rich domain into each other was shown. The EDS-STEM tomography quantification factors calculated using our approach have shown a good consistency with the experimentally measured partial cross-sections from the reference.

We have shown the feasibility of our quantification approaches for EDS-STEM tomography and HEBT applied to experimental datasets. Using SIRT, both EDS-STEM tomography and HEBT have revealed physically meaningful results. Although requiring an optimal alignment of ADF and EDS maps in conventional multi-frame acquisitions, HEBT has shown advantages in image contrast, boundary determination, and noise reduction compared with EDS-STEM tomography. The HEBT technique will play an important role in the characterization of beam-sensitive samples for which the EDS maps are quite noisy and in reducing experimental acquisition time. In the future, the method to better align the ADF and EDS maps will be explored. And the integration of other advanced tomography algorithms as a replacement of SIRT will be implemented to improve the reconstructed images.

6.6 Acknowledgement

Y. Y. acknowledges financial support from Natural Sciences and Engineering Research Council of Canada (NSERC). K. E. M. acknowledges the Deutsche Forschungsgemeinschaft (DFG) for funding this research through Grant HE 7192/1-2. S. M. C. acknowledges support from a University Academic Fellowship at the University of Leeds.

6.7 References

1. Pennycook, S.J. and P.D. Nellist, *Scanning transmission electron microscopy: imaging and analysis*. 2011: Springer Science & Business Media.
2. Lučić, V., F. Förster, and W. Baumeister, *Structural studies by electron tomography: from cells to molecules.* Annu. Rev. Biochem., 2005. **74**: p. 833-865.
3. Bárcena, M. and A.J. Koster. *Electron tomography in life science*. in *Seminars in cell & developmental biology*. 2009. Elsevier.
4. Weyland, M. and P.A. Midgley, *Electron tomography.* Materials Today, 2004. **7**(12): p. 32-40.
5. Pennycook, S., *Z-contrast STEM for materials science.* Ultramicroscopy, 1989. **30**(1-2): p. 58-69.
6. Goris, B., et al., *Monitoring galvanic replacement through three-dimensional morphological and chemical mapping.* Nano Lett, 2014. **14**(6): p. 3220-6.
7. Rossouw, D., et al., *Blind source separation aided characterization of the γ′ strengthening phase in an advanced nickel-based superalloy by spectroscopic 4D electron microscopy.* Acta Materialia, 2016. **107**: p. 229-238.
8. Rueda-Fonseca, P., et al., *Quantitative reconstructions of 3D chemical nanostructures in nanowires.* Nano letters, 2016. **16**(3): p. 1637-1642.
9. Slater, T.J., et al., *STEM-EDX tomography of bimetallic nanoparticles: A methodological investigation.* Ultramicroscopy, 2016. **162**: p. 61-73.

10. MacArthur, K.E., et al., *Quantitative energy-dispersive X-ray analysis of catalyst nanoparticles using a partial cross section approach.* Microscopy and Microanalysis, 2016. **22**(1): p. 71-81.
11. Saghi, Z., et al., *Three-dimensional chemical analysis of tungsten probes by energy dispersive x-ray nanotomography.* Applied Physics Letters, 2007. **91**(25): p. 251906.
12. Burdet, P., et al., *A novel 3D absorption correction method for quantitative EDX-STEM tomography.* Ultramicroscopy, 2016. **160**: p. 118-129.
13. Zanaga, D., et al., *A new method for quantitative XEDS tomography of complex heteronanostructures.* Particle & Particle Systems Characterization, 2016. **33**(7): p. 396-403.
14. Zhong, Z., et al., *A bimodal tomographic reconstruction technique combining EDS-STEM and HAADF-STEM.* Ultramicroscopy, 2017. **174**: p. 35-45.
15. Bender, H., et al., *Combined STEM-EDS tomography of nanowire structures.* Semiconductor Science and Technology, 2019.
16. Cliff, G. and G.W. Lorimer, *The quantitative analysis of thin specimens.* Journal of Microscopy, 1975. **103**(2): p. 203-207.
17. Watanabe, M. and D. Williams, *The quantitative analysis of thin specimens: a review of progress from the Cliff-Lorimer to the new ζ-factor methods.* Journal of microscopy, 2006. **221**(2): p. 89-109.
18. Watanabe, M., D.B. Williams, and Y. Tomokiyo, *Comparison of detectability limits for elemental mapping by EF-TEM and STEM-XEDS.* Micron, 2003. **34**(3-5): p. 173-183.
19. MacArthur, K., et al., *Compositional quantification of PtCo acid-leached fuel cell catalysts using EDX partial cross sections.* Materials Science and Technology, 2016. **32**(3): p. 248-253.
20. Longley, L., et al., *Flux melting of metal–organic frameworks.* Chemical Science, 2019. **10**(12): p. 3592-3601.
21. Collins, S.M., et al., *Phase diagrams of liquid-phase mixing in multi-component metal-organic framework glasses constructed by quantitative elemental nano-tomography.* APL Materials, 2019. **7**(9): p. 091111.
22. Gauvin, R. and P. Michaud, *MC X-Ray, a new Monte Carlo program for quantitative X-ray microanalysis of real materials.* Microscopy and Microanalysis, 2009. **15**(S2): p. 488-489.
23. Armigliato, A., *X-ray Microanalysis in the Analytical Electron Microscope*. 1992, Singapore, World Scientific. p. 431-456.
24. Kak, A. and M. Slaney, *Principles of computerized tomographic imaging IEEE Press.* New York, 1988.
25. Gregor, J. and T. Benson, *Computational analysis and improvement of SIRT.* IEEE transactions on medical imaging, 2008. **27**(7): p. 918-924.
26. Gilbert, P., *Iterative methods for the three-dimensional reconstruction of an object from projections.* Journal of theoretical biology, 1972. **36**(1): p. 105-117.
27. Leary, R.K. and P.A. Midgley, *Electron Tomography in Materials Science*, in *Springer Handbook of Microscopy*. 2019, Springer. p. 2-2.
28. Nikazad, T. and M. Karimpour, *Controlling semi-convergence phenomenon in non-stationary simultaneous iterative methods.* Iranian Journal of Numerical Analysis and Optimization, 2016. **6**(2): p. 51-64.

29. Hansen, P.C. and M. Saxild-Hansen, *AIR tools—a MATLAB package of algebraic iterative reconstruction methods.* Journal of Computational and Applied Mathematics, 2012. **236**(8): p. 2167-2178.
30. Hawkes, P., *Electron Tomography: 3D imaging in the TEM*. 1992, New York: Plenum.
31. Zhong, Z., et al., *Numerical methods for low-dose EDS tomography.* Ultramicroscopy, 2018. **194**: p. 133-142.
32. Browning, R., *Universal elastic scattering cross sections for electrons in the range 1–100 keV.* Applied physics letters, 1991. **58**(24): p. 2845-2847.
33. Bote, D., et al., *Cross sections for ionization of K, L and M shells of atoms by impact of electrons and positrons with energies up to 1 GeV: Analytical formulas.* Atomic Data and Nuclear Data Tables, 2009. **95**(6): p. 871-909.
34. Perkins, S., et al., *Tables and graphs of atomic subshell and relaxation data derived from the LLNL Evaluated Atomic Data Library (EADL), Z= 1--100*. 1991, Lawrence Livermore National Lab., CA (United States).
35. Hasinoff, S.W., *Photon, Poisson Noise*. 2014.
36. Virtanen, P., et al., *SciPy 1.0: fundamental algorithms for scientific computing in Python.* Nature methods, 2020. **17**(3): p. 261-272.
37. Wang, Z., et al., *Image quality assessment: from error visibility to structural similarity.* IEEE transactions on image processing, 2004. **13**(4): p. 600-612.
38. Ruder, S., *An overview of gradient descent optimization algorithms.* arXiv preprint arXiv:1609.04747, 2016.
39. Park, K.S., et al., *Exceptional chemical and thermal stability of zeolitic imidazolate frameworks.* Proceedings of the National Academy of Sciences, 2006. **103**(27): p. 10186-10191.
40. de la Peña, F., et al., *HyperSpy 1.3*. 2017, Hyperspy.
41. Slater, T., et al. *Understanding the limitations of the Super-X energy dispersive X-ray spectrometer as a function of specimen tilt angle for tomographic data acquisition in the S/TEM*. in *Journal of Physics: Conference Series*. 2014. IOP Publishing.

6.8 Supplementary materials

To visualize the intensity variation across the boundary, we plotted the intensity profiles for the reconstructed elemental maps along the red line shown in Figure 6.18 a). Figure 6.18 b) and c) show the intensity profiles for the elemental maps reconstructed using HEBT when $n = 200$ (Figure 6.9). The boundaries between the core and shell of the particle locate at the position of ~65 and ~115 nm. As α increases, the slope of the intensity profile near the boundaries decreases for both Ag and Au, indicating that the boundary becomes blurry.

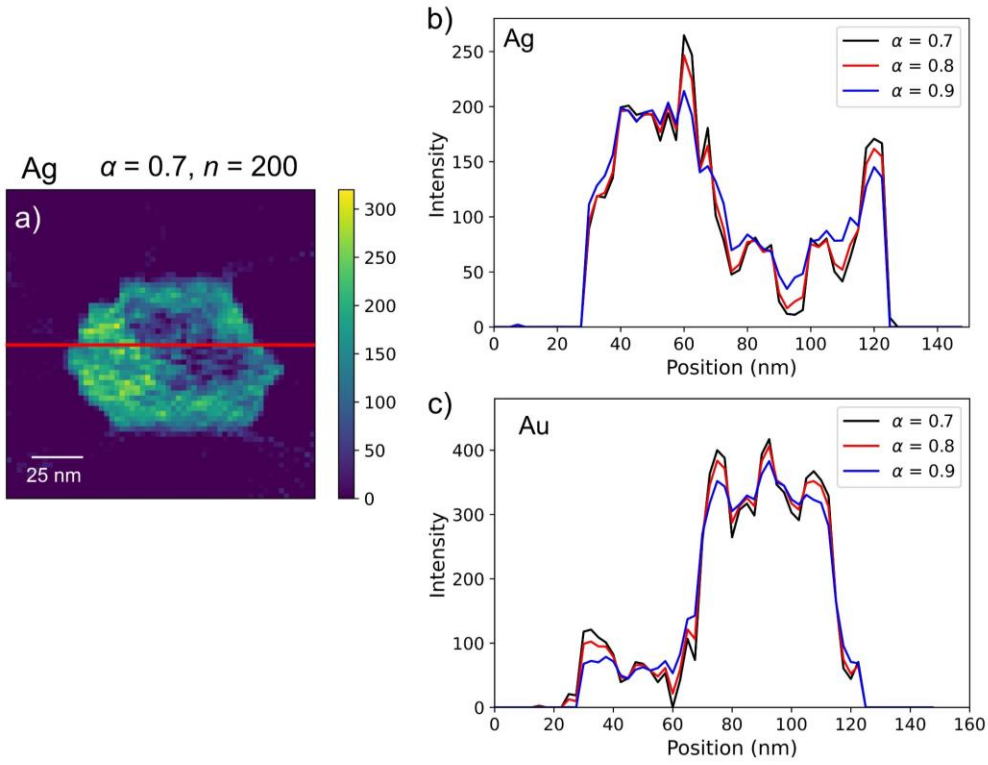

Figure 6.18 a) Elemental map of Ag reconstructed using HEBT for α = 0.7 and n = 200. Intensity profiles for elemental maps of b) Ag (Figure 6.9 a, b, and c) and c) Au (Figure 6.9 d, e, and f) reconstructed using HEBT with different α when n = 200. The intensity profiles were taken along the red line shown in a).

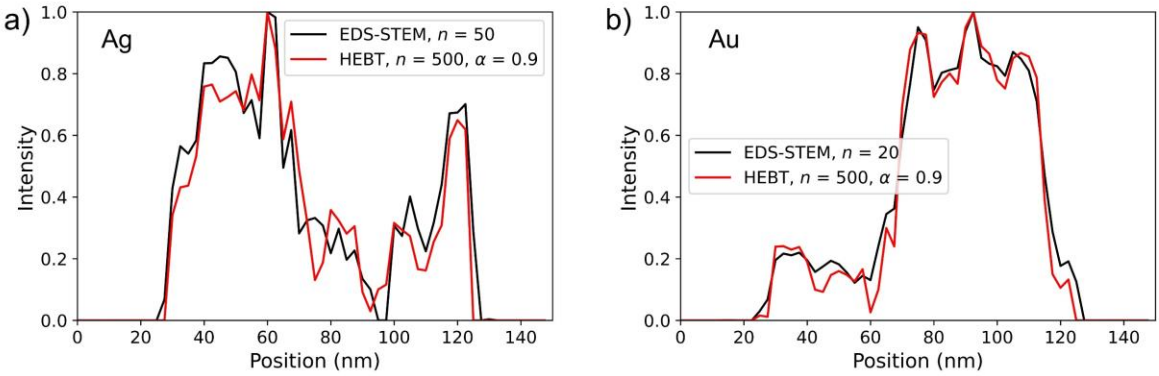

Figure 6.19 Intensity profiles for elemental maps of a) Ag and b) Au reconstructed using the EDS-STEM tomography when n = 50 and 20 for Ag and Au, respectively (Figure 6.3 b and d), and using the HEBT when n = 500 and α = 0.9 (Figure 6.10 c and f) along the red line shown in Figure 6.18 a). Note that the intensities for each elemental map were divided by the maximum value along the line since the intensities for the EDS-STEM tomography reconstruction and the HEBT reconstruction are not at the same scale.

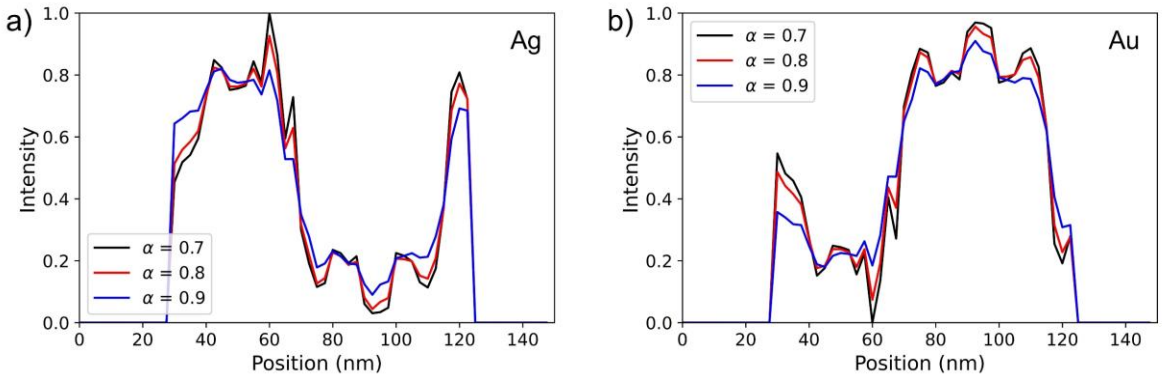

Figure 6.20 Intensity profiles for quantitative elemental maps of a) Ag (Figure 6.11 a, b, and c) and b) Au (Figure 6.11 d, e, and f) reconstructed using HEBT with different α when n = 200 along the red line shown in Figure 6.18 a).

Figure 6.19 compares the intensity profiles of the elemental maps reconstructed using the EDS-STEM tomography and HEBT for Ag and Au. For both reconstruction techniques, the elemental map with the best image quality was chosen for comparison, which is obtained when n = 50 for Ag (Figure 6.3 b) and n = 20 for Au (Figure 6.3 d) for the EDS-STEM tomography, and when n = 500 and α = 0.9 for HEBT (Figure 6.10 c and f). Since the intensities for the elemental maps reconstructed using the two techniques are not at the same scale, the intensities for each line profile were divided by the maximum value along the line to be compared with each other. The exterior boundaries of the particle show up at the position of ~30 nm on the left and ~125 nm on the right. The slope for the boundary on the left side is similar for the two techniques, while the boundary on the right side is sharper for HEBT (red line) than the EDS-STEM tomography (black line).

Figure 6.20 presents the intensity profiles for the quantitative elemental maps reconstructed using HEBT when n = 200 with various α (Figure 6.11). Similarly, the boundary between the core and the shell becomes blurrier as α increases.

Chapter 7. Concluding remarks

7.1 Conclusions

The main objective of this work is to improve the accuracy and universality of quantitative electron-induced X-ray microanalysis for heterogeneous materials. Specifically, a secondary fluorescence correction program, available for three-dimensional (3D) heterogeneous materials, was developed in Chapter 3 and Chapter 4; Chapter 5 introduced a novel inverse modeling algorithm to extract the compositional and structural information simultaneously; and Chapter 6 focused on the quantitative scanning transmission electron microscopy (STEM) tomographic reconstruction. The conclusions are summarized as follows:

1. A secondary fluorescence correction program, applicable to homogeneous and multilayer specimens, was developed using a hybrid model that combines the Monte Carlo simulation and an analytical model. The program uses MC X-ray, a Monte Carlo program, to obtain the generated X-ray intensities and depth distribution curves of the primary X-rays (both characteristic and bremsstrahlung). This information is then used to calculate the multiple integrals in the analytical formula numerically to obtain the secondary fluorescence intensity.

2. The accuracy of the program was tested by comparing the results with both experimental data from references and simulation data from other software (DTSA-II and PENEPMA). In general, suitable matches were shown for both homogeneous bulk and multilayer samples. However, for an Fe substrate with a Ni coating, the calculated bremsstrahlung fluorescence intensity of the Fe Kα line was slightly larger than the data from other software. This was explained by the difference in the bremsstrahlung X-ray intensities arising from different bremsstrahlung cross-section models used in Monte Carlo programs.

   The practicality of the program was evaluated using an efficiency-like metric ϵ_Q, which considers both the computation time and the uncertainty of the value, and compared with other software. When the simulated electron numbers were the same, PENEPMA showed

the worst efficiency due to the high uncertainty. The efficiencies of DTSA-II and our program were at a similar level.

3. The secondary fluorescence correction program was then extended to apply to arbitrary 3D heterogeneous materials using a similar hybrid model by extracting 3D distribution of the primary X-rays from MC X-ray and deriving the analytical formula for small voxels instead of thin slices. An algorithm "SkipVoxel" was proposed to improve the computation efficiency for the voxels out of the primary interaction volume, and it saved more than 80% of the simulation time with a less than 0.1% change in fluorescence intensity. The application of the program was presented for non-diffusion couples and spherical particles embedded inside a matrix. The results demonstrated good agreement with experimental and analytical results from previous studies and simulation results from other Monte Carlo codes. MC X-ray, combined with the fluorescence correction program, provides an accurate prediction of X-ray emission.

4. Following the secondary fluorescence correction, a novel inverse modeling algorithm was introduced to determine the structure and composition of an unknown specimen simultaneously from a series of EDS/WDS experimental measurements under different beam energies and beam positions. The algorithm can be applied to arbitrary 2D heterogeneous materials. It uses an iterative process of forward modeling to determine the optimal composition of each voxel of the specimen to minimize the relative differences between the simulated and experimental X-ray intensities.

   Tests were performed for the simulation dataset of phantom samples to evaluate the performance of the algorithm. For 1D specimens, including multilayer samples and coupled samples separated by vertical boundaries, the results were found to be very close with the phantom samples when appropriate input parameters, including beam positions, beam energies, and voxel size, were chosen. For 2D specimens, the features located at shallower depths were well recognized, while some discrepancies were shown for the features located at deeper depths. These discrepancies were attributed to the errors from the forward modeling and the increased X-ray range with beam energy.

5. A new quantification approach was proposed using the physical parameters acquired from MC X-ray to quantify the 3D elemental distribution of nanostructures reconstructed from

electron tomography. We have shown the feasibility of the quantification approach for EDS-STEM tomography and HAADF-EDS bimodal tomography (HEBT) applied to a simulation dataset of a 2D phantom sample (a single slice) and an experimental dataset of a particle of flux melted metal-organic framework glass.

For the flux melted metal-organic framework glass, the reconstructed weigh fraction maps showed the diffusion of the Zn-rich domain and the Co-rich domain into each other. The EDS-STEM tomography quantification factors calculated using our approach have shown good consistency with the experimentally measured partial cross-sections from reference. In general, HEBT has shown advantages in image contract, boundary determination, and noise reduction in comparison to EDS-STEM tomography due to the high signal-to-noise ratio (SNR) information from the HAADF signal.

7.2 Contributions to original knowledge

The contributions to original knowledge made in this work are summarized as follows:

1. For the first time, this study quantitatively evaluated the practicality of a secondary fluorescence correction program using an efficiency-like metric. The metric considers both the computation time and the uncertainty of the calculated quantity.
2. This is the first study to calculate the secondary fluorescence for voxels, making the approach applicable to arbitrary 3D heterogeneous materials.
3. The inverse modeling algorithm proposed in this work is the first to extract the compositional and structural information simultaneously for an arbitrary 2D heterogeneous material.
4. This is the first study to use the clustering algorithm to estimate possible specimen segmentation in X-ray microanalysis inverse modeling.
5. This study, for the first time, quantified the 3D elemental distribution reconstructed from HEBT, through which high-resolution elemental weight fraction maps were obtained.
6. This is the first study to compare the image qualities of the quantified elemental maps from EDS-STEM tomography and HEBT.

7.3 Future work

1. The developed secondary fluorescence correction program, together with MC X-ray, will be integrated into Dragonfly, a software platform for image analysis, through which the efficiency of the code will be improved, and the new version can simulate the X-ray emission for both designed phantom specimens and experimental datasets.

2. For the inverse modeling algorithm, the determination of the input parameters, including beam energies, beam positions, and voxel size, needs to be further investigated. The algorithm needs to be optimized to recognize the feature located in deeper depths. Furthermore, using the K-line and L-line simultaneously may improve the accuracy of the algorithm.

3. With a better understanding of the algorithm, the 2D inverse modeling algorithm can be extended to 3D inverse modeling in the future.

4. In the current study, the simultaneous iterative reconstruction technique (SIRT) was used for both EDS-STEM tomographic and HEBT reconstruction. More advanced reconstruction techniques can be used to replace SIRT for future work to improve the reconstructed image.